

University of Windsor

Scholarship at UWindor

Electronic Theses and Dissertations

Theses, Dissertations, and Major Papers

2014

Investigation of metallurgical coatings for automotive applications

Jun Feng Su
University of Windsor

Follow this and additional works at: <https://scholar.uwindsor.ca/etd>

Recommended Citation

Su, Jun Feng, "Investigation of metallurgical coatings for automotive applications" (2014). *Electronic Theses and Dissertations*. 5104.
<https://scholar.uwindsor.ca/etd/5104>

This online database contains the full-text of PhD dissertations and Masters' theses of University of Windsor students from 1954 forward. These documents are made available for personal study and research purposes only, in accordance with the Canadian Copyright Act and the Creative Commons license—CC BY-NC-ND (Attribution, Non-Commercial, No Derivative Works). Under this license, works must always be attributed to the copyright holder (original author), cannot be used for any commercial purposes, and may not be altered. Any other use would require the permission of the copyright holder. Students may inquire about withdrawing their dissertation and/or thesis from this database. For additional inquiries, please contact the repository administrator via email (scholarship@uwindsor.ca) or by telephone at 519-253-3000ext. 3208.

INVESTIGATION OF METALLURGICAL COATINGS FOR AUTOMOTIVE APPLICATIONS

by

Jun Feng Su

A Dissertation

Submitted to the Faculty of Graduate Studies
through Mechanical, Automotive & Materials Engineering
in Partial Fulfillment of the Requirements for
the Degree of Doctor of Philosophy at the
University of Windsor
Windsor, Ontario, Canada

2014

©2014 Jun Feng Su

Investigation of Metallurgical Coatings for Automotive Applications

by

Jun Feng Su

APPROVED BY:

Zhibin Ye, External Examiner
Bharti School of Engineering, Laurentian University

C. Chen
Department of Electrical & Computer Engineering

J. Sokolowski
Department of Mechanical, Automotive & Materials Engineering

V. Stoilov
Department of Mechanical, Automotive & Materials Engineering

X. Nie, Advisor
Department of Mechanical, Automotive & Materials Engineering

H. Hu, Advisor
Department of Mechanical, Automotive & Materials Engineering

June 2, 2014

DECLARATION OF CO-AUTHORSHIP/PREVIOUS PUBLICATION

I. CO- AUTHORSHIP DECLARATION

I hereby declare that this dissertation does not incorporate material that is result of joint research. In all cases, the key ideas, primary contributions, experimental designs, data analysis and interpretation, were performed by the author and Dr. H. Hu and Dr. X. Nie as advisors.

I certify that, with the above qualification, this dissertation, and the research to which it refers, is the product of my own work.

II. DECLARATION OF PREVIOUS PUBLICATION

This dissertation includes 5 original papers/reports that have been previously published/submitted for publication in peer reviewed journals/conference proceedings/research reports, as follows:

Thesis Chapter	Publication title/full citation	Publication status
Chapter 2	Jun Feng Su , Xueyuan Nie, Henry Hu, Jimi Tjong, “Friction and counterface wear influenced by surface profiles of plasma electrolytic oxidation coatings on an aluminum A356 alloy”, <i>Journal of Vacuum Science & Technology A</i> , (2012) Vol. 30, 061402-1-11	Published
Chapter 3	Jun Feng Su , Xueyuan Nie, Henry Hu, “Numerical Simulation of Boundary/mixed Lubrication of Plasma Electrolytic Oxidation Coatings under Reciprocating Movement”, <i>STLE Tribology Frontiers Conference</i> , (2014)	Submitted
Chapter 4	Jun Feng Su , Xueyuan Nie, “Characterization of the failure	Published

	mechanisms of thin hard coatings using the impact test”, Auto/Steel Partnership, (2009) Project: ASP230, No.09-2330, Phase I, http://www.a-sp.org/en/Enabling%20Technologies.aspx	
Chapter 5	Jun Feng Su , Xueyuan Nie, Tareena Mulholland, “Combinative influence of impact and pressing forces on coating failure behaviour”, <i>Surface & Coatings Technology</i> (2010) Vol. 205, pp. 1520-1526	Published
Chapter 6	Jun Feng Su , Xueyuan Nie, “Characterization of the failure mechanisms of thin hard coatings using the inclined impact-sliding test”, Auto/Steel Partnership, (2010) Project: ASP230, No. 10-2338, Phase II, http://www.a-sp.org/en/Enabling%20Technologies.aspx	Published
Chapter 7	Jun Feng Su , David Yu, Xueyuan Nie, Henry Hu, “Inclined impact–sliding wear tests of TiN/Al ₂ O ₃ /TiCN coatings on cemented carbide substrates”, <i>Surface & Coatings Technology</i> (2011) Vol. 206, pp. 1998-2004	Published
Chapter 8	Jun Feng Su , Xueyuan Nie, Henry Hu, Darryl Young, Donald Adamski, Dajun Zhou, Eric McCarty, “Substrate effects on failure behavior of hard coatings under inclined cyclical loading conditions”, <i>Nanosmat Conference</i> , (2014)	Submitted

I hereby certify that I have obtained a written permission from the copyright owner(s) to include the above published material(s) in my dissertation. I certify that the above material describes work completed during my registration as graduate student at the University of Windsor. I declare that, to the best of my knowledge, my dissertation does not infringe upon anyone’s copyright nor violate any proprietary rights and that any ideas, techniques, quotations, or any other material from the work of other people

included in my dissertation, published or otherwise, are fully acknowledged in accordance with the standard referencing practices. Furthermore, to the extent that I have included copyrighted material that surpasses the bounds of fair dealing within the meaning of the Canada Copyright Act, I certify that I have obtained a written permission from the copyright owner(s) to include such material(s) in my dissertation.

I declare that this is a true copy of my dissertation, including any final revisions, as approved by my dissertation committee and the Graduate Studies office, and that this dissertation has not been submitted for a higher degree to any other University or Institution.

ABSTRACT

Metallurgical coatings have been widely used in the automotive industry from component machining, engine daily running to body decoration due to their high hardness, wear resistance, corrosion resistance and low friction coefficient. With high demands in energy saving, weight reduction and limiting environmental impact, the use of new materials such as light Aluminum/magnesium alloys with high strength-weight ratio for engine block and advanced high-strength steel (AHSS) with better performance in crash energy management for die stamping, are increasing. However, challenges are emerging when these new materials are applied such as the wear of the relative soft light alloys and machining tools for hard AHSS. The protective metallurgical coatings are the best option to profit from these new materials' advantages without altering largely in mass production equipments, machinery, tools and human labor.

In this dissertation, a plasma electrolytic oxidation (PEO) coating processing on aluminum alloys was introduced in engine cylinder bores to resist wear and corrosion. The tribological behavior of the PEO coatings under boundary and starve lubrication conditions was studied experimentally and numerically for the first time. Experimental results of the PEO coating demonstrated prominent wear resistance and low friction, taking into account the extreme working conditions. The numerical elastohydrodynamic lubrication (EHL) and asperity contact based tribological study also showed a promising approach on designing low friction and high wear resistant PEO coatings.

Other than the fabrication of the new coatings, a novel coating evaluation methodology, namely, inclined impact sliding tester was presented in the second part of this dissertation. This methodology has been developed and applied in testing and

analyzing physical vapor deposition (PVD)/ chemical vapor deposition (CVD)/PEO coatings. Failure mechanisms of these common metallurgical hard coatings were systematically studied and summarized via the new testing methodology. Field tests based on the new coating characterization technique proved that this methodology is reliable, effective and economical.

DEDICATION

I would like to dedicate this dissertation to my wife and my son for their unconditional love, support and encouragement.

I also would like to thank Dr. Xueyuan Nie and Dr. Henry Hu for their unwavering support and encouragement over the years.

ACKNOWLEDGEMENTS

This study could not have been done forward without the financial support from the Ontario Graduate Scholarship (OGS), Natural Sciences and Engineering Council of Canada (NSERC) and partially by Auto/Steel Partnership (A/S P), USA.

I would like to thank my doctoral advisor, Dr. Henry Hu and Dr. Xueyuan Nie, for their valuable suggestions and excellent supervision of this research work during my study.

Many thanks to my committee members(Dr. Jerry Sokolowski, Dr. Vesselin Stoilov, Dr. Chunhong Chen) for their helpful comments and careful review of this work.

I would like to thank Mr. Andy Jenner from University of Windsor for their assistance with the experiments.

Finally, I am thankful to the faculty, staff and graduate students at the Department of Mechanical, Automotive and Materials Engineering of the University of Windsor, particularly my colleagues at the Plasma Surface Engineering/Thin Films and Coatings Research lab, for their support and encouragement.

TABLE OF CONTENTS

DECLARATION OF CO-AUTHORSHIP/PREVIOUS PUBLICATION.....	III
ABSTRACT.....	VI
DEDICATION.....	VIII
ACKNOWLEDGEMENTS	IX
LIST OF TABLES	XV
LIST OF FIGURES	XVI
NOMENCLATURE.....	XXV
SUBSCRIPTS.....	XXVIII
CHAPTER 1 INTRODUCTION.....	1
1. GENERAL OVERVIEW.....	1
2. MOTIVATION.....	3
3. OBJECTIVES	3
4. OUTLINE OF THIS DISSERTATION.....	4
5. METALLURGICAL COATINGS.....	6
6. NUMERICAL LUBRICATION METHOD.....	18
7. COATING CHARACTERIZATION.....	27
8. SUMMARY	30
REFERENCES.....	30
CHAPTER 2 FRICTION AND COUNTERFACE WEAR INFLUENCED BY SURFACE PROFILES OF PLASMA ELECTROLYTIC OXIDATION (PEO) ON AN ALUMINUM A356 ALLOY	39
1.INTRODUCTION	39
2. EXPERIMENT	43
2.1. Materials and PEO process	43
2.2. Tribological tests.....	45
3. RESULTS AND DISCUSSION	47
3.1 COFs	53

3.1.1 PTWA: boundary lubrication vs. starve lubrication	53
3.1.2 PEO S1: boundary lubrication vs. starve lubrication.....	53
3.1.3 PEO S1: as-deposited vs. sanded vs. polished.....	57
3.1.4 PEO S2: boundary lubrication vs. starve lubrication.....	57
3.1.5 PEO S2: as-deposited vs. sanded vs. polished.....	58
3.2 Wear tracks on the coatings	60
3.3 Wear scars on the steel pins	62
4. CONCLUSIONS	67
REFERENCES.....	69

**CHAPTER 3 NUMERICAL SIMULATION OF BOUNDARY/MIXED
LUBRICATION OF PLASMA ELETROLYTIC OXICATION COATINGS
UNDER RECIPROCATING MOVEMENT 73**

1.INTRODUCTION	73
2. SIMUATION.....	75
3. EXPERIMENTAL CASE STUDY	84
4. CONCLUSIONS	87
REFERENCES.....	88

**CHAPTER 4 CHARACTERIZATION OF THE FAILURE MECHANISMS OF
THIN HARD COATINGS USING THE IMPACT TEST..... 89**

1. INTRODUCTION.....	89
2. EXPERIMENTAL DETAILS	90
3. RESULTS AND DISCUSSION	93
3.1 Nanoindentation and microhardness tests.....	93
3.2 Impact fatigue test.....	95
3.2.1 Typical failures	97
3.2.1.1 Cohesive failures.....	97
3.2.1.2 Adhesive failures	98
3.2.1.3 Fatigue cracks	99

3.2.1.4 Materials transfer	100
3.2.2 Experimental results.....	101
3.2.2.1 Hardened SAE 52100 steel ball, 10000 cycles	101
3.2.2.2 Hardened SAE 52100 steel ball, 50000 cycles	110
3.2.2.3 Tungsten carbide (WC) ball, 10000 cycles.....	113
3.2.2.4 Tungsten carbide (WC) ball, 50000 cycles.....	118
3.2.3 Ranking of coatings	123
3.3 FEM analysisImpact fatigue test.....	125
3.3.1 Displacement.....	128
3.3.2 A typical impact process by simulation.....	129
3.3.3 Maximal von Mises stress in the coating.....	129
3.3.3.1 A_TiAlN	130
3.3.3.2 B_TiAlN	133
3.3.3.3 A_CrN.....	135
3.3.3.4 B_CrN.....	136
3.3.3.5 B_TiC.....	138
3.3.3.6 C_TiC.....	140
3.3.4 Remarks	141
4. CONCLUSIONS	142
5. FUTURE WORK IN PHASE II.....	143
REFERENCES.....	144
APPENDIX A.....	145
CHAPTER 5 COMBINATIVE INFLUENCE OF IMPACT AND PRESSING FORCES ON COATING FAILURE BEHAVIOUR.....	149
1. INTRODUCTION	149
2. EXPERIMENTAL DETAILS	150
2.1 The impact factor	150
2.2 Hard coatings	152
2.3 Impact procedure	153
3. RESULTS AND DISCUSSION	153

4. CONCLUSIONS.....	165
REFERENCES.....	167
CHAPTER 6 CHARACTERIZATION OF THE FAILURE MECHANISMS OF THIN HARD COATINGS USING THE INCLINED IMPACT-SLIDING TEST	169
1.INTRODUCTION	169
2. EXPERIMENTAL DETAILS	170
3. RESULTS AND DISCUSSION	170
3.1 Nanoindentation tests.....	172
3.2 Inclined impact fatigue tests	173
3.2.1 Impact and pressing force loading curves.....	173
3.2.2 Typical failures	174
3.2.3 Experimental results.....	175
3.2.3.1 Hardened SAE 52100 steel ball, 1500 cycles	175
3.2.3.2 Hardened SAE 52100 steel ball, 10000 cycles	181
3.2.3.3 Cross section of selected impact-sliding tracks	182
3.3 Ranking of coatings	191
4. CONCLUSIONS	192
CHAPTER 7 INCLINED IMPACT-SLIDING WEAR TEST OF TIN/AL₂O₃/TICN COATINGS ON CEMENTED CARBIDE SUBSTRATES.....	194
1.INTRODUCTION	194
2. EXPERIMENTAL DETAILS	196
3. RESULTS	198
4. DISCUSSION	206
5. CONCLUSION	209
REFERENCE	211
CHAPTER 8 SUBSTRATE EFFECTS ON FAILURE BEHAVIOR OF HARD COATINGS UNDER INCLINED CYCLICAL LOADING CONDITIONS.....	214
1.INTRODUCTION	214
2. EXPERIMENTAL DETAILS	215
3. RESULTS AND DISCUSSION	218

3.1 Mechanical properties of CrN coating and steel substrates	218
3.2 Inclined impact-sliding wear tracks	220
3.2.1 AISI D2	220
3.2.2 NAAMS S2333	222
3.2.3 Toolox 44	224
3.3 Discussion	226
4. CONCLUSIONS	228
REFERENCES	230
CHAPTER 9 CONCLUSIONS AND FUTURE WORK	233
1. GENERAL CONCLUSIONS	233
2. SUGGESTIONS FOR FUTURE WORK	237
CHAPTER 10 CLAIMS TO ORIGINALITY	239
APPENDIX A COPYRIGHT RELEASES FROM PUBLICATIONS	240
CHAPTER 2	240
CHAPTER 4 & 6	241
CHAPTER 5	242
CHAPTER 7	248
PUBLICATION LIST	254
VITA AUCTORIS	257

LIST OF TABLES

Table 1.1 An overall comprison of various surface engineering.....	8
Table 2.1 Process parameters and properties of as deposited PEO coatings and a PTWA coating.....	45
Table 2.2 Average roughness parameters of as deposited, sanded and polished coatings.....	47
Table 3.1 Wear loads of coated samples and steel balls.....	81
Table 3.2 DOE factors.....	82
Table 4.1 Ranking of coating failures under steel ball impacting.....	124
Table 4.2 Ranking of coating failures under WC ball impacting.....	125
Table 4.3 Simulated maximal von Mises stress in the coating and shear stress in the cohesive layer.....	141
Table 5.1 Thickness and mechanical properties of coatings.....	153
Table 6.1 Ranking of coating failures in inclined impact-sliding tests using steel balls.....	192
Table 8.1 Chemical Composition of substrates	216
Table 8.2 Thickness, hardness and elastic modulus of coatings on the tested substrates.....	219

LIST OF FIGURES

Figure 1.1 Coatings for automotive applications.....	7
Figure 1.2 Approximate thickness of various surface engineering treatments.....	9
Figure 1.3 Hardness versus distance from the surface for soft steels with (a) a plasma nitriding treatment (PN), (b) PVD coating, and (c) combination nitriding plus PVD coating. CZ: compound zone, DZ: diffusion zone.....	9
Figure 1.4 Different piston ring treatments and the trend of the wear and scuffing.....	10
Figure 1.5 Surface engineering processes used to prevent wear. CVD, chemical vapor deposition; PVD, physical vapor deposition; EB, electron beam	10
Figure 1.6 Thermal spray coating defects.....	12
Figure 1.7 PVD Processing Techniques.....	13
Figure 1.8 Typical CVD techniques.....	14
Figure 1.9 A typical PEO equipment.....	16
Figure 1.10 Electrode processes in electrolysis of aqueous solutions.....	17
Figure 1.11 Two kinds of current-voltage diagram for PEO processes.....	18
Figure 1.12 Schematic of Stribeck curve.....	19
Figure 1.13 Effect of surface roughness on average film thickness of EHL contact.....	25
Figure 1.14 2010 Light vehicle material content.....	27

Figure 1.15 Typical tribological test methods for coatings.....	29
Figure 2.1 XRD patterns (Cu K α) of the PEO coatings on the A356 alloy.....	48
Figure 2.2 SEM images of surface morphology and EDX spectra of the PTWA and PEO coatings.....	49
Figure 2.3 Schematic of surfaces with (a) positive and negative skewness and (b) kurtosis values lower and higher than three.....	51
Figure 2.4 The average COFs of PTWA and PEO coatings under two different lubrication conditions.....	52
Figure 2.5 Typical surface profiles: (a) PTWA coating and PEO coatings at (b) as-deposited, (c) sanded and (d) polished conditions. SEM images of PEO coatings after sanded and polished to (e) Ra 0.71, (f) Ra 0.42 μm , (g) Ra 0.17 μm and (h) Ra 0.1 μm	55
Figure 2.6 Wear tracks. (a) PTWA_B, (b) PTWA_S and (c) PEO S1_S and (d) EDX spectrum of the bright area in (c) showing material transferred from the steel pin.....	61
Figure 2.7 Experimental data and fitting curves of wear rate of steel pins and average COFs vs (a, d) Ra, (b, e) skewness and (c, f) kurtosis respectively.....	65
Figure 3.1 GT-Suite multibody model of a reciprocating ball-on-plate tribometer.....	76
Figure 3.2 The composite surface standard deviation σ and the asperity radius of curvature β for Greenwood-Tripp asperity contact model.....	78

Figure 3.3 Simulated friction forces of steel ball sliding on coatings.....	80
Figure 3.4 Normalized ternary diagrams of elastic modulus, asperity radius of curvature and asperity density effects on: (a) hydrodynamic friction power loss, (b) asperity contact friction power loss, (c) wear load on steel ball and (d) wear load on coated surfaces.....	83
Figure 3.5 Friction forces of steel balls sliding against coated samples under boundary lubrication (solid lines).....	85
Figure 4.1 Schematic view of the impact fatigue test arrangement.....	91
Figure 4.2 Typical failure zones encountered after the impact fatigue test.....	92
Figure 4.3 Vickers hardness and Berkovich hardness of different coatings. A, B and C denote different suppliers respectively.....	94
Figure 4.4 Elastic modulus of different coatings by nanoindentation.....	96
Figure 4.5 Impacting forces at 10 Hz impact frequency with 0.3 mm gap between ball and sample surface.....	96
Figure 4.6 One pulse showing both the wavy impulse caused by momentum of mass and the wide trough caused by compressive air.....	96
Figure 4.7 Cohesive failure – chipping of the coating. (a) is SEM image of the chipping; (b) is composition at the center of the chipping.....	97

Figure 4.8 Adhesive failures: (a) Peeling; (b) EDS of (a); (c) circular cracks around the crater.....	99
Figure 4.9 Fatigue cracks in the formation of micro bands of A_TiAlN sample.....	100
Figure 4.10 Materials transfer: Tungsten from the WC ball at the B_TiC coating surface. Oxygen appears in the EDS spectrum.....	101
Figure 4.11 A_TiAlN after 10000 cycles (steel ball).....	103
Figure 4.12 B_TiAlN after 10000 cycles (steel ball).....	104
Figure 4.13 A_CrN after 10000 cycles (steel ball).....	106
Figure 4.14 B_CrN after 10000 cycles (steel ball).....	108
Figure 4.15 B_TiC after 10000 cycles (steel ball).....	109
Figure 4.16 C_TiC after 10000 cycles (steel ball).....	109
Figure 4.17 A_CrN after 50000 cycles (steel ball).....	110
Figure 4.18 B_CrN after 50000 cycles (steel ball).....	111
Figure 4.19 B_TiC after 50000 cycles (steel ball).....	112
Figure 4.20 C_TiC after 50000 cycles (steel ball).....	112
Figure 4.21 Diameters of craters after 10000 and 50000 cycles of steel ball impact tests	113

Figure 4.22 A_TiAlN after 10000 cycles (WC ball).....	114
Figure 4.23 B_TiAlN after 10000 cycles (WC ball).....	115
Figure 4.24 A_CrN after 10000 cycles (WC ball).....	115
Figure 4.25 B_CrN after 10000 cycles (WC ball).....	116
Figure 4.26 B_TiC after 10000 cycles (WC ball).....	117
Figure 4.27 C_TiC after 10000 cycles (WC ball).....	118
Figure 4.28 A_TiAlN after 50000 cycles (WC ball).....	119
Figure 4.29 B_TiAlN after 50000 cycles (WC ball).....	119
Figure 4.30 A_CrN after 50000 cycles (WC ball).....	120
Figure 4.31 B_CrN after 50000 cycles (WC ball).....	120
Figure 4.32 B_TiC after 50000 cycles (WC ball).....	121
Figure 4.33 C_TiC after 50000 cycles (WC ball).....	122
Figure 4.34 Diameters of craters impacted by WC balls after 10000 and 50000 cycles.....	123
Figure 4.35 Simulation model of ball-on-plate impact test.....	126
Figure 4.36 A typical mesh denoting the impact ball, coating, interfacial layer and Steel substrate.....	128
Figure 4.37 Von Mises stress distribution of B_CrN during steel ball impact test.....	130

Figure 4.38 A_TiAlN stress distribution at the maximal impact load.....	132
Figure 4.39 B_TiAlN stress distribution at the maximal impact load.....	134
Figure 4.40 A_CrN stress distribution at the maximal impact load.....	136
Figure 4.41 B_CrN stress distribution at the maximal impact load.....	138
Figure 4.42 B_TiC stress distribution at the maximal impact load.....	139
Figure 4.43 C_TiC stress distribution at the maximal impact load.....	140
Figure 5.1 Schematic of the impact tester.....	152
Figure 5.2 Impact forces FI and pressing forces Fp at different distances d under a 400 N driving force FD for one cycle.....	155
Figure 5.3 Crater diameters under different impact forces after 10,000 impact cycles...	157
Figure 5.4 SEM images of coatings after 10,000 impact cycles.....	158
Figure 5.5 SEM images and EDX spectra showing the crater of the CrN coating tested under a 600 N impact force.....	160
Figure 5.6 SEM images and EDX spectra showing failures of the TiAlN coating under a 200 N impact force.....	162
Figure 5.7 SEM images showing failures of the TiAlN and TiC coatings.....	164
Figure 6.1 Schematic of an inclined impact-sliding tester. To the right, a typical normal force vs. time curve during an impact-sliding cycle.....	171

Figure 6.2 Berkovich hardness of different coatings (Phase I & II). A, B and C denotes different suppliers respectively.....	172
Figure 6.3 Elastic modulus of different coatings (Phase I & II) by nanoindentation.....	173
Figure 6.4 A typical load cycle at 5 Hz impact frequency.....	174
Figure 6.5 SEM images and Illustration of failure modes.....	175
Figure 6.6 SEM images of the impact-sliding track of A_TiAlN after 1500 cycles.....	176
Figure 6.7 SEM images of the impact-sliding track of B_TiAlN after 1500 cycles.....	177
Figure 6.8 SEM images of the impact-sliding track of A_CrN after 1500 cycles.....	178
Figure 6.9 SEM images of the impact-sliding track of B_CrN after 1500 cycles.....	179
Figure 6.10 SEM image of the impact-sliding track of B_TiC after 1500 cycles.....	180
Figure 6.11 SEM images of the impact-sliding track of C_TiC after 1500 cycles.....	180
Figure 6.12 SEM images of the impact-sliding track of B_TiC after 10000 cycles.....	181
Figure 6.13 Summary of the impact-sliding tracks of six coatings after 1500 cycles....	182
Figure 6.14 Overall SEM image of the cross section of the B_CrN impact-sliding track after 1500 cycles using a steel ball.....	183
Figure 6.15 Local views of the cross section in Figure 6.14.....	185
Figure 6.16 Overall SEM image of the cross section of the A_TiAlN impact-sliding track after 1500 cycles using a steel ball.....	186

Figure 6.17 Local views of the cross section in Figure 6.16.....	187
Figure 6.18 Overall SEM image of the cross section of the B_TiC impact-sliding track after 10000 cycles using a steel ball.....	188
Figure 6.19 Local views of the cross section in Figure 6.18.....	190
Figure 7.1 Optical images of the wear tracks (craters at left and tails at right) on (a) PM10C, (b) PM25C, (c) PM30C and wear scars on counterpart balls corresponding to (d) PM10C, (e) PM25C and (f) PM30C.....	199
Figure 7.2 SEM (SE) images of the wear scars on (a) PM10C, (b) PM25C and (c) PM30C.....	200
Figure 7.3 The coating failure mechanisms of the impact heads; SEM images of (a) PM10C, (b) PM25C and (c) PM30C; EDX analysis of (d) the undamaged coating surface, (e) chipping and (f) material transfer.....	201
Figure 7.4 Backscattering secondary electron SEM images of impact heads on (a) PM10C and (b) PM30C at 400× magnification.....	203
Figure 7.5 Coating failure mechanisms of the sliding tails; SEM images of (a) PM10C, (b) PM25C and (c) PM30C; EDX Analysis of (d) the Al ₂ O ₃ layer, (e) TiCN layer and (f) material transfer.....	205
Figure 8.1 Vickers indents beneath the CrN coating.....	216
Figure 8.2 Schematic of an inclined impact-sliding tester. To the right, a typical normal force vs. time curve during an impact-sliding cycle.....	217

Figure 8.3 Load conditions for inclined impact-sliding tests.....	218
Figure 8.4 Hardness gradient beneath the CrN coating in three substrates.....	219
Figure 8.5 The Wear track of CrN on D2 substrate after 1000 cycles, 200/400 N impact/pressing forces.....	221
Figure 8.6 Impact-sliding wear track of CrN coating on NAAMS S2333 substrate (impact load 200 / 400 N, 3000 cycles).....	223
Figure 8.7 The Wear track of CrN on S2333 substrate after 15000 cycles, 200/400 N impact/pressing forces.....	224
Figure 8.8 Optical image of the wear track of CrN/Toolox coating after 15000 cycles, 200/400 N impact test.....	225
Figure 8.9 The Wear track of CrN on Toolox substrate after 5000 cycles, 300/600 N impact/pressing forces.....	226

NOMENCLATURE

H_c	Dimensionless center film thickness
h_c	Center film thickness
R'	Reduced radius of curvature
G^*	Materials parameter
U^*	Speed parameter
W'	Load parameter
α	Pressure viscosity coefficient
E'	Reduced Young's modulus
U	Entraining surface velocity
η_0	Viscosity at atmospheric pressure of the lubricant
W	Contact load
H_m	Dimensionless minimum film thickness
h_m	Minimum film thickness
g_V	Dimensionless viscosity parameter
g_E	Dimensionless elasticity parameter
k	Dimensionless ellipticity parameter
C_r	Surface roughness correction factor
γ_c	Surface pattern parameter
P_{asp}	Effective asperity pressure
$F(x)$	Integration function
σ	Composite surface standard deviation

β	Asperity radius of curvature
η	Asperity density
h	Nominal distance between two contact faces
E'	Composite elastic modulus of two materials

ACRONYMS

AHSS	Advanced high strength steel
AISI	American Iron and Steel Institute
AS/P	AutoSteel/Partnership
ASTM	American Society for Testing and Materials
BDC	Bottom dead center
COF	Coefficient of friction
CrN	Chromium nitride
CVD	Chemical vapor deposition
CZ	Compound zone
DOE	Design of experiment
DZ	Diffusion zone
EB	Electron beam
EDM	Electrical discharging machining
EDX/EDS	Energy dispersive x-ray spectroscopy
EHL	Elasto-hydrodynamic lubrication
EIFT	Extended impact fatigue test
FEA	Finite element analysis

FEM	Finite element method
FIB	Focused ion beam
FMEP	Friction mean effective pressure
IBAD	Ion beam-assisted deposition
LPCVD	Low pressure chemical vapor deposition
MMC	Aluminum-based metal matrix composites
NCC	Nickel based ceramic composite
PACVD	Plasma-assisted chemical vapor deposition
PEO	Plasma electrolytic oxidation
PN	Plasma nitriding treatment
PTWA	Plasma transferred wire arc
PVD	Physical vapor deposition
SAE	Society of automotive engineers
SEM	Scanning electron microscopy
TDC	Top dead center
TEM	Transmission electron microscopy
TiAlN	Titanium aluminum nitride
TiC	Titanium carbide
TiCN	Titanium carbo-Nitride
TiN	Titanium nitride
TS	Thermal spray
USAMP/DOE	U.S. Automotive materials partnership/Department of energy
WC	Tungsten carbide

XRD	X-ray diffraction
-----	-------------------

SUBSCRIPTS

IR	Isoviscous-Rigid
------	------------------

VR	Viscous-Rigid
------	---------------

IE	Isoviscous-Elastic
------	--------------------

VR	Viscous-Elastic
------	-----------------

sk	Skewness
------	----------

ku	Kurtosis
------	----------

CHAPTER 1

INTRODUCTION

1. GENERAL OVERVIEW

A metallurgical coating can be defined as a near-surface region having properties differing from the bulk metals and alloys by metallurgical procedures involving deposition, conversion of ion, thermal, mechanical, or chemical treatments, which alter the surface composition or properties[1]. Due to their high hardness, chemical stability including corrosion/oxidation resistance, wear resistance and low friction coefficient to improve tool lifetime and higher surface quality [2-8], metallurgical coatings have been widely used in modern machinery and automotive industry. Typical machinery applications include cutting [9-12], drilling [13-16], milling [17-19], stamping [20, 21], die casting [22-25], etc. In the automotive industry, metallurgical coatings are now widely used to increase load capacity (mechanical, thermal, etc.), extend lifetime, reduce weight, reduce friction and resist corrosion in mass production. Thermal spray (TS), physical vapor deposition (PVD), chemical vapor deposition (CVD) and thermal-chemical heat treatment such as nitriding/nitrocarburizing are utilized to coat the engine components such as piston rings, piston bores, connecting rods, bearings, gears, ball pivots and brake discs, etc.

Although TS/CVD/PVD are widely used in the automotive industry, increasing demands in using light alloy such as aluminum and magnesium alloys to reduce vehicle weight created a new area for surface engineering for a new coating technology: plasma electrolytic oxidation (PEO), especially in cylinder bore surface treatment. PEO coatings

grow inwards and outwards simultaneously at the processed surface, bringing a native high bond strength, and evenly distributed micro pores acting as oil reservoir. These features enable PEO coated light alloys to be ideal for cylinder lubrication and wear resistance, without heavy cast iron liner or costly TS/CVD/PVD coatings. Although Mistry etc [26]. investigated the potential of well lubricated PEO coatings' application in aluminum cylinder bore surface treatment, the most important wear and friction behavior of PEO coatings under boundary conditions is still unclear.

Like the advantages of light metal alloys for vehicles weight reducing, the high strength of advanced high strength steel (AHSS) alloys enables automakers to produce lighter, more crash-resistant and fuel-efficient vehicles. Die stamping is widely used to form AHSS auto body parts with high productivity and low cost. The main drawback of AHSS is that it brings dramatically increased springback compared to milder steel grades. To reduce springback, the forming loads are increased, but the increased loads enlarge tool wear and galling. Protective coatings for stamping dies are the best solution to this challenge, which do not alter the stamping die design and material. To characterize the coating performance, there are various test methods. For instance, there are 838 active ASTM standards on coating properties and measurements, plus 585 active ASTM standards on test methods of coatings till November, 2013. Among this huge collection of coating characterization methods, these standards for friction and tribological evaluation, are based on similar methodologies: pin-on-disk, scratch, indentation or impacting. However, these regular methods cannot work well under stamping condition, i.e., both impacting and sliding occur simultaneously in one same working cycle.

2. MOTIVATION

To explore the application of PEO coatings in aluminum alloys engine cylinder bore protection, a well understanding of PEO coatings' tribological properties, especially under the boundary/mixed lubrication, is needed. With a better understanding, PEO coating surface can be treated by choosing appropriate processing parameters to obtain optimized topography.

As to characterization of complex loading effects on coatings, regular tribological characterization techniques are deficient in evaluating coatings under stamping die working condition, therefore a new methodology for simulating impact-sliding is in demand.

3. OBJECTIVES

The main aims of this study were to experimentally and numerically analyze PEO coatings under boundary/mixed lubrication, and effectively characterize protective coatings under combined impact-sliding loads. The objectives of this study were:

- To develop an experimental technique to evaluate PEO coating tribological properties under boundary lubrication conditions;
- To develop a numerical approach to analyze PEO coating boundary/mixed lubrication;
- To develop a coating characterization technique which can simulate impact-sliding simultaneously occurring in die stamping operation and;
- To evaluate different metallurgical coatings for stamping die protection by using the new developed technique and determine coating failure modes.

4. OUTLINE OF THIS DISSERTATION

This dissertation is organized in nine chapters. Chapter 1 is an introduction to the entire dissertation that starts with a general overview, an outline of the objectives, literature review on metallurgical coatings, lubrication and numerical approaches, and coating characterization techniques.

In Chapter 2, the PEO coating process was employed to produce oxide coatings on an Al alloy A356 for Al engine blocks, to protect against the wear attack. The surface morphology and coating thicknesses were tailored by polishing two PEO coatings. A reciprocating sliding tribometer was used to investigate the tribological and wear behavior of the PEO coatings, counterface materials, and that of a state-of-the-art plasma transferred wire arc coating (as a benchmark) under two lubricated conditions.

Chapter 3 introduced a numerical simulation based on Elasto-hydrodynamic lubrication (EHL)/asperity contacts and multibody dynamics to investigate the PEO coating performance under boundary/mixed lubrication in Chapter 2. A multibody model was built first to construct the dynamic load and movement of the reciprocating ball-on-plate test. An EHL/asperity simulation was set to simulate the contact between the steel ball and plasma transferred wire arc (PTWA)/PEO coatings. A comparison between the simulation results and the experimental data was made to show the surface topographic effects on the friction and wear behavior.

Chapter 4 is the start of the second half of this dissertation, the developing of a novel characterization technique of metallurgical coatings. The novel coating

characterization methodology in this dissertation has been initiated from a project of AutoSteel/Partnership (AS/P) for die protection in die stamping. In this chapter, the failure mechanisms of PVD/CVD coatings in simple simulated stamping loads (stage 1, only impact load without sliding movement) were examined experimentally and analytically.

In Chapter 5, two PVD (CrN and TiAlN) and one CVD (TiC) coatings on D2 substrates were tested at combinations of different impact/pressing loads using the same impact tester in Chapter 4. This test investigated the effects of different loads combinations on coating failure behaviors

More realistic die stamping simulated load conditions, i.e., combination of impact-sliding loads, were investigated in Chapter 6. A novel inclined impact-sliding tester was developed to investigate PVD/CVD coatings adhered to American Iron and Steel Institute (AISI) D2 substrate samples. The impact-sliding wear tracks on the coatings were observed using SEM with Energy Dispersive X-ray (EDX) analysis. The performances of the coatings were ranked according to their failure severity. Furthermore, three selected coatings were dissected using electrical discharging machining (EDM) wire cutting in order to study the coating failure behavior at their cross-sections along the impact-sliding tracks.

In Chapter 7, the fatigue and wear behavior of triple-layered protective CVD coatings on cemented carbide substrates for cemented carbide cutting tools was investigated using the impact-sliding wear tester. The multi layer coatings on the surface and cross-section were studied using SEM with EDX analysis.

Chapter 8 presents substrate effects on failure behavior of hard coatings under inclined cyclical loading conditions. Three different steel substrates treated with the same PVD CrN coating on the top of plasma nitriding layer of the substrate (so called duplex treatment). Effects of the treated substrates' hardness, elastic modulus and microstructural morphology on coating failure behaviour were studied under inclined cyclic loading test conditions with intention to simulate coating failures in stamping operation.

The summary of the preceding chapters is presented in Chapter 9, which enlists the main conclusions of this dissertation. Recommendations for future work were also listed in this chapter.

5. METALLURGICAL COATINGS

Metallurgical coatings have been widely used in the automotive industry. Some coating applications and techniques for automotive industry are illustrated in Fig. 1.1.

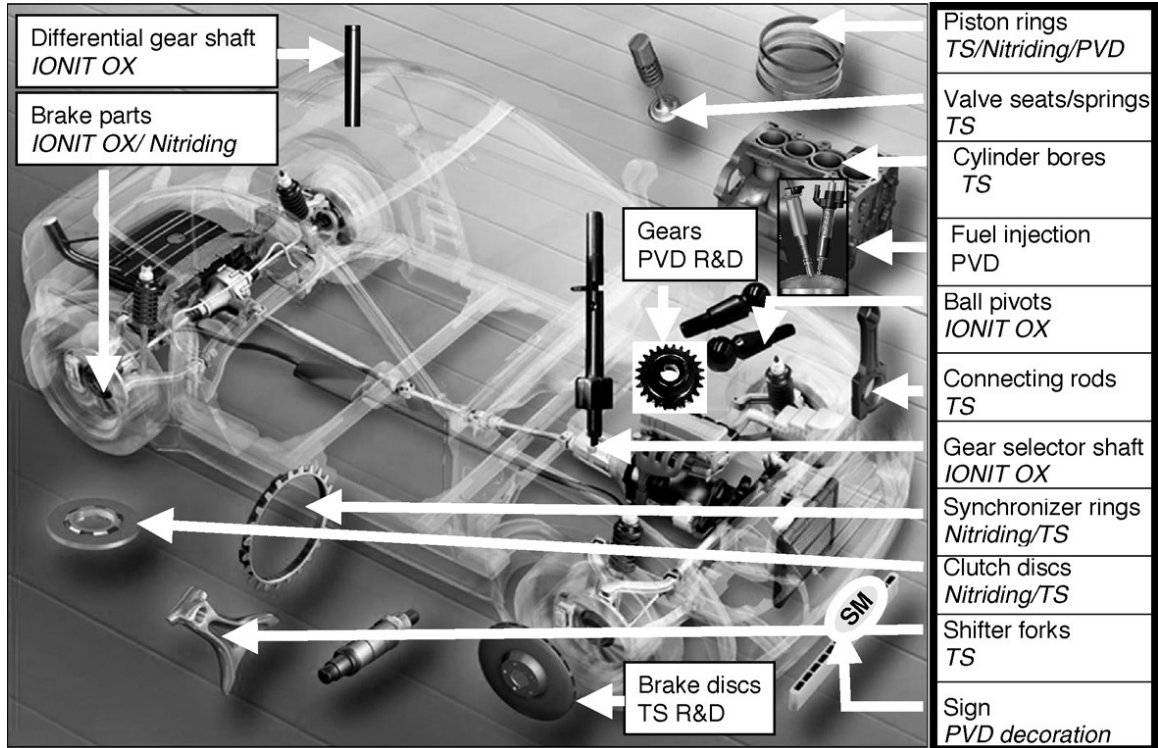


Figure 1.1 Coatings for automotive applications [27].

Each coating technique has their own distinct processing parameters (e.g. temperature, pressure and time), advantages, and limitations as shown in Table 1.1 and Fig. 1.2 [28]. Depending on applications, metallurgical coatings can be fabricated via different approaches. For example, to combat wear and scuffing, multilayer coatings are sometimes coated by more than one techniques [29-35], i.e., deposition on the surface (TiN, CrN by PVD) on modified substrate (plasma nitride). This combination, usually called duplex treatment, results in improved performance such as high wear resistance, high strength and high load capacity due to an increase of substrate hardness, fatigue strength, the wear/corrosion resistant offered by the hard PVD coating and a more gentle transition of elastic-plastic properties between the outermost layer of the coating and the substrate (Fig. 1.3).

Table 1.1 An overall comparison of various surface engineering [28]

Process/ material	Thickness/depth		Surface hardness(a), HRC	Corrosion resistance	Line-of- sight	Substrate temperature		Processing pressure		Processing time(b), h	Visible change	Rework required
	μm	mils				$^{\circ}\text{C}$	$^{\circ}\text{F}$	kPa	torr			
Electroplating	2.5–640	0.1–25	68–70 (hard Cr)	Good (hard Cr)	No	<95	<200	Liquid	Atmosphere	<1–25	Yes	Grinding/polishing, reheat treatment
Thin dense chromium	0.25–13	0.01–0.5	70–72	Good	No	<65	<150	Liquid	Atmosphere	0.01–0.3	Yes	Polishing (sometimes)
Electroless plating	2.5–250	0.1–10	49–70 (Ni-P)	Very good (Ni-P)	No	85–95	185–205	Liquid	Atmosphere	<1–10	Yes	No
CVD	1–1300	0.04–50	90–92 (TiC)	Very good	No	820–1200	1500–2200	0.013–100	0.1–760	10–60	Yes	Reheat treatment
PVD	0.025–10	0.001–0.4	93–95 (B ₄ C)	Excellent	Yes	95–540	200–1000	10^{-8} –0.013	10^{-7} –0.1	1–10	Yes	No
Diamond	1–1000	0.04–40	100–102	Good	No	<1090	<2000	0.013–100	0.1–760	<1–250	Yes	Reheat treatment
DLC	0.025–250	0.001–10	85–95	Good	Yes	>RT	>RT	10^{-8} –1.3	10^{-7} –10	<1–10	Yes	No
Thermal diffusion	51–3800	2–150	49–71 (C, N)	Average to good	No	480–1040	900–1900	40–>100	300–>760	10–100	No, except for C	Reheat treatment
Ion nitriding	51–640	2–25	60–72	Average, poor on stainless steel	No	400–570	750–1050	0.027–0.40	0.2–3	10–50	No	Grinding (sometimes)
TRD process	2.5–20	0.1–0.8	90–93 (VC)	Average	No	870–1040	1600–1900	Liquid	Atmosphere	10–20	No	Reheat treatment
Ion implantation	0.1–1	0.004–0.04	80–90 (N)	Excellent	Yes (beam) No (plasma source)	Usually <150	Usually <300	10^{-7} – 3×10^{-5}	10^{-6} – 2×10^{-4}	1–8	No	No
IBAD	0.1–10	0.004–0.4	91–96 (BN)	Excellent	Yes	Cryogenic– 980	Cryogenic– 1800	10^{-8} – 10^{-4}	10^{-7} – 10^{-3}	1–4	Yes	No
Thermal spray	100–2500	4–100	50–70 (WC)	Excellent	Yes	95–260	200–500	Usually atmosphere		1–10, >10 large areas	Yes	Grinding (usually)
Solid lubricants	0.5–13	0.02–0.5	No increase (MoS ₂)	Good (MoS ₂)	Yes	>RT	>RT	10^{-8} –100	10^{-7} –760	1–4	Yes	No

CVD, chemical vapor deposition; PVD, physical vapor deposition; DLC, diamondlike carbon; TRD, thermoreactive deposition/diffusion process; IBAD, ion-beam-assisted deposition; RT, room temperature. (a) Actual HRC values, or equivalent values derived from microhardness measurements. (b) Includes heating and cooling time, but not preheating and vacuum pumpdown time. Source: R.B. Alexander & Associates, Huntington Woods, MI

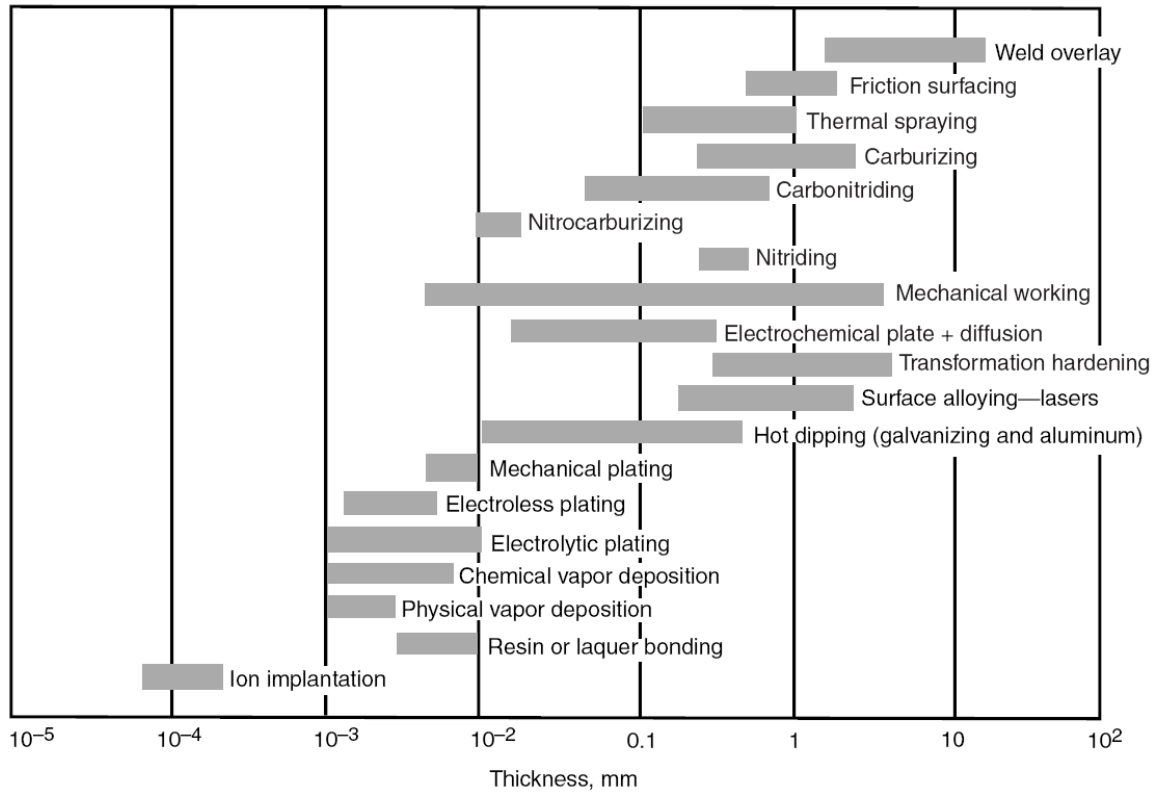


Figure 1.2 Approximate thickness of various surface engineering treatments [28].

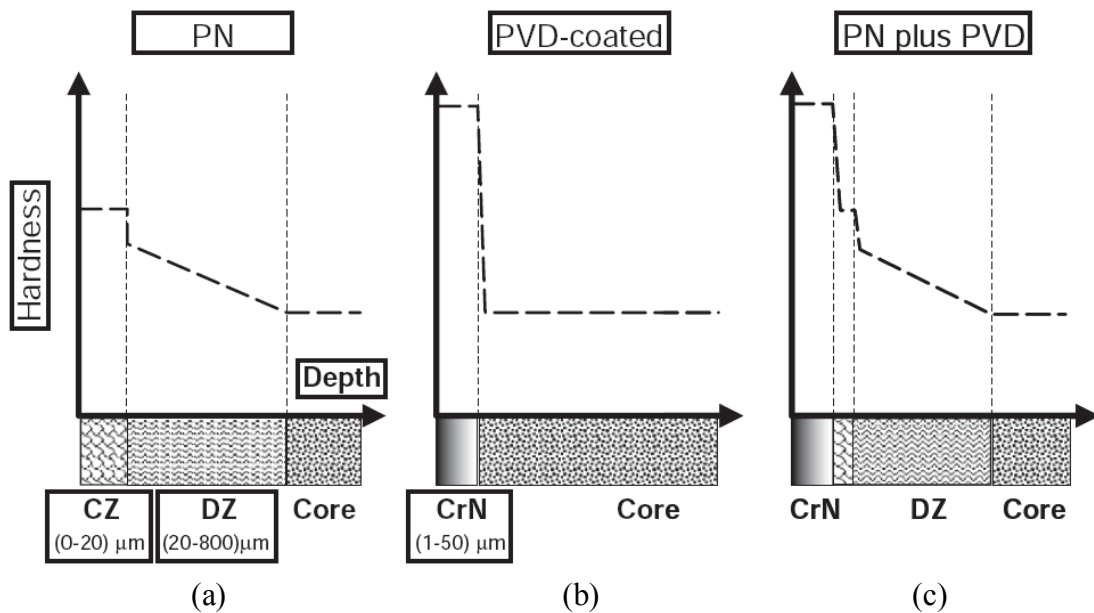


Figure 1.3 Hardness versus distance from the surface for soft steels with (a) a plasma nitriding treatment (PN), (b) PVD coating, and (c) combination nitriding plus PVD coating. CZ: compound zone, DZ: diffusion zone [27].

Another typical multilayer/duplex coating application for piston rings and some regular multilayer/duplex options are shown in Figs. 1.4 and 1.5.

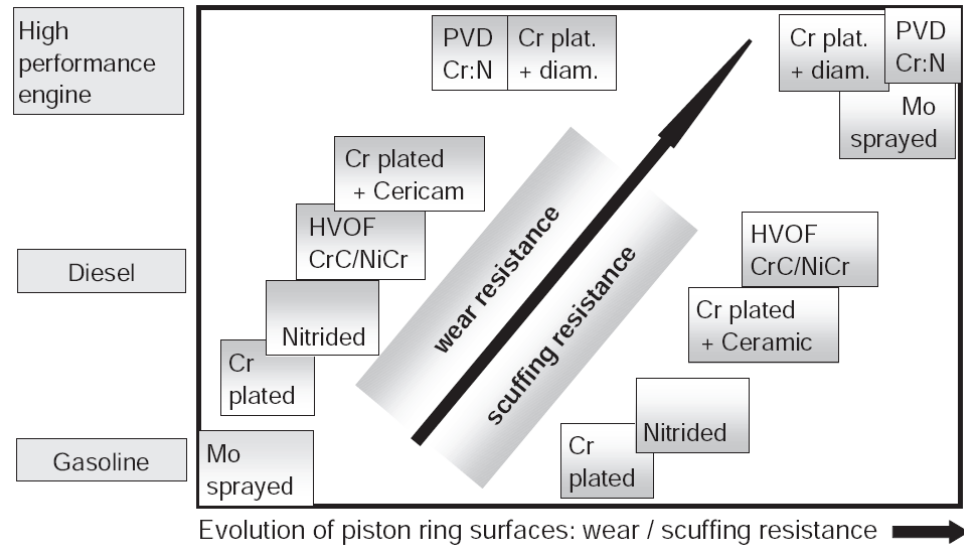


Figure 1.4 Different piston ring treatments and the trend of the wear and scuffing [27].

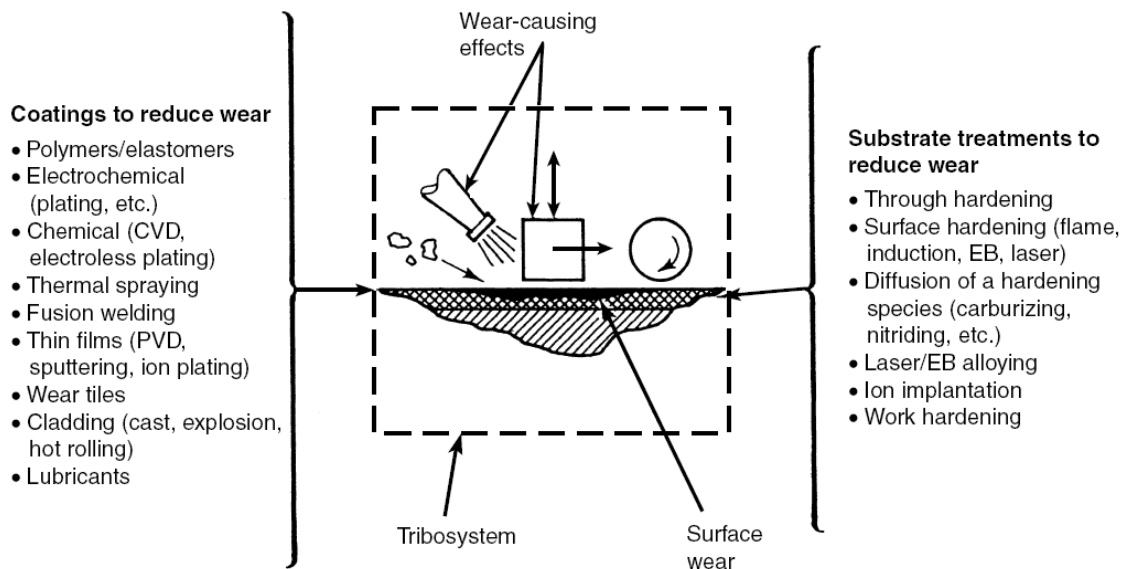


Figure 1.5 Surface engineering processes used to prevent wear. CVD, chemical vapor deposition; PVD, physical vapor deposition; EB, electron beam [28].

Although coating techniques are various for tooling, thermal spray, CVD and PVD coatings are the most commercially available ones. Thermal spray coatings are deposited by impacting molten, semi-molten or solid particles of various materials on the substrate in thicknesses from a few mils to more than 25 mm (Fig. 1.6). Their heating and/or acceleration are practical if they occur in a stream of gas [36]. The unmelted particles, oxidized particles and voids lead to an uneven microstructure and decrease strength and load capacity. However with appropriate equipment and feedstock election, these defects are controllable and the advantages of thermal spray are prominent such as:

- A wide range of materials including metals, alloys, carbides, oxide, nonoxide ceramics, refractory metals, plastics, cermets and combinations of these;
- Rapid rates of deposition, minimal base preparation, wide range of coating thickness, capability of being applied in the field, low deposition cost and;
- Low processing temperature (usually below 150 °C) and minimal thermal degradation to substrate.

The shortcomings of thermal spray coatings are low bond strength, porosity, anisotropic (high longitudinal strength), low loading capacity and line-of-sight process, which means complex shapes or contours are difficult to be coated.

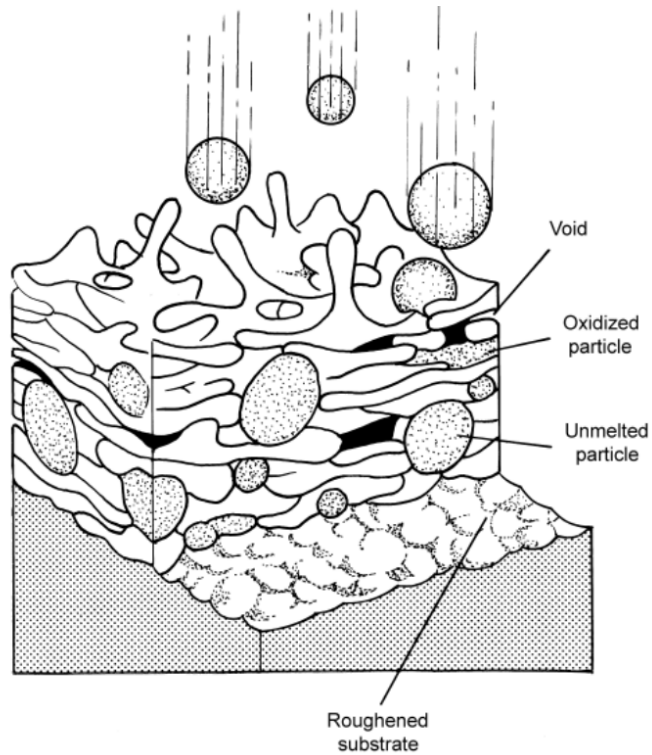


Figure 1.6 Thermal spray coating defects [37].

Compared to TS coatings, vapor deposition coatings have much higher bond strength (minimal tensile strength 103 MPa using ASTM C633) than TS coatings which have a range from 41 to 83 MPa [37]. Other advantages of vapor deposition techniques are controllable structure, high hardness, improved toughness, high corrosion resistance, etc. Typical physical vapor deposition (PVD) and chemical vapor deposition techniques are shown in Figs. 1.7 and 1.8.

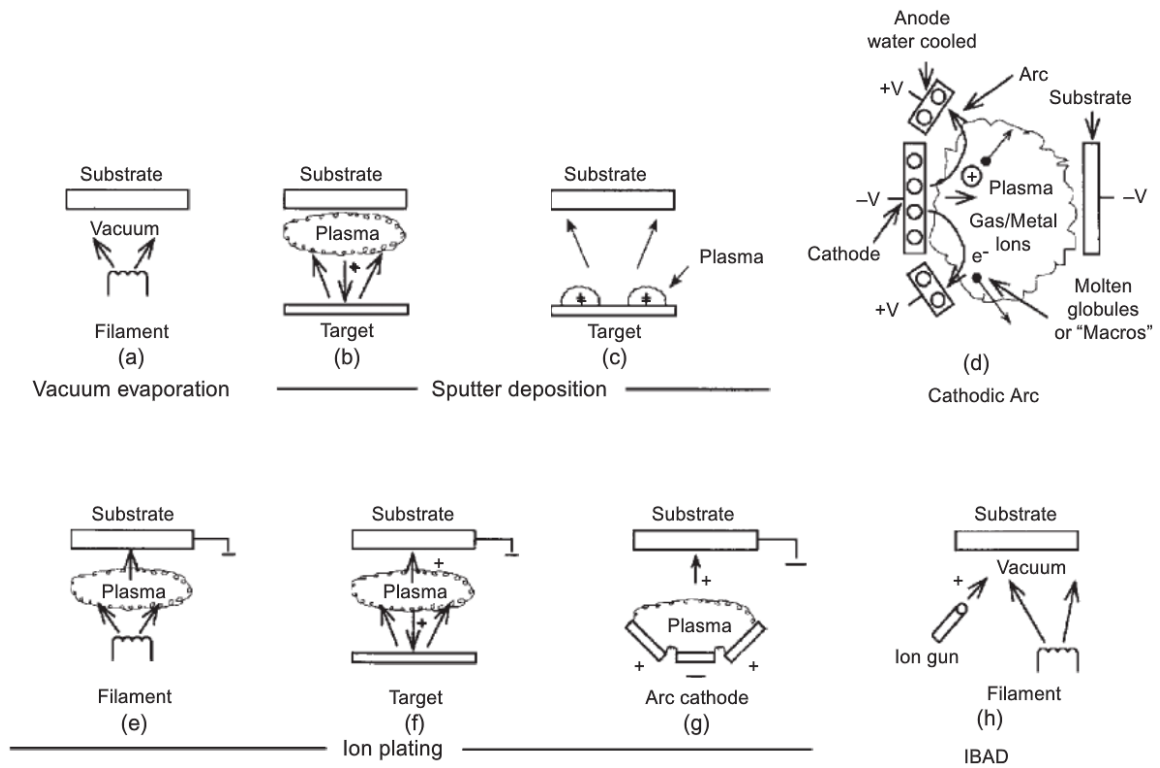


Figure 1.7 PVD Processing Techniques: (a) Vacuum Evaporation, (b) and (c) Sputter Deposition in a Plasma Environment, (d) Sputter Deposition in a Vacuum, (e) Ion Plating in a Plasma Environment with a Thermal Evaporation Source, (f) Ion Plating with a Sputtering Source, (g) Ion Plating with an Arc Vaporization Source, and (h) Ion Beam-Assisted Deposition (IBAD) with a Thermal Evaporation Source and Ion Bombardment from an Ion Gun [38].

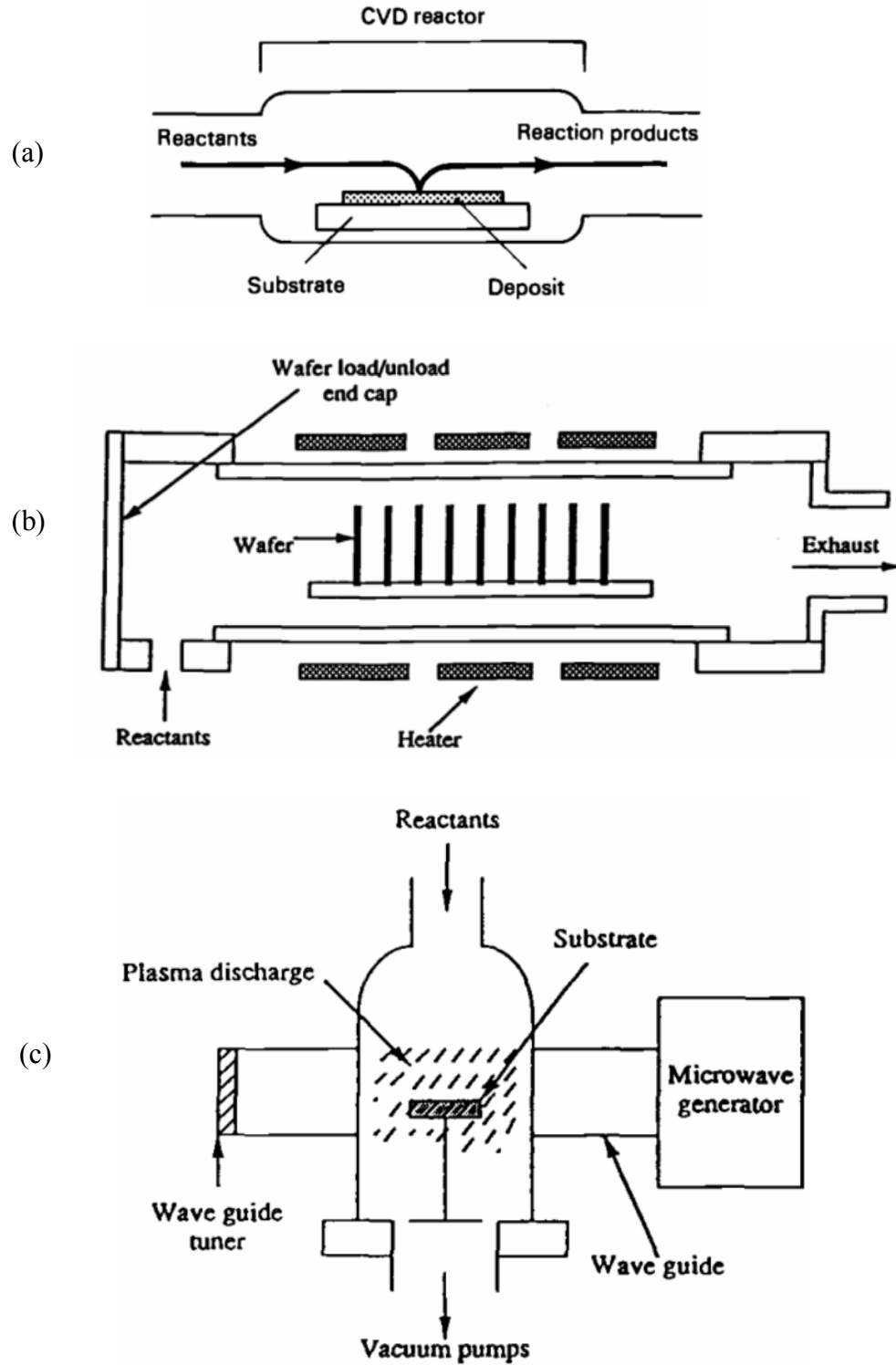


Figure 1.8 Typical CVD techniques[39]: (a) Conventional CVD, (b) Low pressure CVD (LPCVD) and (c) Plasma-assisted CVD (PACVD).

Vapor deposition techniques also have their own advantages and disadvantages. For example, CVD is more conformal than PVD by tracking the morphology, not by line-of-sight deposition. Other strengths of CVD are high aspect ratio holes, deep recesses or 3D configuration processing, high deposition rate, large thickness plus relatively simple equipment without high vacuum like PVD. However, the CVD process is far from an universal technique. First, the processing temperature of CVD is usually around 600 °C or higher and heat treatments may be required for steel workpieces after coating. Therefore CVD is not suitable for precision metal parts. Second, some chemical precursors and byproducts are toxic and corrosive which necessitates careful consideration of disposal processing and incur additional costs. Third, the energy consumption of CVD can be very high due to the high deposition temperatures. On the other hand, PVD also has its advantages and disadvantages. Advantages of PVD are: extreme versatile in coating materials including metal, alloy, refractory or intermetallic compound, capability in deposit unusual microstructures such as amorphous; wide temperature range of the substrate; high purity; high bond strength; fine surface finish; less pollutants from the PVD processes. Disadvantages are: difficulties in coating complex shapes due to line-of-sight process; high vacuum, high process cost and complexity of the process. Therefore it is not appropriate to claim that PVD is superior to CVD or vice versa; both the processes have advantages and drawbacks. Selecting the right coating or surface modification technique depends on materials and applications.

Owing to superior coating performance, simplicity of operation compared with vacuum deposition and electroplating techniques, process cost effectiveness and environmental friendliness, the PEO attracts increasing attention for the surface treatment

of lightweight metals, in particular Al, to enhance their hardness, wear and corrosion resistance [40-42]. A typical PEO equipment is shown in Fig. 1.9 and the electrode processes in electrolysis of aqueous solutions are given in Fig. 1.10. The equipment is in a room temperature and air pressure environment. The workpiece is immersed in the bath and attached to the current supply. By adjusting the working parameters, different treatment regimes can be controlled (Fig. 1.11) to obtain desired surface topography.

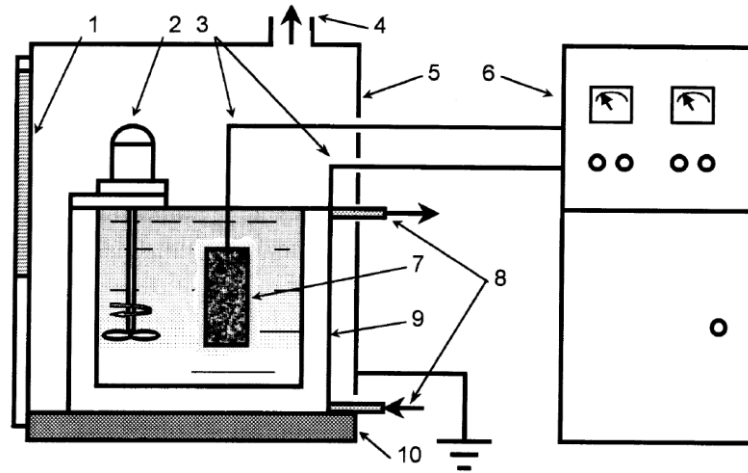


Figure 1.9 A typical PEO equipment: (1) window, (2) mixer, (3) connecting wires, (4) exhaust/ventilation system, (5) grounded case, (6) power supply, (7) workpiece, (8) cooling system, (9) bath and (10) insulating plate [40].

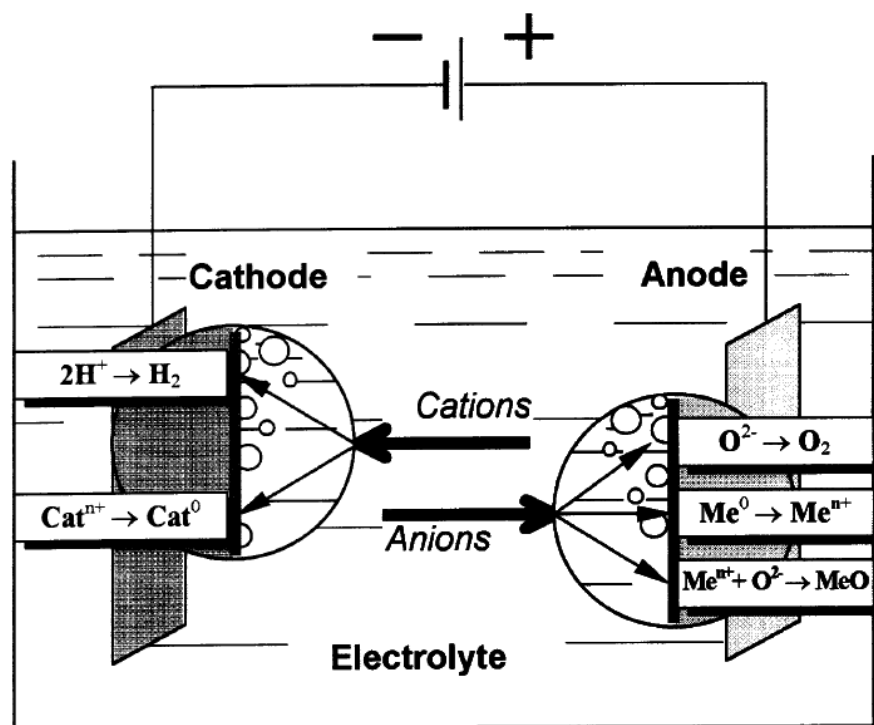


Figure 1.10 Electrode processes in electrolysis of aqueous solutions[40].

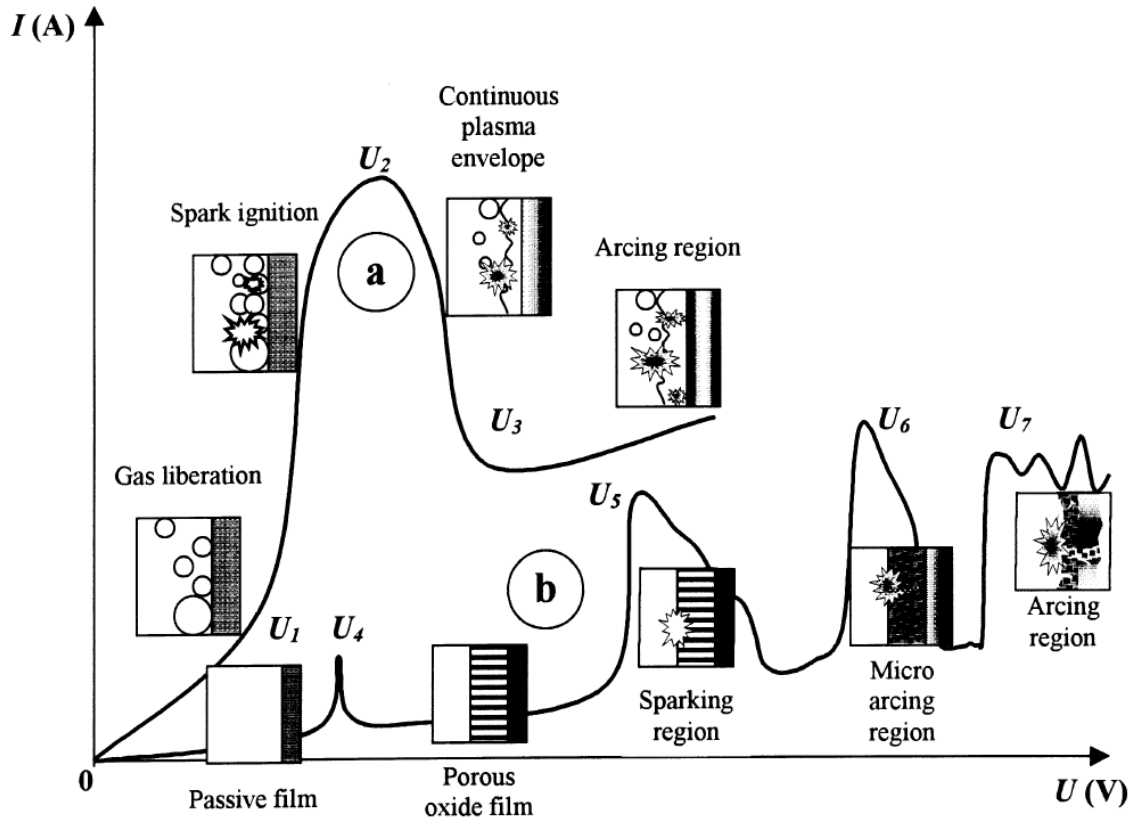


Figure 1.11 Two kinds of current-voltage diagram for PEO processes: (a) near electrode area and (b) in the dielectric film on the electrode surface [40].

6. NUMERICAL LUBRICATION METHOD

As shown in well-known Stribeck curve (Fig. 1.12), the coefficient of friction (COF) in boundary lubrication regions (lubrication film is about the same thickness as the surface roughness) is high and leads to energy loss, wear and material damage. The worst worn areas of cylinder bores are at top dead center/bottom dead center (TDC/BDC) in a firing engine, where the lubrication is always in the boundary/starve region at high temperature. Therefore, the tribological study of PEO coatings under boundary/starve lubrications is a key aspect for the PEO application in piston ring/aluminum bore contact.

The Stribeck curve was first used to illustrate a journal bearing system under different regimes of lubrication, i.e., full film hydrodynamic, mixed and boundary film lubrications. Friction in the boundary lubrication regime is mainly the asperity contact, and in hydrodynamic regime is the mainly viscous shear. The mixed lubrication regime is the combination of these two.

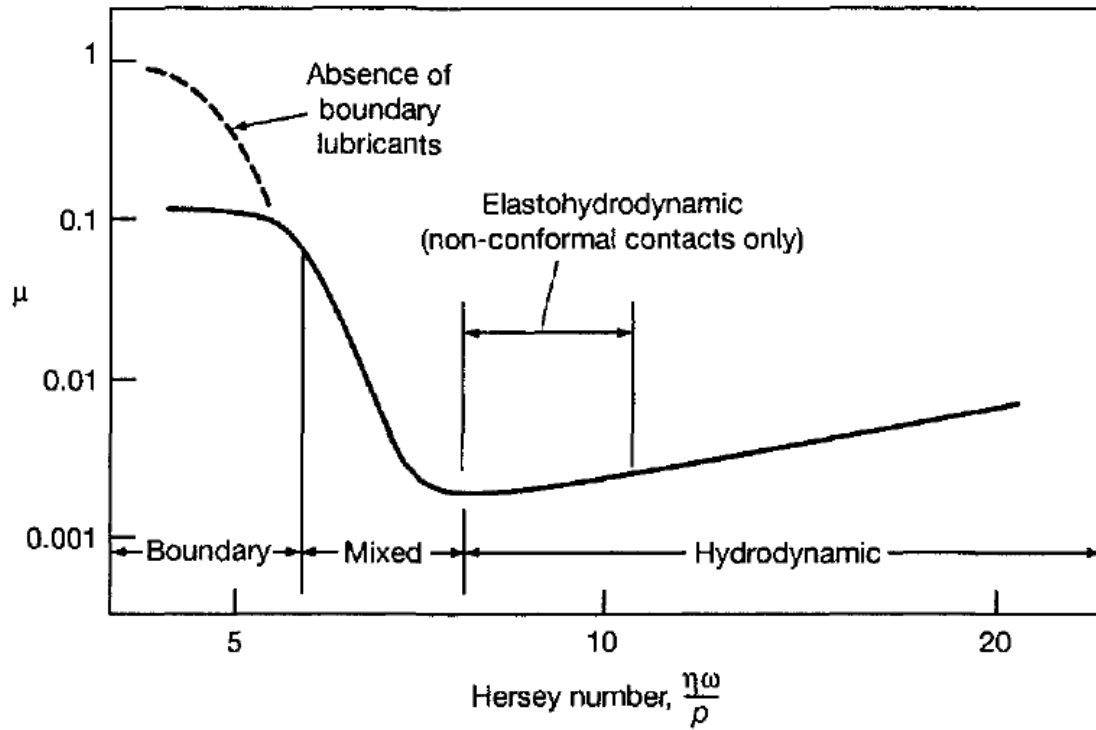


Figure 1.12 Schematic of Stribeck curve. η is viscosity, ω is speed and p is the load [43].

Tribological contacts can be classified into two catalogues: conformal and nonconformal. A conformal contact happens between a convex surface and a concave surface such as a journal bearing or a slider bearing; a nonconformal contact happens between two convex or flat surfaces, such as gears, rolling bearings, cams, ball-on-plate, etc. Usually the conformal contact deal with elements of the same nominal diameters, for

example, the journal shaft and journal shell. Therefore, the conformal contacts occur in a large area between two surfaces. Nonconformal contacts, on the contrary, usually happen in a much smaller area than the conformal contacts, typically three orders of magnitude less than that of a conformal conjunction [43].

The milestone theoretical lubrication analysis was carried on journal bearing experiments by Reynolds [44]. The Reynolds equations published in 1886 are the foundation of hydrodynamic lubrication theory [44]. Since the journal bearings analysis always deal with conformal contacts, the hydrodynamic pressure in the fluid film is low (normally less than 1 GPa) and the Reynolds equations work well within this range. However, later researchers faced the difficulty on applying Reynolds equations in nonconformal contacts, which contact pressures were much higher than conformal contacts. For example, Martin [45] found that the predicted oil film thickness in spur gears line contact was much more smaller than the experimental observations. From 1930s, researchers began introducing either the local elastic deformation of the contact surfaces or the lubricant viscosity increase due to high pressure into hydrodynamic lubrication. The first elastohydrodynamic lubrication (EHL) theory to include the effects of both elastic deformation and viscosity increase was published by Grubin in 1949 [46], with two assumptions: the elastically deformed lubricated cylinder has the same shape as in a dry contact; the hydrodynamic pressure at the inlet border of the Hertzian contact zone reaches infinity. The line contact EHL dimensionless film thickness was then derived as:

$$H_c = h_c/R' = 1.95 (G^*U^*)^{8/11}/W^{*1/11} \quad (1.1)$$

where, h_c is the central film thickness, R' is the reduced radius of curvature, G^* is materials parameter, U^* is speed parameter, W^* is load parameter as:

$$G^* = \alpha E' \quad (1.2)$$

$$U^* = \frac{U \eta_0}{E' R'} \quad (1.3)$$

$$W^* = \frac{W}{E' R'^2} \quad (1.4)$$

α is the pressure viscosity coefficient, E' is the reduced Young's modulus, U is the entraining surface velocity, η_0 is the viscosity at atmospheric pressure of the lubricant and W is the contact load.

To remove above mentioned two assumptions, full numerical solutions were developed during 1950-1970s. In spite of deficiency in high power computing for full numerical solutions, Dowson and Higginson developed a new inverse solution to overcome the slow convergence and published the equation for line contact EHL minimum film thickness [47] as Eq. 1.5. Dowson and Toyoda [48] published central film thickness as Eq. 1.6:

$$H_m = h_m/R_x = 1.6G^{*0.6}U^{*0.7}W^{*(-0.13)} \quad (1.5)$$

$$H_c = h_c/R' = 3.06G^{*0.56}U^{*0.69}W^{*(-0.10)} \quad (1.6)$$

Full numerical solutions for point contacts were not available till 1975 due to the deficiency in additional computing power for higher concentrated stress. Hamrock and Dowson published a series of papers on point contacts under different conditions such as speed, load, materials properties and contact ellipticity. The curve-fitting equations for point contact are [49]:

$$H_c = 2.69G^{*0.53}U^{*0.67}W^{*(-0.067)}(1 - 0.61e^{-0.73k}) \quad (1.7)$$

$$H_m = 3.63G^{*0.49}U^{*0.68}W^{*(-0.073)}(1 - e^{-0.68k}) \quad (1.8)$$

These equations used similar dimensionless parameters as in Eqs. 1.1, 1.5 and 1.6, except a factor of ellipticity, $k=b/a$, was introduced into the load parameter to take into account the effect of point contact geometry. Generally the nonconformal contacts with very low and very high ellipticity ratios can be treated as circular and line contacts respectively. Due to the facts that high elastic deformation and increased lubricant viscosity attributed to high pressure, nonconformal point contacts can be identified as four lubrication regimes and equations for each regime are listed below[43]:

1. Isoviscous-Rigid: the magnitude of elastic deformation of contact surfaces is insignificant and the contact pressure is too low to induce an increase in lubricant viscosity, therefore, both of those effects on lubrication can be neglected. The dimensionless minimum or central film thickness parameter are written as:

$$(H_{min})_{IR} = (H_c)_{IR} = 128 \alpha_r [0.131 \tan^{-1} \left(\frac{\alpha_r}{2} \right) + 1.683]^2 \varphi^2 \quad (1.9)$$

where

$$\alpha_r = \frac{R_y}{R_x} = k^{\pi/2} \quad (1.10)$$

$$\varphi = \left(1 + \frac{2}{3\alpha_r} \right)^{-1} \quad (1.11)$$

2. Viscous-Rigid: the elastic deformation is negligible but the high conjunction pressure effect in lubricant viscosity is considered. The dimensionless minimum or central film thickness are expressed as:

$$(H_{min})_{VR} = (H_c)_{VR} = 141g_V^{0.375}(1 - e^{-0.0387\alpha_r}) \quad (1.12)$$

3. Isoviscous-Elastic: it is also called soft EHL where elastic deformation cannot be neglected but the contact pressure is too low to affect lubricant viscosity. The dimensionless minimum film thickness parameters are written as:

$$(H_{min})_{IE} = 8.70g_E^{0.67}(1 - 0.85e^{-0.31k}) \quad (1.13)$$

$$(H_c)_{IE} = 11.15g_E^{0.67}(1 - 0.72e^{-0.28k}) \quad (1.14)$$

4. Viscous-Elastic: i.e., hard EHL where both the effects of elastic deformation and contact pressure (typical between 0.5 to 3 GPa) should be considered.

The minimum and central film thicknesses for the VE (hard EHL) regime are:

$$(H_{min})_{VE} = 3.42g_V^{0.49}g_E^{0.17}(1 - e^{-0.68k}) \quad (1.15)$$

$$(H_c)_{VE} = 3.61g_V^{0.53}g_E^{0.13}(1 - 0.61e^{-0.73k}) \quad (1.16)$$

where the dimensionless viscosity and elasticity parameter are defined as

$$g_V = GW^3/U^2 \quad (1.17)$$

$$g_E = W^{8/3}/U^2 \quad (1.18)$$

Hence to obtain the minimum and central thicknesses, the dimensionless viscosity and elasticity parameters are calculated first and then the lubrication regime is determined, the thickness equations according to the lubrication regime are applied.

The conventional lubrication theory and EHL film thickness formulas, such as above mentioned equations, based on the assumption that both the contact surfaces are smooth. However, most engineering surfaces are rough compared to the thin lubricant film, and the effect of roughness cannot be ignored. For roughness effect in lubrication, there are basically two numerical approaches: stochastic and deterministic. The stochastic

approach utilizes the selected statistic parameters to represent the rough surface, such as root mean square roughness R_q . In automobile industry, the stochastic model developed by Patir and Cheng [50], has enjoyed wide recognition and is used in piston ring/skirt/bore friction prediction by mainstream automobile analysis software such as Ricardo, AVL and GT-Suite. This kind of stochastic approach is relatively simple and efficient, but they only provide mean values of lubricant film thickness and hydrodynamic and contact pressure. The stochastic approach cannot provide more detailed information about local pressure peaks, local film fluctuations and asperity deformation. Therefore, the second approach, using real surface topography to replace the simple statistic parameters has been developed to investigate these detailed information. Validated cases of deterministic approach can be found in references [51-53]. Zhu and Cheng [54] obtained the effects of surface roughness on point contacts using the average flow factors developed by Patir and Cheng. The effect of surface roughness on average film thickness of EHL contacts can be described by the surface roughness correction factor as expressed by Eq. 1.19 and shown in Fig. 1.13:

$$C_r = \frac{(h_{min})_{rough}}{(h_{min})_{smooth}} \quad (1.19)$$

where, the surface pattern parameter γ_c for purely transverse, isotropic, and purely longitudinal patterns are 0, 1 and ∞ , respectively. However, the deterministic approach demands high computing power and is still quite time consuming with current computers.

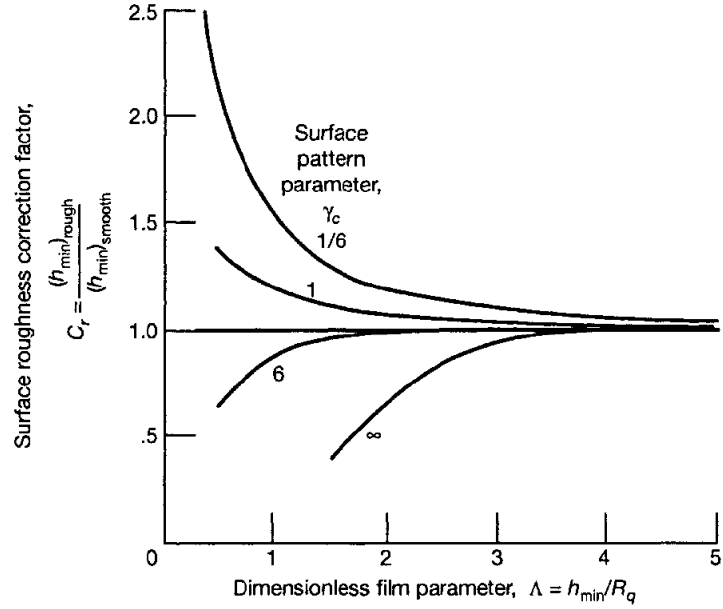


Figure 1.13 Effect of surface roughness on average film thickness of EHL contact [54]

Another method to evaluate the surface roughness effects in boundary/mixed lubrication is to calculate asperity contact (dry contact) pressure and EHL contact pressure separately and then superimpose these two pressures to balance the load. Again, there are two approaches for asperity contact study: statistic and deterministic. Statistic approaches based on simple asperity shapes and fixed curvatures were proposed by Greenwood and Williamson [55], Greenwood and Tripp [56], and Onons and Archard [57], while deterministic models employed simplified or measured real rough 3D surfaces as the input of the numerical solution. The 3D rough surfaces have large amount of detailed information and may become strongly time-dependent due to deformed asperities, which make the analysis time-consuming and difficult to converge. Additional references can be found in references [58, 59].

Greenwood-Tripp asperity contact model is the most popular statistical asperity contact model. This model assumes a Gaussian distribution of the actual surface points about a mean, nominal surface. Asperities are in Gaussian distribution and constant in the average radius of curvature of asperity tops. A special integration function (Eq.1.21) is used to calculate the contact area and elastic deformation of asperities for a given distance. The effective asperity pressure and the integration functions are shown below as [56]:

$$P_{asp} = \frac{16\sqrt{2}}{15} \pi (\sigma \beta \eta)^2 E' \sqrt{\frac{\sigma}{\beta}} F\left(\frac{h}{\sigma}\right) \quad (1.20)$$

$$F(x) = \frac{2}{\sqrt{\pi}} \int_x^{\infty} (s - x)^{5/2} e^{-s^2/2} ds \quad (1.21)$$

where, σ is the composite surface standard deviation, β is the asperity radius of curvature, η is the asperity density, h is the nominal distance between two contact faces, and E' is the composite elastic modulus of two materials in contact (Eq. 1.22).

$$\frac{1}{E'} = \frac{1-\nu_A^2}{E_A} + \frac{1-\nu_B^2}{E_B} \quad (1.22)$$

σ , β , and η can be extracted from raw profilometer data by the method proposed by Tomanik [60]. Then the contact force can be obtained by multiplying the effective pressure with the nominal area of the contact. For reciprocating movement, the friction force can be calculated using a continuous friction law [61]:

$$F^f = \mu_k(V_r) F^n \text{sign}(V_r) \left(1 - e^{-\frac{|V_r|}{V_0}}\right) \quad (1.23)$$

Noticeable, the nominal distance h is a variant when oil film thickness is not a constant in mixed lubrication analysis.

7. COATING CHARACTERIZATION

The below chart (Fig. 1.14) shows steel still plays a significant role in the average vehicle. The aluminum represents about 8.6 percent, mostly in engine/powertrain castings. According to the latest industry research, newly developed grades of advanced high-strength steel (AHSS) significantly outperform competing materials for current and future automotive applications [62]. Die stamping dies for structural vehicle parts therefore need better protection from high combined stamping loads. To choose the better candidate for stamping die and mold protective coatings, a suitable and economical characterization technique is necessary to be determined.

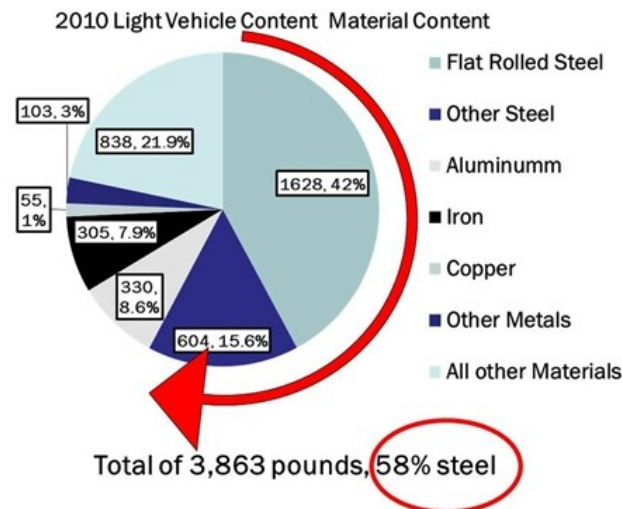
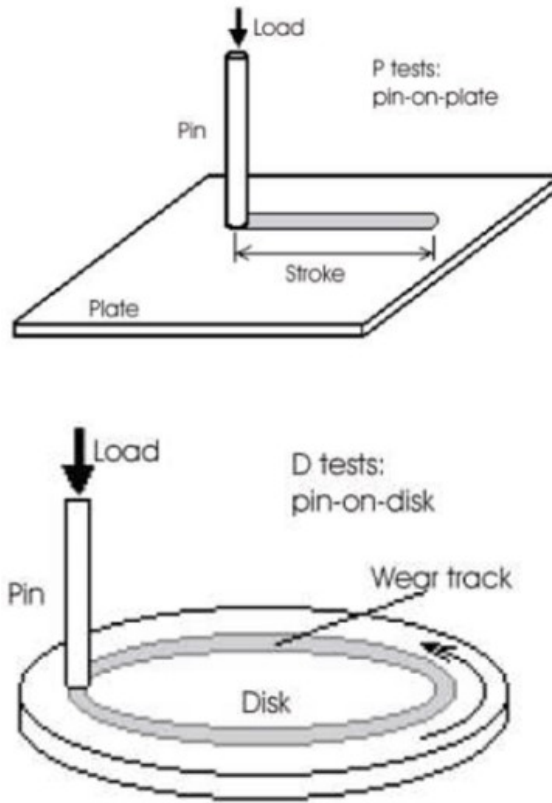


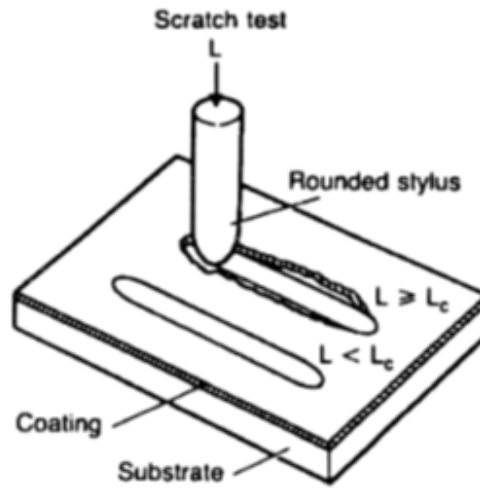
Figure 1.14 2010 Light vehicle material content [62]

Similar to the discussion in cons and pros for different coating technologies above, there are a lot of coating characterization techniques available, either commercial or lab-made. Coatings properties include: film thickness, surface topography, hardness,

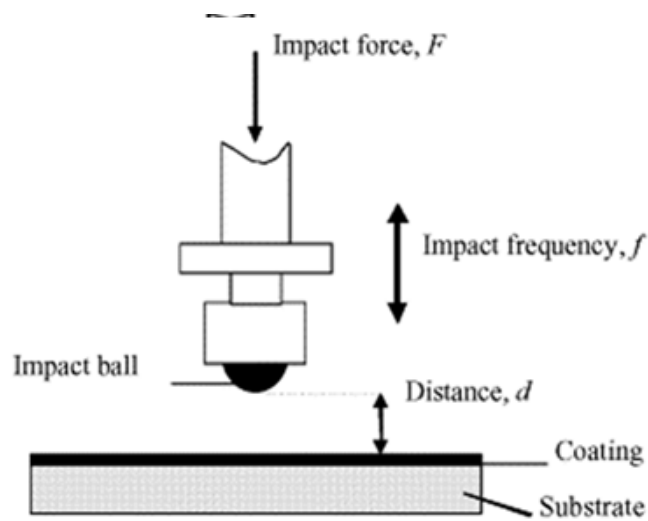
corrosion resistance, mechanical (freestanding films, adhesion to substrate), residual stress, thermomechanical stability, microstructure, tribological (wear, friction and lubrication), optical, magnetic etc. Fig. 1.15 shows a few typical testers used to characterize coating mechanical responses and fatigue resistance under cyclical loading. As mentioned above, none of them can fit well to evaluate coating performances with stamping conditions involving simultaneous impacting and sliding. Therefore, a tester which meets the above specific requirement is needed.



(a)



(b)



(c)

Figure 1.15 Typical tribological test methods for coatings: (a) pin-on-disk, (b) scratch and (c) impact.

8. SUMMARY

The above review in this chapter gives an overall perspective of metallurgical coating properties, pros and cons of different coatings, numerical lubrication methods, and coating characterizations. Although metallurgical coatings for both engine and machining have been used for many years, studies on PEO coating for cylinder bore protection and coating evaluation under stamping loads are still limited.

Therefore, the purposes of this study are:

- To investigate PEO lubrication properties both experimentally and numerically and establish a numerical approach to predict tribological behavior of PEO coatings under boundary/mixed lubrication regimes; and
- To develop a new coating characterization methodology which can simulate stamping loads; and to investigate coatings failure mechanism under simulated stamping loads.

REFERENCES

1. R.F. Bunshah and D.M. Mattox, *Applications of metallurgical coatings*. Physics Today, 1980. **33**(5): p. 50-5.
2. S. PalDey and S.C. Deevi, *Single layer and multilayer wear resistant coatings of (Ti,Al)N: a review*. Materials Science and Engineering: A, 2003. **342**(1–2): p. 58-79.
3. H.G. Prengel, P.C. Jindal, K.H. Wendt, A.T. Santhanam, P.L. Hegde, and R.M. Penich, *A new class of high performance PVD coatings for carbide cutting tools*. Surface and Coatings Technology, 2001. **139**(1): p. 25-34.
4. B. Lux, C. Colombier, H. Altena, and K. Stjernberg, *Preparation of alumina coatings by chemical vapour deposition*. Thin Solid Films, 1986. **138**(1): p. 49-64.
5. A.A. Layyous, D.M. Freinkel, and R. Israel, *Al₂O₃-coated cemented carbides: optimization of structure, number of layers and type of interlayer*. Surface and Coatings Technology, 1992. **56**(1): p. 89-95.
6. F.H.W. Löffler, *Systematic approach to improve the performance of PVD coatings for tool applications*. Surface and Coatings Technology, 1994. **68–69**(0): p. 729-740.
7. S. Hogmark, S. Jacobson, and M. Larsson, *Design and evaluation of tribological coatings*. Wear, 2000. **246**(1–2): p. 20-33.
8. R. Buhl, H.K. Pulker, and E. Moll, *TiN coatings on steel*. Thin Solid Films, 1981. **80**(1–3): p. 265-270.
9. F. Klocke and T. Krieg, *Coated Tools for Metal Cutting – Features and Applications*. CIRP Annals - Manufacturing Technology, 1999. **48**(2): p. 515-525.

10. H.G. Prengel, W.R. Pfouts, and A.T. Santhanam, *State of the art in hard coatings for carbide cutting tools*. Surface and Coatings Technology, 1998. **102**(3): p. 183-190.
11. W. Kalss, A. Reiter, V. Derflinger, C. Gey, and J.L. Endrino, *Modern coatings in high performance cutting applications*. International Journal of Refractory Metals and Hard Materials, 2006. **24**(5): p. 399-404.
12. T. Leyendecker, O. Lemmer, S. Esser, and J. Ebberink, *The development of the PVD coating TiAlN as a commercial coating for cutting tools*. Surface and Coatings Technology, 1991. **48**(2): p. 175-178.
13. T. Cselle and A. Barimani, *Today's applications and future developments of coatings for drills and rotating cutting tools*. Surface and Coatings Technology, 1995. **76–77, Part 2**(0): p. 712-718.
14. V. Derflinger, H. Brändle, and H. Zimmermann, *New hard/lubricant coating for dry machining*. Surface and Coatings Technology, 1999. **113**(3): p. 286-292.
15. W.D. Sproul and R. Rothstein, *High rate reactively sputtered TiN coatings on high speed steel drills*. Thin Solid Films, 1985. **126**(3–4): p. 257-263.
16. S. Kalidas, R.E. DeVor, and S.G. Kapoor, *Experimental investigation of the effect of drill coatings on hole quality under dry and wet drilling conditions*. Surface and Coatings Technology, 2001. **148**(2–3): p. 117-128.
17. J. Gu, G. Barber, S. Tung, and R.-J. Gu, *Tool life and wear mechanism of uncoated and coated milling inserts*. Wear, 1999. **225–229, Part 1**(0): p. 273-284.

18. P. Koshy, R.C. Dewes, and D.K. Aspinwall, *High speed end milling of hardened AISI D2 tool steel (~58 HRC)*. Journal of Materials Processing Technology, 2002. **127**(2): p. 266-273.
19. J.A. Ghani, I.A. Choudhury, and H.H. Masjuki, *Performance of P10 TiN coated carbide tools when end milling AISI H13 tool steel at high cutting speed*. Journal of Materials Processing Technology, 2004. **153–154**(0): p. 1062-1066.
20. H. Karbasian and A.E. Tekkaya, *A review on hot stamping*. Journal of Materials Processing Technology, 2010. **210**(15): p. 2103-2118.
21. X.T. Zeng, S. Zhang, and T. Muramatsu, *Comparison of three advanced hard coatings for stamping applications*. Surface and Coatings Technology, 2000. **127**(1): p. 38-42.
22. C. Mitterer, F. Holler, F. Üstel, and D. Heim, *Application of hard coatings in aluminium die casting — soldering, erosion and thermal fatigue behaviour*. Surface and Coatings Technology, 2000. **125**(1–3): p. 233-239.
23. D. Heim, F. Holler, and C. Mitterer, *Hard coatings produced by PACVD applied to aluminium die casting*. Surface and Coatings Technology, 1999. **116–119**(0): p. 530-536.
24. A. Lousa, J. Romero, E. Martínez, J. Esteve, F. Montalà, and L. Carreras, *Multilayered chromium/chromium nitride coatings for use in pressure die-casting*. Surface and Coatings Technology, 2001. **146–147**(0): p. 268-273.
25. S. Gulizia, M.Z. Jahedi, and E.D. Doyle, *Performance evaluation of PVD coatings for high pressure die casting*. Surface and Coatings Technology, 2001. **140**(3): p. 200-205.

26. K. Mistry, M. Priest, and S. Shrestha, *The potential of plasma electrolytic oxidized eutectic aluminium-silicon alloy as a cylinder wall surface for lightweight engine blocks*. Proceedings of the Institution of Mechanical Engineers, Part J: Journal of Engineering Tribology, 2010. **224**(2): p. 221-229.
27. J. Vetter, G. Barbezat, J. Crummenauer, and J. Avissar, *Surface treatment selections for automotive applications*. Surface and Coatings Technology, 2005. **200**(5–6): p. 1962-1968.
28. J.R. Davis, *Surface engineering for corrosion and wear resistance*. 2001: ASM international.
29. C. Friedrich, G. Berg, E. Broszeit, F. Rick, and J. Holland, *PVD CrxN coatings for tribological application on piston rings*. Surface and Coatings Technology, 1997. **97**(1–3): p. 661-668.
30. M. Zlatanović, *Deposition of (Ti,Al)N coatings on plasma nitrided steel*. Surface and Coatings Technology, 1991. **48**(1): p. 19-24.
31. M. Van Stappen, B. Malliet, L. Stals, L. De Schepper, J.R. Roos, and J.P. Celis, *Characterization of TiN coatings deposited on plasma nitrided tool steel surfaces*. Materials Science and Engineering: A, 1991. **140**(0): p. 554-562.
32. J. Smolik, J. Walkowicz, and J. Tacikowski, *Influence of the structure of the composite: 'nitrided layer/PVD coating' on the durability of tools for hot working*. Surface and Coatings Technology, 2000. **125**(1–3): p. 134-140.
33. A.D. Wilson, A. Leyland, and A. Matthews, *A comparative study of the influence of plasma treatments, PVD coatings and ion implantation on the tribological*

- performance of Ti-6Al-4V*. Surface and Coatings Technology, 1999. **114**(1): p. 70-80.
34. J.C.A. Batista, M.C. Joseph, C. Godoy, and A. Matthews, *Micro-abrasion wear testing of PVD TiN coatings on untreated and plasma nitrided AISI H13 steel*. Wear, 2001. **249**(10-11): p. 971-979.
 35. S. Ma, Y. Li, and K. Xu, *The composite of nitrided steel of H13 and TiN coatings by plasma duplex treatment and the effect of pre-nitriding*. Surface and Coatings Technology, 2001. **137**(2-3): p. 116-121.
 36. L. Pawlowski, *The science and engineering of thermal spray coatings*. 2008: John Wiley & Sons.
 37. J.R. Davis, *Handbook of thermal spray technology*. 2004: ASM international.
 38. D.M. Mattox, *Handbook of physical vapor deposition (PVD) processing*. 2010: Elsevier.
 39. R. Bunshah, *PVD and CVD coatings*. ASM International, ASM Handbook, 1992. **18**: p. 840-849.
 40. A.L. Yerokhin, X. Nie, A. Leyland, A. Matthews, and S.J. Dowey, *Plasma electrolysis for surface engineering*. Surface and Coatings Technology, 1999. **122**: p. 73-93.
 41. X. Nie, X. Li, and D.O. Northwood. *Corrosion behavior of metallic materials in ethanol-gasoline alternative fuels*. 2007. Trans Tech Publ.
 42. X. Nie, X. Li, L. Wang, and D.O. Northwood, *Corrosion protection properties of anodic oxide coatings on an Al-Si alloy*. Surface & Coatings Technology, 2005. **200**: p. 1994-2000.

43. B.J. Hamrock, S.R. Schmid, and B.O. Jacobson, *Fundamentals of fluid film lubrication*. Vol. 169. 2004: CRC press.
44. O. Reynolds, *On the Theory of Lubrication and Its Application to Mr. Beauchamp Tower's Experiments, Including an Experimental Determination of the Viscosity of Olive Oil*. Proceedings of the Royal Society of London, 1886. **40**(242-245): p. 191-203.
45. H. Martin, *Lubrication of gear teeth*. Engineering, London, 1916. **102**: p. 199.
46. A. Grubin, *Fundamentals of the hydrodynamic theory of lubrication of heavily loaded cylindrical surfaces*. Investigation of the contact Machine Components, 1949(30): p. 115-166.
47. D. Dowson and G. Higginson, *New roller-bearing lubrication formula*. Engineering (London), 1961. **192**(4972): p. 158-159.
48. D. Dowson and S. Toyoda. *A central film thickness formula for elastohydrodynamic line contacts*. in *Proceedings of the 5th Leeds-Lyon Symposium on Tribology, London*. 1978.
49. B.J. Hamrock and D. Dowson, *Ball bearing lubrication: the elastohydrodynamics of elliptical contacts*. John Willey & Sons, 1981.
50. N. Patir and H. Cheng, *An average flow model for determining effects of three-dimensional roughness on partial hydrodynamic lubrication*. Journal of Lubrication Technology, 1978. **100**: p. 12.
51. D. Zhu, *On some aspects of numerical solutions of thin-film and mixed elastohydrodynamic lubrication*. Proceedings of the Institution of Mechanical Engineers, Part J: Journal of Engineering Tribology, 2007. **221**(5): p. 561-579.

52. Y. Liu, Q.J. Wang, D. Zhu, W. Wang, and Y. Hu, *Effects of differential scheme and viscosity model on rough-surface point-contact isothermal EHL*. Journal of tribology, 2009. **131**(4).
53. W. Wang, Y. Hu, Y. Liu, and D. Zhu, *Solution agreement between dry contacts and lubrication system at ultra-low speed*. Proceedings of the Institution of Mechanical Engineers, Part J: Journal of Engineering Tribology, 2010. **224**(10): p. 1049-1060.
54. D. Zhu and H.S. Cheng, *EFFECT OF SURFACE ROUGHNESS ON THE POINT CONTACT EHL*. Journal of Tribology, 1988. **110**(1): p. 32-37.
55. J. Greenwood and J. Williamson, *Contact of nominally flat surfaces*. Proceedings of the Royal Society of London. Series A. Mathematical and Physical Sciences, 1966. **295**(1442): p. 300-319.
56. J. Greenwood and J. Tripp, *The contact of two nominally flat rough surfaces*. Proceedings of the institution of mechanical engineers, 1970. **185**(1): p. 625-633.
57. R. Onions and J. Archard, *The contact of surfaces having a random structure*. Journal of Physics D: Applied Physics, 1973. **6**(3): p. 289.
58. B. Bhushan, *Contact mechanics of rough surfaces in tribology: multiple asperity contact*. Tribology Letters, 1998. **4**(1): p. 1-35.
59. Y.-Z. Hu and Z. Dong, *A full numerical solution to the mixed lubrication in point contacts*. Journal of tribology, 2000. **122**(1): p. 1-9.
60. E. Tomanik, H. Chacon, and G. Teixeira, *A simple numerical procedure to calculate the input data of Greenwood-Williamson model of asperity contact for actual engineering surfaces*. Tribology Series, 2003. **41**: p. 205-215.

61. *GT-Suite™ Manual Version 7.3*. Gamma Technologies, 2013.
62. *Steel is the Solution to Achieve 54.5 MPG by 2025*. 2013; Available from:
<http://www.autosteel.org/Research/Growth%20of%20AHSS.aspx>.

CHAPTER 2

FRICTION AND COUNTERFACE WEAR INFLUENCED BY SURFACE PROFILES OF PLASMA ELECTROLYTIC OXIDATION (PEO) ON AN ALUMINUM A356 ALLOY

1. INTRODUCTION

To reduce fuel consumption and CO₂ emission, it is becoming increasingly important to reduce vehicle weight. Aluminum represents 7.8 percent of vehicle curb weight internationally in today's family cars, trucks and minivans [1]. This increased use is due primarily to many cost and fuel economy benefits that lightweight aluminum offers (40~50% weight reduction than gray cast iron for gasoline engines) [2]. AlSi alloys such as Al 356 and Al 390 have been commercially used to produce engine blocks due to their high strength over weight ratios. The engine block cylinder guides the reciprocating sliding motion of the piston and piston ring under mechanical and thermal cyclic stresses. Therefore, good wear resistance is a critical property to engine block life. Due to the low surface hardness of aluminum alloys, the cylinder bore surface needs to be modified to obtain high wear resistance. Generally gray cast iron liners, which have high hardness with embedded graphite flakes acting as solid lubricants, have a resistance to galling and seizing higher than aluminum alloys, and are widely used as cylinder bore surface materials for light metal engines [3, 4]. However, the relatively heavy cast iron liners, along with the difference of thermal expansion coefficients between light metals and the cast iron and its low thermal conductivity compared to aluminium may lead to degradation of engine performance and increase of emission and fuel consumption [2].

To avoid cast iron liners, one option is using coated cylinder bores such as nickel based ceramic composite (NCC) coatings [5]. Nikasil is such an electrodeposited lipophilic nickel matrix silicon carbide coating for piston engine cylinder bores. It allows large cylinder bores with tight tolerances and thus facilitates the redesign of existing engines. However, Nikasil and its similar coatings are vulnerable to the sulfur found in low quality gasoline. The sulfur can cause some Nikasil cylinders to break down over time and costly engine failures [6]. Lokasil bore surfaces are comprised of silicon fibers in a binding process that, when inserted into the block mold, burns out the fibers, leaving the high-content silicon surface directly in the bores. The hard silicon surface possesses the high wear resistance of Lokasil cylinders [7]. Another similar cylinder which is armored with hard silicon crystals is Alusil, a hypereutectic AlSi alloy $\text{AlSi}_{17}\text{Cu}_4\text{Mg}$. Silicon crystals are homogeneously distributed in the area of the surface of the cylinder bore in the cast Alusil engine block. In contrast to honing grey cast iron liners, the honing process for Lokasil and Alusil cylinders does not aim at achieving a surface structure that generates tribological advantages on the cylinder surface by using the cross hatching process. The honing process is mainly intended for establishing a perfect bore geometry during the course of the silicon exposure. The silicon crystals are exposed from the surrounding aluminium matrix up to a certain depth. In this honing process, not only the silicon crystals are rounded but also an oil-retaining volume is generated between the crystals that is required for ensuring the lubrication of the associated parts piston and cylinder block [2]. Disadvantages that have to be considered for Alusil are the poor machinability of these engine blocks, because of the high hardness of the Si grains, and the high cost of the material.

Recently, engine manufacturers have applied a Plasma Transferred Wire Arc (PTWA) technique to produce a wear resistant coating on the internal surface of engine block cylinder bores [8, 9]. During the PTWA process, a supersonic plasma jet melts a single conductive wire, atomizes it and propels it onto the substrate to be coated. After atomization, the stream of molten droplets is transported by forced air onto the bore wall. The particles impinge on the surface of the substrate and flatten due to the high kinetic energy. The particles rapidly solidify upon contact and stack to make up a high wear resistant coating. For AlSi alloy blocks, PTWA provides a lower cost and weight-saving alternative to cast iron liners, while delivering increased displacement in the same size engine package and a potential for better heat transfer.

Aluminum-based metal matrix composites (MMC) also exhibit a better wear resistance than the unreinforced Al alloys by adding the reinforced materials into the Al matrix. The manufacturing cost of the Al-based MMC can be lower than that of the hypereutectic Al alloys by choosing proper reinforced materials [10]. However, a disadvantage of hypereutectic Al alloys and MMC composites is that, under a high contact stress, the soft Al matrix can still be plastically deformed, causing the precipitated Si particles or the reinforced materials to detach from the matrix. The detached hard particles adhere to the counterface and abrade the matrix, resulting in a high wear rate and friction [11]. As a new approach to create a cylinder bore, SiO₂ particulate Al MMC was developed as the raw material of a cylinder liner to protect the engine block, made of the hypoeutectic Al alloys, from the wear attack [4, 12]. To improve the wear performance of the MMC under a high contact stress but also avoid the honing process, a proprietary oxide coating process based on a modified PEO method was used to produce

thin oxide coatings on the MMC samples. It was found that, with a proper combination of the volume content of SiO₂ and coating thickness, the coated MMC presented a much higher wear resistance and a lower friction coefficient than the uncoated MMC.

Owing to superior coating performance, process cost effectiveness and environmental friendliness, the PEO process attracts increasing attention for the surface treatment of lightweight metals, in particular Al, to enhance their hardness, wear, corrosion resistance and thermal protection [13-20]. Compared with Nikasil, Lokasil, Alusil and PTWA, the PEO process utilizes almost no foreign coating materials such as a conductive wire in PTWA or silicon fibers in Lokasil; it is also independent on the high content of Si to resist wear. Therefore, PEO coatings can be economical and environmentally friendly. On the other hand, only 12% of the fuel in internal combustion engine finds its way to the driving wheels in a vehicle [21]. Friction between piston rings and cylinder bores accounts for a loss of over 15~20% of the total vehicle power [5, 21-23]. Therefore, the coefficient of friction of PEO coatings on aluminum alloys is an important factor as the coatings are considered to be used for the application in engine cylinders. As-deposited PEO coatings on aluminum alloys have a dimple-like porous surface that allows lubricants to be retained in the coating, similar to the oil retaining function provided by the traditional plateau honing. This feature of thin PEO coatings improves lubricant retention and reduces the wear and friction. Previous investigations show that PEO coatings on aluminum alloys yield low friction and high wear resistance comparable to those of cast iron [24, 25] and Nikasil [26]. These PEO coatings were thick (>20 μm) and had a very hard surface. Since the PEO processing is usually performed at room temperature, small thermal stress is expected. Residual stress can also

be released by micro cracks and their networks. However, little is known about the effects of coating surface profiles on counterface wear (ring wear) and the wear and tribological properties of thin PEO coatings, which are often desirable since they demand shorter processing time and less consumption of electrical power and electrolytic materials.

In this paper, the PEO technique was used to produce thin oxide coatings on an aluminum A356 alloy. A reciprocating tribometer was used to investigate the wear and tribological behaviors of two PEO coatings and a PTWA coating (as reference) under two lubricated conditions. The effect of surface morphology on the tribological and wear properties was particularly studied based on the two PEO coatings polished to different roughnesses and thicknesses. Scanning Electron Microscopy (SEM) and surface profilometry were used to investigate the topography of as-deposited and polished coatings, as well as wear tracks.

2. EXPERIMENT

2.1 Materials and PEO process

Two A356 samples with dimensions of 20 mm x 10 mm x 3 mm were cut from a PTWA-coated cylinder bore (beneath the PTWA coating) in a Ford Shelby GT500 aluminum block. Specimens were polished with SiC sandpapers up to 2500 Grit, rinsed and dried before the treatment by the PEO process. After polishing, both samples had aluminium alloy surfaces without PTWA coatings. During the PEO process, the A356 samples (anode) and a stainless steel plate (cathode) were immersed into two different electrolytes and connected to a pulsed DC power supply, operating at a frequency of 2

kHz and a duration time of 80% duty cycle. During the coating process, the current density was maintained at 0.1 A/cm^2 and the voltage was increased gradually with time, as the coating thickness increased. The processing parameters for the coated PEO samples are listed in Table 2.1. A cooling system maintained the electrolyte temperature below $30 \text{ }^\circ\text{C}$ during the process. The surface morphology and composition of the coatings were characterized using a JEOL 2100 Scanning Electron Microscope (SEM) with an energy dispersive x-ray analysis system (EDX). The phase structures were analyzed using X-ray diffraction (XRD). The x-ray is a Cu $K\alpha$ radiation with a wavelength of 0.154 nm . The PTWA specimen was cut from the unworn PTWA coated surface of the same cylinder bore for the purpose of comparison. The PTWA coating has the final finished surface and it has been optimized by automakers to get the best possible tribological performance. The PTWA surface was kept as received from a manufacturer without manipulating, therefore, its skewness, kurtosis and roughness can be used as a benchmark for the comparison. Coating thicknesses of these samples were determined from cross sectional views under SEM observations. Vickers hardness tests were carried out using 0.02 N load to determine the hardness of coating/substrate systems. The relatively-high indenting load was selected to clearly distinguish the indentation marks for the as-received PTWA and PEO coatings. A Mitutoyo surface profiler SJ201P was used to measure the roughness of PEO and PTWA samples.

Table 2.1 Process parameters and properties of as deposited PEO coatings and a PTWA coating

Sample	Electrolyte composition	Current (A/cm ²)	Treatment time (min)	Average Thickness (μm)	Average Vickers Hardness (HV _{0.2})
PEO S1	K ₄ P ₂ O ₇ 12 g/l	0.1	10	7.8	370
PEO S2	K ₄ P ₂ O ₇ : Na ₂ SiO ₃ 6:6 g/l	0.1	10	6.4	258
PTWA	NA	NA	NA	115.2	318

2.2 Tribological tests

To evaluate tribological properties at the micro-scale, reciprocating sliding tribotests were performed on PEO and PTWA coated samples under a normal load of 2 N (maximum Hertz contact stress 980 MPa) for 220 m sliding distances. The stroke distance was 10 mm, and frequency 4Hz. Before tribological tests, the surface roughness of PEO coated sample S1 was manipulated with SiC sandpapers (2500 and 4000 Grit) and polished using Al₂O₃ powder (1 μm) to obtain three areas with different average roughness R_a , i.e., 1.0 μm (as-deposited), 0.71 μm (sanded) and 0.17 μm (polished). Similarly, the roughness R_a of three areas of PEO S2 were 0.70 μm (as-deposited), 0.42 μm (sanded) and 0.10 μm (polished). Both PEO samples were then cleaned with acetone to remove debris. The surface roughness R_a of the PTWA coated sample was 0.4 μm

(Table 2.2). AISI 52100 steel balls (ϕ 5.5 mm) were selected as counterpart pins. Two different lubrication conditions were applied. One was the boundary lubrication condition, i.e., PEO S1, S2 and PTWA coatings were tested with the existence of 5 ml 5W30 engine oil at the contact area around the pin. Under starve lubrication condition, the samples were immersed into 5W30 for 1 minute and then hung up for 1 day before the tests. The excessive engine oil was naturally drained off and a thin layer of lubricant was formed as lubricant film on the coating surfaces. This condition was used to simulate a simplified lubrication starve situation at the initial stage of the restarting of an engine after a long period of inactivity. The sliding distance of the tribological tests was set to be 220 m. After tribological tests, the wear tracks were investigated using SEM observations with EDX analysis on the top view.

Table 2.2 Average roughness parameters of as deposited, sanded and polished coatings

	Sanding and Polishing	Thickness (μm)	Roughness R_a (μm)	Skewness	Kurtosis
PTWA	N/A	115.2	0.40	-0.71	2.83
PEO S1	As deposited	7.8	1.00	0.07	-0.83
	By 2500/4000 grit SiC	6.0	0.71	-0.49	-0.68
	By 1 μm Al_2O_3	3.9	0.17	-1.68	7.02
PEO S2	As deposited	6.4	0.70	0.25	-0.13
	By 2500/4000 grit SiC	4.6	0.42	-0.84	0.20
	By 1 μm Al_2O_3	3.5	0.10	-5.80	74.10

3. RESULTS AND DISCUSSION

Fig. 2.1 shows XRD patterns (Cu $K\alpha$) of two PEO samples on the 356 alloy. The aluminum (Al) and silicon (Si) peaks in Fig. 2.1 were detected from the AlSi alloy substrates. The two PEO coatings were mainly composed of $\alpha\text{-Al}_2\text{O}_3$ and $\gamma\text{-Al}_2\text{O}_3$. The phase structures of the two PEO coatings were similar.

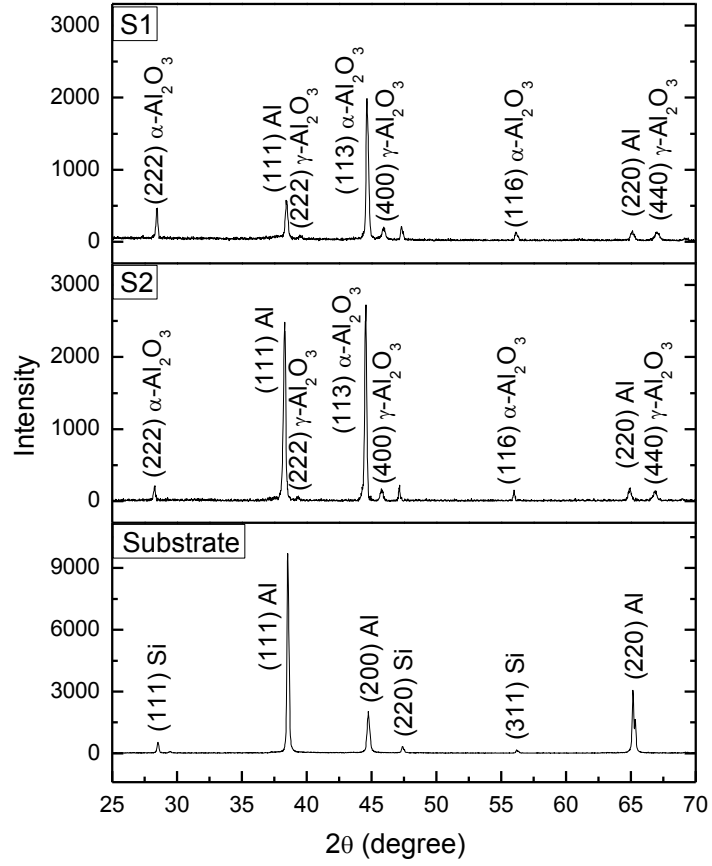


Figure 2.1 XRD patterns (Cu K α) of the PEO coatings on the A356 alloy.

Fig. 2.2 is the SEM micrographs of surface morphology and EDX spectra of the PTWA, PEO S1 (as-deposited) and S2 (as-deposited) samples. The surface texture of PTWA coating was finished by honing and cross-hatching. Its average_Vickers hardness was 318 HV0.2. PEO coatings are shown in both top and 45° tiled cross section views in Figs. 2.2c to 2.2f. The EDX spectrum in Fig. 2.2a shows the Fe/FeO existence from the laminate structure on the bore consisting of a nanocrystalline material—iron and ferrous-oxide (FeO, known as Wuestite) [9] with minor amounts of Cr and Si. PEO S1 and S2 coatings have similar chemical compositions as demonstrated by their spectra in Figs. 2.2c and 2.2e. The Si peaks result from the AlSi substrate.

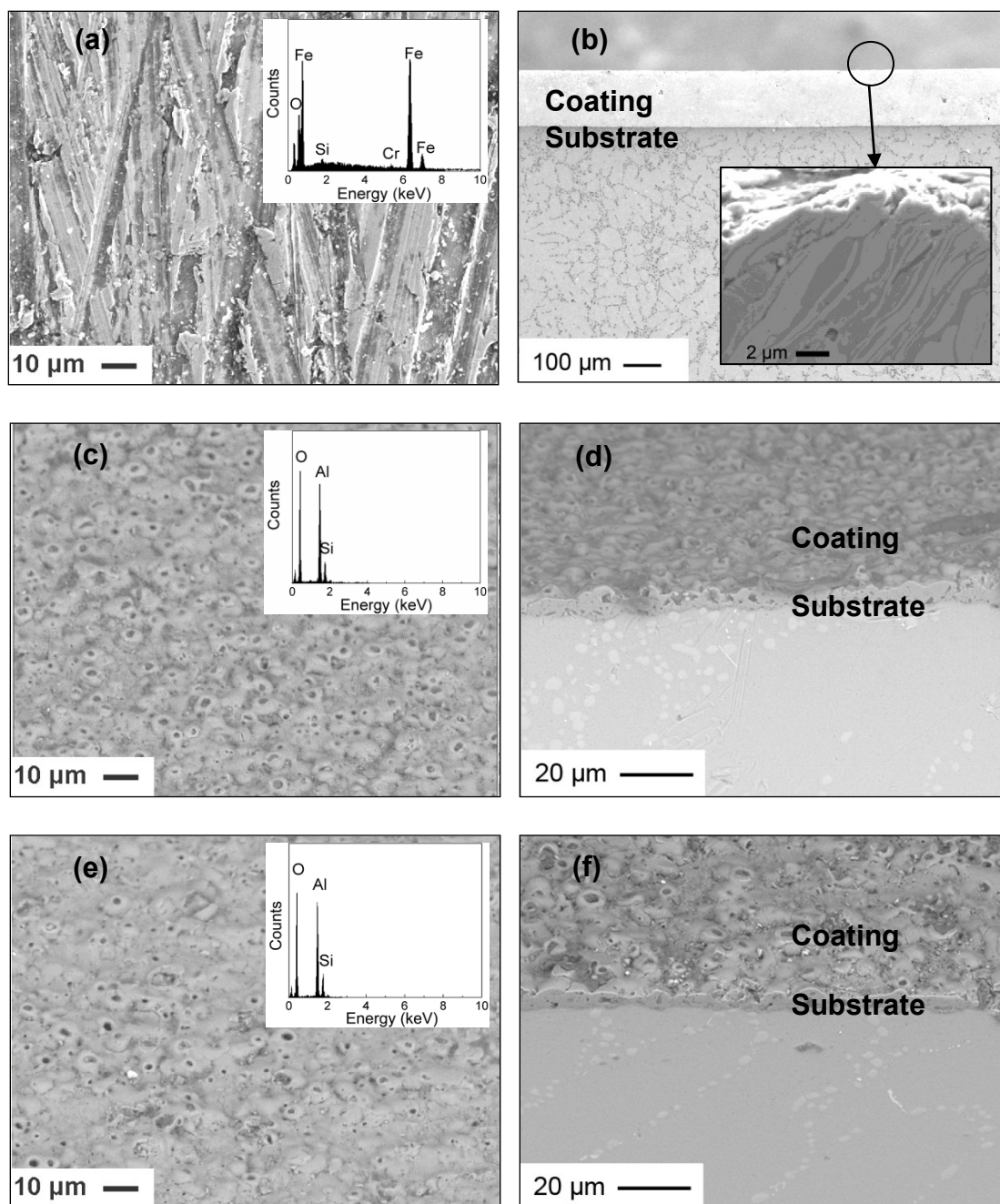


Figure 2.2 SEM images of surface morphology and EDX spectra of the PTWA and PEO coatings. (a) PTWA (as-deposited), (b) cross-section view of PTWA, (c) PEO S1 (as-deposited), (d) 45 tilted cross-section view of S1, (e) PEO S2 (as-deposited) and (d) 45 tilted cross-section view of S2.

The profiles of the different PEO samples and the PTWA sample obtained using the Mitutoyo surface profiler SJ201P were used to calculate the average roughness R_a , skewness R_{sk} , and kurtosis R_{ku} , which were found important to the tribological properties of the surface. Skewness R_{sk} describes the asymmetry of the height distribution histogram. If $R_{sk} = 0$, height distributions on the surface is symmetric, such as, a Gaussian distribution. If $R_{sk} < 0$, the surface is featured with holes and if $R_{sk} > 0$ the surface is flat with peaks. Kurtosis R_{ku} describes the flatness or peakedness of the surface topography. Surfaces with high kurtosis tend to have distinct peaks near the mean, decline rather rapidly, and have heavy tails. Surfaces with low kurtosis tend to have flat tops near the mean rather than a sharp peak. A schematic of surfaces with positive and negative skewness values, as well as with kurtosis values lower and higher than three is shown in Fig. 2.3 [27]. For lubricated sliding contact, surfaces with more negative skewness and higher kurtosis, in which the surface was relatively flat with many deep valleys, resulted in low friction [28-30]. Sedlacek et al. found that for a boundary lubrication, the most dominant parameter was R_{sk} . The more negative R_{sk} was, the lower the friction was, even at higher average surface roughness [29]. However, a computer modeling [28] indicated that decreasing skewness led to an increase in the maximum real area of contact experienced during the engine cycle. Therefore, surfaces of very low skewness might experience scuffing, as has been observed in real engine situations [28].

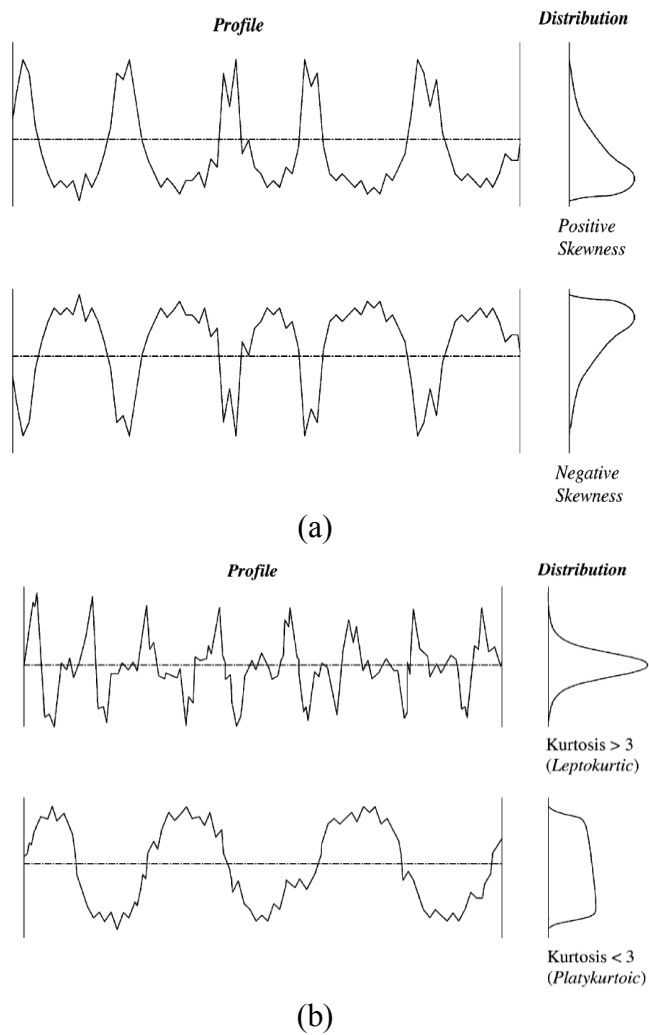


Figure 2.3 Schematic of surfaces with (a) positive and negative skewness and (b) kurtosis values lower and higher than three.

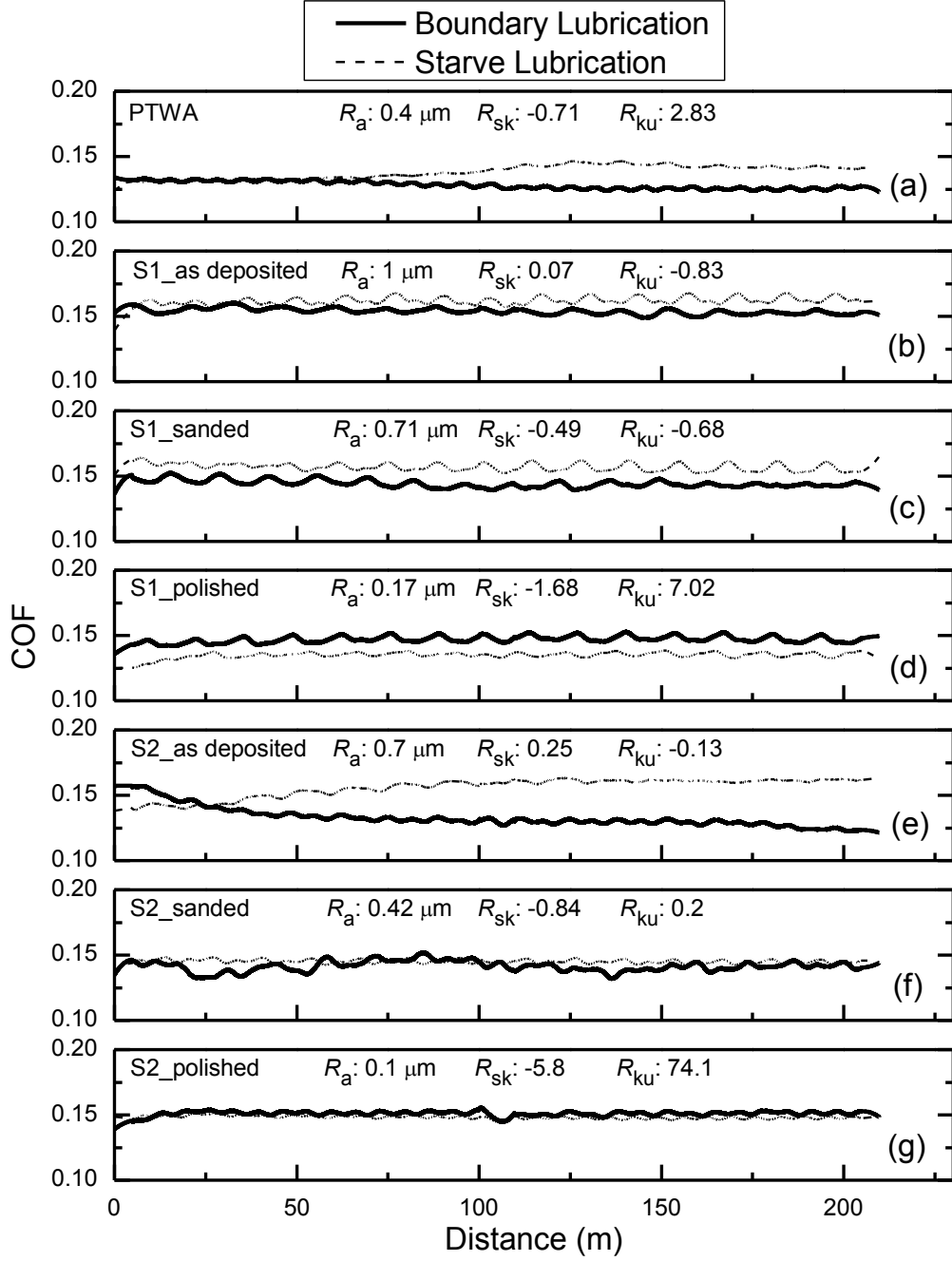


Figure 2.4 The average COFs of PTWA and PEO coatings under two different lubrication conditions. (a) PTWA, (b) PEO S1 as-deposited, (c) PEO S1 after sanding, (d) PEO S1 after sanding, (e) PEO S2 as-deposited, (f) PEO S2 after sanding and (g) PEO S2 after polishing. Solid lines are of boundary lubrication and dashed lines for starve lubrication.

Fig. 2.4 presents the smoothed coefficient of friction (COF) curves of the PTWA and PEO coatings under two lubrication conditions: boundary lubrication and starve lubrication. The boundary lubrication condition was better lubricated because the lubricant could be observed around the contact area between the pin tip and the coating surface during the reciprocating tribo tests. The COFs were smoothed by the Savitzky-Golay method.

3.1 COFs

3.1.1 PTWA: boundary lubrication vs. starve lubrication

The COF curves of PTWA coating are presented in Fig. 2.4a. The COF of PTWA_B (B denotes boundary lubrication) decreased steadily from 0.13 at the beginning to 0.125 at the end of the test. The mild decrease from the beginning might be the result of a break-in procedure because the wear track on the coating could be observed. The PTWA_S (S denotes starve lubrication) coating demonstrated a different behavior on stability of COF after break-in as shown by the dashed line in Fig. 2.4a. The COF increased from 0.13 to 0.15 around 125m and stayed at 0.15 to the end. The COF under the boundary condition was lower than that of starve lubrication. In both cases, the COF curves approached their own horizontal position at the end. The horizontal orientation suggested that the friction and wear behaviors became stabilized.

3.1.2 PEO S1: boundary lubrication vs. starve lubrication

The COF of as-deposited S1_B (Fig. 2.4b) was lower than the less lubricated S1_S. The sanded PEO S1 (Fig. 2.4c) coating performed in a trend similar to as-

deposited PEO S1, featured in a lower COF of S1_B than that of S1_S. For the polished PEO S1 (Fig. 2.4d) which had a smoother surface (smaller R_a) than the sanded and as-deposited PEO S1, COFs behaved differently: oil drop lubricated S1_B showed a higher COF than that of S1_S. This may be explained by the change of lubricant retention capability of PEO coatings. Micro-valleys or scratches acted as wear traps and/or reservoirs for the lubricant, just like the honed grooves in the PTWA coatings. A negative R_{sk} described surfaces with deep valleys and a deficiency of high peaks; R_{ku} exceeding 3 depicted surfaces with high peaks and deep valleys. The combination of negative R_{sk} and high R_{ku} denoted plateau-like smooth surfaces with deep valleys (Figs. 2.5c and 2.5d), which was desirable for low friction applications [28-30]. In addition, porous PEO coatings on Al alloys have the potential to reserve lubricant in micro pores (i.e., dimples) and crack networks in the PEO coatings. Curran et al. [31] found that PEO coatings on aluminium alloys were approximately 20% porous and this level of porosity was largely surface-connected. For as-deposited PEO coatings, micro valleys (Fig. 2.5) were main reservoirs of lubricant compared to the inherent micro pores and micro cracks in the coating. For boundary lubrication, lubricant existed mainly between micro valleys, while micro pores and cracks absorbed a relatively small amount of lubricant. For starve lubrication, the lubricant existed less in micro valleys than in micro pores and cracks after dipping into lubricant for 1 minute and hung for 1 day. Therefore, lubricant involved in sliding for as-deposited PEO S1 under boundary lubrication was somehow more than that of starve lubrication. As a result, the COF for the boundary lubrication was lower than that for starve lubrication.

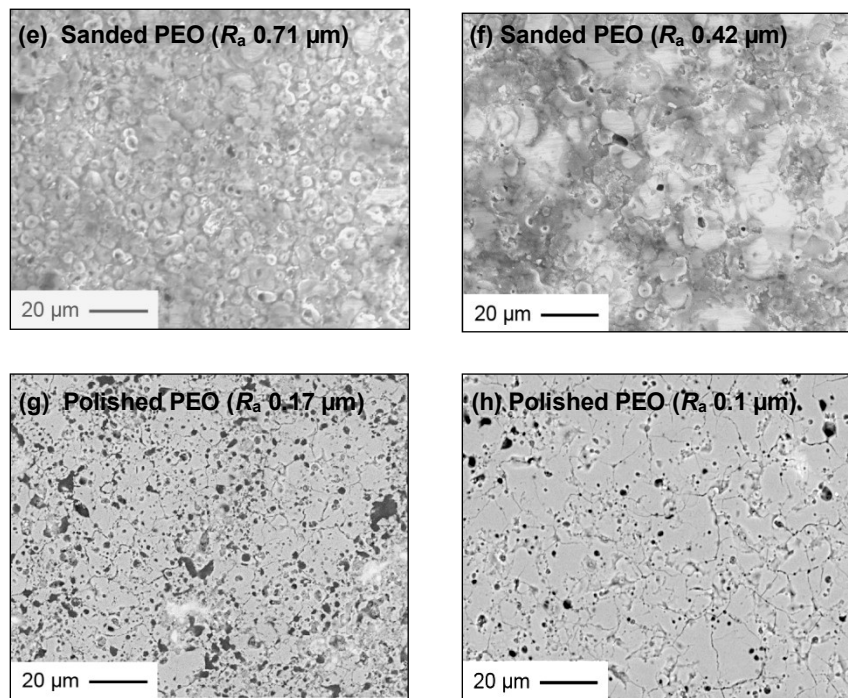
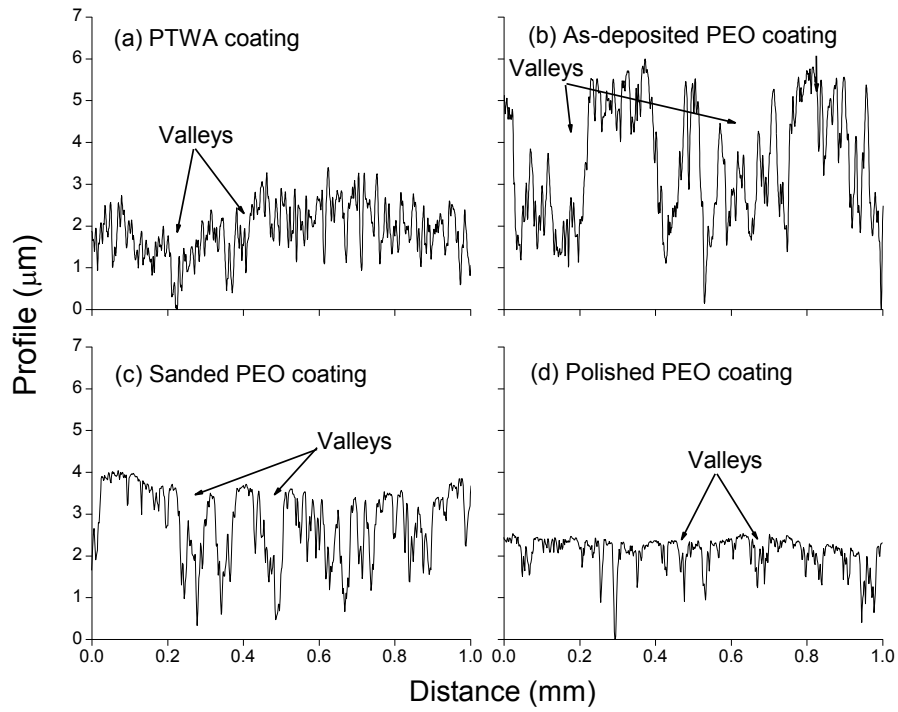


Figure 2.5 Typical surface profiles: (a) PTWA coating and PEO coatings at (b) as-deposited, (c) sanded and (d) polished conditions. SEM images of PEO

coatings after sanded and polished to (e) Ra 0.71, (f) Ra 0.42 μm , (g) Ra 0.17 μm and (h) Ra 0.1 μm .

For the sanded PEO S1 coating (Figs. 2.5c and 5e), micro valleys became shallow and micro bumps became flat after sanding, represented by more negative skewness and higher kurtosis. The ratio of the volume of micro valleys and the volume of micro pores and cracks changed to a lower level and the lubricant retention ability of the boundary lubrication condition decreased. However, the lubricant retention may be still dominated by micro valleys for the sanded case. The COF for the boundary lubrication was consequently lower than that of starve lubrication. After the PEO sample was polished to be smooth enough (Figs. 2.5d and 5h), micro pores and micro cracks presumably dominated the lubricant retention ability. Although the amount of lubricant applied between the pin tip and the coating surface was sufficient in the boundary lubrication condition at the beginning of the tribo test, the coating surface was not as well wetted and lubricated as the starve lubrication treated condition; the latter had been immersed in the lubricant and wetted by oil for a longer time and was thus already covered by a thin but uniform lubricant film before the test. The flattened coating surface due to the polishing squeezed out the lubricant oil and thus reduced the oil retention between the contact faces at the boundary lubricated condition, and as a result, the COF of the polished PEO S1_B was higher than that of S1_S. It should be noted that the polished coating surface condition may benefit the mixed and hydrodynamic lubrication conditions.

3.1.3 PEO S1: as-deposited vs. sanded vs. polished

The COF curve of as-deposited PEO S1 under boundary lubrication fluctuated around 0.15 while the sanded PEO S1 curve fluctuated slightly below 0.15. The polished PEO S1 curve under boundary lubrication seemingly returned to 0.15. The COFs under the starve lubrication decreased from about 0.16 to around 0.15 then around 0.14 with the average R_a decreasing from 1 μm to 0.71 μm , 0.17 μm . Noticeably, the most cases in the COFs of PEO S1 were somewhat higher than that of the PTWA coating. However, long-term use of the PEO coating would reduce surface roughness due to the coating polishing effect, which would lead to friction reduction opposite to the situation of the PTWA coating.

3.1.4 PEO S2: boundary lubrication vs. starve lubrication

For as-deposited PEO S2 (Fig. 2.4e), the COF under the boundary lubrication dropped continuously from around 0.16 along the whole reciprocating sliding distance to about 0.12 at the end, which was the lowest COF obtained. On the contrary, the COF for the starve lubrication increased from around 0.14 to 0.16 at 100 m and then stabilized around 0.16 to the end. This may be due to the contact models of the boundary lubrication. For the starve lubrication, the load was carried by the surface asperities; for boundary lubrication, asperity forces supported load at discrete points while hydrodynamic fluid pressure held load elsewhere. Boundary lubrication was initially formed under the pin tip before sliding began. Upon the commencement of the sliding, the fluid gradually filled and saturated the space between pin tip and underneath coated surface along the whole sliding track to form the lubrication film. Therefore, the COF of

S2_B went downward in the Fig. 2.4e. Micro bumps on the as-deposited PEO S2 surface were sparse, whereas micro bumps on as-deposited PEO S1 surface were dense. Thus, the PEO S2 had few asperities but more oil fluid (held by valleys) on its coating surface involved in carrying the test load than the PEO S1. Therefore, the S2_B was more like a mixed lubrication situation after the running-in was completed, leading to a lower COF comparing to the S1_B. As depicted in the Stribeck curve [32], the COF of a mixed lubrication was lower than that of a boundary lubrication. The boundary lubrication herein denoted a constant contact between the friction surfaces through a large number of high surface points (microbumps); the mixed lubrication regime denoted an intermittent contact at a few surface points (microbumps) due to the separation of oil fluid between the friction surfaces, which fell in the intermediate regime between boundary lubrication and hydrodynamic friction.

Similar to PEO S1, the COF curve of the as-deposited PEO S2 under the starve lubrication was located above that of boundary lubrication (Fig. 2.4e). After sanding, the COF curve under the starve lubrication almost overlapped with that of boundary lubrication (Fig. 2.4f). Polishing the PEO S2 pushed the COF curve under the starve lubrication slightly below the one for the boundary lubrication (Fig. 2.4g). This shift of the COF curves could still be explained by the rationale discussed above for the PEO S1.

3.1.5 PEO S2: as-deposited vs. sanded vs. polished

The overall trend of the COF curves of the PEO S2 under the starve lubrication were similar to that of PEO S1: the lower average R_a , the lower COFs, although the COF curves of the sanded and polished samples were at almost the same level. However, under

the boundary lubrication, this trend was changed. The COFs became high when the average R_a decreased. This indicated the valleys were playing the dominating role in S2 with a lower amount of pores. The polishing removing the valleys led to a reduction in oil retention. Consequently, the COFs increased from 0.12 to 0.14 then 0.15 at the end of sliding with the average R_a decreasing from 0.7 μm to 0.42 μm then 0.1 μm . This could be explained by the decrease in lubricant film thicknesses and the increase in load support from the surface asperities without much sharing of the pressurized oil lubricant present between the contact faces. The sanded and polished coatings had more and finer asperities, which shared more the load than that of the as-deposited coating. The lubricant films were also thinner than that of the as-deposited coating. As a result, the COFs of sanded and polished coatings were higher than that of the as-deposited coating. Remarkably, for both sanded and polished PEO S1 and S2, the effects of asperity distribution and lubrication film thicknesses on the COF behavior under the boundary lubrication was limited, which was evidenced by an almost constant COF value of 0.15. Comparing to the PTWA coating, R_{sk} and R_a of sanded S2 were close to those of the PTWA sample. Presuming that there was no material affinity effect between friction surfaces due to the oil separations during the lubricant tests, the COFs were determined by R_{ku} , i.e., the higher R_{ku} , the lower COF [28-30]. The COF of PTWA with higher R_{ku} (2.83) was then lower than the sanded S2 ($R_{ku} = 0.2$) under boundary lubrication. On the other hand, although the smoothest polished S2 coating had the lowest R_{sk} and highest R_{ku} , the COF curve fluctuated at a relatively high level under boundary lubrication. The high COF might be explained by the very large real area of contact, where no

hydrodynamic pressure was generated and the entire load was supported by asperity contact [28].

3.2 Wear tracks on the coatings

Wear tracks were studied using SEM. Wear tracks of the PTWA sample are presented in Figs. 2.6a and 2.6b. The wear track under the oil dipping (starve) lubrication condition was wider than that of the oil-drop (boundary) lubrication condition. The tested PEO coatings performed so well that the sliding track on PEO S1_S could only be observed by SEM, highlighted by transferred material from the steel pin (Fig. 2.6c). No wear on other PEO coating samples could be obviously distinguished using SEM. The surface profiler was used with intention to measure the profile of wear tracks of PEO coatings but no grooves or wear tracks could be measured.

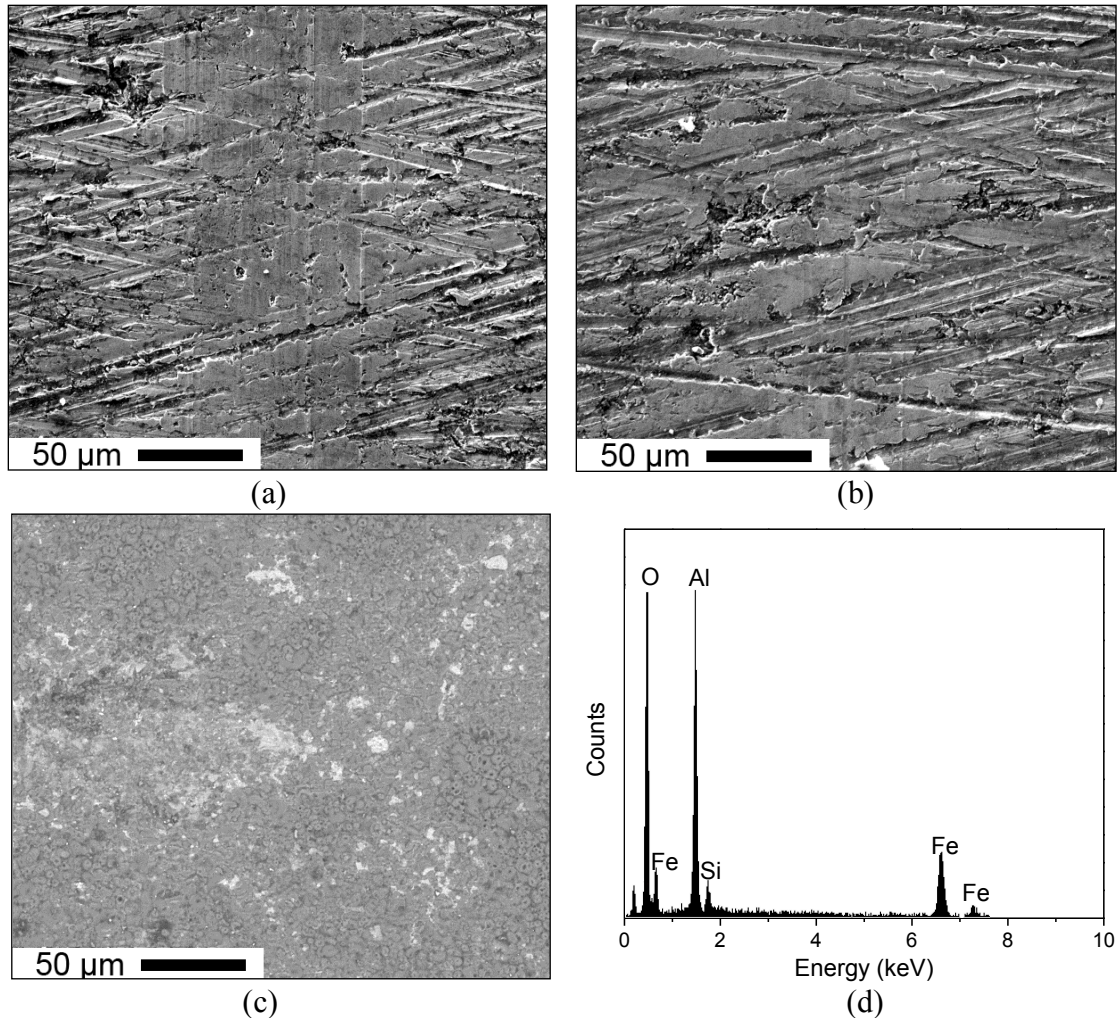


Figure 2.6 Wear tracks. (a) PTWA_B, (b) PTWA_S and (c) PEO S1_S and (d) EDX spectrum of the bright area in (c) showing material transferred from the steel pin.

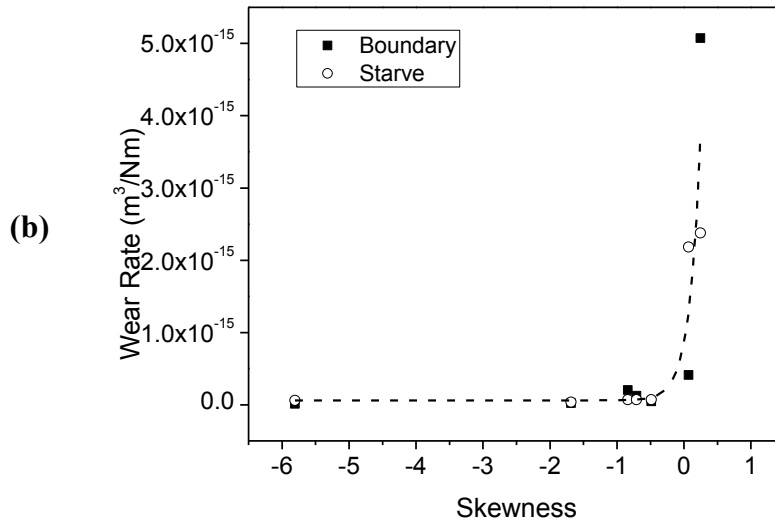
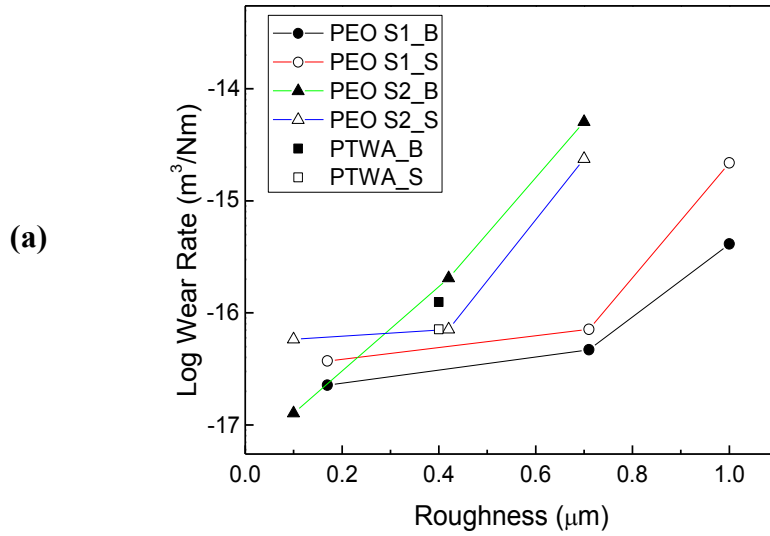
Under the testing conditions, the PEO coatings exhibited a minimum wear and similar friction coefficient compared to the PTWA coating. The selected 2 N load was found to be high enough to cause the wear of the PTWA coated bore surface to some extent. Therefore, the 2 N loading condition was considered to be sufficient to perform a comparable study of the PEO coatings to the PTWA coating. Compared with Alusil and Lokasil cylinder bores, which utilized high hardness of Si particles, the PEO coated Al

alloy offered micro bumps with high hardness on its surface, acting similarly to those protruded Si particles in Alusil and Lokasil. The large number of dimples on the PEO coating surfaces also presumably conferred a further lubricant oil retention capacity. The PEO coatings also provided a hard layer of oxide that could bear the load and protect the soft Al substrate from plastic deformation. The experimental results showed that the wear of the thin PEO coatings was negligible and almost no plastic deformation in substrate could be observed. Therefore, it is suggested that the PEO process could be a promising candidate for aluminum cylinder bore hardening surface treatment. However, only the as-deposited PEO S2_B (after the running-in process) offered COF comparable to the PTWA. The wear scar on the steel pin counterpart of the as-deposited PEO S2_B was the largest. This might be caused by the skewness-positive surface as well as the possible loose particles on the coating surface, which likely braded the counterface ball during the initial running-in (break in) period (the first 25 m, Fig. 2.4e). Slightly buffing the coating surface might be able to avoid this wear issue. On the other hand, the polished PEO_S1 appeared to be the best in terms of the low COF and the compatibility to the counterface in the present study.

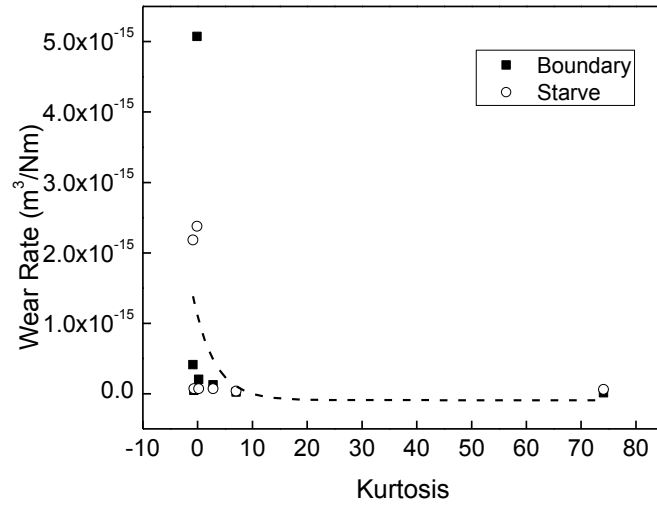
3.3 Wear scars on the steel pins

The wear in PEO coating tests mainly occurred on the steel pins. The lower amount of asperities on the S2 surface caused a very high contact stress which led to a difficulty in formation of the oil lubricant film in the oil drop case. For the oil dipping (starve) case, the thin oil film was already formed before the test. Thus, the oil drop (boundary) lubricant condition resulted in a higher wear on the ball. For the polished

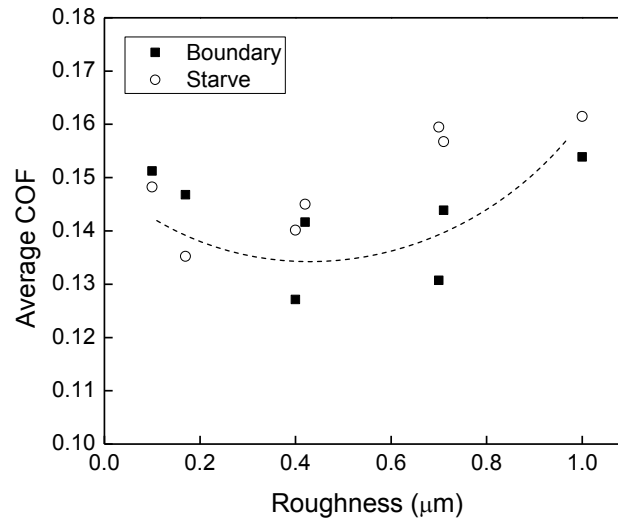
situation of S2, the very smooth surface gave rise to a low contact stress, which had a lower tendency to squeeze out the lubricant. Hence, the oil drop would provide excessive oil lubrication, compared to the oil-dipping case, and consequently led to small counterface wear.



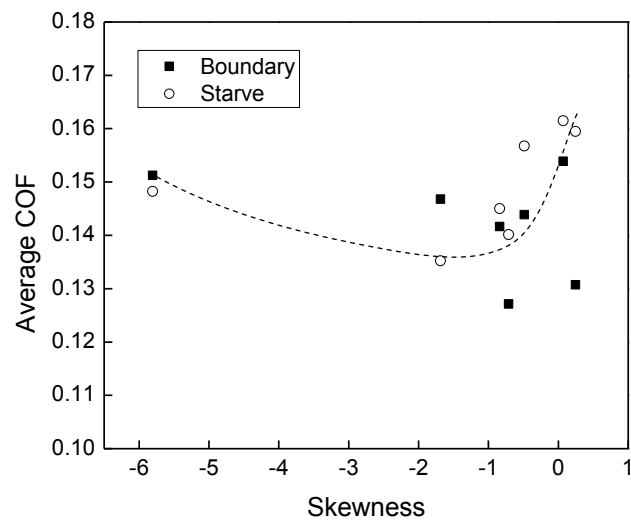
(c)



(d)



(e)



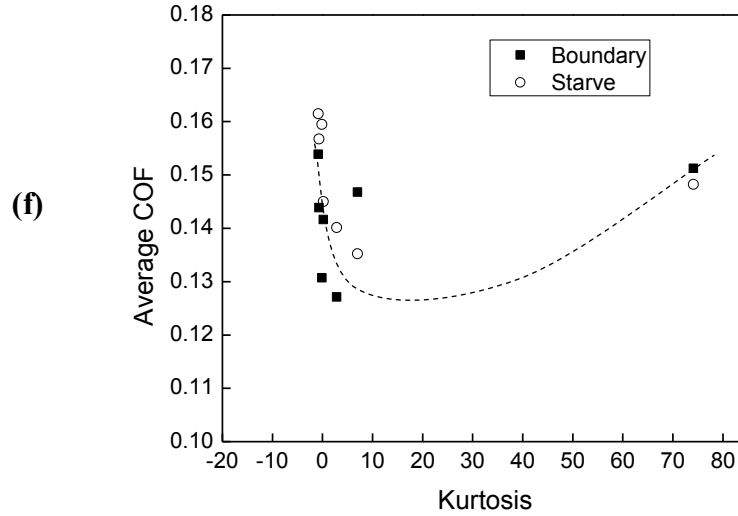


Figure 2.7 Experimental data and fitting curves of wear rate of steel pins and average COFs vs. (a, d) Ra, (b, e) skewness and (c, f) kurtosis respectively. The inset in (a) is an optical image of a typical wear scar on the counterpart steel pin.

Fig. 2.7a presents the wear rates of the steel pins after the tribotests. Except for the as-deposited coatings, all other PEO coatings generated wear scars on the counterface comparable to the PTWA coating. For the PEO S1, the wear scar of steel pins under the starve lubrication was more severe than that of the boundary lubrication. This was normal for the surface on which asperities, pores and valleys were evenly distributed. The sanding and polishing did not significantly alter the surface morphology in terms of the ratio of asperities, pores and valleys. Thus, the smoother the surface, the less wear the counterface had. But the less lubrication, the more severe wear the counterface experienced. Wear scars of as-deposited and sanded PEO S2 under boundary lubrication were significantly larger than that of the starve lubrication. Only the polished PEO S2_B had smaller wear scar than that of the counterpart with the starve lubrication. For both the

sanded coatings, probably due to the presence of a similar skewness level, thus a similar contact stress and oil pressure between the contact surfaces, S1 caused a similar wear on the counterface ball even though it had a much higher surface roughness than S2. This deduction was suggested by the relationship of the skewness of surface profiles and the wear rate as shown in Fig. 2.7b. The wear rate on the steel pin decreased approximately exponentially with the decreasing skewness, showing insignificant effects from materials (PTWA or PEO), surface processing (as-deposited, sanding or polishing) and lubrication (boundary or starve) on the wear behavior when skewness was less than -2.

Figs. 2.7d-2.7f depict the relationship between the average COFs and topographic features. Despite lacking some topographic data points in Figs. 2.7e and 2.7f, the average COFs appeared to reach the minimum values under optimized surface parameters as shown by dashed lines. The relatively high COFs at $R_{sk} = -5.8$ and $R_{ku} = 74.1$ might be due to the very large real areas of contact for the polished S2 sample as mentioned above [29]. Based on the current test conditions, the results suggested that the optimal roughness, skewness and kurtosis for maintaining low COFs and wear should be around $0.4 \mu\text{m}$, -1.8 and 10 , respectively. For a piston ring/liner case under hydrodynamic lubrication, the hydrodynamic friction mean effective pressure (FMEP), a measure of total friction power loss over the engine cycle, kept almost constant with decreasing R_{sk} and seemingly intersected with the boundary FMEP curve at around $R_{sk} = -1.6$ (Figs. 2.5-10 in Ref. [29]) through extrapolation of the curves. The hydrodynamic friction at $R_{sk} = -1.6$ might be among the lowest values. However, when the entire FMEP regime (hydrodynamic and boundary FMEPs) was considered, the minimum friction with changes of surface roughness appeared at around $R_a = 0.1 \mu\text{m}$ (Figs. 2.5-6 in Ref. [29]).

In other words, the optimal roughness and skewness for both boundary and hydrodynamic conditions could be around $0.1\ \mu\text{m}$ and -1.6 . Therefore, further investigation is needed in obtaining a better understanding of the PEO coatings in the entire lubrication regime.

4. CONCLUSIONS

A PEO process has been performed to form a protective layer on cylinder bores made of Al alloy A356 against wear at minimum lubricant conditions. Two electrolytes were used to produce PEO coatings with different hardness and surface morphologies. Both kinds of PEO coatings (S1 and S2) were processed to have various thicknesses and topography. On the one hand, all the prepared PEO coatings performed well in reciprocating sliding tribotests. Compared with the PTWA reference coating as a benchmark, the coefficients of friction of the PEO coatings were low, and wear and plastic deformation of the coatings were minimal. Therefore, PEO coatings can be good candidates for engine cylinder bore surface protection, especially considering economic and environmental advantages of the PEO coating process. On the other hand, the difference of the two PEO coatings in tribological properties was likely due to their different topographic features such as micro bump distribution, porosity and lubricant retention capability. Surface roughness and topography such as R_a , R_{sk} , and R_{ku} were found somehow correlated to the wear and COF behaviors of porous PEO coatings in the tested conditions. The wear losses of the counterface balls appeared to have an exponential relationship to the R_{sk} and R_{ku} values. A lower R_{sk} and a higher R_{ku} would offer a large contact surface area, less sharp asperities—cutting/scratching, and

consequently cause less wear loss of the counterface pins. A lower COF could be obtained by optimizing the surface topographic parameters, i.e., R_a , R_{sk} and R_{ku} . It should be noticed that the test result was more relevant to simulated conditions of cold engine start operation. Further investigation in effects of topography manipulation, testing loads and hydrodynamic lubrication conditions on tribological properties of the coatings and wear losses of counterparts (such as pins and piston rings) would provide a better understanding of the full potential of the PEO process in coating aluminum cylinder bores for gasoline or even diesel engine applications.

REFERENCES

1. The Aluminum Association, Inc., Auto Aluminum Growth, WWW Document, (<http://aluminumintransportation.org/main/growth/auto-aluminum-growth>).
2. KS-Aluminium-Technologie, *Aluminum Cylinder Blocks - Designs, materials, casting methods and cylinder bore surface technologies for lightweight passenger-car engines*. Verlag Moderne Industrie, 2005.
3. A.D. Sarkar, *Friction and wear*. Academic Press, London, 1980.
4. P. Zhang, X. Nie, H. Henry, and J. Zhang, *Preparation and tribological properties of thin oxide coatings on an Al₃Si/SiO₂ metallic matrix composite*, Surface and Coatings Technology, 2010. **205**: p. 1689-1696.
5. K. Funatani and K. Kurosawa, *Composite coatings improve engines*, Advanced Materials and Processes, 1994. **146**: p.27-30.
6. J. Goodman, Engine Professional. Oct-Dec, 18 (2008).
7. E. Köhler, F. Ludescher, J. Niehues, and D. Peppinghaus, ATZ. Automobiltechnische Zeitschrift. 38 (1996).
8. K. Bobzin, F. Ernst, K. Richardt, T. Schläfer, C. Verpoort, and G. Flores, *Thermal spraying of cylinder bores with the Plasma Transferred Wire Arc process*, Surface and Coatings Technology, 2008. **202**: p. 4438-4443.
9. K. Bobzin, F. Ernst, J. Zwick, T. Schläfer, D. Cook, K. Nassenstein, A. Schwenk, F. Schreiber, T. Wenz, G. Flores, and M. Hahn, *Coating Bores of Light Metal Engine Blocks with a Nanocomposite Material using the Plasma Transferred Wire Arc Thermal Spray Process*, Journal of Thermal Spray Technology, 2008. **17**: p. 344-351.

10. D. J. Lloyd, *International Materials Reviews*, 1994. **39**: p. 1-23.
11. D. Roy, B. Basu, and A. Basu Mallick, *Tribological properties of Ti-aluminide reinforced Al-based in situ metal matrix composite*, *Intermetallics*, 2005. **13**: p. 733-740.
12. P. Zhang, X. Nie, L. Han, and H. Hu, *Wear Protection of Al383/SiO2 Metal Matrix Composites by Plasma Electrolytic Oxidation (PEO) Process*, *SAE International Journal of Materials and Manufacturing*, 2010. **3**: p. 55-62.
13. X. Nie, X. Li, and D. O. Northwood, *Corrosion behaviour of metallic materials in ethanol-gasoline alternative fuels*, *Materials Science Forum*, 2007. **546-549**: p. 1093-1100.
14. X. Nie, X. Li, L. Wang, and D. O. Northwood, *Corrosion protection properties of anodic oxide coatings on an Al-Si alloy*, *Surface and Coatings Technology*, 2005. **200**: p. 1994-2000.
15. A. L. Yerokhin, X. Nie, A. Leyland, A. Matthews, and S. J. Dowey, *Plasma electrolysis for surface engineering*, *Surface and Coatings Technology*, 1999. **122**: p. 73-93.
16. A. L. Yerokhin, A. Shatrov, V. Samsonov, P. Shashkov, A. Pilkington, A. Leyland, and A. Matthews, *Oxide ceramic coatings on aluminium alloys produced by a pulsed bipolar plasma electrolytic oxidation process*, *Surface and Coatings Technology*, 2005. **199**: p. 150-157.
17. T. Lampke, D. Meyer, G. Alisch, B. Wielage, H. Pokhmurska, M. Klapkiv, and M. Student, *Corrosion and wear behavior of alumina coatings obtained by various methods*, *Materials Science*, 2011. **46**: p. 591-598.

18. L. Ceschini, C. Martini, G. Sambogna, and F. Tarterini, *Dry Sliding Behaviour of Peo (Plasma Electrolytic Oxidation) Treated AA 2618/20% Al₂O_{3p} Composite*, Material Science Forum, 2011. **678**: p. 61-74.
19. R. C. Barik, J. A. Wharton, R. J. K. Wood, K. R. Stokes and R. L. Jones, *Corrosion, erosion and erosion-corrosion performance of plasma electrolytic oxidation (PEO) deposited Al₂O₃ coatings*, Surface and Coatings Technology, 2005. **199**: p. 158-167.
20. J. A. Curran and T. W. Clyne, *Thermo-physical properties of plasma electrolytic oxide coatings on aluminium*, Surface and Coatings Technology, 2005. **199**: p. 168-176.
21. B. Andersson, *Vehicle tribology*, Elsevier Tribology Series, 1991. **18**: p. 503-506.
22. D. A. Parker and D. R. Adams, *Friction losses in the reciprocating internal combustion engine*, Tribology - Key to the Efficient Engine. (Inst. Mech. Eng. Conf. Pub., London, England, 1982. p. 31-39.
23. M. Priest and C. M. Taylor, *Automobile engine tribology — approaching the surface*, Wear, 2000. **241**: p. 193-203.
24. B.L. Jiang, J. Zhu, and L.J. Bai, *Wear-Resistance of Microarc Oxidation Coating on Aluminum Alloy under Oil Lubrication*, Mocaxue Xuebao/Tribology, 2004. **24**: p. 220-225.
25. V. D. N. Rao, H. A. Cikanek, B. A. Boyer, L. N. Lesnevsky, N. M. Tchernovsky, and N. V Tjurin, *Friction and Wear Characteristics of Micro-Arc Oxidation Coating for Light Weight, Wear Resistant, Powertrain Component Application*, SAE Technical Paper 970022, 1997.

26. K. Mistry, M. Priest, and S. Shrestha, *The potential of plasma electrolytic oxidized eutectic aluminium-silicon alloy as a cylinder wall surface for lightweight engine blocks*, Proceedings of the Institution of Mechanical Engineers, Part J: Journal of Engineering Tribology, 2010. **224**: p. 221-229.
27. E. S. Gadelmawla, M. M. Koura, T. M. A. Maksoud, I. M. Elewa, and H. H. Soliman, *Roughness parameters*, Journal of Materials Processing Technology, 2002. **123**: p. 133-145.
28. V. Wong, T. Tian, L. Moughon, R. Takata, and J. Jocsak, *Low-engine-friction technology for advanced natural-gas reciprocating engines*, DOE Cooperative Agreement No. DE-FC26-02NT41339, Massachusetts Institute of Technology, Cambridge, Massachusetts, USA (2005).
29. M. Sedlacek, B. Podgornik, and J. Vizintin, *Correlation between standard roughness parameters skewness and kurtosis and tribological behaviour of contact surfaces*, Tribology International, 2012. **48**: p. 102-112.
30. M. Sedlacek, B. Podgornik, and J. Vizintin, *Influence of surface preparation on roughness parameters, friction and wear*, Wear, 2009. **266**: p. 482-487.
31. J. A. Curran and T. W. Clyne, *Porosity in plasma electrolytic oxide coatings*, Acta Materialia, 2006. **54**: p. 1985-1993.
32. R. Stribeck, *Die Wesentlichen Eigenschaften der Gleit- und Rollenlager*, VDI-Z, 1902. **46**: p. 1341-1342.

CHAPTER 3

NUMERICAL SIMULATION OF BOUNDARY/MIXED LUBRICATION OF PLASMA ELECTROLYTIC OXIDATION COATINGS UNDER RECIPROCATING MOVEMENT

1. INTRODUCTION

Recently, the investigation of PEO coatings in aluminum engine cylinder surface protection has been reported in Ref [1]. Compared to the competent in the market such as PTWA, Alusil, Nikasil, Lokasil, etc., PEO coatings have the advantages such as cohesive bonding to substrate material, small residue stress, high hardness, high corrosion resistance, high wear resistance, low production cost, low environmental pollution and especially the premier tribological performance under boundary lubrication caused by the good oil retention ability of their porous structure. Also, PEO coating surfaces can vary in roughness and topography easily by controlling the processing parameters such as electrolyte composition, current and treatment time. This variety provides the ability for PEO surfaces optimization in friction reduction. Therefore, a good understanding of tribological behavior of PEO coatings is essential. For internal combustion engines, piston rings and the cylinder bores work under boundary lubrication at top dead center (TDC) and bottom dead center (BDC) where combustion load is high and moving speed is low. A steel ball-on-plate reciprocating tribometer has been applied to study the friction behavior of PEO coatings. The boundary lubrication cases, i.e., 1 drop of 5W30 engine oil applied between the steel ball and 3 coated samples before the ball-on-plate

testing, were discussed in Ref [1]. A well-known Stribeck curve can be used to illustrate boundary and mixed lubrication regimes as shown in Fig. 1.12.

As reviewed in Chapter 1, the reciprocating ball-on-plate movement is under a point contact lubrication condition. Hamrock and Dowson's curve-fitting equations for point contact are [2]:

$$H_c = 2.69G^{*0.53}U^{*0.67}W^{*(-0.067)}(1 - 0.61e^{-0.73k}) \quad (3.1)$$

$$H_m = 3.63G^{*0.49}U^{*0.68}W^{*(-0.073)}(1 - e^{-0.68k}) \quad (3.2)$$

where, $k=b/a$ is a factor of ellipticity, h_c is the central film thickness, R' is the reduced radius of curvature, G^* is materials parameter, U^* is speed parameter, W^* is load parameter (see Chapter 1).

Based on EHL/asperity contacts studies, the application of numerical simulation techniques together with the advancements of computer hardware enabled end users to evaluate more complicated lubrication problems such as piston ring/sikrt/bore contacts which include boundary, mixed EHL and hydrodynamic lubrication conditions. However, the utilization of numerical simulation on analyzing real contact phenomenon with lubricant is raw. In the following sections, numerical simulation based on Eqs. 3.1 and 3.2 plus the Greenwood and Tripp asperity contact theory (Eqs. 1.20 and 1.21) is conducted by using a commercial package GT-Suite. The prediction is compared with selected cases in Ref [1]. A design of experiment (DOE) is also employed to reveal the variation of the lubrication behavior of PEO coatings with surface topographies.

2. SIMULATION

The commercial GT-Suite package is a versatile multiphysics platform with a focus on the engine and vehicle industry. It can address many different technical needs from multibody, flow, thermal, chemical, mechanical and control areas. Also GT-Suite offers convenient tools based on hydrodynamic and asperity contacts to analyze friction, wear and lubrication. In this section, the procedures of analysis on friction of lubricated sliding movement are presented and application guidelines are provided. For the reciprocating ball-on-plate movement, the velocity of ball can be obtained by Eq. 3.3,

$$v = \omega r \sin(\omega t) \quad (3.3)$$

For example, where r is 5 mm, ω is 8π rad/s, therefore, v is from -0.126 m/s to 0.126 m/s [1]. When the velocity is not zero, hydrodynamic lubrication happens. When the velocity is approaching zero, hydrodynamic lifting force decreases and asperity contact increases. Although the oil film at the dead ends of the reciprocating tracks acts as squeeze bearing to some extent, this squeeze bearing effect is not considered because it does not affect friction. In this study, a multibody dynamic model was built using GT-Suite to simulate the reciprocating ball-on-plate tribometer as shown in Fig. 3.1. The rotary speed driver, the cam, sliding joint and two guide rails converted the rotary motion to a sine-wave reciprocating movement at 4 Hz. The stroke was 10 mm. The load of 2 N was applied on the coated sample surface. A Contact2D connector was used to simulate the asperity contact and EHL contact. The key contact parameters were contact geometry, contact stiffness, contact damping and surface topography. The steel ball contact surface was modeled as a ball of 2.75 mm in radius; the PTWA coating surface was modeled as a

cylinder of 50 mm in radius (PTWA sample was cut from a coated cylinder bore of 100 mm in diameter); PEO coatings' surfaces were modeled as planes. The contact stiffness were calculated dynamically depending on contact materials properties (elastic modulus of contact pairs), contact geometry and surface topography. The measured elastic modulus of the PTWA, PEO S1 and PEO S2 coated samples by indentation were 318 GPa, 370 GPa and 258 GPa, respectively [1]. These measured elastic modulus were used to represent the mixed elastic modulus of the coating/substrate surface. The elastic modulus of steel balls was 210 GPa for simulation. Because the R2.75 mm steel balls and 5W30 engine oil were used under the same 2 N load for all tests, the damping coefficients/gaps used to model oil damping force were assumed to be the default value for 5W30 oil as 1000 N-m/s and 50 μm for all cases. The dry friction coefficient (asperity contact) between the steel ball and coated samples was set as 0.3.

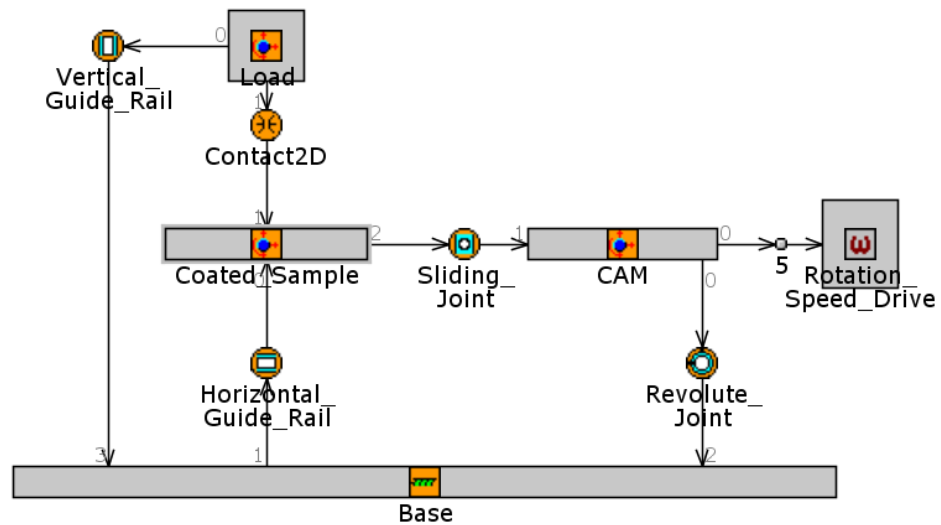


Figure 3.1. GT-Suite multibody model of a reciprocating ball-on-plate tribometer.

Surface topographic parameters for Greenwood-Tripp Model were obtained by Tomanik method. The asperity peak height and radius of curvature of Greenwood-Tripp model parameters are presented in Fig. 3.2. The asperity mean peak height of the PTWA coating was the lowest (0.47 μm), followed by PEO S2 (0.72 μm) and PEO S1 (1.2 μm) coatings; the same sequence appeared in the composite surface standard deviation σ . For the asperity radius of curvature β , the PEO S2 coating was the largest (7.2 μm), followed by the PTWA (7.1 μm) and PEO S1 (6.4 μm). The asperity density η for PTWA, PEO S1 and PEO S2 were calculated as 3.211e9, 1.761e9 and 1.406e9 1/m², respectively. Steel balls (R2.75 mm) were not easy to be measured using profilometer, so a simple R_q of 2 μm was used in the simulation. Lubrication variants such as viscosity pressure effects and shear thinning (Carreau equation) effect of 5W30 engine oil were also calculated by built-in functions of this software package.

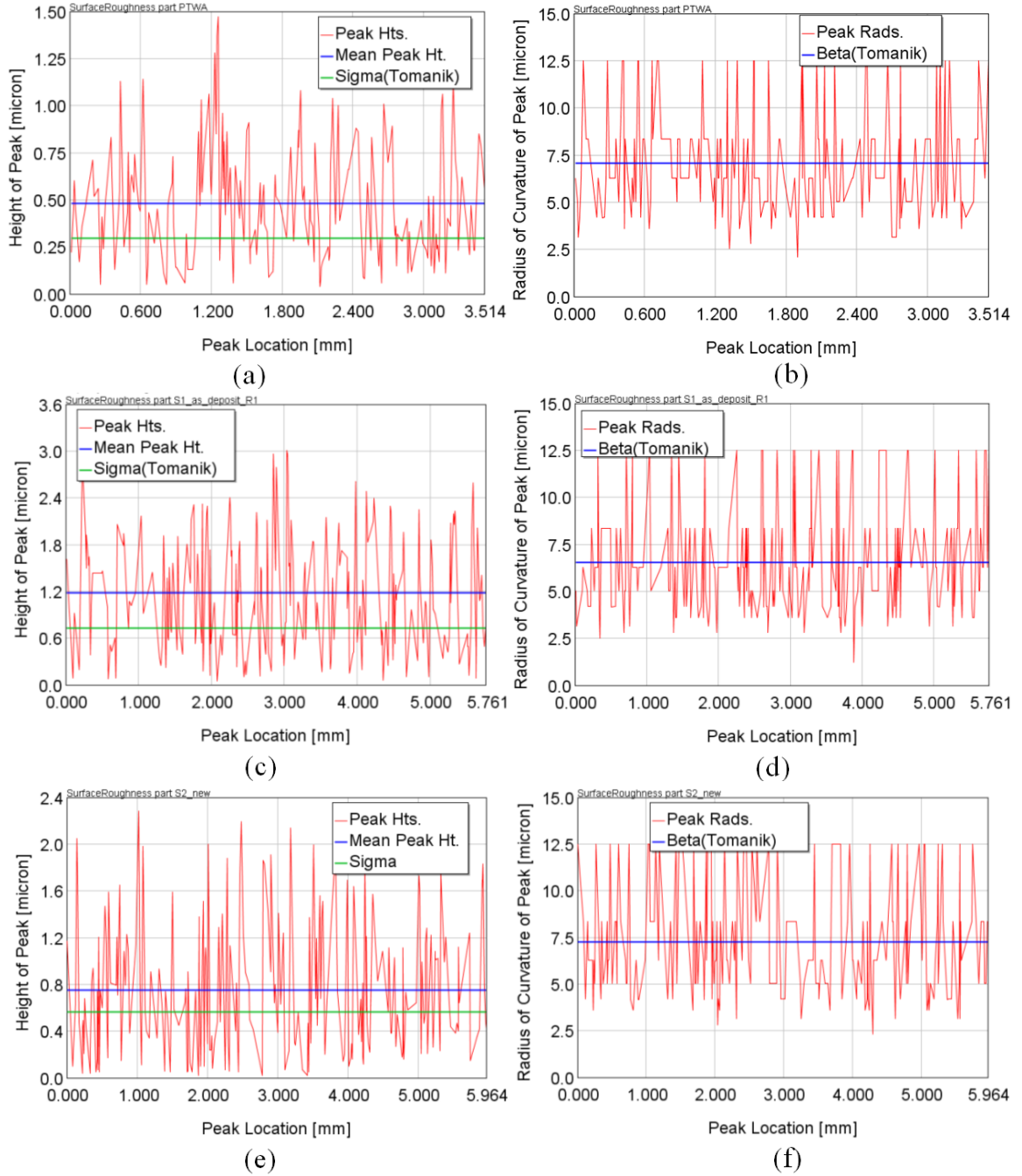


Figure 3.2 The composite surface standard deviation σ and the asperity radius of curvature β for Greenwood-Tripp asperity contact model. (a) σ of PTWA/steel ball, (b) β of PTWA coating; (c) σ of PEO S1/steel ball, (d) β of PEO S1 coating; (e) σ of PEO S2/steel ball, (f) β of PEO S2 coating.

Based on above conditions, the asperity contact pressure and EHL pressure were simulated and friction forces were calculated individually from shear force and asperity normal force multiplied by the coefficient of friction. The friction forces are plotted in Fig. 3.3. The EHL friction forces of three contact pairs were slightly different: PEO S2 was the largest (0.11 N) and PEO S1 (0.05 N) was the smallest. On the contrary, the PEO S2 was the smallest in asperity friction (0.12 N), followed by PTWA (0.58 N) and PEO S1 (0.62 N) had the largest asperity friction force.

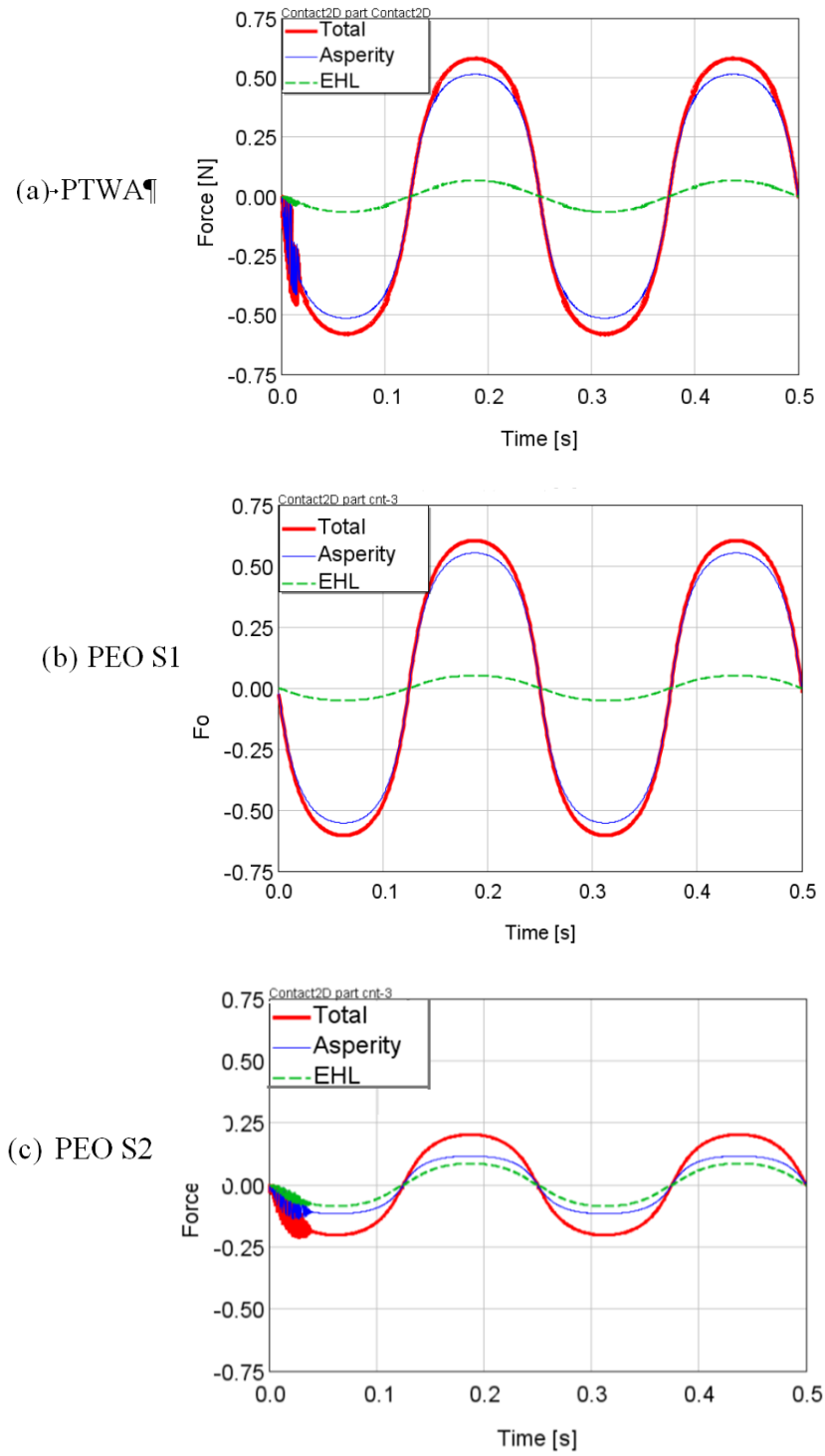


Figure 3.3 Simulated friction forces of steel ball sliding on coatings. Dashed lines are EHL friction, thin solid lines are asperity friction and thick solid lines are the total of EHL and asperity friction. (a) PTWA, (b) PEO S1 and (c) PEO S2.

The work done by wear (dry scrubbing contact) is defined as a time-averaged wear load as

$$W_{wear} = \int P_{ni} V_r dt / \Delta t \quad (3.4)$$

where P_{ni} is the pressure of the instantaneous normal contact force F_n at node i averaged over the instantaneous contact area A_c , V_r is the relative (scrubbing) velocity between the two surfaces in contact, and Δt is the averaging period (simulation time, or period in periodic simulations) [3].

The wear load of PTWA, PEO S1, PEO S2 coatings and the counterpart steel balls were calculated in the simulation and listed in Table 3.1.

Table 3.1 Wear loads of coated samples and steel balls

Coated Samples	Wear load (kW/m ²)	
	on Coating	on Steel Ball
PTWA	456	50905
PEO S1	101	16272
PEO S2	73	9962

To investigate the influence of contact parameters on friction and wear behavior, a design of experiment (DOE) simulation of coated surfaces was performed. The equations of EHL point contacts show that the oil film thickness depends on the reduced radius of curvature R' , the pressure viscosity coefficient α , the reduced Young's modulus E' , the entraining surface velocity U , the viscosity at atmospheric pressure of the lubricant η_0 and the contact load W . The last three parameters were the same for the simulation of three coated samples; while the former three parameters are all elasticity

dependent. The asperity contact also highly depends on elasticity. Other parameters that dominate asperity contact fraction are topographical, i.e., the composite surface standard deviation σ , the asperity radius of curvature β and the asperity density η . A 10^3 full factorial design on three factors at 10 levels (Table 3.2) was chosen for DOE simulation. The three factors were elastic modulus, asperity radius of curvature and asperity density of coated surfaces. The elastic modulus was set from 70 GPa to 400 GPa to cover the modulus range from the soft aluminum substrate to the hard PEO coatings/substrate systems. The asperity radius of curvature was from 5 μm to 8 μm and the asperity density was from $1\text{e}9\text{ 1/m}^2$ to $3.5\text{e}9\text{ 1/m}^2$, corresponding to the measured asperity value ranges of the three coated samples. Normalized ternary diagrams of elastic modulus, asperity radius of curvature and asperity density of the coated surface are given in Fig. 3.4. The total points increase factor and the thin plate spline parameter for smoothing the layer boundary ternary diagrams were 100 and 0.05, respectively.

Table 3.2 DOE factors

Level	Factors		
	Elastic modulus (GPa)	Asperity radius of curvature (μm)	Asperity density ($1/\text{m}^2$)
1	70.0	5.0	1.0e9
2	106.7	5.3	1.3e9
3	143.3	5.7	1.6e9
4	180.0	6.0	1.8e9
5	216.7	6.3	2.1e9
6	253.3	6.7	2.4e9
7	290.0	7.0	2.7e9
8	326.7	7.3	3.0e9
9	363.3	7.7	3.2e9
10	400.0	8.0	3.5e9

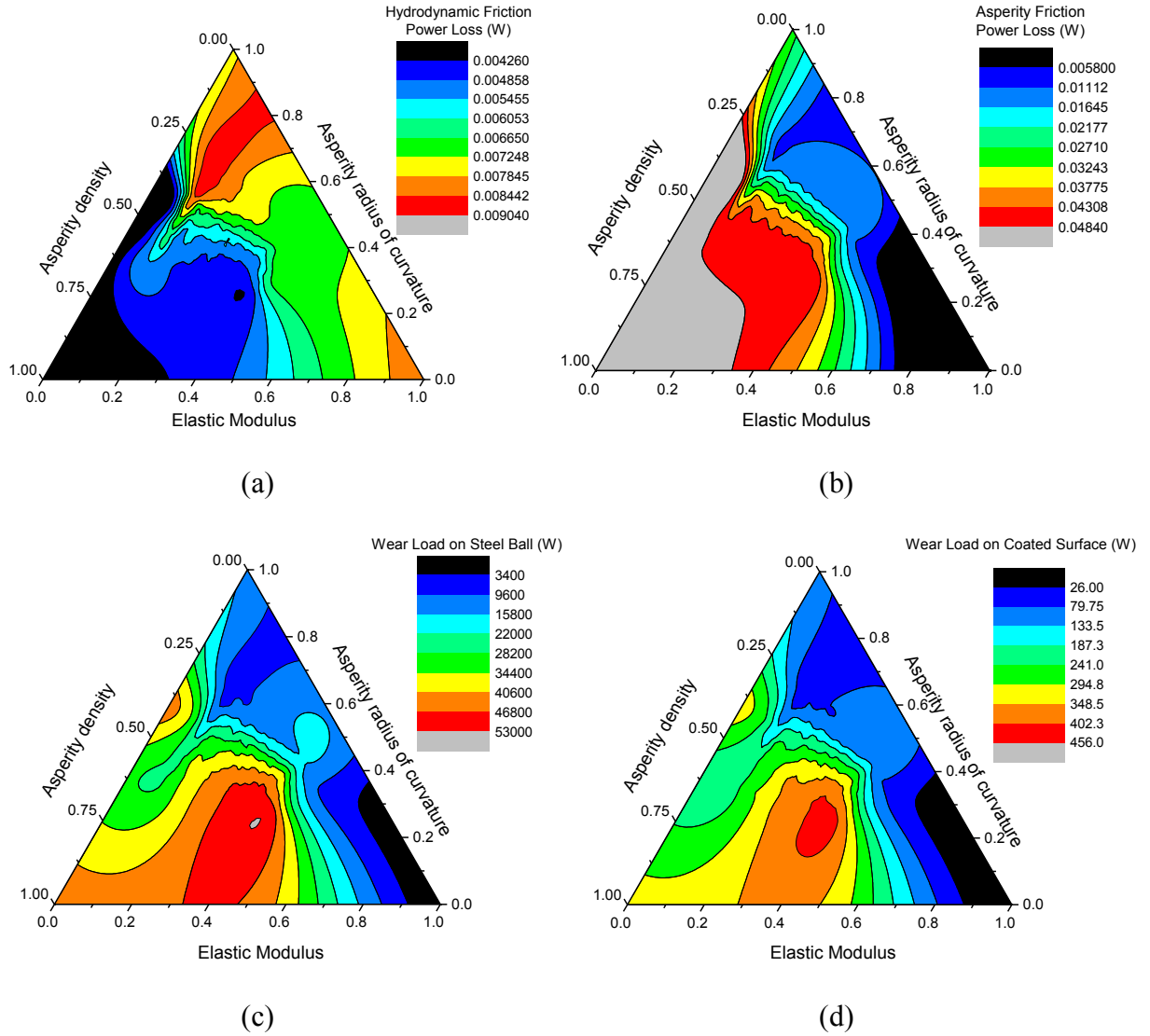


Figure 3.4 Normalized ternary diagrams of elastic modulus, asperity radius of curvature and asperity density effects on: (a) hydrodynamic friction power loss, (b) asperity contact friction power loss, (c) wear load on steel ball and (d) wear load on coated surfaces.

The ternary diagrams in Fig. 3.4a reveal that all the three factors affect the hydrodynamic friction power loss. While the asperity density dominates asperity contact (Fig. 3.4b): the higher asperity density leads to a larger contact area and a higher friction

power loss as a result. Fig. 3.4c and Fig. 3.4d are similar in the wear areas and trends: higher asperity density tends to cause higher friction force, higher friction power loss and higher wear loads (Fig. 3.4b). Fig. 3.4c and 3.4d also demonstrates that the relatively low elastic contact part suffers from wear more than the higher counterpart. To sum up, asperity density appears to be the dominant factor in this DOE study.

3. EXPERIMENTAL CASE STUDY

The comparison study of PEO/PTWA coatings for aluminium alloy engine cylinder protection was reported in reference 1. The boundary lubrication for steel balls sliding on PEO/PTWA coated samples with a drop of 5W30 engine oil was simulated using the GT-Suite model described in last section. Because the contact area was always immersed in the oil during reciprocating sliding tests, the asperity contact dominating boundary lubrication (at the ends of the sliding tracks) and mixed lubrication (middle of the sliding tracks) were considered. Fig. 3.5 shows the average COF curves (solid lines) of as-deposited PEO/PTWA. The friction force of the PTWA coating reduced from the beginning (break-in) and stabilized at around 125 m of sliding and kept this trend to the end of 220 m distance. This can be explained by the fact that the PTWA coating had the highest wear load on the counterpart steel ball, which worn out the relatively soft steel ball. However, because of the increased contact area due to wear/scuffing, plus the possible work hardening of both the iron based surface, the wear reduced and kept stable from 125 m. On the contrary, the harder PEO S1 and S2 coatings demonstrated continuous decreasing in friction: the trend of the PEO S1 was slight while the one for the PEO S2 was evident. Both coatings' surfaces were observed without distinguishable wear

after testing and the counterpart steel balls were all worn out to some extent. The PEO S2 produced the lowest wear load but the most severe wear scar on the steel ball, i.e., a consistently lighter wear load led to severer wear on the soft steel ball. The diameters of wear scars on the steel balls after 250 m sliding tests were 0.2/0.14 mm, 0.3 mm and 0.56 mm for PTWA, PEO S1 and PEO S2 coatings, respectively. The wear scar of the steel ball against PTWA coated sample was elliptical (0.2/0.14 mm) as a result of the ball in cylinder contact geometry. The wear scar size trend was PEO S2>PEO S1>PTWA, the inverse order of the wear load amplitudes.

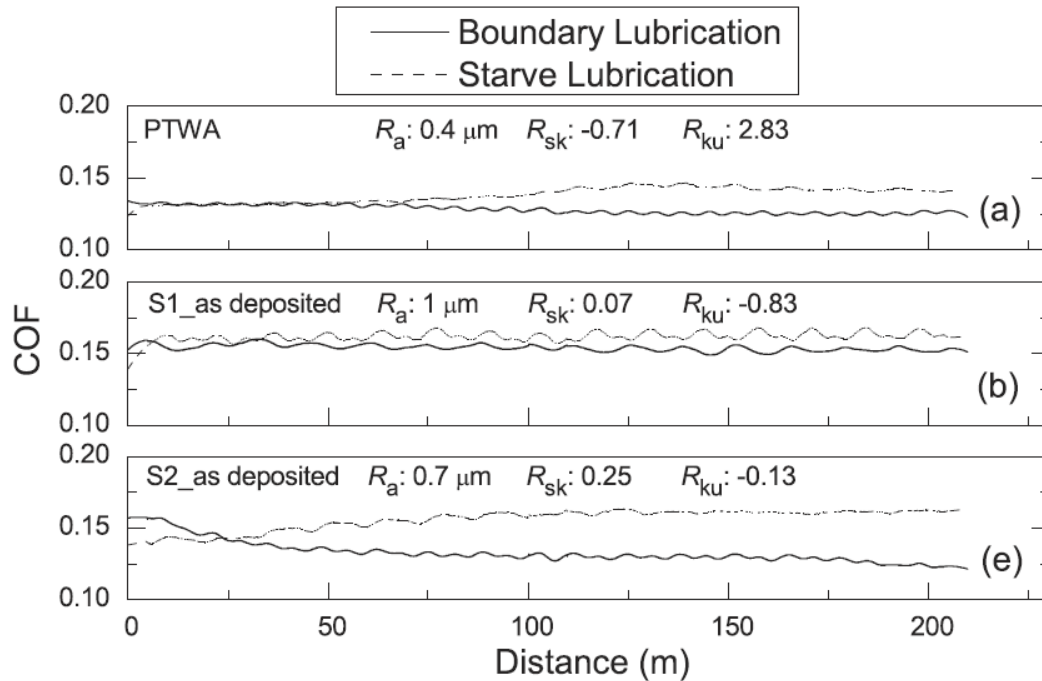


Figure 3.5 Friction forces of steel balls sliding against coated samples under boundary lubrication (solid lines) [1].

Fig.3.3 shows that the simulated friction force of the PEO S2 was much lower than the PTWA and PEO S1 samples, coinciding with the experimental measurements while the final COF of the PEO S2 coating was the lowest. It is also shown in Fig. 3.3

that the EHL friction forces of three coatings were in the same range with little differences less than 0.1 N. Considering the identical 2 N normal load and R2.75 mm steel balls, the lubrication contributions should be similar. The PEO S2 coating had the largest asperity radius of curvature (Fig. 3.2) and lowest asperity density (1406 1/m^2) among the three coated surfaces, which means the asperity contact generated less asperity pressure force/wear load and the PEO S2 wore the steel ball the slowest.

Different parameters have been varied to investigate their effects on friction behavior in simulation. The DOE simulation demonstrated that the surface features such as asperity density affected the friction considerably; while the influence of elastic modulus and asperity radius of curvature of coated surfaces were not ignorable. Examination of experimental results revealed that the GT-Suite has the exploitable capability to analyze EHL/asperity point contacts in reciprocating movements.

Other factors might also affect simulation. For instance, worn surfaces could change the above EHL and asperity contact pressures since they cannot be taken as point contact, or line contact to which those empirical equations are applicable. The Reynolds equations should be built on this new worn boundary and the approach is not available in commercial software packages. Another issue is that, traditional EHL without coating can be fast evaluated from the Hertz theory to obtain the nominal maximum contact pressure and contact half-width. However, for coated surfaces the classic Hertz theory may not be applicable. For example, a stiff coating tends to increase the contact pressure but decrease the contact radius, as well as the central and minimum film thicknesses for point contact [4]. It is also found that a thin stiff coating may be utilized to reduce the friction and wear for parts subjected to conventional EHL in the elastic piezoviscous regime (hard EHL)

through film thickness enhancement. Or a thick compliant coating can significantly affect the EHL performance in the elastic isoviscous regime than does a stiff coating [5].

4. CONCLUSIONS

The EHL lubrication equations of point contacts and Greenwood-Tripp asperity contact have been briefly reviewed in Chapter 1. Based on these two theories, a comparison of EHL and asperity contact simulation with experimental measurements of PTWA/PEO coating tribological behavior has been made. The multibody dynamic model based on EHL/asperity contacts showed that when the normal load and contact geometry were identical, surface topography was the most important factor for friction. On one hand, the simulation results predicted the surface with denser and smaller asperities (PTWA and PEO S1) had higher COF, which is the same as experimental observations. On the other hand, the highest wear load of PTWA coating in simulation led to the least worn scar in the counterpart steel ball. This prediction suggested the wear might be reached a balance dynamically in the reality. The wear changed the boundary conditions of Reynolds equations, therefore EHL lubrication equations need to be adapted.

This work also showed that, commercial software packages can facilitate tribological study by offering convenient modules with DOE capability to evaluate friction and wear behavior, without high demands in user's programming and algorithms skills. With this DOE tool, by easily varying processing parameters, numerical design of high wear resistant and low friction PEO coatings becomes feasible and promising.

REFERENCE

1. J.F. Su, X. Nie, H. Hu, and J. Tjong, *Friction and counterface wear influenced by surface profiles of plasma electrolytic oxidation coatings on an aluminum A356 alloy*. Journal of Vacuum Science & Technology A, 2012. **30**(6): p. 061402-1-11.
2. B.J. Hamrock and D. Dowson, *Ball bearing lubrication: the elastohydrodynamics of elliptical contacts*. John Willey & Sons, 1981.
3. G.-P.U.s. Manual, *GT-Suite™ Version 7.3*. Gamma Technologies, 2013.
4. S. Liu and Q. Wang, *Studying contact stress fields caused by surface tractions with a discrete convolution and fast Fourier transform algorithm*. Journal of tribology, 2002. **124**(1): p. 36-45.
5. Y. Liu, *EHL of Coated Bodies*, in *Encyclopedia of Tribology*. 2013, Springer. p. 847-852.

CHAPTER 4

CHARACTERIZATION OF THE FAILURE MECHANISMS OF THIN HARD COATINGS USING THE IMPACT TEST

1. INTRODUCTION

Due to the increasing use of advanced high strength steels (AHSS), die wear prevention has become an important issue in the stamping of automotive parts. Since physical vapor deposition (PVD) coatings usually has a much higher hardness and resistance of wear than electroplated or electroless coatings and nitrided steels, PVD coatings have been considered as necessary top layers on dies surface to battle the wear problems.

There exist three causes of failure for the hard PVD coating: 1) spallation within the coating caused by fatigue stress, 2) spallation caused by cracking initiated at the interface due to the sudden change in stress or strain, and 3) spallation initiated at the interface due to improper substrate surface finish. Since most lab tests use operating conditions that do not correspond to actual conditions in production stamping dies, the lab tests may provide misleading results. Therefore, in the proposed research, accelerated tests for investigation of spallation are based on actual stresses applied to coatings in production stamping dies. Ball-on-plate impact fatigue tests with 1.5-2.5 GPa maximum contact pressure, and an extended impact fatigue test with added sliding motions will be chosen as the accelerated lab tests to simulate the wear conditions of spallation failure.

This project was designed to have a better understanding of coating failure behavior so that the smart use of PVD hard coatings will be one of the solutions in dealing with the wear problems. In this project, the accelerated tests with testing

conditions similar to actual stresses in producing stamped parts were carried out to determine spallation behaviors for different coating/substrate systems. Recommendation on selections of coating and substrate materials and methods for substrate surface preparation was made.

This report was the first part of a basic feasibility study to establish the need for a larger research project from Auto/Steel Partnership, USAMP/DOE. This functioned as a starting point to develop further collaborative research with auto industries. The research would benefit the R&D activities in both USA and Canada.

2. EXPERIMENTAL DETAILS

A ball-on-plate impact fatigue test allows the investigation of coating properties under dynamic loading, simulating a wide range of tribological systems [1] including stamping conditions. Basically, a hydrostatic stress state is created beneath the centre of the indented surface. Immediately adjacent to the contact area there is a zone of high tensile stress in the vicinity of the surface. In hard brittle materials, this zone is particularly susceptible to cracking. The maximum shear stress has been reported to occur at a depth of $0.47D$, where D is the contact diameter of the elastic flattening zone at the moment of impact [2]. Therefore, for PVD thin coatings, this area is within the substrate. It is important to note that the hydrostatic stress state exists in homogeneous (bulk) materials; for thin hard PVD coatings having different elastic and plastic constants from those of the substrate, the stress distribution differs from hydrostatic. Even for the case where a hydrostatic stress produces elastic volume changes and does not lead to

plastic deformation, high shear stresses under the indentation are expected to occur at the coating/substrate interface.

During the impact fatigue test, a hard ball (the impact body) is set in a vertical oscillatory motion with a double-way piston driven by compressed air. The impact force, F , which is the main parameter of the impact fatigue test, is affected by the impact mass, m , frequency, f , impact ball to sample distance, d , and the static air pressure, P .

$$d = \frac{1}{2}at^2 = \frac{1}{2} \frac{PA + mg}{m} t^2 \quad (4.1)$$

A is the section area of cylinder bore, a is the acceleration rate and t is the traveling time of the ball. The velocity of impact mass reaching sample surface is given by

$$v = at = \frac{PA + mg}{m} t \quad (4.2)$$

The resulting impact force is assessed by means of a load cell. The test response is the critical number of loading cycles up to the point at which the coating surface shows no further damage. A schematic diagram of the impact fatigue test is shown in Fig. 4.1.

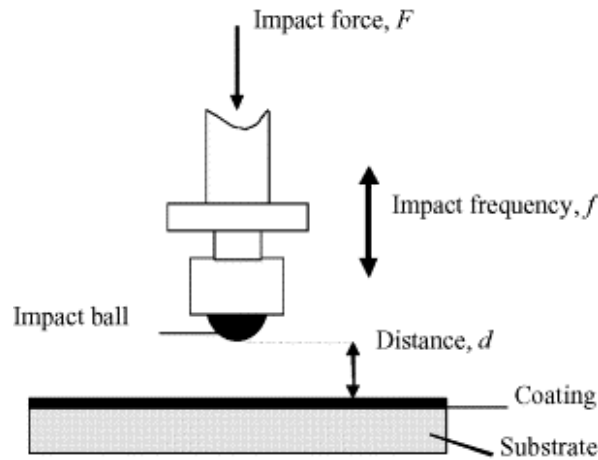


Figure 4.1 Schematic view of the impact fatigue test arrangement.

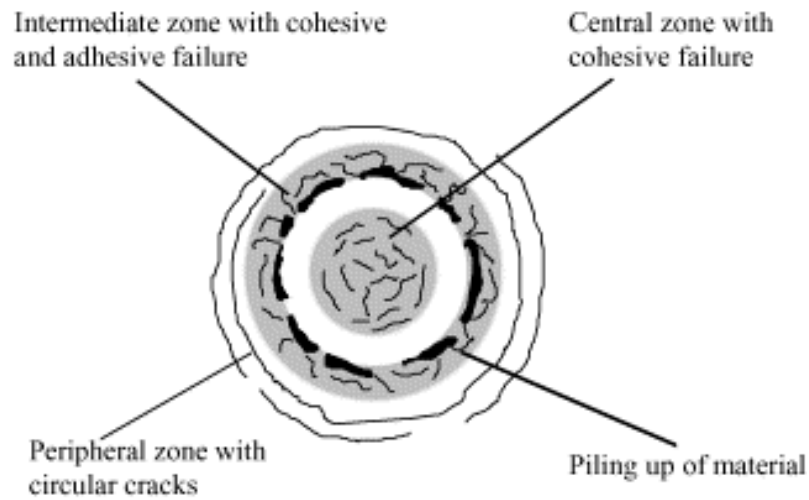


Figure 4.2 Typical failure zones encountered after the impact fatigue test [1].

A model of coating degradation under repeated impact loading has been developed by Bantle and Matthews [1]. During the impact fatigue test, stepwise deformation takes place which leads to piling up of material. Three failure zones can often be distinguished (Fig. 4.2): a central zone with cohesive failure, an intermediate zone with cohesive and adhesive failure and a peripheral zone with circular cracks. In the intermediate zone, cohesive and adhesive failures are caused by bending stresses, frictional forces acting during indentation and piling up of the substrate material causing shear stresses in the interfacial region. The cracks in the peripheral zone arise from tensile stresses, as a result of the ball/coated surface contact conditions. To reduce the stress in the coating during the impact, it starts to build a network of macrocracks inside the impact crater. Multilayered coatings, possessing high toughness, have also been reported to yield excellent performance under impact fatigue tests. The impact wear resistance of materials can be further optimized by either depositing coatings that are sufficiently elastic to accommodate any substrate deformation or increasing the load support beneath the coating to reduce surface deformation. Hence, a duplex treatment

(PVD + hardened/nitrided substrate) is expected to provide a superior impact performance.

3. RESULTS AND DISCUSSION

Depending on the recommendation of the A-SP and availability of test samples provided from the A-SP, the coatings tested included:

- PVD coatings
 - A_TiAlN
 - B_TiAlN
 - A_CrN
 - B_CrN
- CVD coatings
 - B_TiC
 - C_TiC
- Substrate
 - D2 tool steel

A, B and C denote 3 different coating suppliers. The work plan and experimental results for the Plasma Surface Engineering and Tribology Lab at the University of Windsor are described as follows:

3.1 Nanoindentation and microhardness tests

Nanoindentation (Hysitron) was used to measure mechanical properties (hardness and elastic modules) of the coatings and substrate materials. The obtained information will be usefully for Finite Element Analysis (FEA) and for better understanding coating

mechanism later on. Hardness, elastic modulus and hardness/elastic modulus are presented in Fig. 4.3 and Fig. 4.4. It seems TiAlN samples have higher hardness and elastic modulus. Hardness and elastic of TiC and CrN from different suppliers are quite different. The hardness of CrN coatings are generally lower than of TiAlN and TiC samples. While the hardness of TiC from supplier C is around 14 GPa, not only lower than its counterparts from supplier B, but also is the lowest among others. Considering its multilayer coating structure found in the following tests, this value is not real and will only be considered as a reference. As to elastic modulus, CrN from supplier A is the lowest as compared with other samples. Again, elastic modulus of TiC from supplier C is the obtained from the top layer of the coating, not from TiC layer itself.

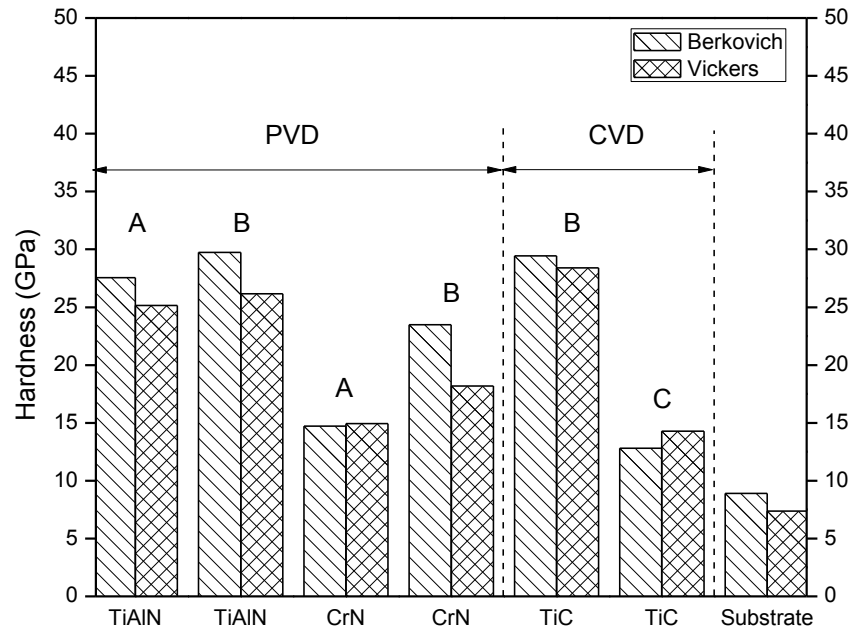


Figure 4.3 Vickers hardness and Berkovich hardness of different coatings. A, B and C denote different suppliers respectively.

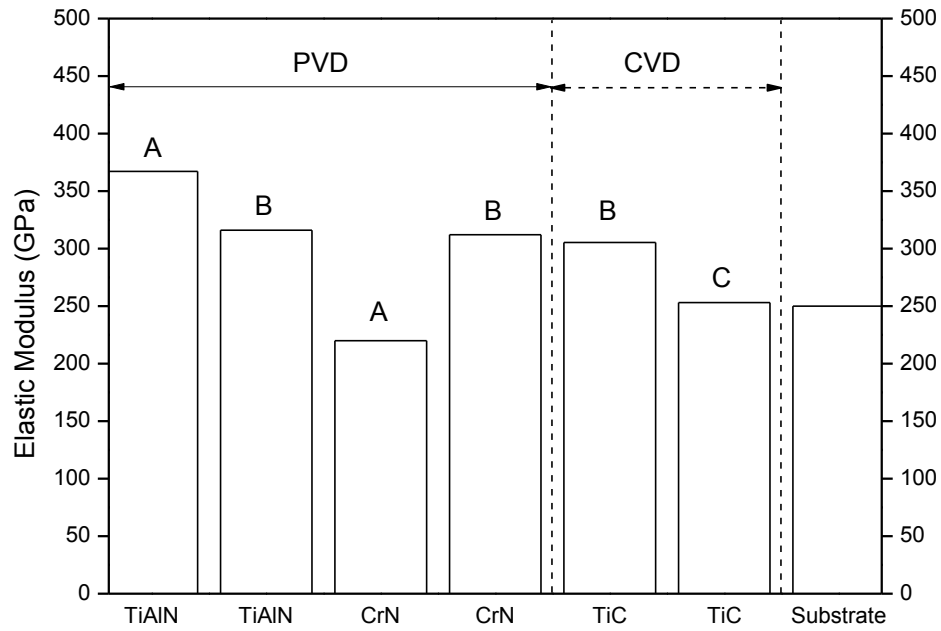


Figure 4.4 Elastic modulus of different coatings by nanoindentation.

3.2 Impact fatigue test

Two test loads (for simulated stamping pressures) and different balls (tungsten carbide and hardened steel balls) will be used ball-on-plate impact fatigue tests. Coating failure mechanisms will be investigated for the different coatings that will be tested.

The impact frequency, f , and ball to sample distance, d , were set at 10 Hz and 0.3 mm, respectively, in all tests and the static air pressure, P , is set around 35 PSI. Impact forces were calibrated at a maximal load of 400 N by an OMEGA LCKD-500 load cell and impacting loads were recorded by a KYOWA PCD-300A Sensor Interface System. A typical impact force vs. time curve is given in Fig. 4.5. A local view in Fig. 4.6 demonstrates that there is a wavy impulse due to the momentum of impact mass. The amplitude of this impulse can be controlled by adjusting the distance d without changing

other conditions. The impulse is around 400 N if d is higher than 0.3 mm. When distance d is zero, the impulse disappears and only air pressure works at continuous contact mode.

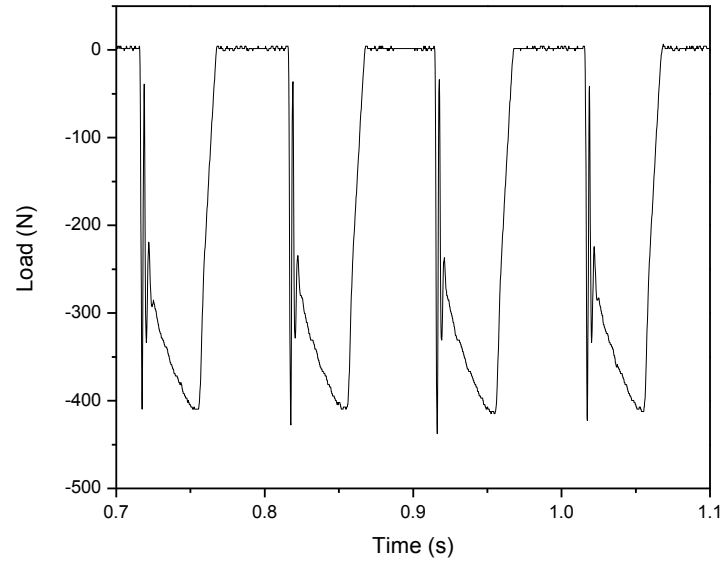


Figure 4.5 Impacting forces at 10 Hz impact frequency with 0.3 mm gap between ball and sample surface.

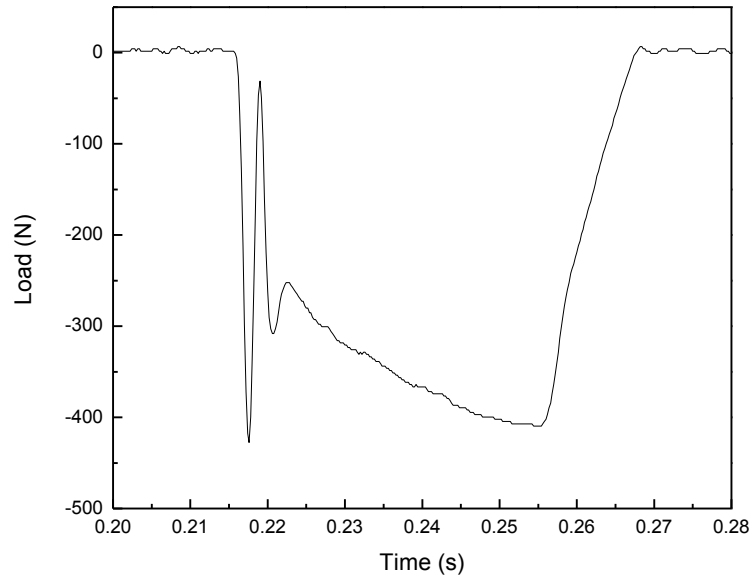


Figure 4.6 One pulse showing both the wavy impulse caused by momentum of mass and the wide trough caused by compressive air.

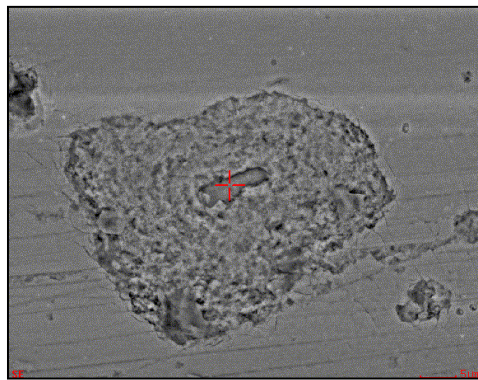
3.2.1 Typical failures

In this project, there are mainly 4 failure mechanisms:

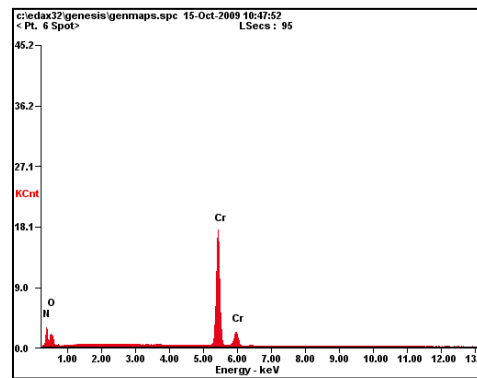
- Cohesive failures
- Adhesive failures
- Fatigue cracks
- Material transfer

3.2.1.1 Cohesive failures

Cohesive failures are usually attribute to stresses within the coating, for instance, chipping as shown in Fig. 4.7. Although the chipping seems to penetrate the coating to the substrate, the Energy Dispersive X-Ray Spectrometry (EDS) shows that the center of the chipping is still CrN and no Iron from the substrate appears. The micro cracks transverse to sanding scratches demonstrates that a concentrated stress exceeds the material's cohesive strength. If cohesive failures are severe, a cohesive failure zone will be generated in a larger scale as shown in the schematic of Fig. 4.2.



(a) SEM of B_CrN coating

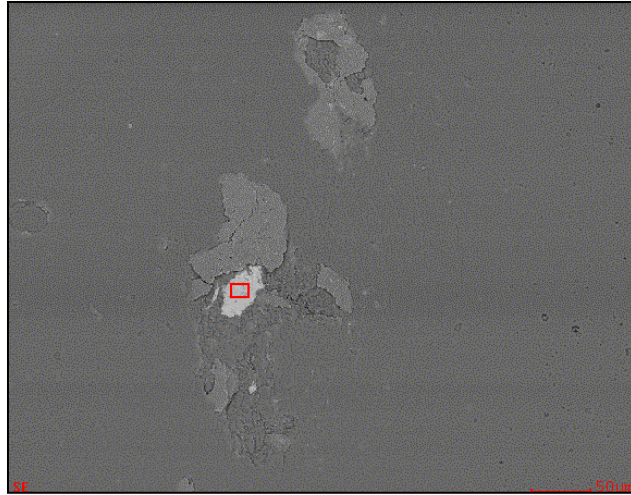


(b)EDS at the center of the chipping

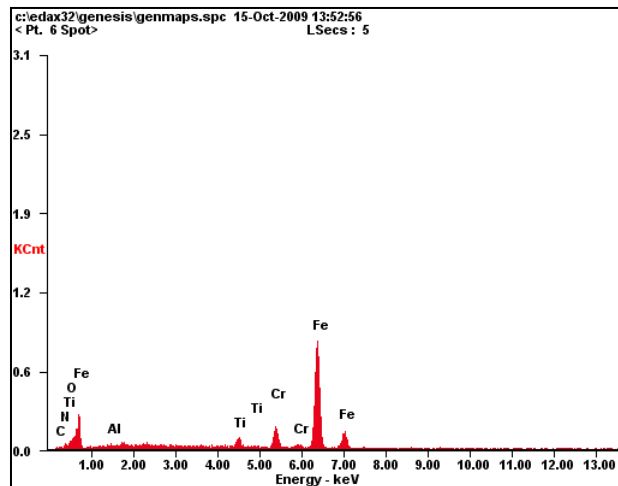
Figure 4.7 Cohesive failure – chipping of the coating. (a) is SEM image of the chipping; (b) is composition at the center of the chipping.

3.2.1.2 Adhesive failures

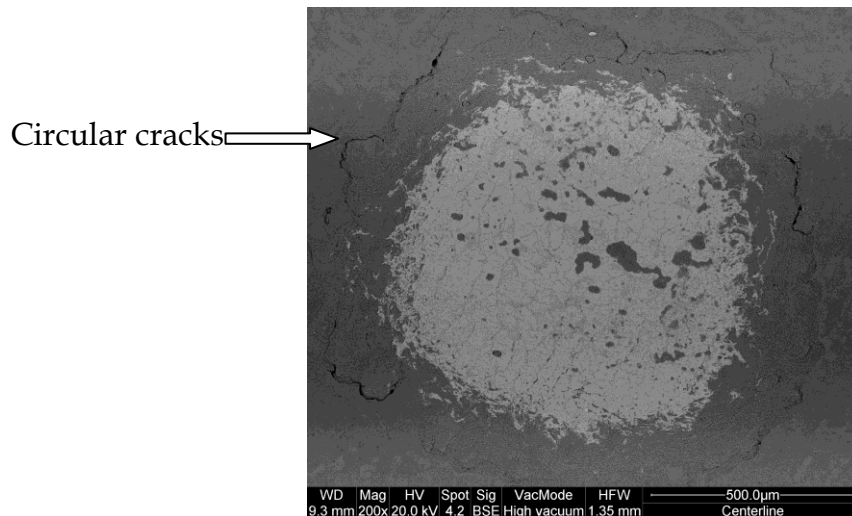
Adhesive failures occur at the interface between the coating and the substrate due to the stress concentration at the interface. Two adhesive failures appeared in this study: peeling and circular cracks. In the case of peeling, the substrate exposed after the peeling occurred. Usually, the peeling is accompanied by surrounding chippings.



(a)Peeling of A_TiAlN coating



(b) EDS spectrum of the rectangle area marked in (a) showing Fe and Cr from the D2 substrate



(c) Circular cracks around the crater of C₂TiC coating

Figure 4.8 Adhesive failures: (a) Peeling; (b) EDS of (a); (c) circular cracks around the crater.

3.2.1.3 Fatigue cracks

Fatigue is one of the primary reasons for the failure of coatings. The path of a fatigue crack has two parts, initiation and propagation. Stress concentration, cycling stress and bond rupture play major roles in the fatigue crack initiation phase of ceramic materials. It has been observed in this study that after a large number of impacting cycles, propagation of crack generated from micro bands, i.e., fatigue cracks and developed to severe failures such as chipping and peeling in a larger scale.

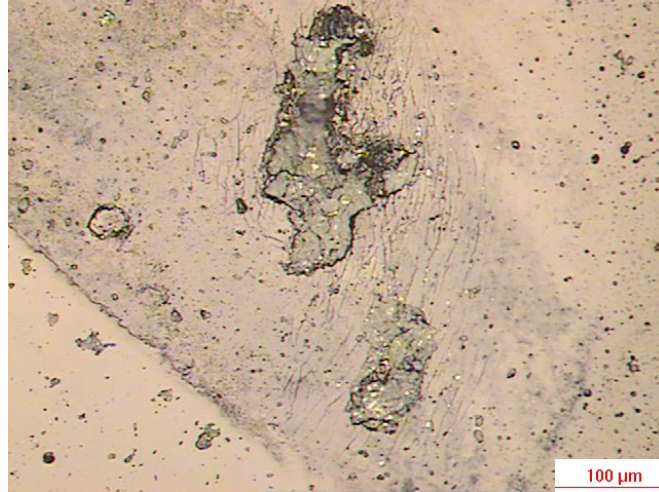


Figure 4.9 Fatigue cracks in the formation of micro bands of A_TiAlN sample.

3.2.1.4 Materials transfer

Materials transfer is a common phenomenon in impact test. Both the impact ball and the coating can transfer their surface materials to their counterparts to some extent. One example is presented in Fig. 4.10. Noticeable, for both steel ball and WC ball impact tests, the concentration of oxygen was high when materials transfer occurred. Therefore, concentration of oxygen and iron can be used to distinguish peeling and materials transfer, i.e., high oxygen and low iron denote materials transfer for steel ball impact tests. For WC ball tests, the existence of tungsten is sufficient for characterizing materials transfer. Other elements are also useful to determine the failure type. For instance, the content of Fe can be directly used to determine peeling or materials transfer for WC impact tests.

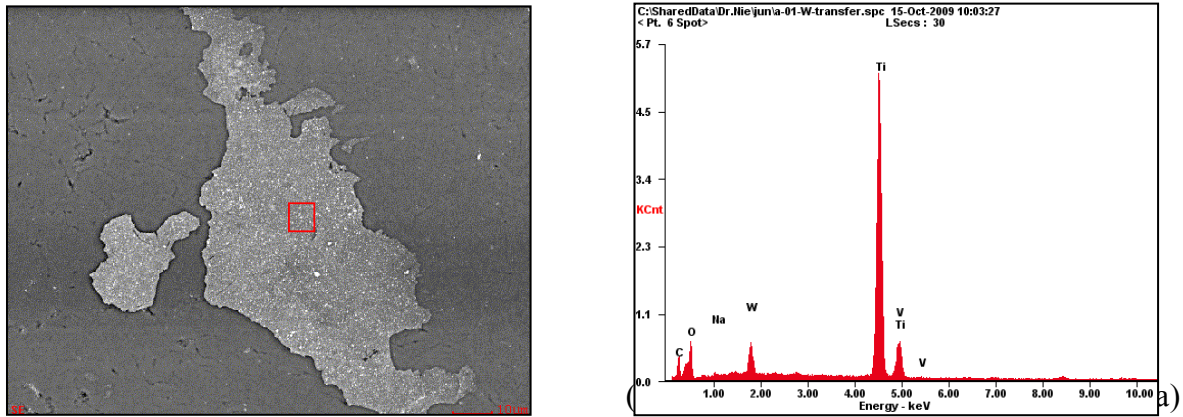


Figure 4.10 Materials transfer: Tungsten from the WC ball at the B_TiC coating surface.

Oxygen appears in the EDS spectrum.

The above failure mechanisms were observed to occur concurrently in most cases. For example, fatigue cracks may lead to cohesive failure such as chipping and adhesive failure such as peeling. Materials transfer may occur more severe at the spot where the surface is not smooth due to other failures. Cohesive and adhesive failures may also act as fatigue crack initiations and interact with each other.

3.2.2 Experimental Results

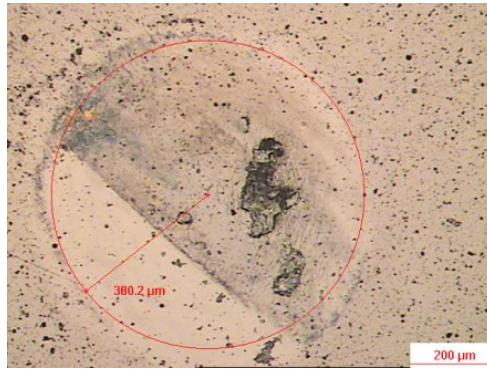
Samples were subjected to impacts under unlubricated conditions. The impact balls were always changed after each test. After the test, samples were observed and analyzed using optical microscope and SEM to investigate coating failure.

3.2.2.1 Hardened SAE 52100 Steel Ball, 10000 cycles

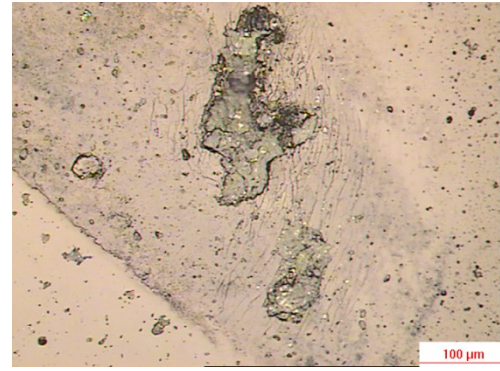
A_TiAlN appeared all the four failure mechanisms as shown in Fig. 4.11. Peelings with surrounded chipping and fatigue cracks were found (Fig. 4.11a and 11b). Backscattered electron images were taken to determine the composition of the failure

area. The very high Al and Ti contents in Fig. 4.11d indicate the TiAlN coating still exists on top of the substrate, while the high Fe and O suggest the steel ball materials transferring with some oxidation occurs during the impact test. On the contrary, the low Al and Ti contents and high Fe content in Fig. 4.11f indicate the occurrence of peeling.

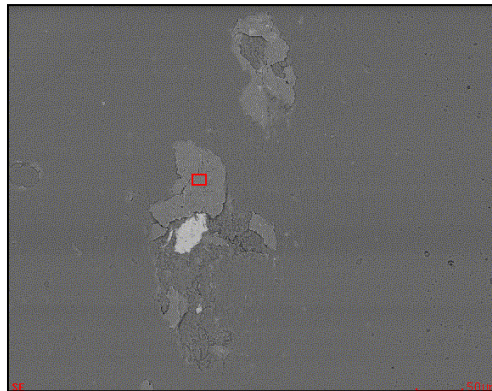
B_TiAlN showed low resistance to impact of steel ball (Fig. 4.12). A large cohesive failure zone formed at the center of the crater where severe plastic deformation of the substrate was also observed. EDS spectrum in Fig. 4.12e taken from the center of the crater showed absence of Ti and Al elements evidencing the disappearance of the coating at the area. Chippings and fatigue cracks also occurred outside the cohesive failure zone (Fig. 4.12b and 12c).



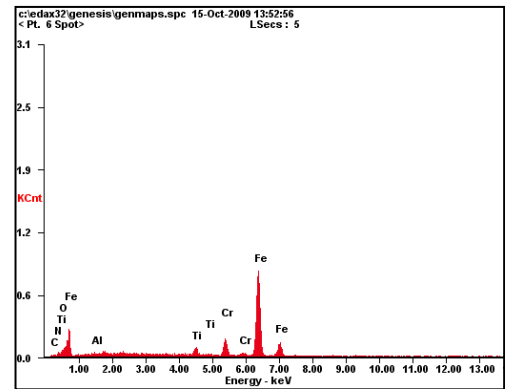
(a)



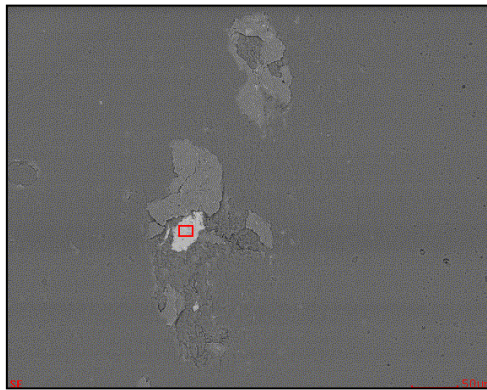
(b)



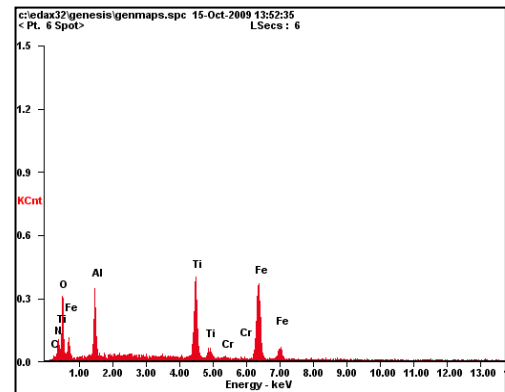
(c)



(d)



(e)



(f)

Figure 4.11 A_TiAlN after 10000 cycles. (a) Overview, the dark band is due to material transfer from the ball; (b) local view showing fatigue cracks; (c) peeling with surrounded chipping; (d) EDS spectrum of the peeling showing Fe from substrate; (e) materials transfer; (f) EDS spectrum of (e).

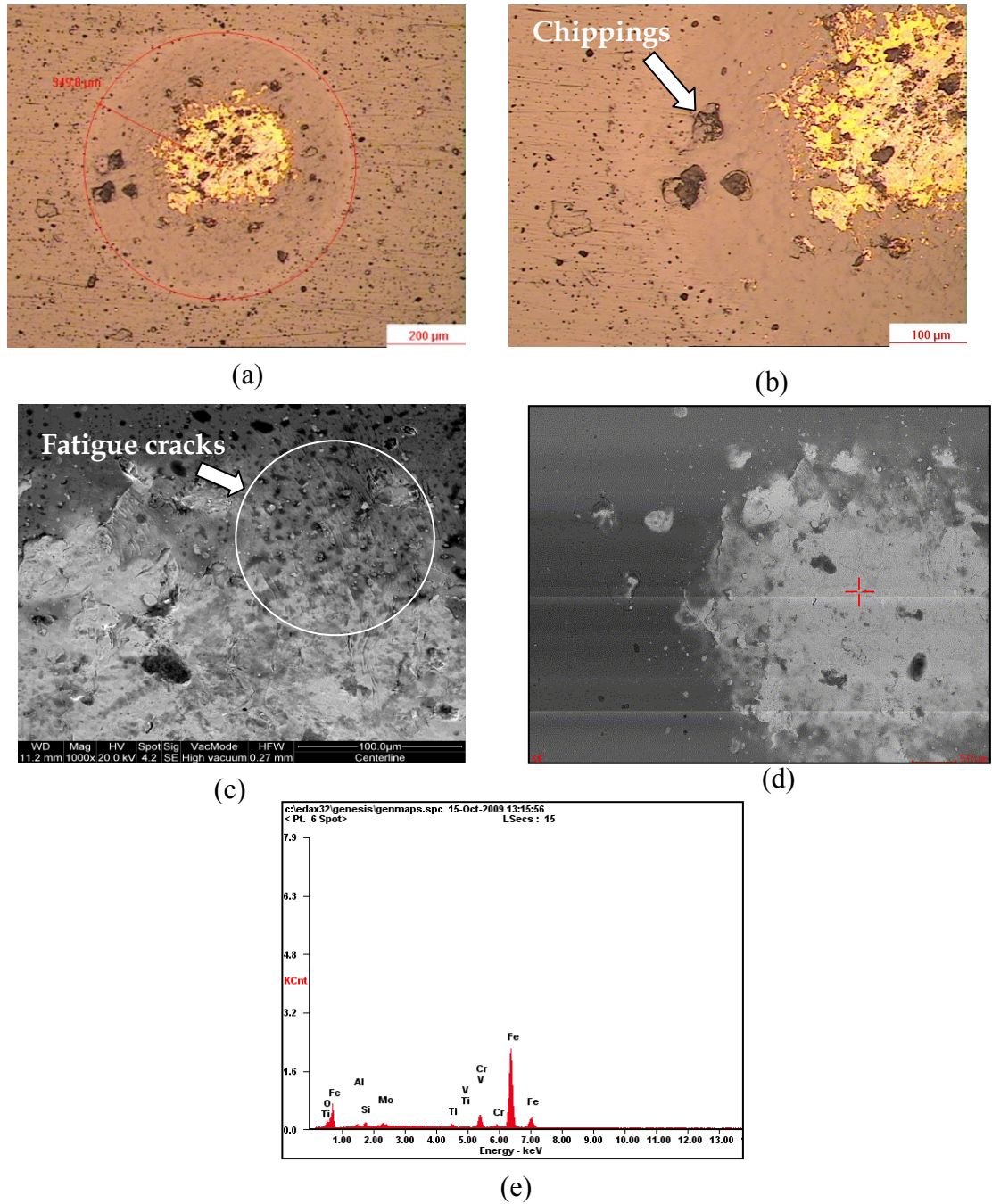
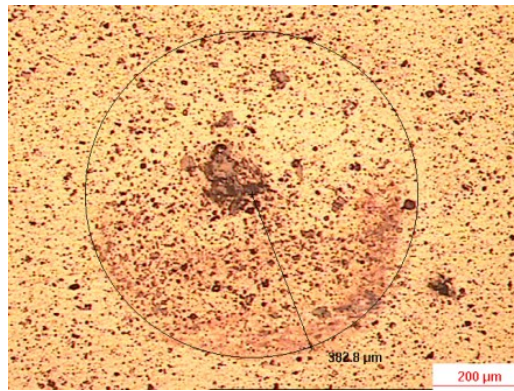


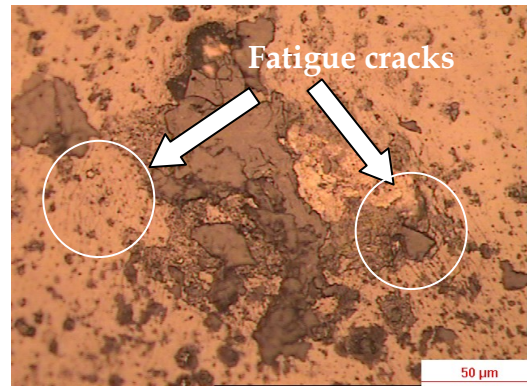
Figure 4.12 B_TiAlN after 10000 cycles. (a) Overview; (b) local view showing center cohesive failure zone and coating chipping; (c) fatigue cracks; (d) backscattered electron images of the cohesive failure zone; (e) EDS spectrum

of marked area in (d) demonstrates the Fe from the substrate in the cohesive zone.

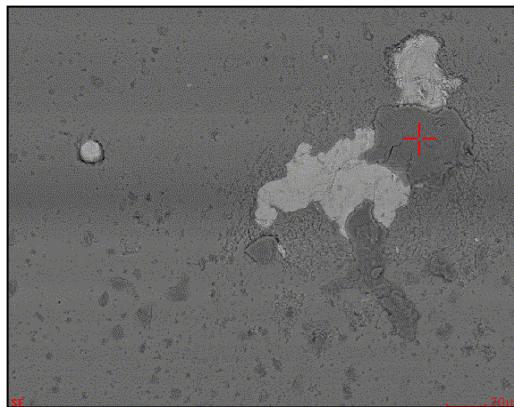
Two CrN samples after 10000 cycles are presented in Fig. 4.13 and Fig. 4.14. Both samples showed better resistance to impact than TiAlN samples. The crater of A_CrN coating impact test is shown in Fig. 4.13. Fig. 4.13b shows fatigue cracks around the failure area. In Fig. 4.13d, the lower concentration of Fe than that of Cr and high O concentration show that Fe was transferred from steel ball in the marked dark area in Fig. 4.13c. In the Fig. 4.13f, the high concentration of Fe in bright area in Fig. 4.13e demonstrates that iron was from substrate by peeling.



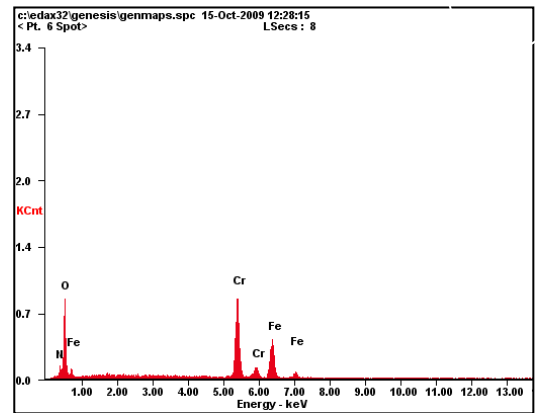
(a)



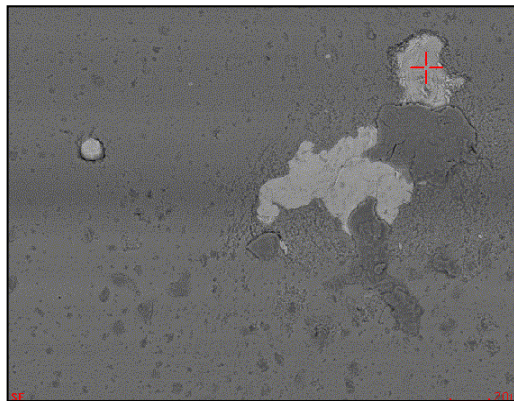
(b)



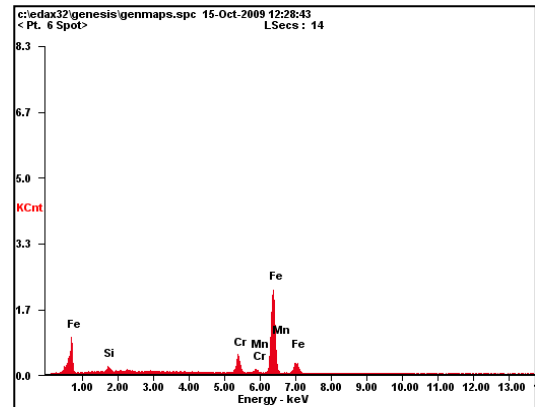
(c)



(d)



(e)



(f)

Figure 4.13 A_CrN after 10000 cycles. (a) Overview; (b) fatigue cracks; (c) backscattered electron image; (d) EDS spectrum of marked spot in dark area in (c), the lower concentration of Fe than of Cr and high O show that

Fe is transferred from steel ball; (e) backscattered electron image; (f) EDS spectrum of marked spot in bright area in (e), the high concentration of Fe demonstrates that iron is from substrate by peeling.

B_CrN performed well in the steel ball impact test. The dark areas in the crater Fig. 4.14a contain iron transferred from the steel ball with high oxygen content due to Fe oxidation during the impact as shown in the spectrum in Fig. 4.14c. Noticeable, the dark area in the SEM image (Fig. 4.14b) is the bright area in the optical image (Fig. 4.14a). It was also found that small chippings happened at both the center and the edge of the crater (Fig. 4.14d).

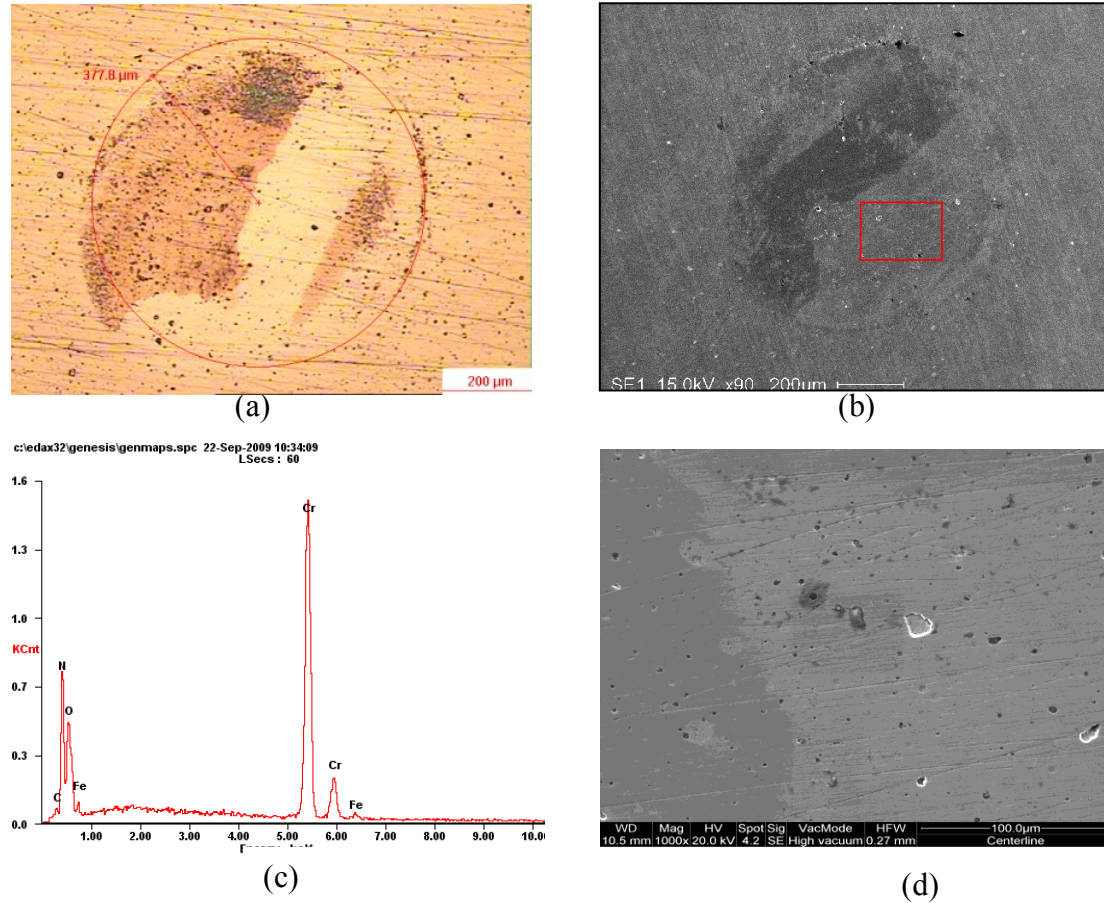


Figure 4.14 B_CrN after 10000 cycles: (a) overview, (b) SEM image of the crater, the dark area is the bright area in optical image, (c) EDS of marked area in (b), and (d) chippings at the centre of the crater.

TiC samples after 10000 cycles are shown in Fig. 4.15 and Fig. 4.16. It seems B_TiC has no obvious failures. C_TiC sample has a two layers coating. The first layer seems to be oxide of Ti or Fe on the top of TiC (Fig. 4.16d). Chippings happened at the edge of the crater as shown in Fig. 4.16b. In respect that elastic modulus and hardness were obtained by nanoindentation technique, which can only acquire the mechanical properties of the top surface, the analysis and FEM simulation of this sample are only for reference.

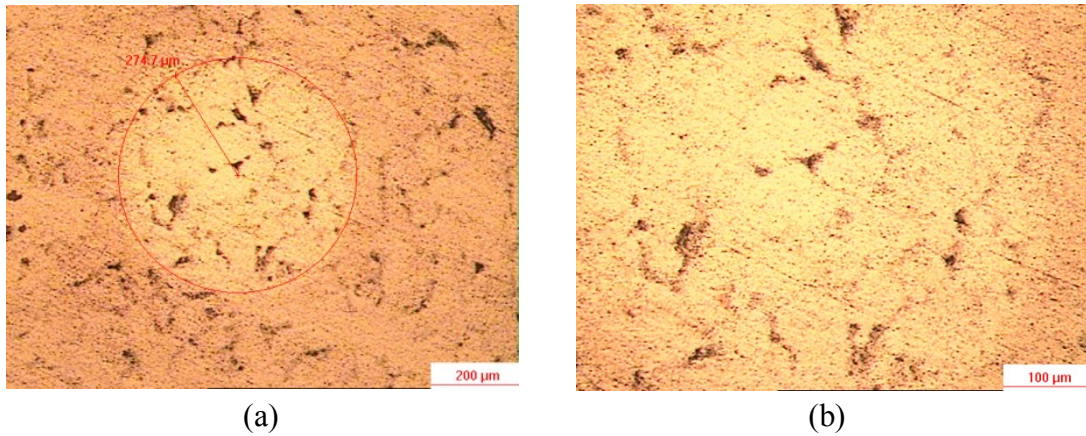


Figure 4.15 B_TiC after 10000 cycles. (a) Overview and (b) the center of the crater.

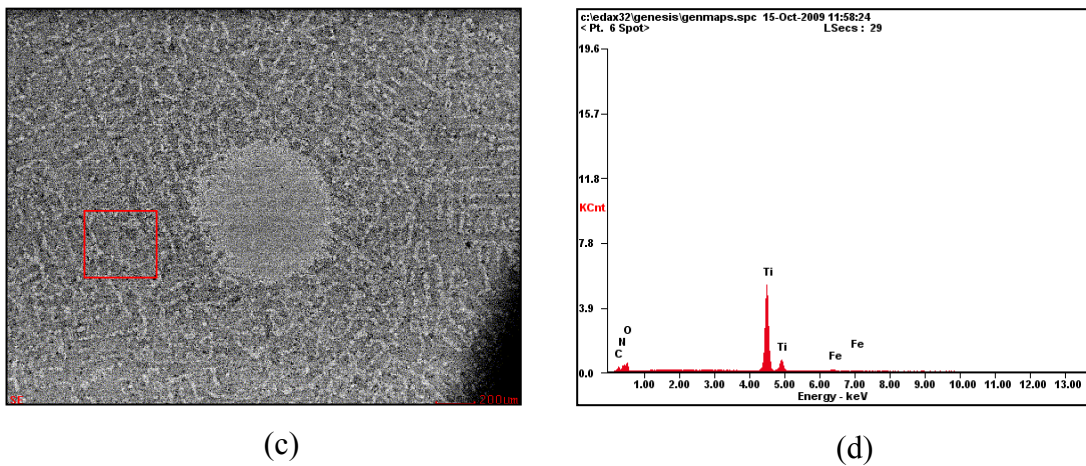
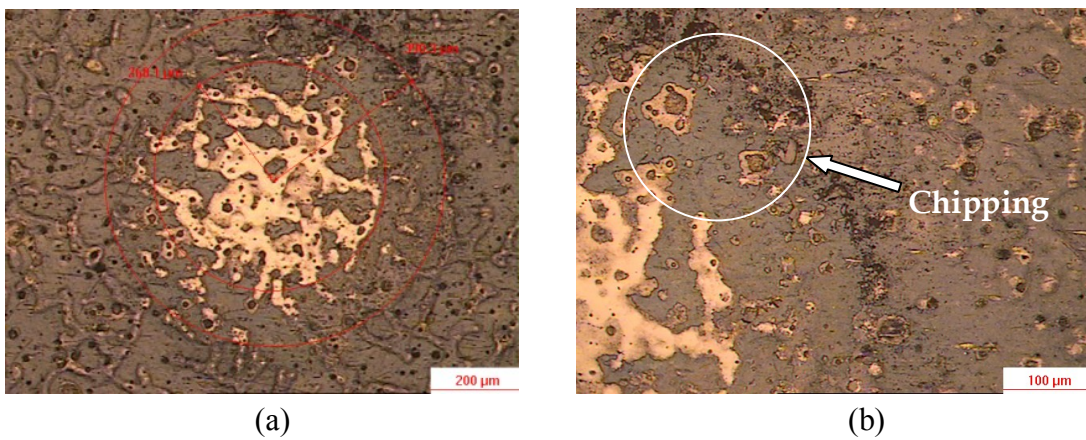


Figure 4.16 C_TiC after 10000 cycles. (a) Overview; (b) the edge of the crater showing coating chipping; (c) backscattered electron image of surface layer; (d) EDS spectrum of surface layer.

3.2.2.2 Hardened SAE 52100 Steel Balls, 50000 cycles

50000 cycles' impact tests on selected four samples with fewer failures at tests of 10000 cycles' impacts have also been performed to study the long time fatigue of coatings. A_CrN totally failed in the impact test of 50000 cycles as shown in Fig. 4.17. B_CrN showed good resistance to impacting. In Fig. 4.18a, dark areas are attributing to materials transfer from steel ball. Only small chippings occurred at the center and the edge (Fig. 4.18b and 18c).

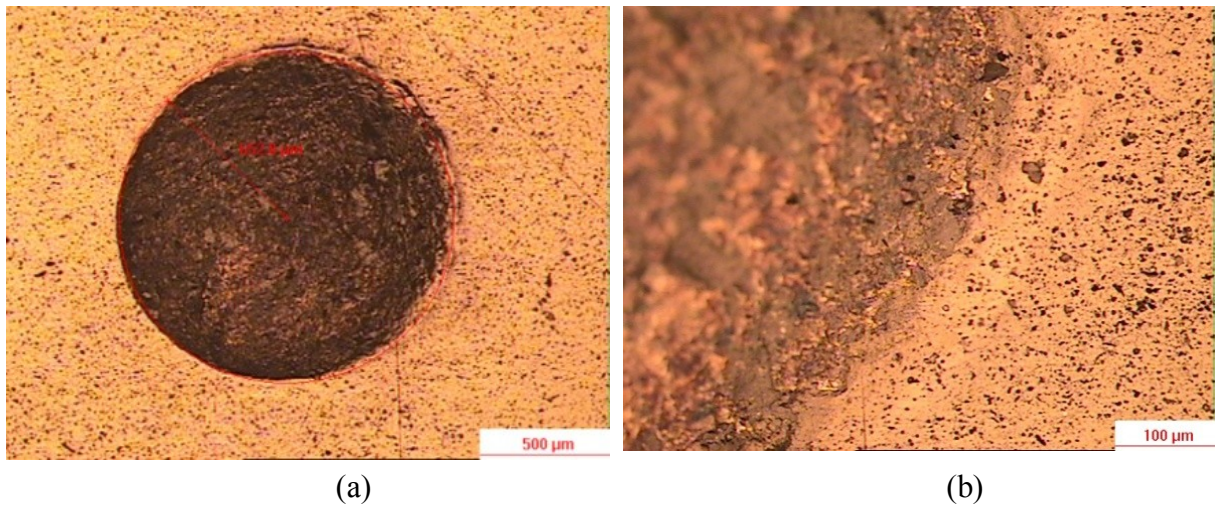


Figure 4.17 A_CrN after 50000 cycles. (a) Overview, (b) local view at the edge of crater.

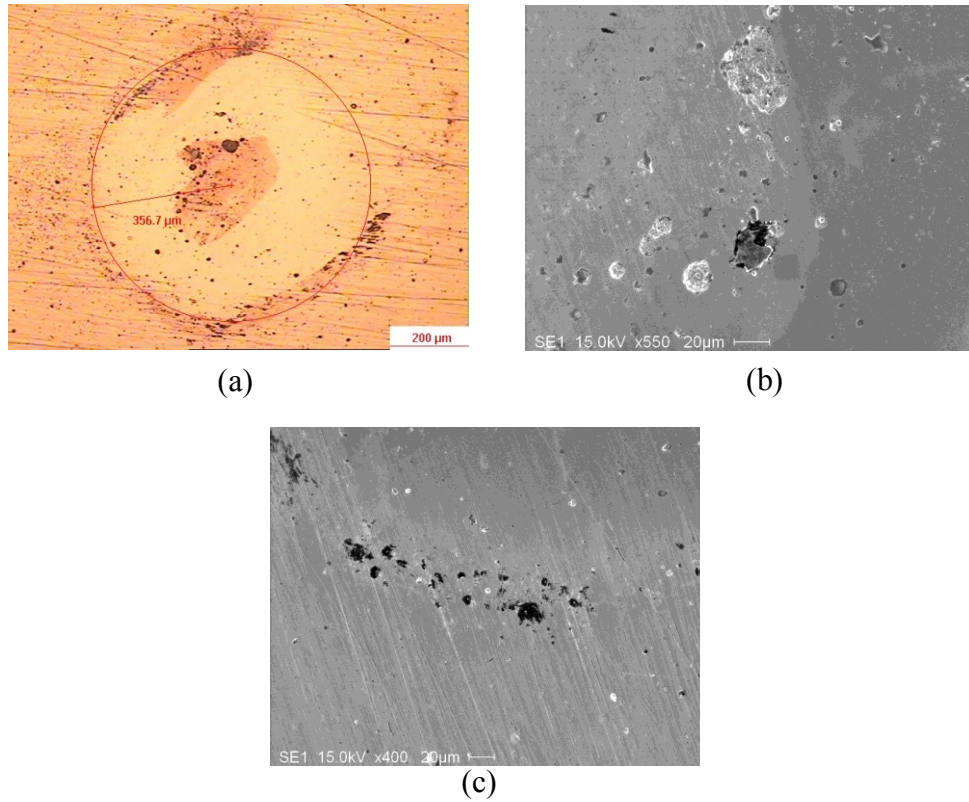


Figure 4.18 B_CrN after 50000 cycles. (a) Overview; (b) chippings at the center of the crater; (c) local view at the edge of crater showing chippings.

B_TiC shows chipping (Fig. 4.19a) and materials transfer at the edge of the crater (Fig. 4.19b). Although there are chippings near the center of the crater, it seems these cracks generated from the inherent flaws of the coating (Fig. 4.19a).

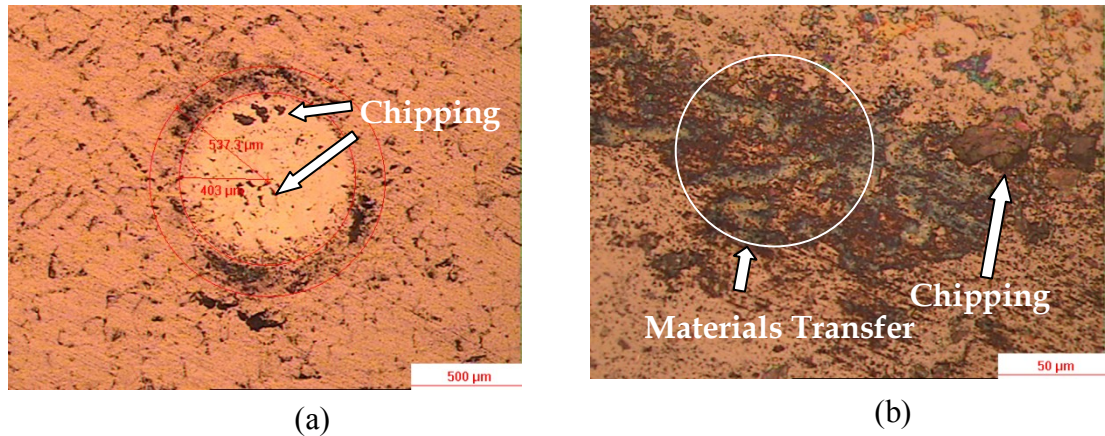


Figure 4.19 B_TiC after 50000 cycles. (a) Overview; (b) local view at the edge of crater showing materials transfer and chipping.

C_TiC coating behaved differently. The first layer of coating seemed to be worn out in the crater and the second TiC layer was in good condition after 50000 cycles (Fig. 4.20). Only chippings were found near the edge of the crater as shown in Fig. 4.20b.

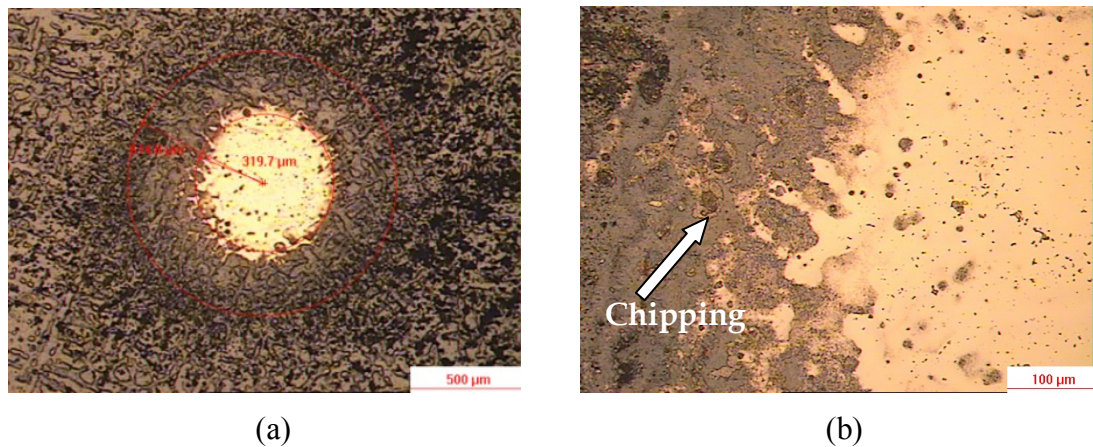


Figure 4.20 C_TiC after 50000 cycles. (a) Overview; (b) local view at the edge of crater showing chippings.

Diameters of craters after 10000 and 50000 cycles steel ball tests are given in Fig. 4.21. Generally speaking, the diameters of craters are similar indicating the substrate

dominates the effect of the plastic deformation of the coated samples. The dramatic increase of the diameters from 10000 to 50000 cycles of A_CrN can be explained by coating failures resulting in hard debris which may act as grinding media and wear off the substrate in the following impacts. Therefore, the diameter of the crater after 50000 cycles increased sharply.

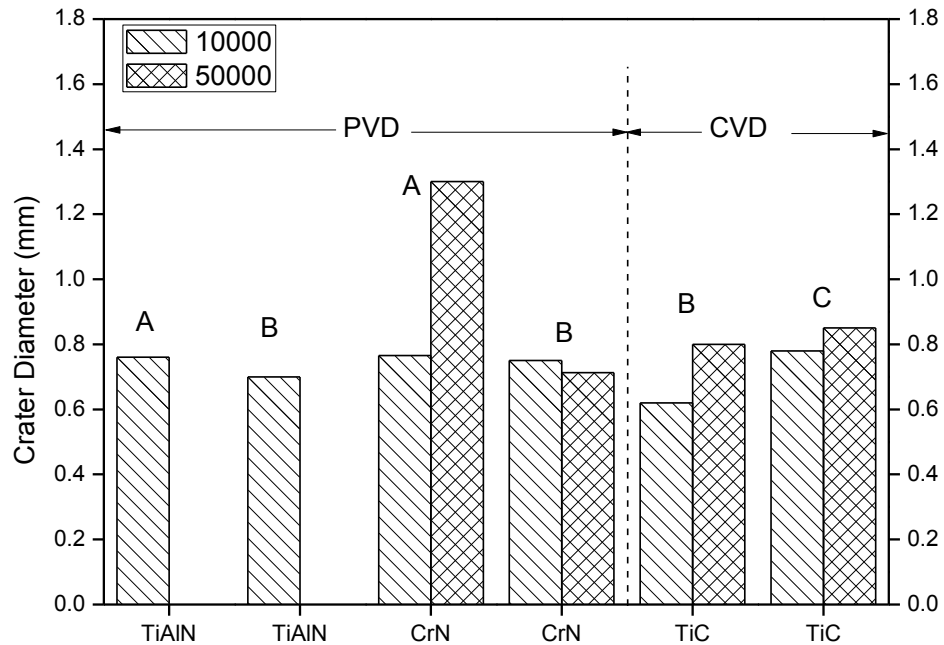


Figure 4.21 Diameters of craters after 10000 and 50000 cycles of steel ball impact tests.

3.2.2.3 Tungsten carbide (WC) ball, 10000 cycles

Because WC ball impact tests produced some debris, samples have been cleaned using acetone and observed by SEM. SEM images of craters formed by WC balls impacting 10000 cycles are presented as follows. Every sample showed coating failures to some extent, which means the 400 N impact load is high enough for the study on coating failure mechanism using WC balls.

A_TiAlN coating under WC ball impacting is shown in Fig. 4.22. Small chippings are shown in Fig. 4.22b. The bright area in Fig. 4.22c is a thin layer containing tungsten (EDS spectrum shown in Fig. 4.22d) from the WC ball. B_TiAlN coating failed with materials transfer, peeling and chipping and fatigue cracks as given in Fig. 4.23.

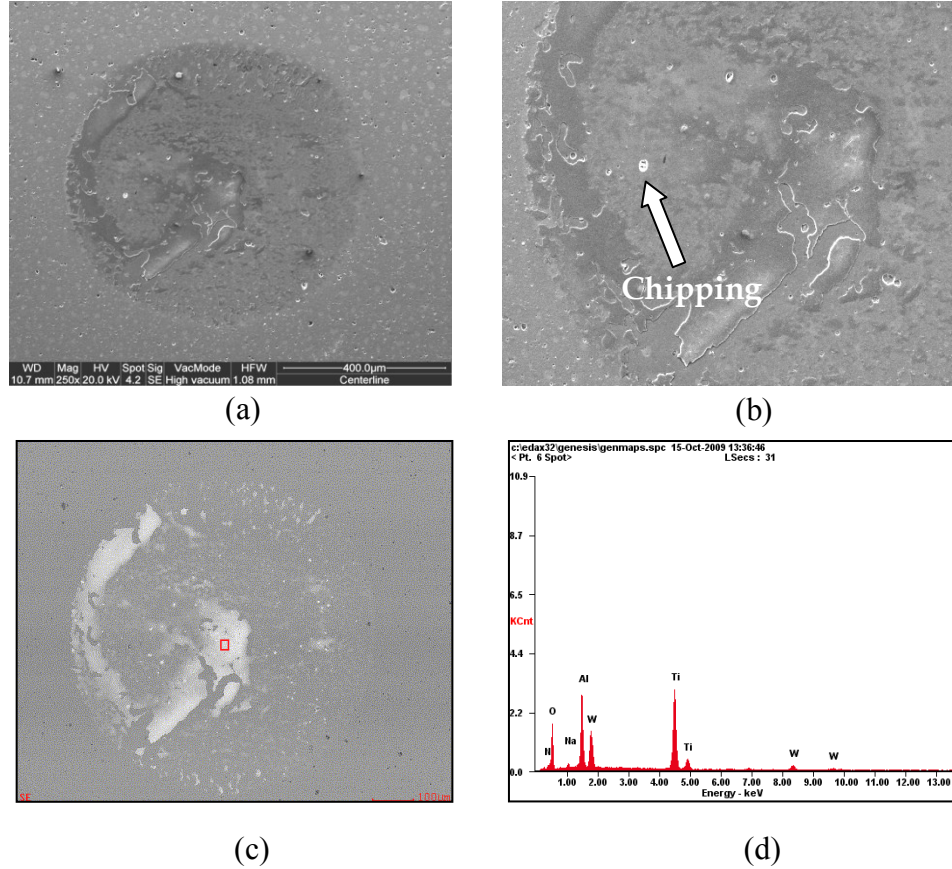


Figure 4.22 A_TiAlN after 10000 cycles. (a) Overview SEM image; (b) local view showing chipping; (c) backscattered electron image; (d) EDS spectrum of the marked area in (c).

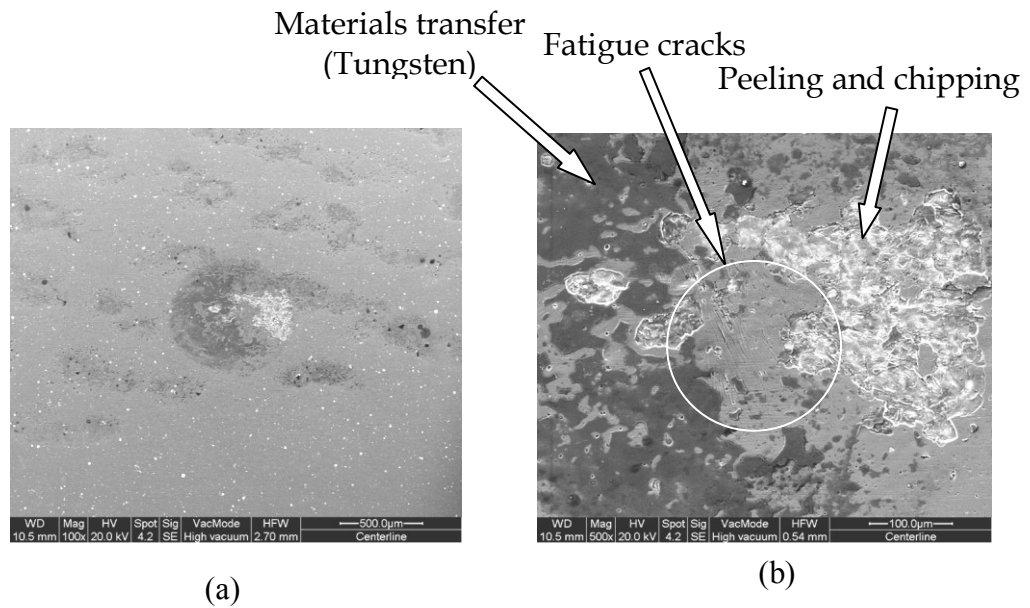


Figure 4.23 B_TiAlN after 10000 cycles. (a) Overview; (b) local view showing peeling, chipping, materials transfer and fatigue cracks.

A_CrN coating has a few chippings and materials transfer near the edge of the crater as shown in Fig. 4.24. Compared with A_CrN, B_CrN performed better with fewer chippings and materials transfer. As presented in Fig. 4.25, the B_CrN was almost intact.

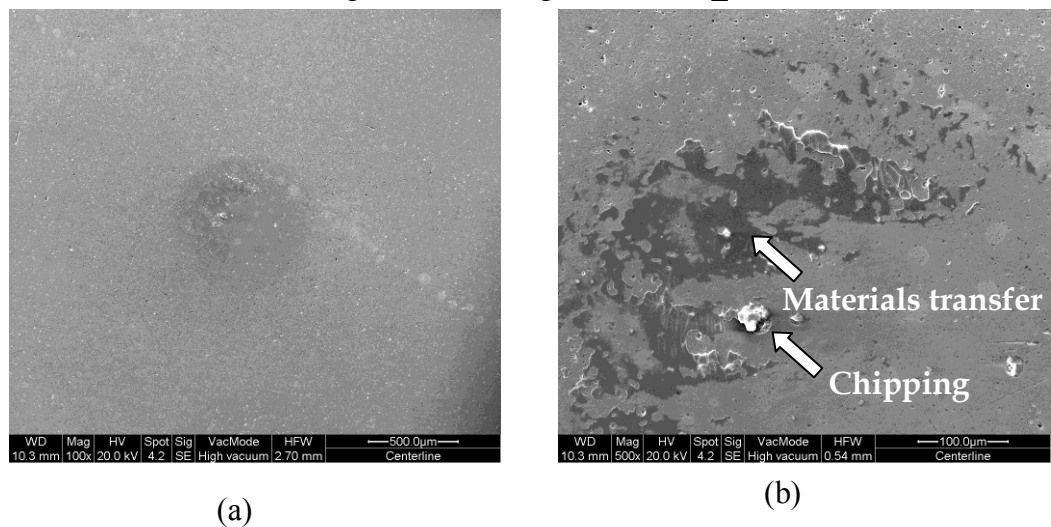


Figure 4.24 A_CrN after 10000 cycles. (a) Overview; (b) local view showing chipping and materials transfer (dark area).

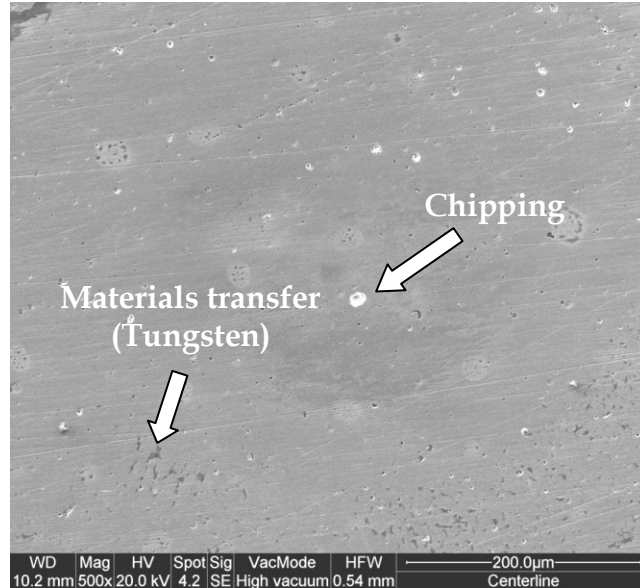


Figure 4.25 B_CrN after 10000 cycles.

B_TiC coating after 10000 cycles is presented in Fig. 4.26. Fig. 4.26b shows the cohesive failure zone with materials transfer (tungsten is brighter in backscattered electron image). Fig. 4.26c is the EDS spectrum of the whole area of Fig. 4.26b. The spectrum demonstrates that no iron exists from substrate, which means only chipping occurred.

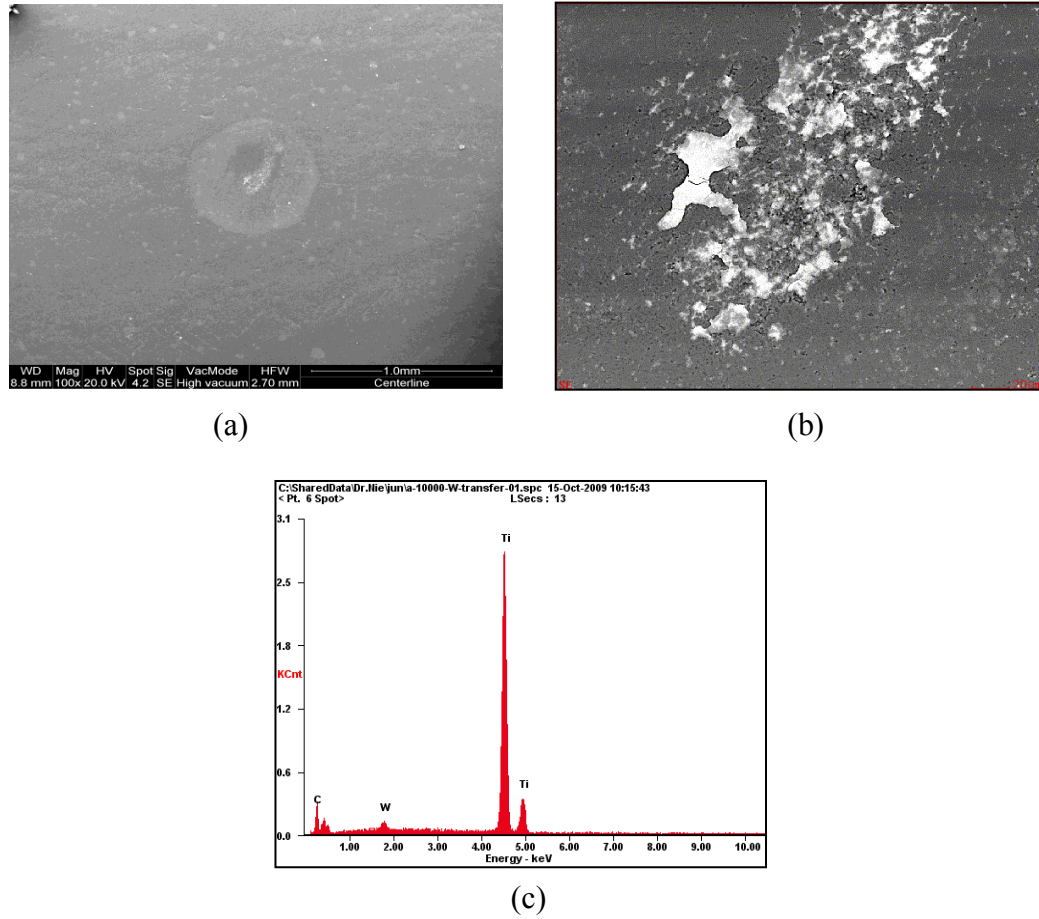


Figure 4.26 B_TiC after 10000 cycles. (a) Overview; (b) backscattered electron image of the center of the crater showing cohesive failure and materials transfer (bright area); (c) EDS spectrum showing no Fe element.

Fig. 4.27 presents C_TiC coating after 10000 impact cycles. Chipping occurred at the center of the crater and the inexistence of iron (Fig. 4.27c) at the chipping demonstrates that the coating was not totally penetrated. The EDS spectrum in Fig. 4.27c also has a peak of tungsten, proving materials transfer from WC ball.

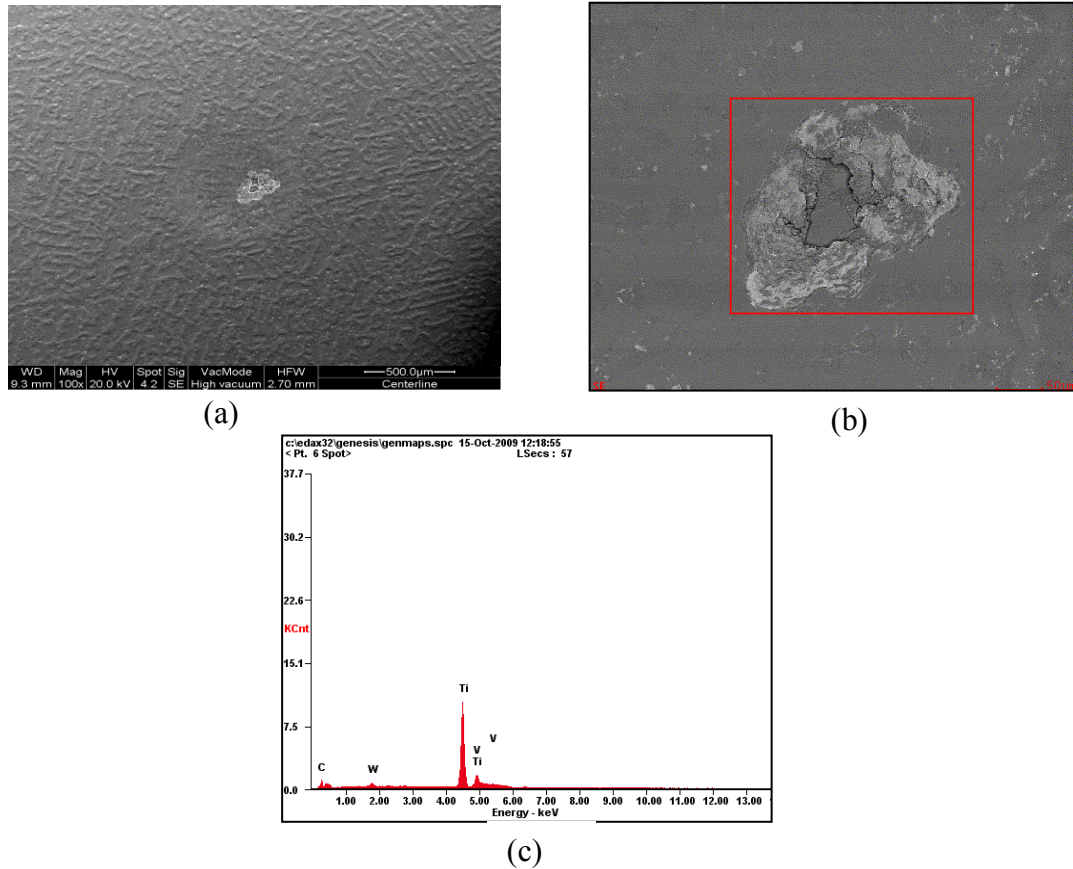


Figure 4.27 C_TiC after 10000 cycles. (a) Overview; (b) local view at the center of crater showing chipping and materials transfer; (c) EDS spectrum showing materials transfer of tungsten and inexistence of iron.

3.2.2.4 Tungsten Carbide (WC) Balls, 50000 cycles

The 50000 cycles impacting tests have also been carried out to study the failure mechanism under increased impact cycles. Most samples showed severe damages of coatings. Fig. 4.28 shows that the A_TiAlN coating failed at the center with chipping and materials transfer around the edge. Fig. 4.29 presents the totally damaged B_TiAlN coating after 50000 impact cycles.

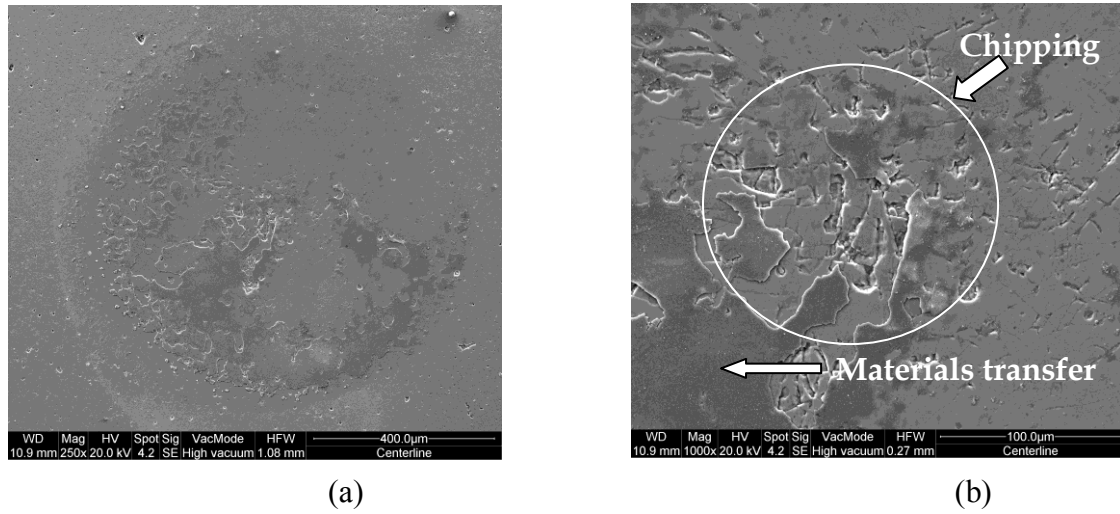


Figure 4.28 A_TiAlN after 50000 cycles. (a) Overview showing materials transfer (darker area); (b) local view showing chippings, materials transfer.

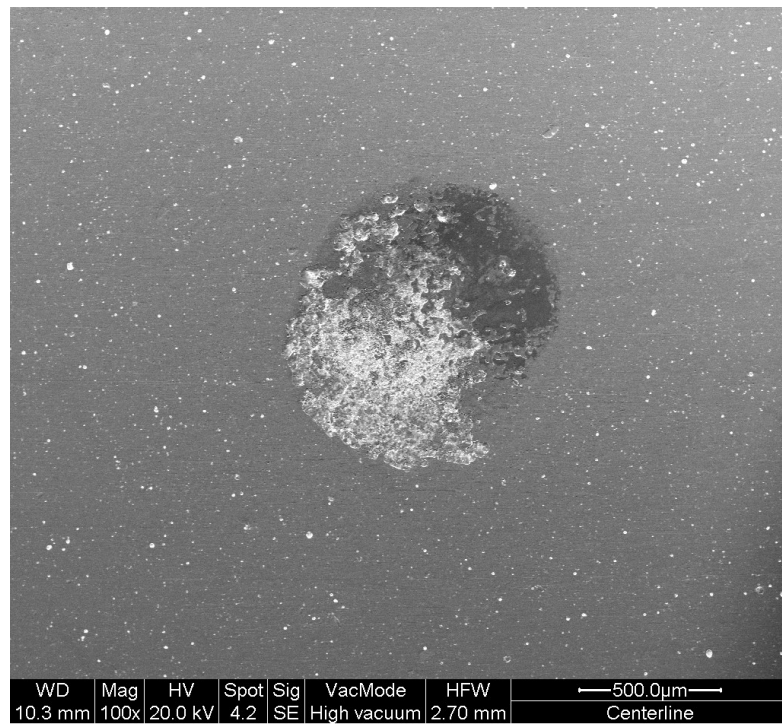


Figure 4.29 B_TiAlN after 50000 cycles impact.

Fig. 4.30 demonstrates the center cohesive failure zone (Fig. 4.30a) and a peeling at the edge of A_CrN coating (Fig. 4.30b).

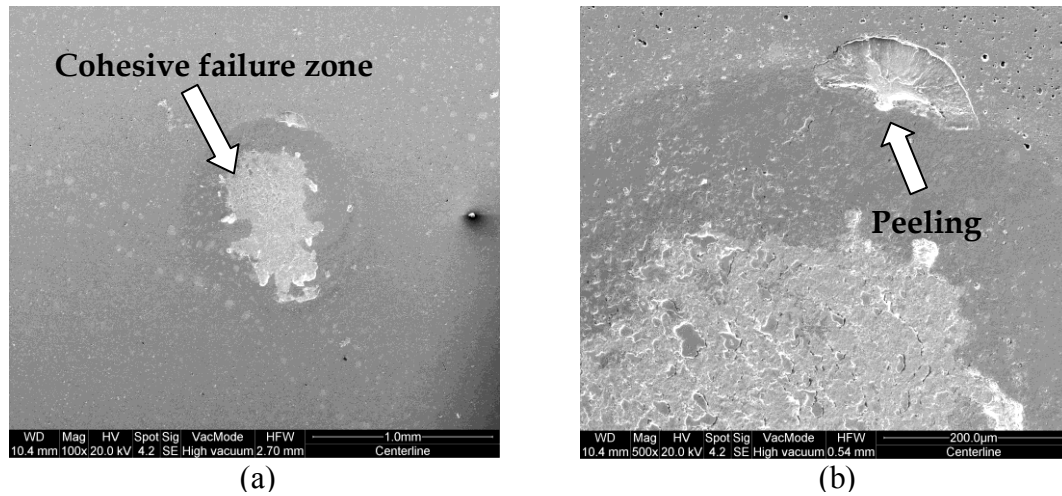


Figure 4.30 A_CrN after 50000 cycles. (a) Overview; (b) local view at the edge of the crater.

Fig. 4.31 presents the B_CrN coating after 50000 cycles. Although this coating has the highest resistance to WC ball impacting in this study, fatigue cracks and chippings still existed.

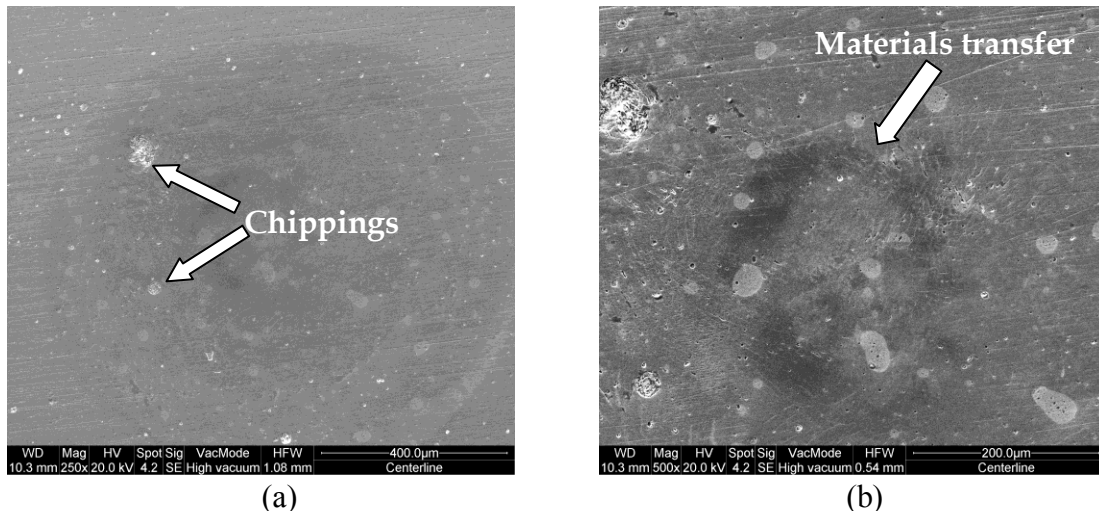


Figure 4.31 B_CrN after 50000 cycles. (a) Overview with small chippings; (b) fatigue cracks at the center of the crater and dark area of materials transfer.

Fig. 4.32 shows B_TiC coating after 50000 cycles impact. Cohesive failure zones are shown in Fig. 4.32a. Local view and EDS spectrum of the local view are presented in Fig. 4.32b and 32c respectively. A peak of tungsten in the EDS spectrum is from materials transfer of the WC ball.

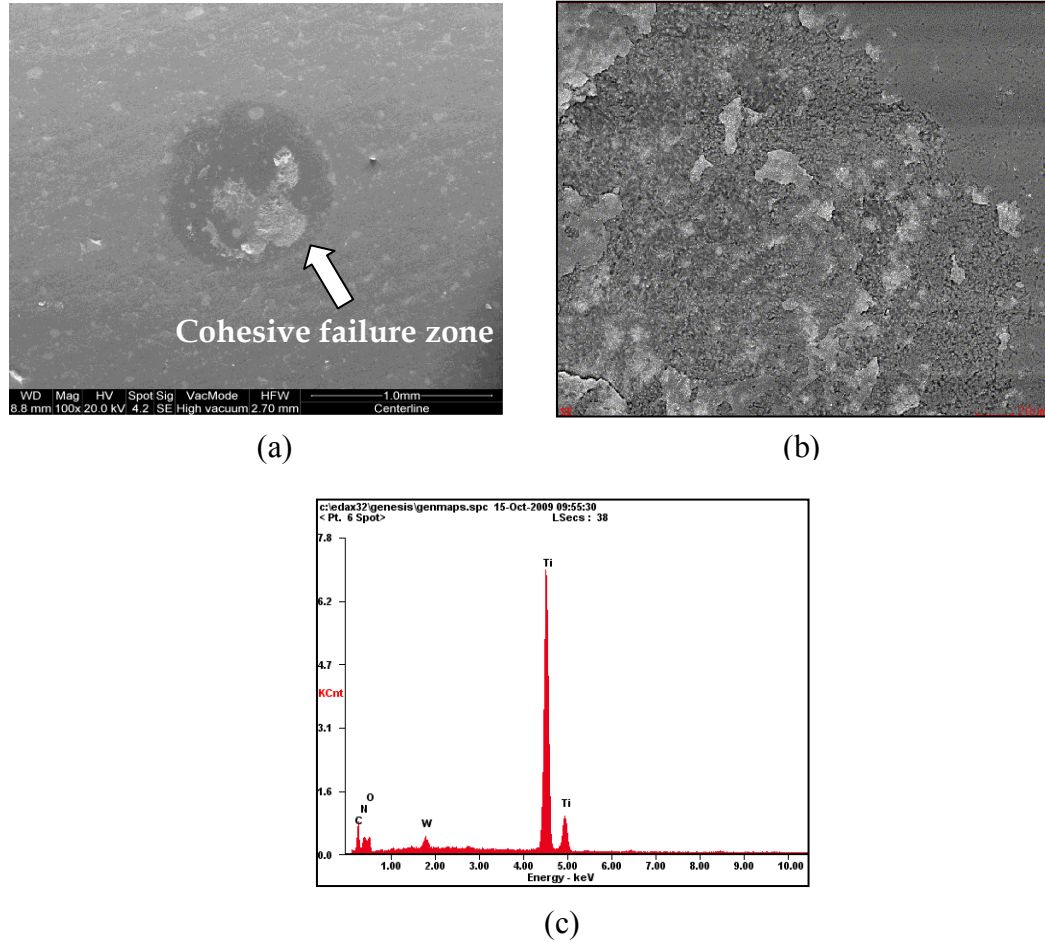


Figure 4.32 B_TiC after 50000 cycles. (a) Overview; (b) local view backscattered electron image showing cohesive failure zone; (c) EDS spectrum of the whole area of (b) showing the peak of tungsten.

C_TiC after 50000 WC ball impacting is given in Fig. 4.33. This coating has been damaged totally in the crater and circular cracks occurred around the edge of the crater (Fig. 4.33b).

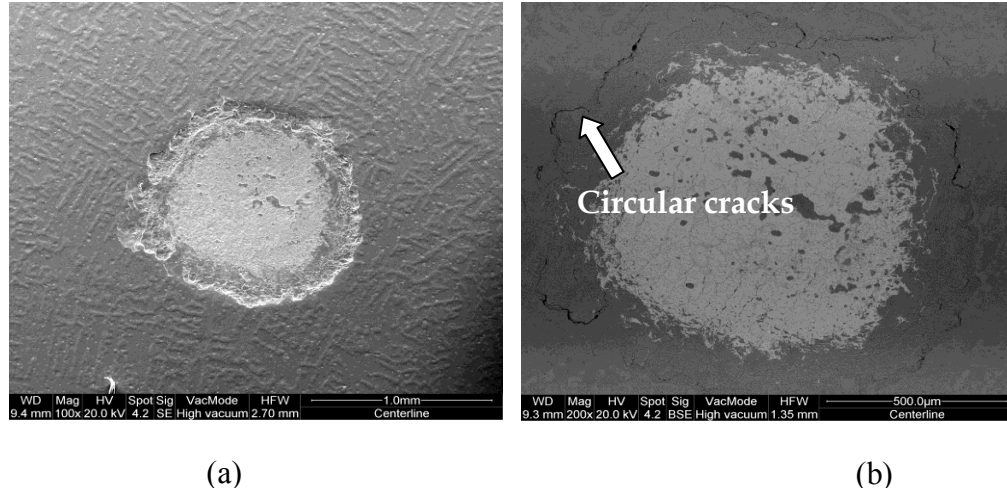


Figure 4.33 C_TiC after 50000 cycles. (a) Overview; (b) backscattered electron image showing center cohesive zone and circular cracks around the crater.

Diameters of craters impacted by WC balls after 10000 and 50000 cycles are given in Fig. 4.34. Diameters of 10000 cycles and 50000 cycles impact tests are around 0.7 mm and 0.9 mm respectively. Under the same impact conditions, i.e., ball material and impact cycles, the steel substrate dominates the plastic deformation of the crater regardless of difference in coating properties.

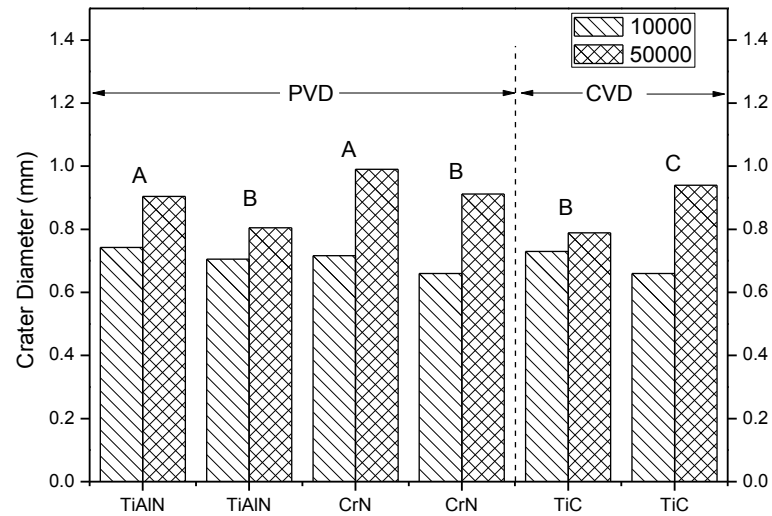


Figure 4.34 Diameters of craters impacted by WC balls after 10000 and 50000 cycles. A, B and C denote 3 different coating suppliers.

3.2.3 Ranking of coatings

Failures of different coatings using steel balls and WC balls are distinguished and evaluated in Table 4.1 and Table 4.2. From Table 1 and Table 2, B_CrN is the best coating for ball-on-plate impact fatigue test. TiC samples performed much better during the impact test using steel balls than using WC balls. Therefore, carbide (TiC) against carbide (WC) may not be a good combination in impact tests.

Table 4.1 Ranking of coating failures under steel ball impacting

Coating	Impact Cycles	Cohesive Failure	Adhesive Failure	Fatigue Crack	Material Transfer	Rank
A_TiAlN	10000	XX	X	XX	XX	5
B_TiAlN	10000	XXX	XXX	XX	XX	6
A_CrN	10000	XX	XX	X	X	4
	50000	XXX	XXX	?	XXX	
B_CrN	10000	X			X	1
	50000	X			X	
B_TiC	10000				X	1
	50000	X			X	
C_TiC	10000			Wear	X	1
	50000	X		Wear	X	

X: Severity.

Table 4.2 Ranking of coating failures under WC ball impacting

Coating	Impact Cycles	Cohesive Failure	Adhesive Failure	Fatigue Cracks	Materials Transfer	Rank
A_ TiAlN	10000	X			XX	2
	50000	XXX			XXX	
B_ TiAlN	10000	XX	XX	XX	XX	6
	50000	XXX	XXX	XXX	XXX	
A_ CrN	10000	X			XX	3
	50000	XXX	XXX	XXX	XX	
B_ CrN	10000	X			X	1
	50000	X		XX	X	
B_ TiC	10000	XX	XX		XX	5
	50000	XXX	XXX	XXX	XX	
C_ TiC	10000	XXX			X	4
	50000	XXX	XXX	XXX	XX	

3.3. FEM analysis

The impact process is complex, so simplifications and assumptions have to be made to achieve low numerical cost but of course sufficient accuracy. For instance, we assume the surface of the specimen as ideally smooth, whereas in reality a certain roughness may be present. The impact process is considered to be dynamic. For the experiments, both steel ball and tungsten carbide ball were applied in the simulation. The

ball was 10 mm in diameter and the size of the sample was chosen so that the boundaries of the substrate do not influence the results. The half plane of substrate is defined as 5mm in width and 4mm in height. Due to axisymmetry it is sufficient to model only the right half of the substrate. The nodes at the bottom of the Steel substrate are fixed in all directions. The load is applied at the top of the ball and only one impact cycle is simulated. The model is depicted in Fig. 4.35.

Figure 4.35 Simulation model of ball-on-plate impact test.

The coating is defined as a thin layer of 5~15 μm . Between coating and Steel substrate, a cohesive layer of 0.1 μm in thickness is set to act as the bonded interface of coating and substrate. For CrN coatings, the cohesive layer is taken as Cr; for TiAlN and TiC coatings, the cohesive layer is taken as Ti. The cohesive behavior is defined as continuum which means the initial response of the cohesive element is linear until a damage initiation criterion is met. However, for coating systems in this study, the damage criterions such as fracture energy were unknown. Therefore the simulation package will evaluate the maximum von Mises stress; there is no effect on the response of the cohesive element (i.e., no damage will occur). A larger von Mises value implies that the material is

closer to the yield point. The position and amplitude of the maximum stress will be used to obtain a better understanding of experimental results.

For the ball/coating interaction, a Lagrange method is used to handle surface-to-surface contact. The contact surfaces are thereby treated with the master-slave concept. Therein the master, in our case the ball, is trying to penetrate into the coating which is the slave. The nodes of the slave are not allowed to penetrate into the master's surface whereas the nodes of the master are allowed to penetrate into the surface of the coating. Noticeable materials transfer will not be considered in the simulation. The friction also has an effect on the stresses in the neighbourhood of the impact interface and is applied in the simulation. In this simulation, the research focuses on the stress distribution in coating and interface layer.

The steel ball and Steel substrate are assumed to be elastic-plastic work hardening and strain-rate dependent. Coatings and the WC ball are defined as elastic bodies because their yield strengths are very high. Key parameters of each coating, steel ball, WC ball and Steel substrate are listed in Table 3 and Appendix A. A typical mesh is given in Fig. 4.36.

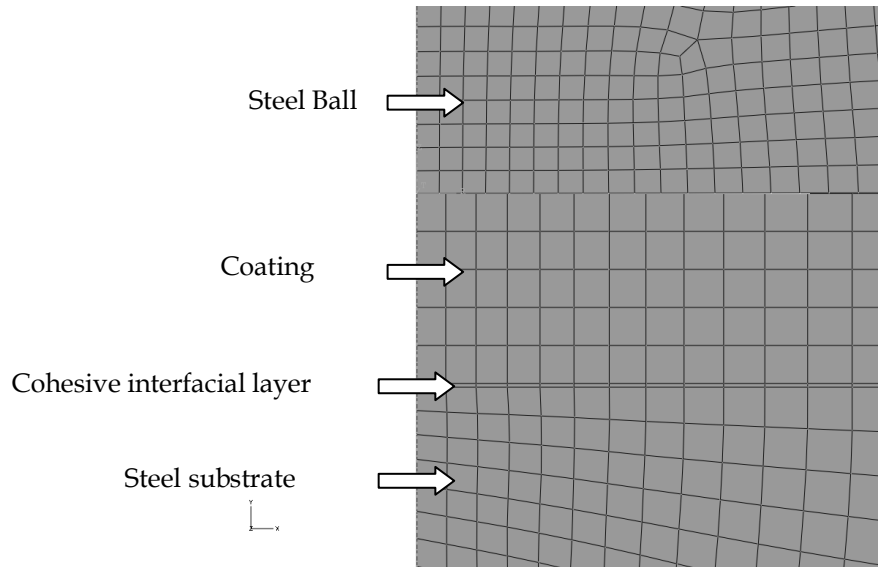


Figure 4.36 A typical mesh denoting the impact ball, coating, interfacial layer and Steel substrate.

3.3.1 Displacement

The displacement (1 cycle) at the center of the crater has been computed for different balls and coatings. Simulation results showed that the maximal impact displacement (elastic plus plastic) and residual depth (plastic) of the crater under the same load (400 N) only depend on the ball materials. The maximal displacement of steel ball impact tests is 6.3 μm and residual depth is 2.2 μm after one punch. For WC ball, maximal displacement is 8.7 μm and residual depth is 4.4 μm . Simulation results demonstrate that the crater size is determined by the substrate and ball materials. For long running tests (50000 cycles), crater behavior is more substrate-dependent. This can be verified by the experimental crater size in Fig. 4.21 and Fig. 4.34, in which the diameter of each craters are in the same level except A_CrN, which has been explained already.

3.3.2 A typical impact process by simulation

A typical von Mises stress distribution during impact procedure is given in Fig. 4.37. The maximal stress area in the coating moves outwards along the radius direction and resides near the crater edge.

3.3.3 Maximal von Mises stress in the coating

To predict yielding of materials under multiaxial loading conditions, von Mises stress is used to utilize results from simple uniaxial tensile tests. A larger von Mises value implies that the material is closer to the yield point. In the following section, the von Mises stress distribution of different coatings are chosen when the von Mises stress of the whole model reaches its maximal during the impact procedure, usually it is the time when load reaches the second peak of -400 N in Fig. 4.7. The cohesive interfacial layer works as a bonding layer between the coating and substrate. Therefore, shear stress of the bonding layer will provide information regarding the possibility of adhesive failure. For comparison with experimental results, optical/SEM images of 10000 cycles impact tests will be presented.

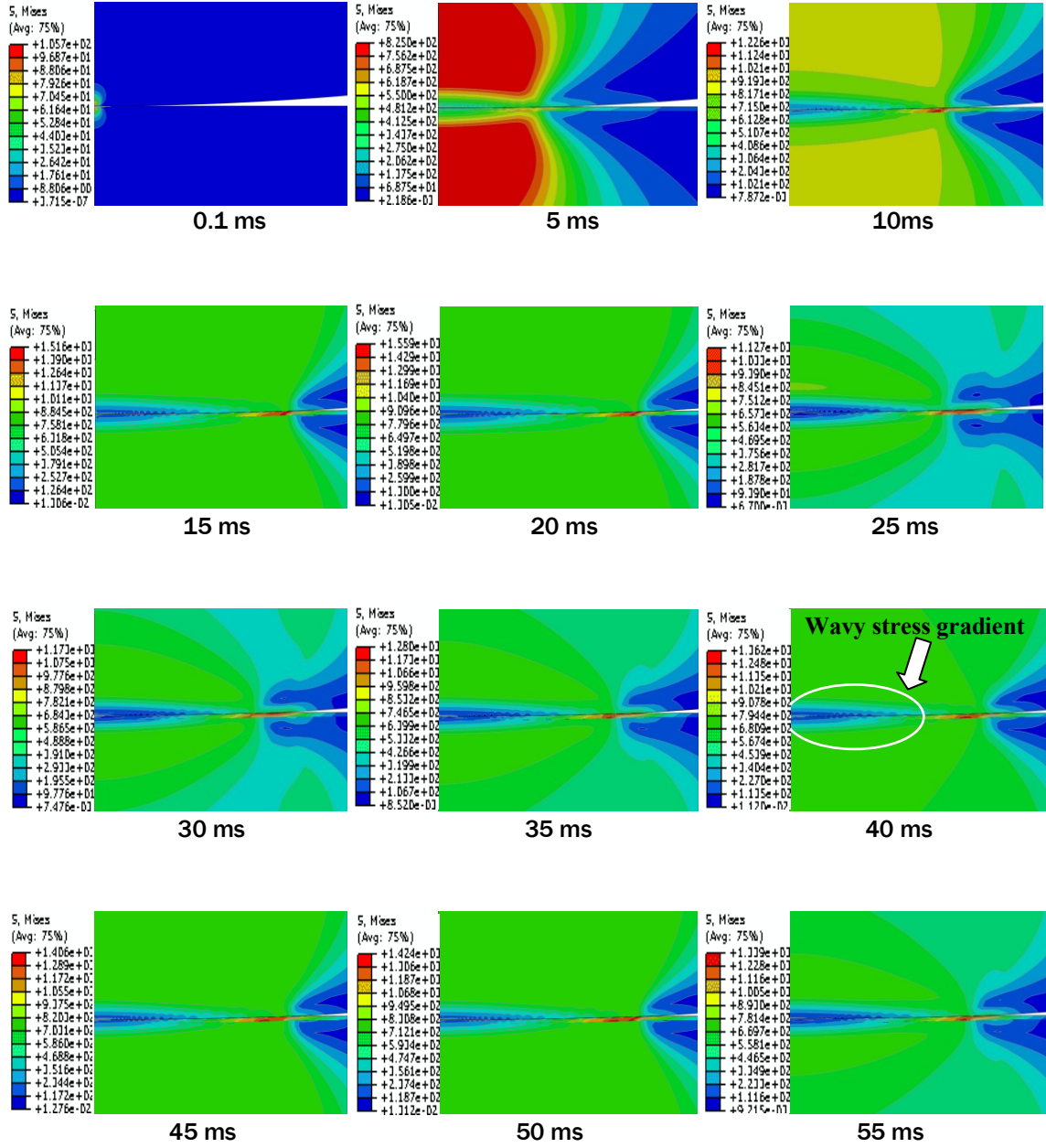


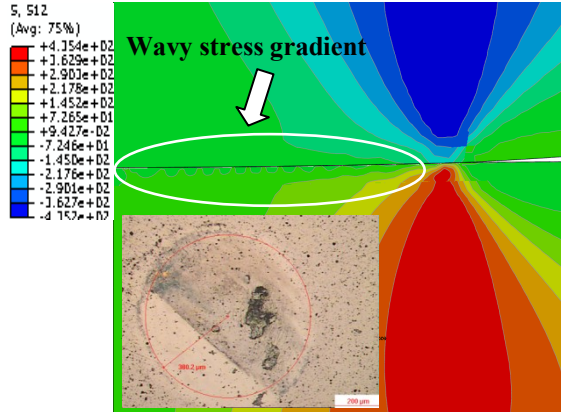
Figure 4.37 Von Mises stress distribution of B_CrN during steel ball impact test.

3.3.3.1 A_TiAlN

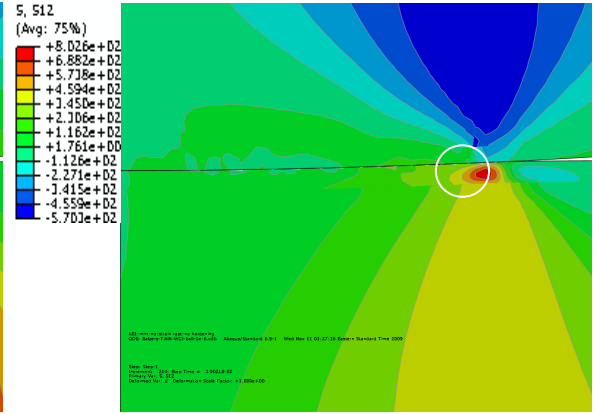
The von Mises stress distribution of A_TiAlN under 400 N peak force is given in Fig. 4.38. The maximal von Mises stress σ_v in coating is 1.830 GPa. The displacement is all the same 6.3 μm and the contact area is all the same 0.25 mm^2 for all simulations under

steel ball impacting. An optical image of 10000 impact cycles is also presented in the figure. At this moment, the maximal shear stress σ_{I2} in cohesive layer is 359 MPa at the position as marked in Fig. 4.38b. Fig. 4.38c and 38d show the stress distribution under WC ball impact. The maximal von Mises stress σ_v in coating is 2.596 GPa. Again, the displacement is 8.3 μm and the contact area is 0.21 mm^2 for all simulations under WC ball impacting. An SEM image of 10000 impact cycles is also presented in the figure. The maximal shear stress σ_{I2} in cohesive layer is 451 MPa.

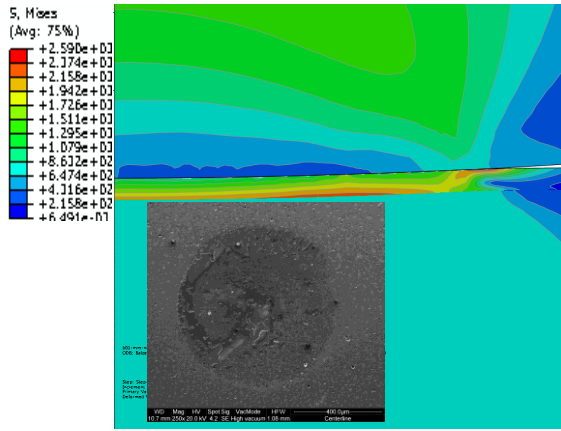
For steel ball impacting, the position of the maximal σ_v is far from the center. As a result, the possible failure may occur at the contact boundary and move oppositely to the center. This can be partially verified by the experimental result which the failure area is not at the center. However, after failures initiate, the stress distribution by simulation is not applicable and the failure evolution is not predictable.



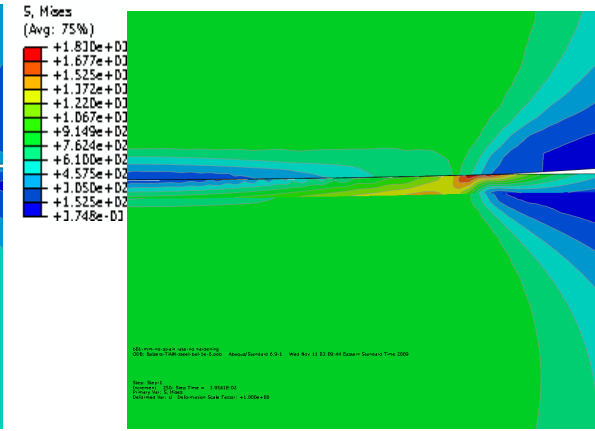
(a) σ_v under steel ball impacting



(b) σ_{12} under steel ball impacting



(c) σ_v under WC ball impacting



(d) σ_{12} under WC ball impacting

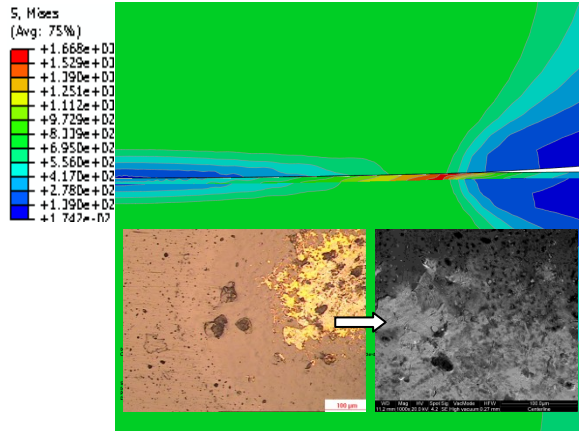
Figure 4.38 A_TiAlN stress distribution at the maximal impact load. (a) Von Mises stress σ_v of steel ball impact; (b) shear stress σ_{12} of steel ball impact; (c) σ_v of WC impact; (d) σ_{12} of WC ball impact.

Although the amplitude of maximal σ_v of WC ball is higher than that of steel ball, the experimental result of 10000 WC ball impact test shows that the damage is not severe as of steel ball impact test. This can be explained by the two factors: The first is the difference in stress gradient. For steel ball, the top of the coating has higher stress than

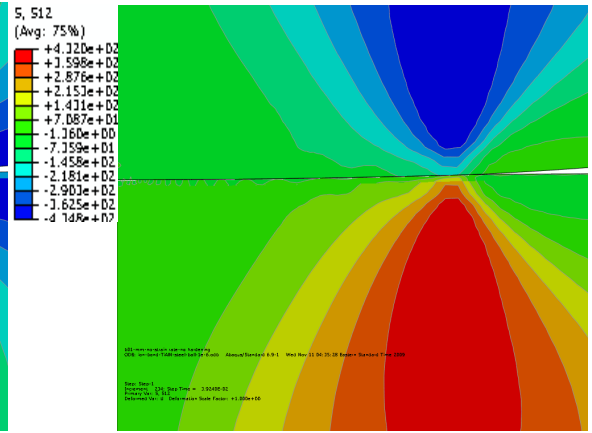
inside the coating and the interfacial layer as shown in Fig. 4.38a. For WC ball, this trend still exists but is not distinct as shown in Fig. 4.38c. Second, a wavy stress gradient phenomenon does not occur in WC ball simulation. However, the wavy phenomenon can be found in the steel ball simulation. This phenomenon (similar to the wave from 10 ms to 55 ms in Fig. 4.37) may be due to friction between ball and coating and the interacting between the steel ball and coating. The wavy stress may cause the band of fatigue cracks in Fig. 4.11b and the failure initiates from these fatigue cracks. In addition, there are always one high stress spot as marked in Fig. 4.38b. In all experiments, chippings were common around this area.

3.3.3.2 B_TiAlN

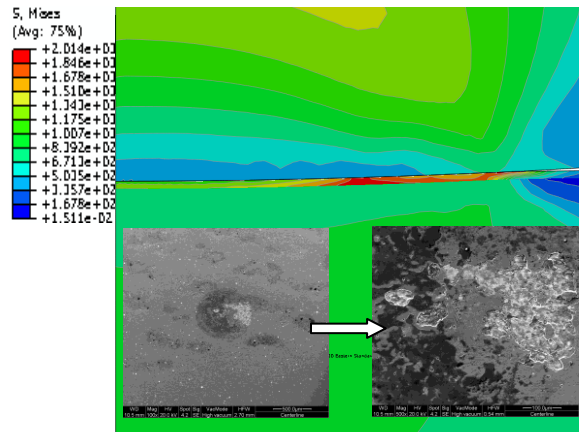
The von Mises stress distribution of B_TiAlN is given in Fig. 4.39. The maximal σ_v of steel ball and WC ball impacting are 1.668 GPa and 2.014 GPa. The maximal σ_{12} in cohesive layer of steel ball and WC ball impacting are 166 MPa and 363 MPa. The wavy gradient of stress has been found in both steel ball and WC ball simulations. The difference of the wavy phenomenon between A_TiAlN and B_TiAlN may be due to different elastic modulus and thickness of the coatings. Fatigue cracks were also found in both steel ball and WC ball 10000 cycles impact tests in Fig. 4.12c and Fig. 4.23b.



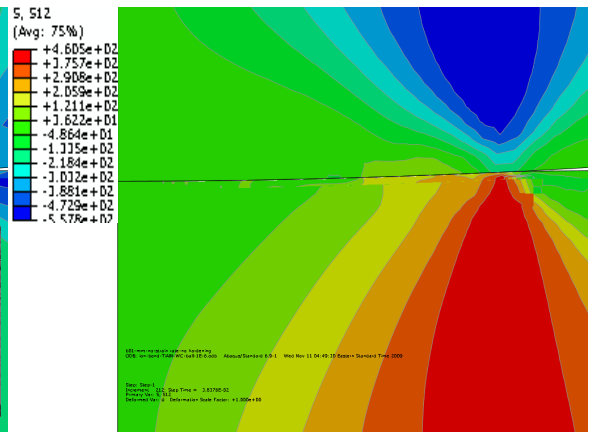
(a) σ_v under steel ball impacting



(b) σ_{I2} under steel ball impacting



(c) σ_v under WC ball impacting

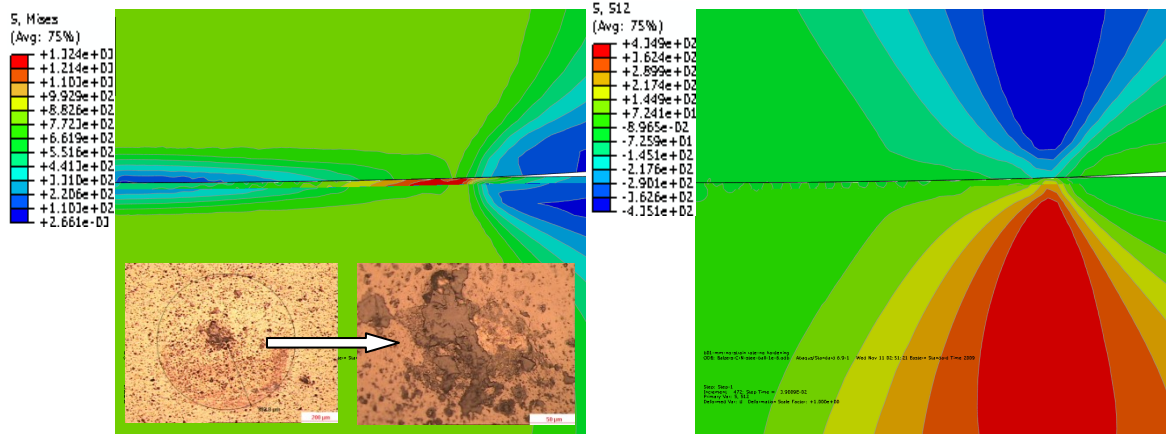


(d) σ_{I2} under WC ball impacting

Figure 4.39 B_TiAlN stress distribution at the maximal impact load. (a) Von Mises stress σ_v of steel ball impact; (b) shear stress σ_{I2} of steel ball impact; (c) σ_v of WC impact; (d) σ_{I2} of WC ball impact.

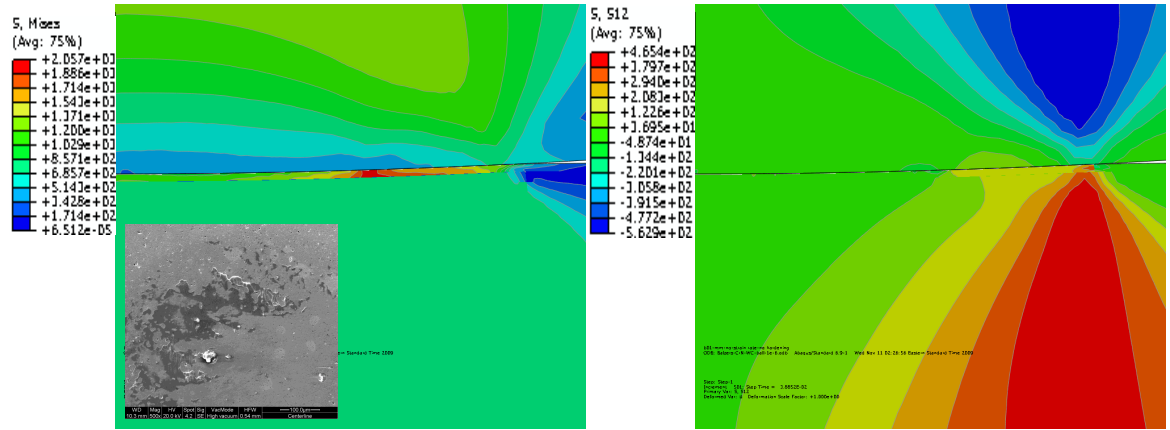
3.3.3.3 A_CrN

The von Mises stress distribution of A_CrN is given in Fig. 4.40. The maximal σ_v of steel ball and WC ball impacting are 1.324 GPa and 2.057 GPa. The maximal σ_{I2} in cohesive layer of steel ball and WC ball impacting are the same 163 MPa. The peeling and chipping near the center of the crater may be caused by flaws inherent from the coating. The wavy gradient of stress appears in the steel ball case and fatigue cracks have been observed in 10000 cycles impact tests (Fig. 4.13b). For the simulation of WC ball without the wavy phenomenon, no fatigue cracks have been found in the experiment.



(a) σ_v under steel ball impacting

(b) σ_{12} under steel ball impacting



(c) σ_v under WC ball impacting

(d) σ_{12} under WC ball impacting

Figure 4.40 A_CrN stress distribution at the maximal impact load. (a) Von Mises stress σ_v of steel ball impact; (b) shear stress σ_{12} of steel ball impact; (c) σ_v of WC impact; (d) σ_{12} of WC ball impact.

3.3.3.4 B_CrN

The von Mises stress distribution of B_CrN is given in Fig. 4.41. The maximal σ_v of steel ball and WC ball impacting are 1.426 GPa and 2.207 GPa. The maximal σ_{12} in

cohesive layer of steel ball and WC ball impacting are the same 163 MPa. The wavy stress gradient phenomenon exists in simulations of both steel ball and WC ball impacting. However, fatigue cracks have not been observed in 10000 cycles impact tests using both steel ball and WC ball. For the B_CrN, the 10000 cycles might not be high enough for this σ_v to induce fatigue cracks. While for 50000 cycles impact tests, both the impact cycles and the maximal σ_v might be higher than the threshold for fatigue crack initiation. Therefore, after 50000 impact cycles, impact cycle might reach a threshold and fatigue cracks were found in the crater generated by WC ball impact test (Fig. 4.31b).

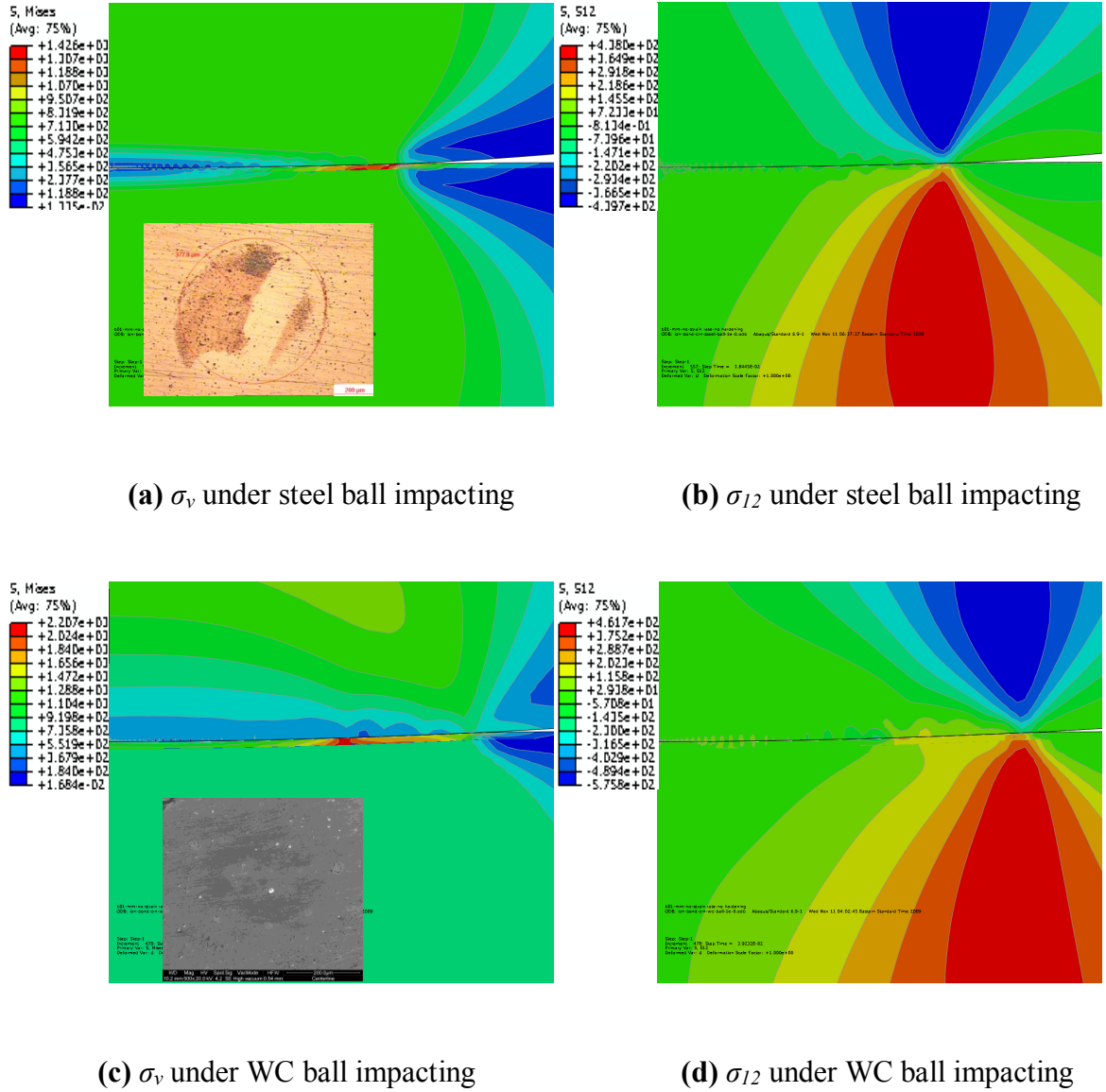
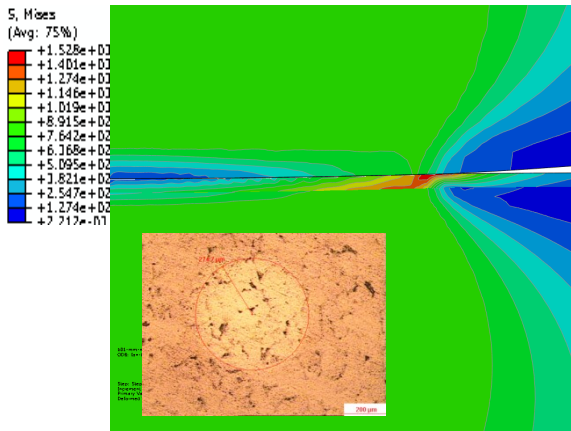


Figure 4.41 B_CrN stress distribution at the maximal impact load. (a) Von Mises stress σ_v of steel ball impact; (b) shear stress σ_{12} of steel ball impact; (c) σ_v of WC impact; (d) σ_{12} of WC ball impact.

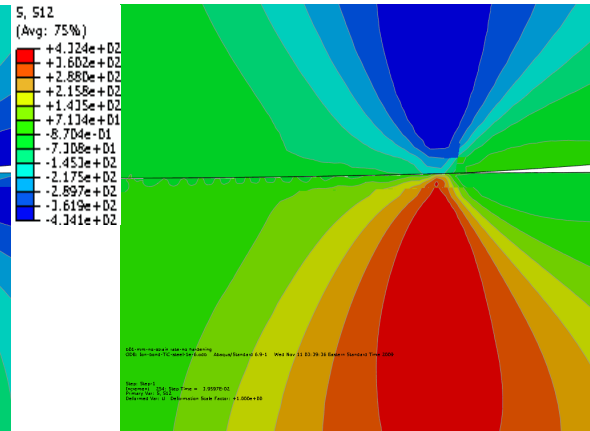
3.3.3.5 B_TiC

The von Mises stress distribution of B_TiC is given in Fig. 4.42. The maximal σ_v of steel ball and WC ball impacting are 1.528 GPa and 2.037 GPa. The maximal σ_{12} in

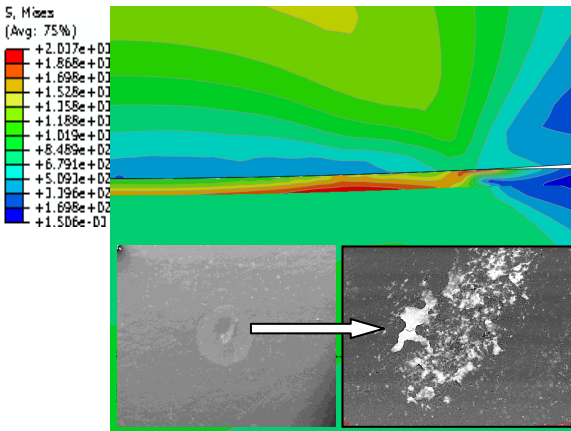
cohesive layer of steel ball and WC ball impacting are 324 MPa and 453 MPa. Wavy gradient of stress appears for the steel ball simulation. Similar to A_CrN and B_CrN cases explained previously, no obvious fatigue cracks have been observed in 10000 cycles impact tests.



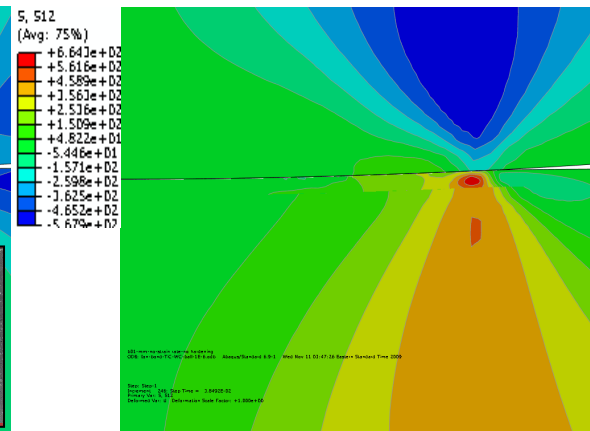
(a) σ_v under steel ball impacting



(b) σ_{12} under steel ball impacting



(c) σ_v under WC ball impacting



(d) σ_{12} under WC ball impacting

Figure 4.42 B_TiC stress distribution at the maximal impact load. (a) Von Mises stress σ_v of steel ball impact; (b) shear stress σ_{12} of steel ball impact; (c) σ_v of WC impact; (d) σ_{12} of WC ball impact.

3.3.3.6 C_TiC (Only for reference due to multilayer structure of coating)

The von Mises stress distribution of C_TiC is given in Fig. 4.43. The maximal σ_v of steel ball and WC ball impacting are 1.385 GPa and 1.953 GPa. The maximal σ_{12} in cohesive layer of steel ball and WC ball impacting are 308 MPa and 450 MPa. Due to the fact that the coating is multilayer, simulation is not useful in this study.

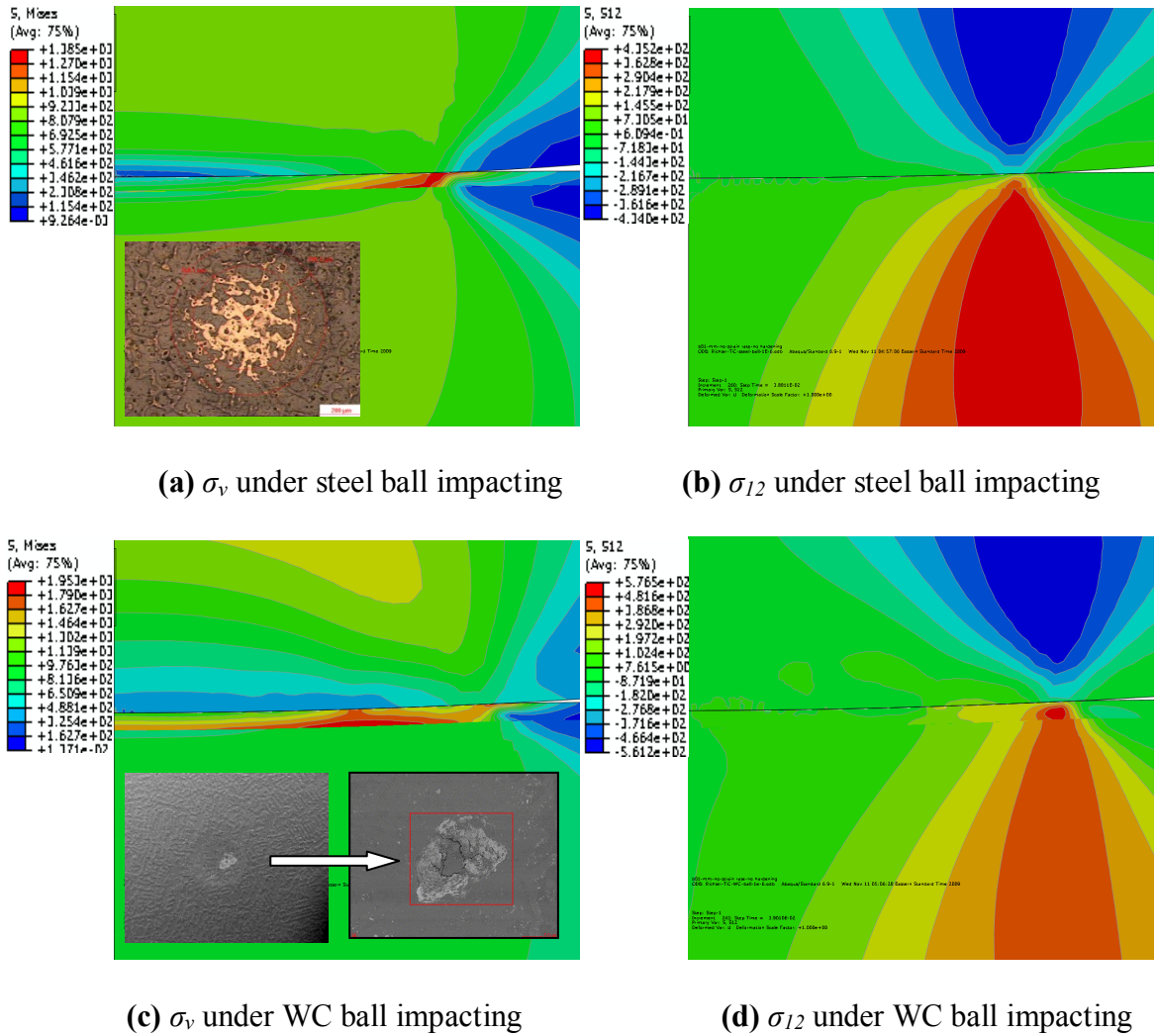


Figure 4.43 C_TiC stress distribution at the maximal impact load. (a) Von Mises stress σ_v of steel ball impact; (b) shear stress σ_{12} of steel ball impact; (c) σ_v of WC impact; (d) σ_{12} of WC ball impact.

3.3.4 Remarks

Table 4.3 Simulated maximal von Mises stress in the coating and shear stress in the cohesive layer

Supplier	Interfacial Layer	Elastic Modulus (GPa) (Nanoindentation)	Thickness for simulation (μm)	Maximal σ_v in Coating (GPa)		Maximal σ_{I2} in cohesive layer (GPa)	
				Steel Ball	WC Ball	Steel Ball	WC Ball
A_TiAlN	Ti	367.2	15	1.830	2.596	0.359	0.451
B_TiAlN	Ti	315.9	5	1.668	2.014	0.166	0.363
A_CrN	Cr	219.9	5	1.324	2.057	0.163	0.163
B_CrN	Cr	312.1	5	1.426	2.207	0.163	0.163
B_TiC	Ti	305.2	12	1.528	2.037	0.324	0.453
C_TiC	Ti	253.1	12	1.385	1.953	0.308	0.450

The interfacial bonding layer plays a key role in the simulation. Taken Cr as the interfacial layer, the σ_v of coatings layers and the σ_{I2} in the interfacial layer are lower than others with Ti interfacial layer. As a result, A_CrN and B_CrN behaved better than 2 TiAlN coatings with high maximal σ_v in 10000 cycles steel ball impact tests.

According to the simulation, the maximal σ_{12} in cohesive layer seems to be the same for coatings in the same thickness. And another finding is that the higher thickness, the higher shear stress in interfacial layer and higher von Mises stress in the coating.

4. CONCLUSIONS

Impact fatigue testing methodology has been developed and used to study coating failure behavior under simulated stamping conditions. Experiments and FEM analyses of ball-on-plate impact fatigue tests have been performed on six samples. All the six coated samples showed good adhesion to their substrate. Depends on ball materials, coatings performed differently. Both approaches showed that CrN on D2 substrate from supplier B was the best among all the coatings in both steel ball and WC ball impact tests.

Both TiAlN coatings do not perform as well as expected. Steel ball counterfaces cause more severe failure on the nitride based coatings than WC ball counterfaces. However, carbide based coatings perform better when against steel balls than against WC balls. Generally, the thick coatings did not perform better than the thin coatings particularly after high number of impact cycles. All coatings showed good coating adhesion. Cohesive chipping, peeling, ball material transfer, and fatigue cracking appeared in the craters.

FEM analyses have been carried out to get a further understanding of coating failure mechanism. The simulation indicated that the WC ball causes a wider area having a maximum stress than the steel ball. A wavy stress gradient occurs in some coating/ball

combinations. The varied stress may be the reason for the fatigue cracking bands appeared in the experiments.

Noticeable, some parameters such as elastic modulus were taken from nanoindentation and literature. Some other important parameters of coatings from suppliers such as thickness, interfacial composition, density, Poisson ratio, etc. are not accurate. Without such information, simulation results may not be accurate. However, the simulation has verified some experimental results well. Base on this approach, accurate prediction on coating design is achievable.

5. FUTURE WORK IN PHASE II

First is to get the information of the coatings, for instance, acquire the thickness, composition of the coatings and interfacial layer and crack propagation in the coating by TEM/FIB or other available techniques. The second is the Extended Impact Fatigue Test (EIFT), which will be used to study the effect of sliding on the substrate under stamping conditions. During the EIFT a hard ball is attached to a pre-compressed spring. The ball is in contact with the substrate. The substrate itself is being moved up and down and sideways (slid). The critical parameters in the test are the loading force F , the frequency of the repetition of the loading and the length of the sliding track. The test response is the critical number of loading cycles up to the point at which the coating surface shows damage (i.e., spallation, cracking). Two test loads (for simulated stamping pressures) and tungsten carbide balls will still be used for extended ball-on-plate impact fatigue tests. Finite element analysis and contact stress analysis may be also conducted to for better understanding of effects of stress distributions on coating failure mechanism.

REFERENCES

1. R. Bantle and A. Matthews. *Investigation into the impact wear behaviour of ceramic coatings*. in *Fourth International Conference on Plasma Surface Engineering, 19-23 Sept. 1994*. 1995. Switzerland: Elsevier.
2. O. Knotek, B. Bosserhoff, A. Schrey, T. Leyendecker, O. Lemmer, and S. Esser. *A new technique for testing the impact load of thin films: the coating impact test*. in *19th International Conference on Metallurgical Coatings and Thin Films, 6-10 April 1992*. 1992. Switzerland.

APPENDIX A:

D2 Steel substrate: $\rho=7.8 \text{ g/cm}^3$, $E=200 \text{ GPa}$, Poisson's ratio=0.3

Yield	Strain	Rate
776	0	0
809	0.01	0
829	0.02	0
842	0.03	0
866	0.06	0
883	0.1	0
895	0.15	0
910	0.25	0
922	0.4	0
953	2	0
791	0	0.001
824	0.01	0.001
846	0.02	0.001
863	0.03	0.001
899	0.06	0.001
931	0.1	0.001
958	0.15	0.001
995	0.25	0.001
1030	0.4	0.001

1170	2	0.001
799	0	0.01
831	0.01	0.01
855	0.02	0.01
874	0.03	0.01
916	0.06	0.01
955	0.1	0.01
989	0.15	0.01
1040	0.25	0.01
1090	0.4	0.01
1280	2	0.01
805	0	0.1
838	0.01	0.1
863	0.02	0.1
884	0.03	0.1
933	0.06	0.1
978	0.1	0.1
1020	0.15	0.1
1080	0.25	0.1
1140	0.4	0.1
1390	2	0.1
808	0	1
842	0.01	1

869	0.02	1
893	0.03	1
946	0.06	1
998	0.1	1
1050	0.15	1
1120	0.25	1
1190	0.4	1
1490	2	1
810	0	10
846	0.01	10
876	0.02	10
901	0.03	10
960	0.06	10
1020	0.1	10
1070	0.15	10
1150	0.25	10
1240	0.4	10
1600	2	10
812	0	100
850	0.01	100
882	0.02	100
909	0.03	100
974	0.06	100

1040	0.1	100
1100	0.15	100
1190	0.25	100
1280	0.4	100
1700	2	100
815	0	1000
855	0.01	1000
888	0.02	1000
917	0.03	1000
987	0.06	1000
1060	0.1	1000
1130	0.15	1000
1230	0.25	1000
1330	0.4	1000
1810	2	1000

CHAPTER 5

COMBINATIVE INFLUENCE OF IMPACT AND PRESSING FORCES ON COATING FAILURE BEHAVIOUR

1. INTRODUCTION

Since physical and chemical vapor deposition (PVD/CVD) coatings usually have a much higher hardness and resistance of wear than electroplated or electroless coatings and nitrided steels, hard coatings have been considered as necessary top layers of a wide variety of mechanical components to battle the wear problems. The hard coatings are growingly being used to improve the tribological properties and wear resistance of various tools for metal cutting, forming and stamping [1]. For instance, due to the increasing use of advanced high strength steels, die wear prevention has become an important issue in the stamping of automotive parts. The hard coatings have a trend to be used as much-needed protective top layers on surfaces of stamping dies thereby to extend the tool life and improve the quality of the stamped products [2-6]. The coatings must have good adhesion to the base material to withstand the high loads and shearing forces without chipping or peeling, and low friction coefficient to reduce wear [7, 8]. The coating fatigue strength is also one of critical parameters that have to be taken into account during the selection of the appropriate coating/substrate system for applications such as stamping. Therefore, mechanical properties of hard coatings to be concerned include not only hardness, residual stress and adhesion, but also cohesion and fatigue failure behavior.

Most practical adhesion test methods such as pressure-sensitive tape test, pull-off, scratch and indentation involve static or quasistatic elastoplastic loading [9, 10]. For applications that dynamic repetitive loadings are applied, a ball-on-plate impact test was first introduced to evaluate the adhesive and cohesive failures of hard coatings [11, 12]. Bantle and Matthews indicated that three failure zones are involved in the impact indent: a central zone with cohesive failure, an intermediate zone with cohesive and adhesive failures and a peripheral zone with circular cracks failure plus pilling up of the material [13]. Knotek et al. [11] and Bouzakis et al. [14, 15] showed that the degradation of the coating induced by repetitive dynamic impact is a fatigue behavior. However, the previous research work did not carefully look into the combinative loading process of impact force and pressing force. The impact and pressing force combination is actually the case during the stamping. Thus, in the present work, three different combinations of impacting/pressing loads were used to evaluate three types of hard coatings, CrN, TiAlN and TiC, during the ball-on-plate impact tests. The selection of the coatings was based on their good performance in an industrial auto stamping plant. The influence of the impact forces on the crater sizes of the coated and uncoated substrates and failure behaviour of the coating/substrate systems were then discussed.

2. EXPERIMENTAL DETAILS

2.1 The impact tester

The schematic of the impact tester is shown in Fig. 5.1. A hardened SAE 52100 steel ball of 10 mm in diameter is driven by a two-way stroke air cylinder with compressed air. The quasi-static driving force F_D was assumed to be constant for a given

air pressure, neglecting friction force. With a fixed impact mass m , the relationship between distance d and traveling time of the ball to the sample surface t is

$$d = \frac{1}{2}at^2 = \frac{1}{2} \frac{F_D + mg}{m} t^2 \quad (5.1)$$

The velocity of impact mass reaching sample surface, v is given by

$$v = at = \frac{F_D + mg}{m} \sqrt{\frac{2md}{F_D + mg}} = \sqrt{2d\left(\frac{F_D}{m} + g\right)} \quad (5.2)$$

By adjusting d , the velocity, v , changes and thus impact force and momentum change. The driving load F_D and distance d can be changed by adjusting the air pressure and the height of sample holder, respectively. In the present experiment, the frequency was controlled at 10 Hz. To determine the impact force, the impact ball was driven under an air pressure to hit on a thin steel button connected to an OMEGA LCKD-500 load cell directly. The button was used to protect the load cell from impacting damage. The impact force F_I and quasi-static pressing force F_P were then obtained and calibrated by a KYOWA PCD-300A data acquisition system. The pressing force F_P depended on the air pressure applied and did not change with varying the distance d under the given air pressure for the air cylinder. After the impact force was obtained, samples were placed at the same distance d and were impacted under the same driving force F_D . Impact tests were carried out at three different distances d . Impact forces at the three distances d under a 400 N driving force were recorded.

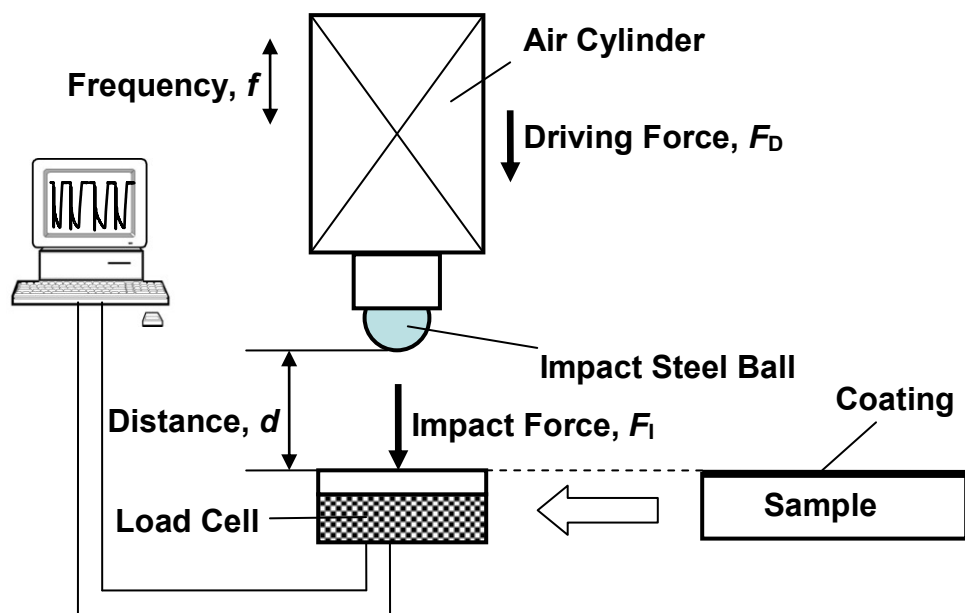


Figure 5.1 Schematic of the impact tester.

2.2 Hard coatings

The samples were coated on 25 mm x 25 mm x 8 mm AISI D2 substrates. The substrates were pre-polished with 600 grit sandpaper, and heat treated to be 58.5~59.2 HRC. The coatings on the AISI D2 samples included two PVD coatings, CrN and TiAlN and one CVD coating, TiC. The coating thickness was determined on cross sections of the coatings using an optical microscope. Nanoindentation (Hysitron Ubi1) was used to measure the elastic modulus and hardness of each coating. The testing load used was a 1 mN with the loading and unloading time of 10 seconds, respectively. For comparison, a Vickers microhardness tester was also used to obtain the hardness using an indentation load of 25 grams. The microhardness of coatings was slightly lower than the nanohardness likely due to the deeper indentation during the Vickers tests and the consequent contribution from the softer substrate. Table 5.1 gives the thickness and mechanical properties of the coatings.

Table 5.1. Thickness and mechanical properties of coatings

Coatings	Thickness	Berkovich hardness	Vickers Hardness	Elastic Modulus
	(μm)	(GPa)	(GPa)	(GPa)
CrN	7.1	18.9	18.2	312.1
TiAlN	2.9	29.7	26.2	315.9
TiC	9.2	29.4	28.4	305.2

2.3 Impact procedure

The frequency of impact was set as 10 Hz and the driving force was set as 400 N. By varying the distances d , impact forces were set as 200 N, 400 N and 600 N. 10,000 cycles of impacts were carried out for each coating at the three distances (i.e., the three loads), respectively. The impacts were also performed on the substrate under 7 impact loads ranged from 100 N to 600 N. Prior to the experiment, both the impact ball and samples were cleaned with acetone. A new steel ball was used for each impact test. After impacts, the coatings were cleaned with acetone and the crater sizes were measured using a Buehler Omnimet optical microscope. In addition, a scanning electron microscope (JEOL JSM-5800LV) with energy dispersive x-ray (EDX) analysis operating at a 15 kV voltage was used to evaluate the failure behaviour in the impacted regions.

3. RESULTS AND DISCUSSION

Impact forces at the three distances d under a 400 N driving force were recorded and shown in Fig. 2. During the impacts, the driving force applied on the piston in the air cylinder by air pressure accelerated the impact body which generated the impact force

when the impact ball punched the tested samples surface. Then, the driving force transformed into a quasi-static build-up force during the late stage of the impact cycle and acted as a pressing force applied on the sample surface after the early impacting. According to the Eq. 5.2, under the constant driving force F_D , the three accelerating distances d would lead to three different velocities and thus produce three impacting forces which were determined as ~ 200 N, ~ 400 N and ~ 600 N (Fig. 5.2) by the OMEGA LCKD-500 load cell (Fig. 5.1). Thus, the forces of the impact tests in this work were three combinations of impact/pressing forces, i.e., 200 N/400 N, 400 N/400 N and 600 N/400 N. These combinations allowed to studying the combinative effect of impact/static forces on deformation of the coated substrate and failure behaviour of the coating/substrate systems.

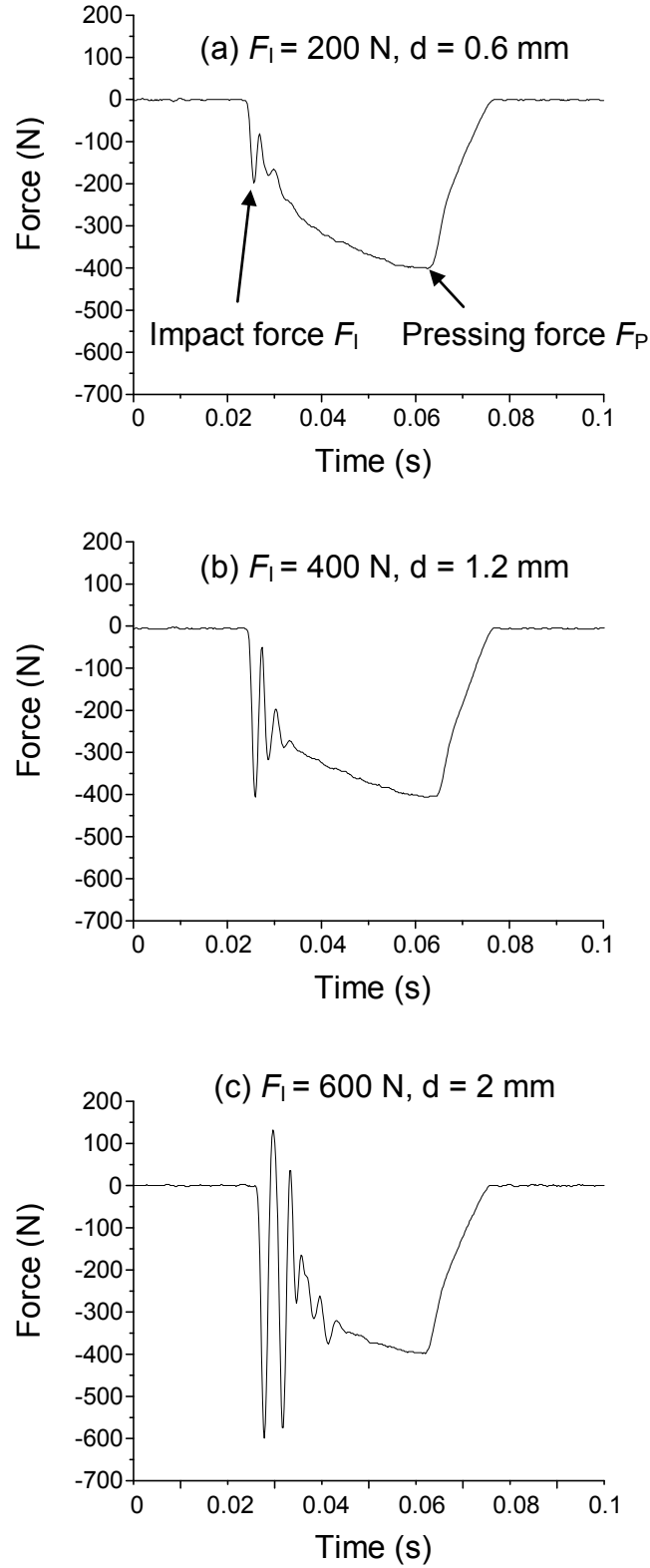


Figure 5.2 Impact forces F_I and pressing forces F_P at different distances d under a 400 N driving force F_D for one cycle. (a) 200 N/400 N impact/pressing force; (b) 400 N/400 N impact/pressing force; (c) 600 N/400 N impact/pressing force.

From the curves of Fig. 5.2, it was noticeable that the impact test system vibrated at the initial stage of impact. After the vibration force waveform was suppressed by the driving force, the pressing force was built up to the driving force of 400 N. The peak with the maximum amplitude of the vibration was defined as impact force F_I . With the increasing of distance d , the vibration cycles increased from 2 (for a 200 N impact force) to 5 (for a 600 N impact force). As a result, more impact energy might be transferred into the impacted subject. The impact and pressing force combination as well as vibration force waveform can actually occur during the stamping. Hence, a stiffer stamping equipment and tighter tolerance may reduce the vibration.

To investigate the effect of impact/pressing forces on the deformations of the coated and uncoated D2 substrates, the diameters of the impacted craters were measured from SEM images and plotted in Fig. 5.3. Impact tests on the D2 substrate steel were carried out at 7 impact/pressing forces. The diameters of craters on the D2 steel increased almost linearly with the impact loads from 100 N to 600 N where the pressing force was consistent at 400 N. The samples coated with the CrN and TiC followed the same trend as the D2 steel. The crater diameters on the CrN coating were correlated well with the curve of D2 steel while those of the TiC sample seemed to shift down to some extent from the curve of D2 steel. This shift might be caused by the highest hardness and largest thickness of TiC coating, which reduced the plastic deformation on the D2 substrate. However, with the increasing of impact forces, the shift was minimized. The TiAlN coating demonstrated different behaviour in the crater sizes. When the impact load is as low as 200 N, the coating failures were minimal and the crater diameter was in the same level as of the D2 steel. With increasing the impact force to 400 N, severe coating failures

occurred and the coating in the crater was broken into a large number of debris. Under the steel ball impacting, abrasive wear caused by the debris began to work as the main mechanism. The crater size increased abnormally as a result of impact and abrasive wear. However, the crater diameter of the TiAlN coating under the 600 N impact force was in the same level as other coatings and the D2 steel.

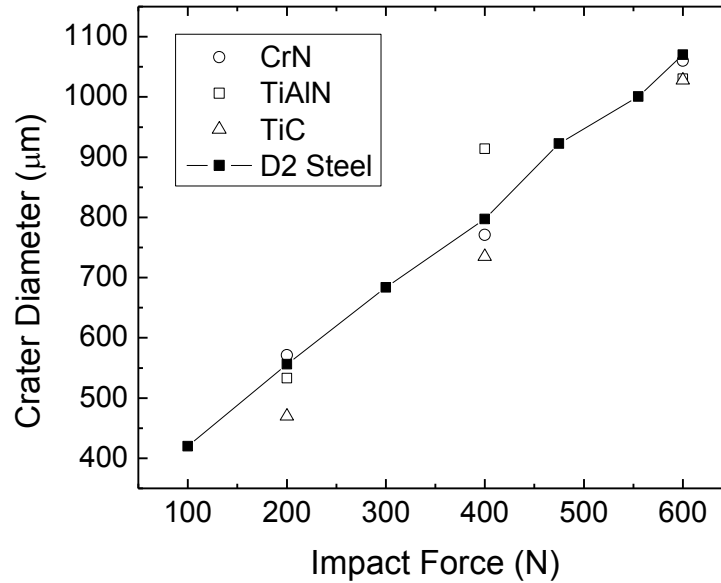


Figure 5.3 Crater diameters under different impact forces after 10,000 impact cycles

Although a coating (such as TiC) with a high hardness and large thickness could reduce the plastic deformation of the coated substrate at a low impact load, the effect was limited at a high impact force. It should be noted that the pressing force did not contribute the formation of the craters. The craters were created by the impact dynamic energy during the impact hammering process. In general, the crater sizes were more corresponded to the substrate property but less depended on the coatings. The coatings were still too thin to provide extra load-bearing capability to the substrate under the extremely high impact stress during tests in this work.

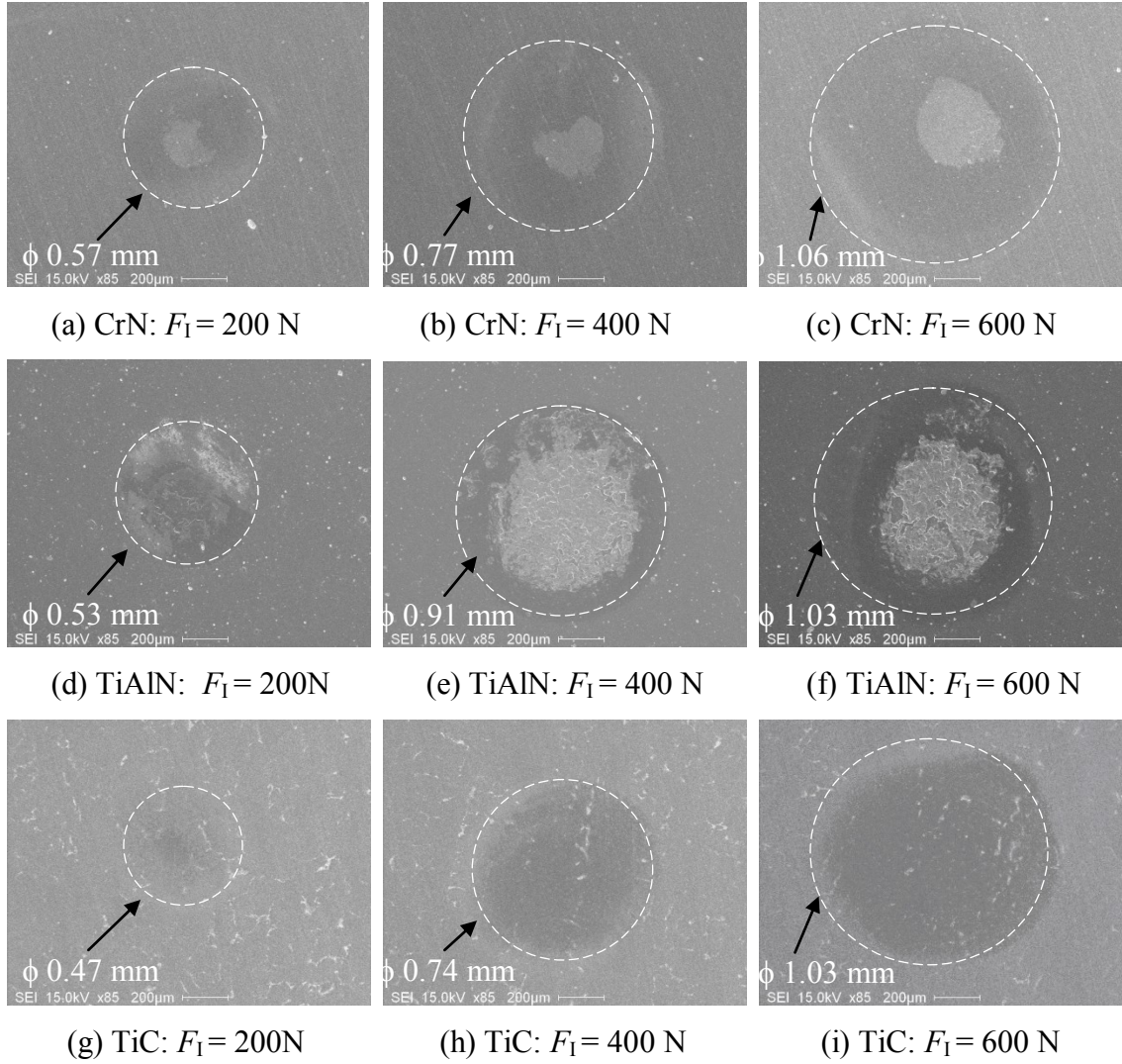


Figure 5.4 SEM images of coatings after 10,000 impact cycles. (a-c) CrN; (d-f) TiAlN; (g-i) TiC.

Fig. 5.4 gives the overall results of the 10,000 impact cycles. After 10,000 impact cycles, the PVD CrN coating showed the strongest resistance to impact, except a few inherent defects (bright dots in Fig. 5.5a) existed in the craters. A relatively bright area (Fig. 5.5c and Fig. 5.5e) appeared in all craters of the CrN coating after tested at the three loads. Fig. 5.5d and Fig. 5.5f show the compositions of the bright area and surrounding

dark area on the crater after a 600 N impact test. The EDX analysis shows the existence of Fe in the bright area. However, the surface topography and the texture of the bright area and surrounding area were consistent. It suggested that the Fe was transferred from the steel ball during impacting and diffused into the CrN coating probably due to a thermal effect induced by impact energy lost. This kind of material transfer was not a real failure and would not be destructive because the surface topography of the coating was still intact. The bright area increased with the increase of the impact force due to the increased contact area. The O element could be found on both the bright and dark areas.

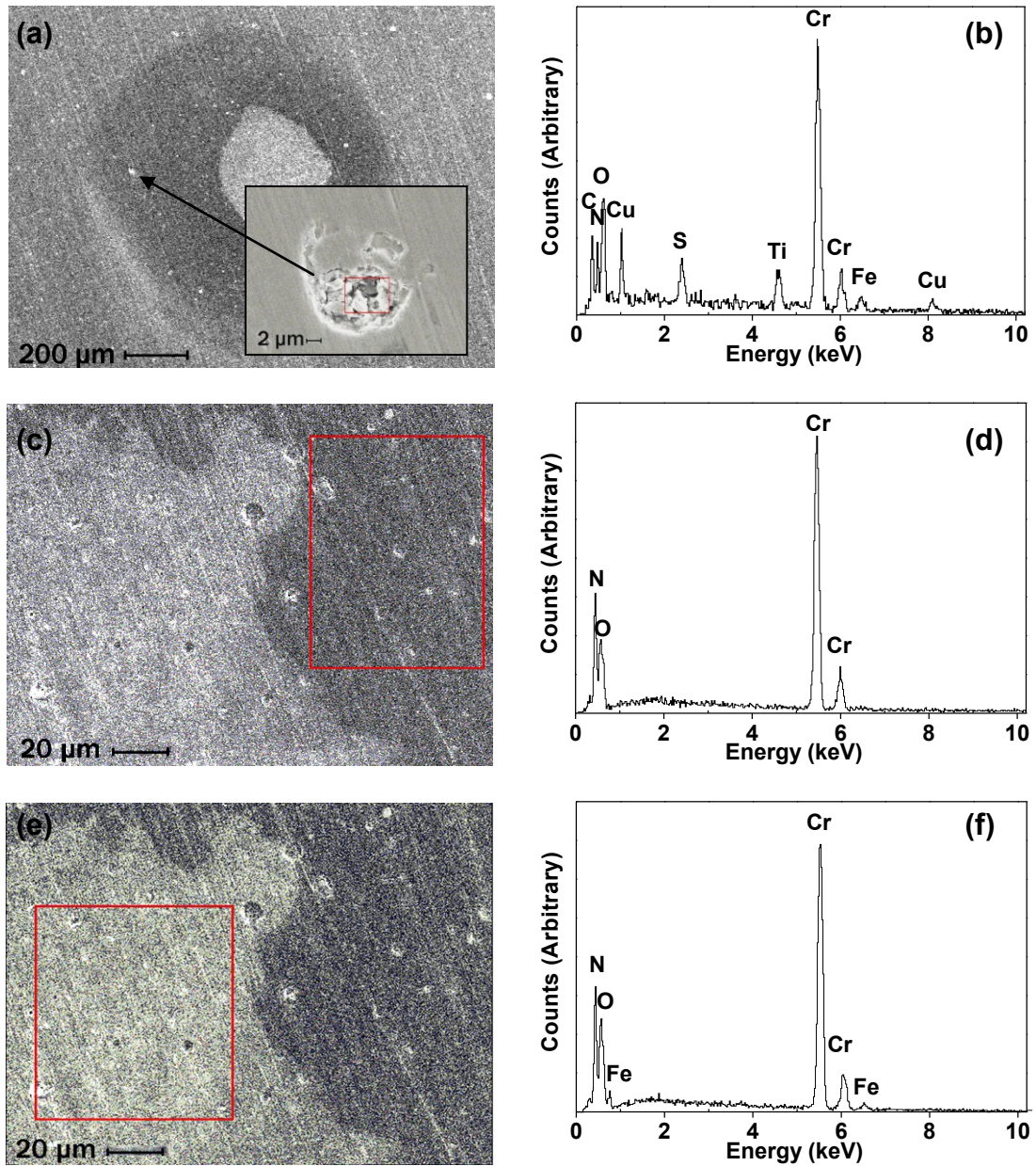


Figure 5.5 SEM images and EDX spectra showing the crater of the CrN coating tested under a 600 N impact force. (a) Inherent chipping; (b) EDX spectrum of the inherent chipping containing impurities; (c) the dark area surrounding the bright area at the center of the crater; (d) EDX spectrum of the marked dark area in (c); (e) the bright area; (f) EDX spectrum of the marked bright area in (e) showing the existence of Fe.

The resistance of the PVD TiAlN coating to impacting was found the least. Cohesive failures such as chipping at the coating surface, adhesive failures such as peeling between the coating and substrate, or materials transfer could all be found after the test under a 200 N impact load. Fig. 5.6a and Fig. 5.6b presents the materials transfer phenomenon that iron (Fe) from the steel ball and oxygen (O) were detected by EDX. This material transferring was dissimilar to the phenomenon occurred on the CrN coating. For the case of TiAlN coating, a material mixture from the coating and the steel ball was accumulated to protrude from the coating surface to form a new layer. The new layer might cause concentration of stresses during impacting and result in the enhanced adhesive wear, therefore, this kind of material transfer was considered as a failure. Peelings were observed in Fig. 5.6c where the substrate exposed without coating as evidenced by a high Fe content in the EDX spectrum (Fig. 5.6d). Chippings also occurred without penetrating the whole coating (Fig. 5.6e, 5.6f).

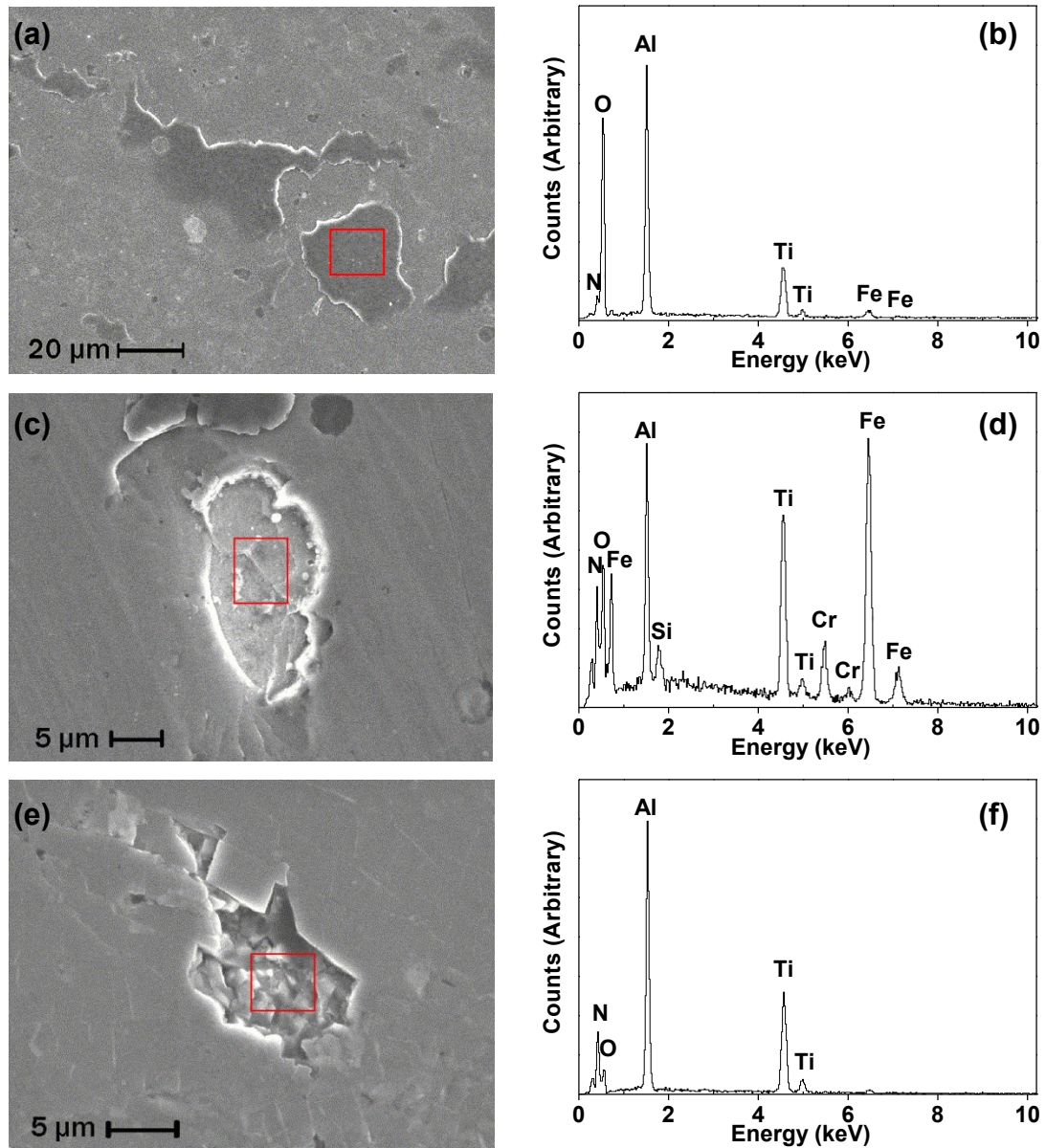


Figure 5.6 SEM images and EDX spectra showing failures of the TiAlN coating under a 200 N impact force. (a) Material transfer; (b) EDX showing Fe from the steel ball; (c) peeling; (d) EDX showing Fe from the substrate; (e) chipping; (f) EDX showing TiAlN coating still existed.

Failures were severer when impact forces on the TiAlN coating increased to 400 N and 600 N. Other than the materials transfer and the peeling/chipping around the edge of the crater, a cohesive and adhesive failure zones with fatigue cracks (Fig. 5.7a) could be found in the crater central and intermediate areas. The EDX spectrum proved that the coating in the zone was totally damaged and the substrate was exposed. The thickest and hardest TiC coating showed a good resistance to impact. Cohesive chippings were only observed in the TiC coatings under 600 N impact force (Fig. 5.7b).

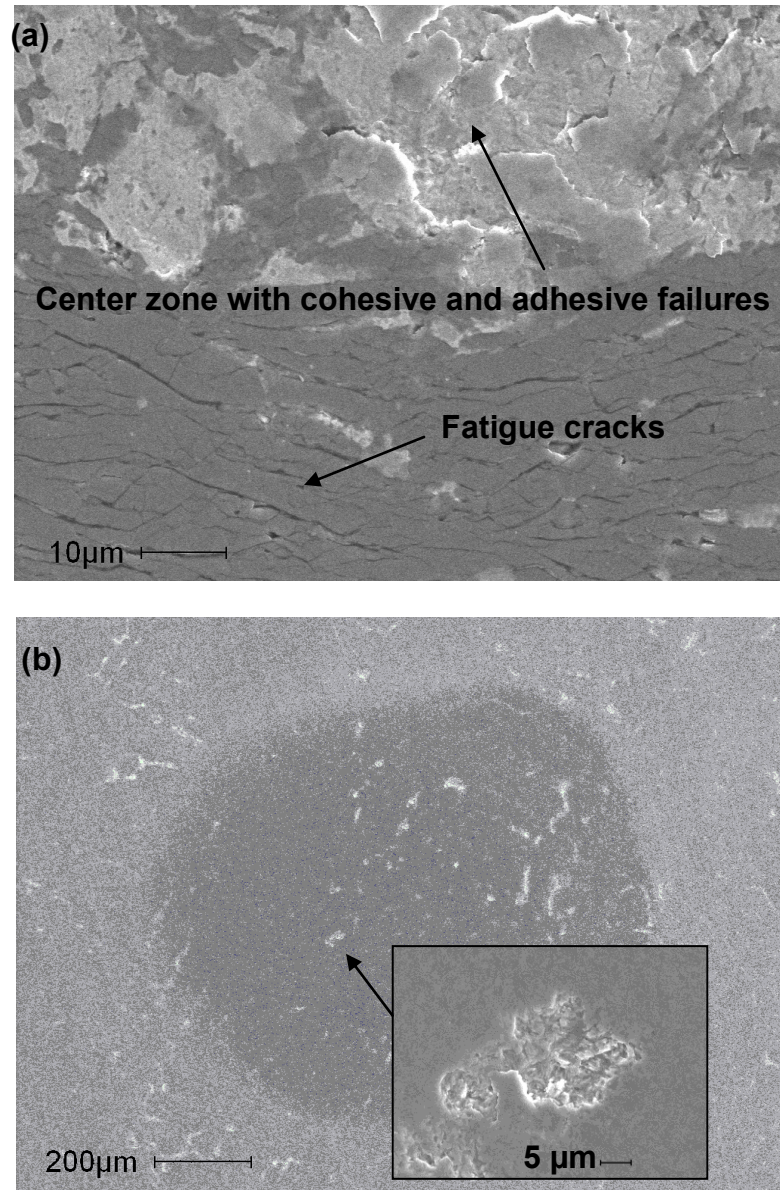


Figure 5.7 SEM images showing failures of the TiAlN and TiC coatings. (a) The center zone of cohesive and adhesive failures and fatigue cracks of the TiAlN coating under a 400 N impact force; (b) chipping in the TiC coating under a 600 N impact force.

Based on the test results presented above, the PVD CrN coating was found to be the best in this study. The CVD TiC coating also performed well during the impact tests.

The TiAlN coating was not as good as expected in resistance to the high impact forces under the tested conditions, although it may be excellent for applications in such as high temperature and high speed cuttings.

4. CONCLUSIONS

Ball-on-plate impact fatigue tests on CrN, TiAlN and TiC coatings were done at different combinations of impact/pressing forces. The impact forces were varied by changing impact velocities through adjusting the distances between the impact ball and the plate surface under the same 400 N driving force, and three combinations of impact/pressing forces were generated, i.e., 200 N/400 N, 400 N/400 N and 600 N/400 N. As expected, increased impact forces would cause the increase in deformation sizes of the craters, severity of cohesive and adhesive failures as well as of fatigue cracks. For the coatings with a less degree of failure, the crater sizes were less dependent on the hardness and thickness of coatings but more dependent on the property of the substrate. The crater sizes almost linearly increased with the impact forces. For the coating (i.e., TiAlN) with a large degree of failure, abrasive wear was also the factor influenced the crater size. The CrN coating had the best performance during all the impact tests. Although it had the deformation crater size similar to other coatings, no obvious failure was observed. The TiC coating was also very good, and chipping due to cohesive failure only occurred at the highest impact force (i.e., the 600N impact force). However, cohesive (chipping) and adhesive (peeling) failures as well as fatigue cracks could be observed on the thin TiAlN coating. The experimental results showed that the impact tester could be used to study

fatigue cracking as well as peeling and chipping failure behaviour of hard coatings under high cyclic impact loading conditions.

REFERENCES

- [1] R. Bunshah, C. Weissmantel, Handbook of hard coatings, William Andrew Publishing, Norwich, NY (US), 2000.
- [2] H. Holleck, V. Schier, *Multilayer PVD coatings for wear protection*, Surface and Coatings Technology, 1995. **76-77**: p. 328-336.
- [3] J. Vetter, R. Knaup, H. Dwuletzki, E. Schneider, S. Vogler, *Hard coatings for lubrication reduction in metal forming*, 23rd International Conference on Metallurgical Coatings and Thin Films, 1996. **86-87**: p. 739-747.
- [4] X.T. Zeng, S. Zhang, T. Muramatsu, *Comparison of Three Advanced Hard Coatings for Stamping Applications*, Surface and Coatings Technology, 2000. **127**: p. 38-42.
- [5] X. Nie, P. Zhang, A.M. Weiner, Y.-T. Cheng, Nanoscale Wear and Machining Behavior of Nanolayer Interfaces, Nano Letters, 2005. 5 (2005): p. 1992-1996.
- [6] L. Wang, X. Nie, J. Housden, E. Spain, J.C. Jiang, E.I. Meletis, A. Leyland, A. Matthews, *Material transfer phenomena and failure mechanisms of a nanostructured Cr-Al-N coating in laboratory wear tests and an industrial punch tool application*, Surface and Coatings Technology, 2008. **203**: p. 816-821.
- [7] A.A. Voevodin, J.M. Schneider, C. Rebholz and A. Matthews, *Multilayer Composite Ceramicmetal-DLC Coatings for Sliding Wear Applications*, Tribology International, 1996. **29**: p. 559-570.
- [8] C. Subramanian, K.N. Strafford, *Review of multicomponent and multilayer coatings for tribological applications*, Wear, 1993. **165**: p. 85-95.

- [9] P.R. Chalker, S.J. Bull, D.S. Rickerby, *A review of the methods for the evaluation of coating substrate adhesion*, Materials Science and Engineering A, 1991. **A140**: p. 583-592.
- [10] J. Valli, *A Review of Adhesion Test Methods for Thin Hard Coatings*, Journal of Vacuum Science & Technology A, 1986. **4**: p. 3007-3014.
- [11] O. Knotek, B. Bosserhoff, A. Schrey, T. Leyendecker, O. Lemmer, S. Esser, *A new technique for testing the impact load of thin films: the coating impact test*, Surface and Coatings Technology, 1992. **54-55**: p. 102-107.
- [12] X. Nie, A. Leyland, H.W. Song, A.L. Yerokhin, S.J. Dowey, A. Matthews, *Thickness effects on the mechanical properties of micro-arc discharge oxide coatings on aluminium alloys*, Surface and Coatings Technology, 1999. **116**: p. 1055–1060.
- [13] R. Bantle, A. Matthews, *Investigation into the impact wear behaviour of ceramic coatings*, Surface and Coatings Technology, 1995. **74-75**: p. 857-868.
- [14] K.D. Bouzakis, N. Vidakis, T. Leyendecker, O. Lemmer, H.G. Fuss, G. Erkens, *Determination of the fatigue behaviour of thin hard **coatings** using the impact test and a FEM simulation*, Surface and Coatings Technology, 1996. **86-87**: p. 549-556.
- [15] K.D. Bouzakis, N. Vidakis, T. Leyendecker, G. Erkens, R. Wenke, *Determination of the fatigue properties of multilayer PVD coatings on various substrates based on the impact test and its FEM simulation*, Thin Solid Films, 1997. **308-309**: p. 315-322.

CHAPTER 6

CHARACTERIZATION OF THE FAILURE MECHANISMS OF THIN HARD COATINGS USING THE INCLINED IMPACT- SLIDING TEST

1. INTRODUCTION

Impact fatigue testing methodology has been developed and used to study coating failure behavior under vertical impacting motions in Chapter 4. Experiments and FEM analyses of this vertical ball-on-plate impact fatigue tests have been performed on six samples. All six coated samples showed good adhesion to their substrate. However, depending on coating materials and even the same coating materials but from different coating suppliers, the coatings performed differently in severity of cohesive chipping, adhesive peeling, ball material transfer, and fatigue cracking.

Since stamping likely includes not only impacting but also sliding motions, an Extended Impact Fatigue Test (EIFT) was used to simulate the impact-sliding wear conditions in Phase II of the project. In the period of Phase II, six coatings provided from A/S P were tested. Steel balls were used as the impacting and sliding counter materials. The impact-sliding wear tracks on the coatings were studied using Scanning Electron Microscopy (SEM) and Energy Dispersive X-ray analysis (EDX). The performance of the coatings was ranked according to their failure severity. Also, three selected coatings were dissected using Electrical Discharging Machining (EDM) wire cutting to show the coating failure behavior at the cross sections along the impact-sliding tracks. Failure mechanisms of the three coatings were then discussed. This report is to present the

research results obtained in Phase II, the second part of the project *Coating Impact Fatigue Test* funded by Auto/Steel Partnership through USAMP/DOE.

2. EXPERIMENTAL DETAILS

A schematic drawing of the inclined impact-sliding tester used in Phase II of this project is shown in Fig. 6.1. During the inclined impact-sliding fatigue test, a hard ball (the impact body) is mounted on the shaft of a double-way air cylinder with the piston driven by compressed air producing vertical oscillatory motions. The sample is set on an inclined rotary sample holder which can return its position by a spring. An OMEGA LCKD-500 load cell is placed on the sample holder to record the normal force on the sample surface during the impact-sliding movement. To reduce friction, a thin layer of lubricant is applied on the load cell surface. The desired normal impact and pressing forces are obtained by adjusting the pre-strain of the spring and the pressure in the air cylinder. For all the tests in Phase II, the impact and pressing loads were set as 80 N and 200 N, respectively. After the impact/pressing forces are measured and recorded, the load cell is removed and coated samples are placed on the sample holder for impact tests. The distance d between ball and the sample needs to be the same as the previous distance between the load cell and the ball. In Phase II, each coated sample was scheduled to be impacted 1500 cycles or 10000 cycles. After the test, a crater head and a sliding wear track appeared on the coating surface as illustrated in Fig 6.1.

3. RESULTS AND DISCUSSION

The samples to be tested in Phase II are from the same suppliers as in Phase I. The samples include:

- PVD coatings
 - A_TiAlN
 - B_TiAlN
 - A_CrN
 - B_CrN
- CVD coatings
 - B_TiC
 - C_TiC

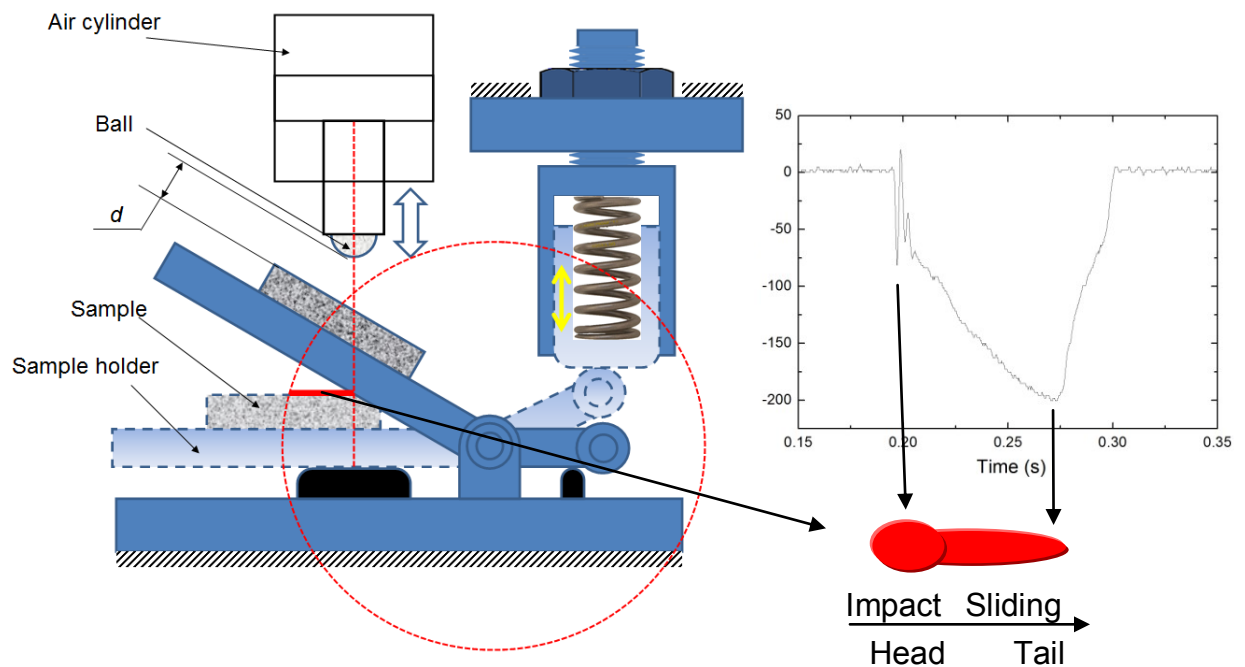


Figure 6.1 Schematic of an inclined impact-sliding tester. To the right, a typical normal force vs. time curve during an impact-sliding cycle.

A, B and C denotes the three (3) different coating suppliers. The research work and experimental results obtained from the Plasma Surface Engineering and Tribology Lab at the University of Windsor are described as follows:

3.1 Nanoindentation tests

Nanoindentation (Hysitron) was used to measure the mechanical properties (hardness and elastic modulus) of each coating. Hardness and elastic modulus with comparison between Phase I and Phase II are presented in Fig. 6.2 and Fig. 6.3, respectively. Big differences in hardness and elastic modulus between Phase I and Phase II appear in the B_TiAlN coatings. Similar to the cases in Phase I, hardness and elastic modulus of coatings from different suppliers are quite different. A_TiAlN and B_TiC coatings have the highest hardness. Again, the hardness and elastic modulus of C_TiC are low. The low hardness and elastic modulus values of C_TiC coating are likely due to the two-layer coating structure which has a softer top layer, possibly caused by the coating heat treatment.

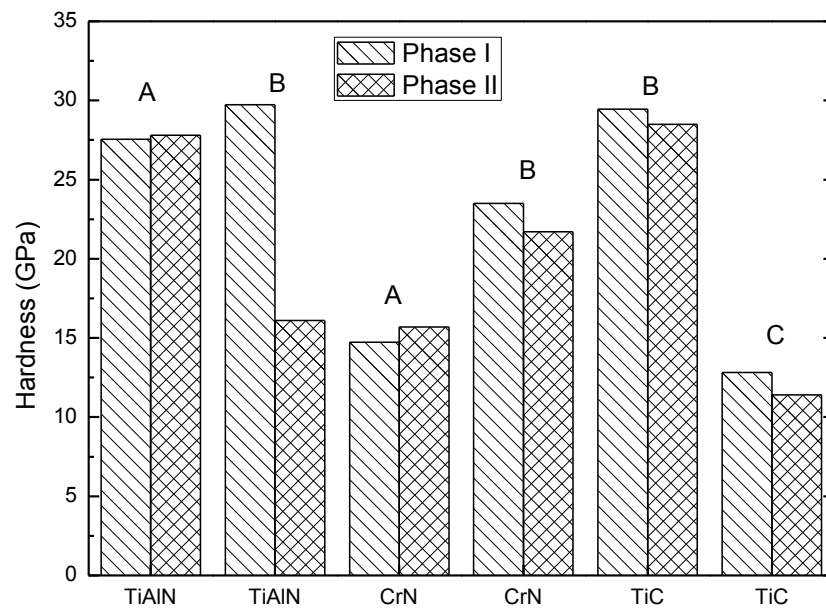


Figure 6.2 Berkovich hardness of different coatings (Phase I & II). A, B and C denotes different suppliers respectively.

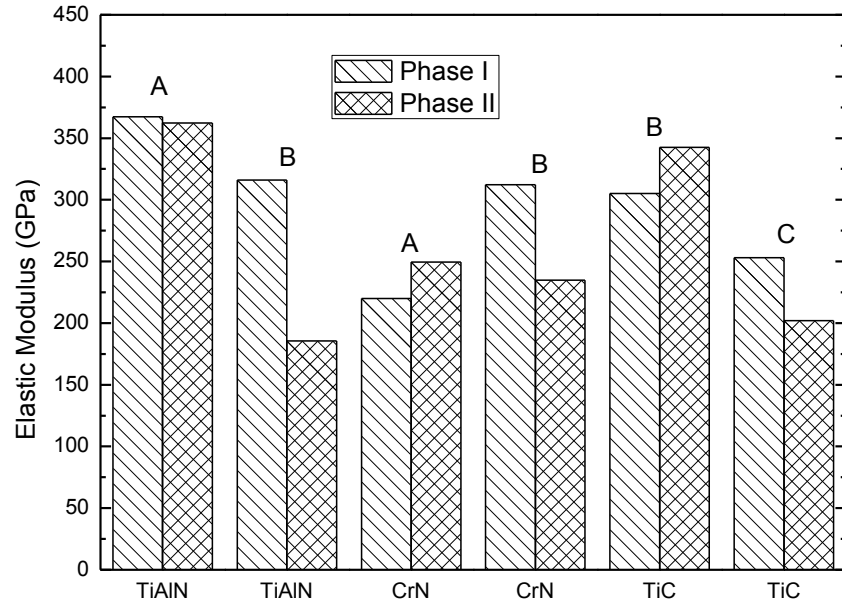


Figure 6.3 Elastic modulus of different coatings (Phase I & II) by nanoindentation.

3.2 Inclined impact fatigue test

3.2.1 Impact and pressing force loading curves

A selected test loading condition (i.e., 80 N impact force and 200 N pressing force) and hardened SAE 51000 steel balls (10mm in diameter) were used for the inclined impact-sliding fatigue tests. Coating failure mechanisms were investigated for the different coatings that were tested at the same conditions above. The impact frequency, f , and ball to sample distance, d , were set at 5 Hz and 1 mm, respectively, in all tests and the static air pressure, P , was set around 0.11 MPa. Thus, the maximum impact force was 80 N and pressing forces 200 N, determined by an OMEGA LCKD-500 load cell measurement. The impact and pressing force loading curves were recorded by a KYOWA PCD-300A Sensor Interface System. A typical load cycle is presented in Fig. 6.4.

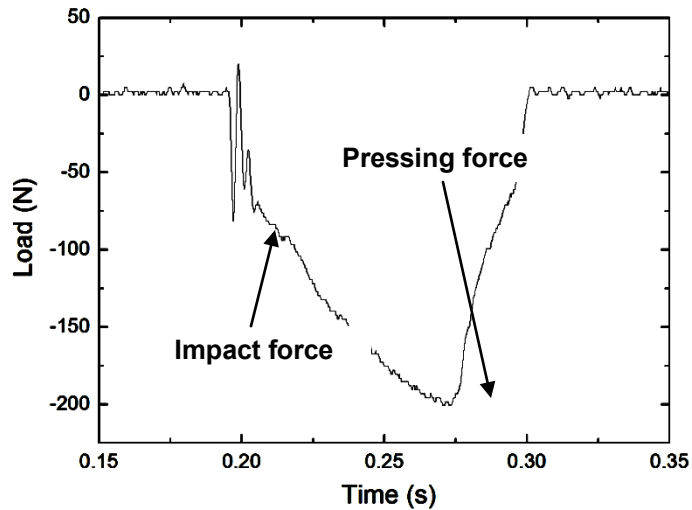


Figure 6.4 A typical load cycle at 5 Hz impact frequency.

3.2.2 Typical Failures

In Phase II, there were still 4 primary failure mechanisms as in Phase I, namely,

- cohesive failures (mainly chipping),
- adhesive failures (mainly peeling),
- material transfer, and
- fatigue cracks.

A schematic of these failures is given in Fig. 6.5. The characterization of failure modes was based on the EDX analysis method as used in Phase I. All the coating failure mechanisms mentioned above could be observed in most cases. Fatigue cracks may be the main reason for the coatings to initiate cohesive and adhesive failures. For example, fatigue cracks may lead to chipping (cohesive failure) and peeling (adhesive failure). Material transfer may be more severe at the spot where the surface became rough due to other failures. The locations where cohesive and adhesive failures occur may also in

return act as initiation sites of fatigue cracking and as a result, the chipping and peeling areas increased at a fast path.

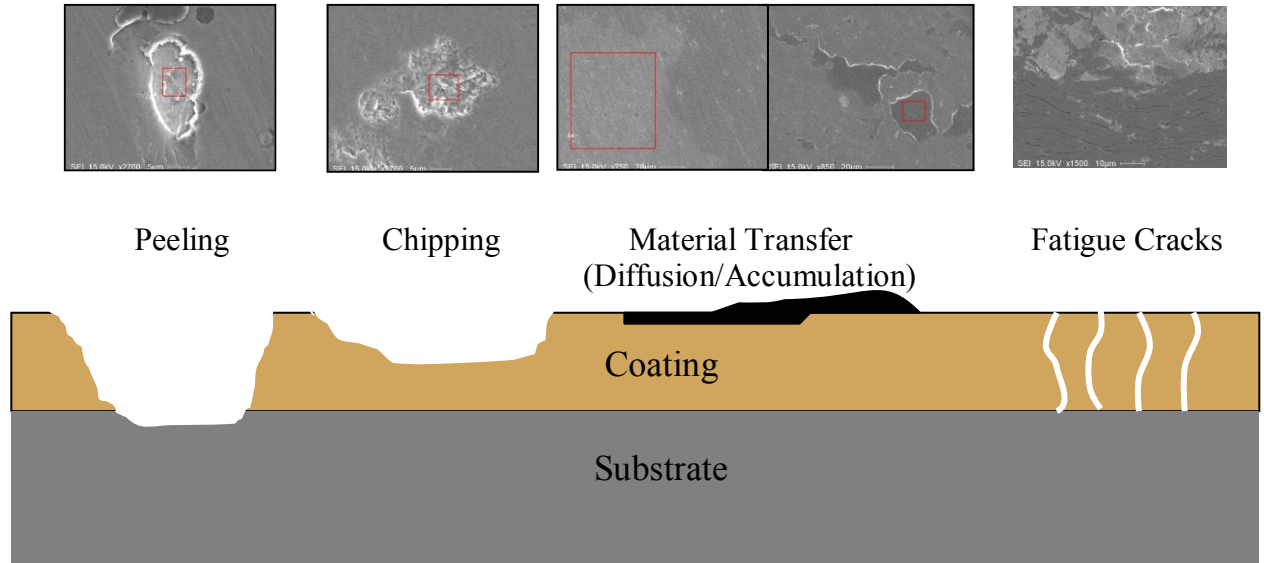


Figure 6.5 SEM images and Illustration of failure modes.

3.2.3 Experimental results

Samples were subjected to impact testing under unlubricated conditions. The impact balls were changed after each sample was tested. After the tests, the samples were observed and analyzed using a SEM with EDX to investigate coating failure behavior. Therein, the test results were summarized after the following test conditions:

- Tests with Steel Balls and 1500 Cycles
- Tests with Steel Balls and 10000 Cycles

3.2.3.1 Hardened SAE 52100 steel ball, 1500 cycles

The A_TiAlN coating displayed all four primary failure mechanisms as shown in Fig. 6.6. Peeling with surrounding chipping and fatigue cracks were found at the impact-induced crater. The TiAlN coating materials still existed at the center of the crater with Fe

transferred from the steel ball. Fatigue cracks appeared at the boundary of the crater and along most of the sliding track as shown in Fig. 6.6b and Fig. 6.6c.

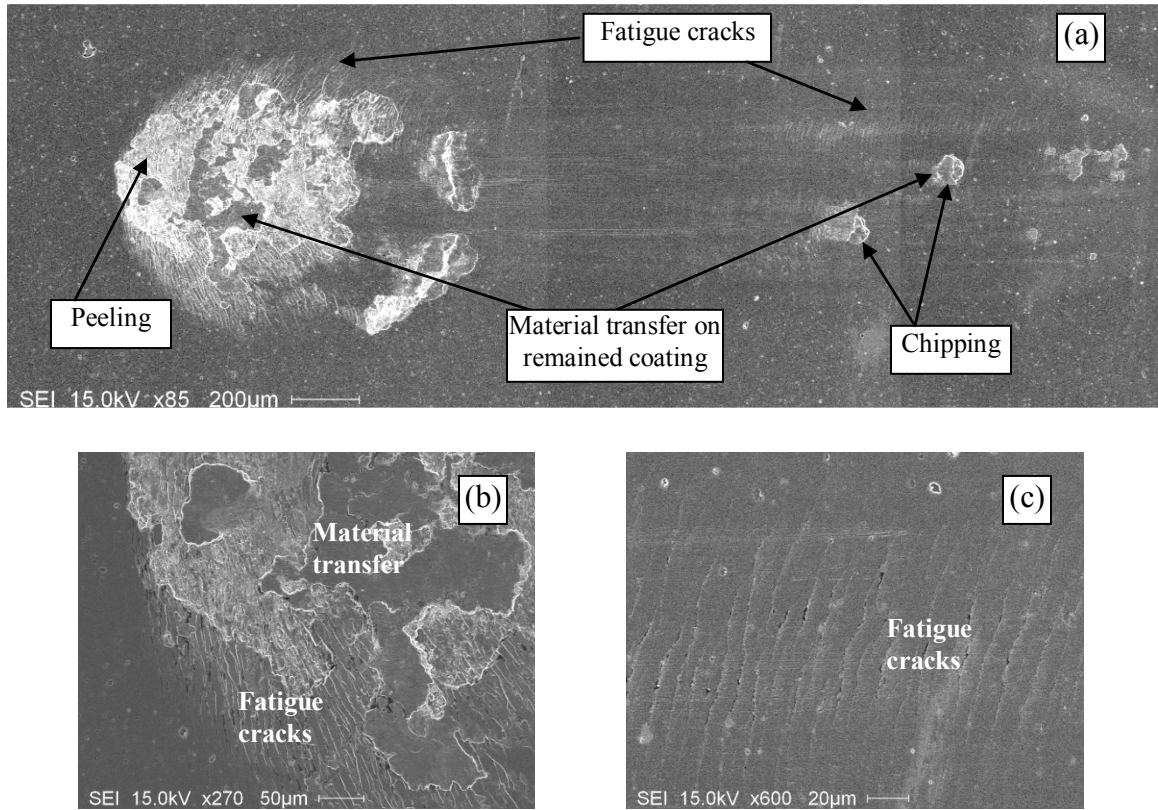


Figure 6.6 SEM images of the impact-sliding track of A_TiAlN after 1500 cycles. (a) Overview; (b) fatigue cracks at the edge of the crater; (c) fatigue cracks in the sliding track.

Although the hardness and elastic modulus of the B_TiAlN sample were lower in Phase II than in Phase I, B_TiAlN acted similarly to its counterpart in Phase I which showed low resistance to impact and sliding of steel ball (Fig. 6.7) compared with A_TiAlN. Cohesive failure zones formed at the center of the crater and along the sliding track. EDX analysis also showed the material transfer from the steel ball occurred (dark area in the impact-sliding track). Fatigue cracks and chippings were found around the track (Figures 7b and 7c).

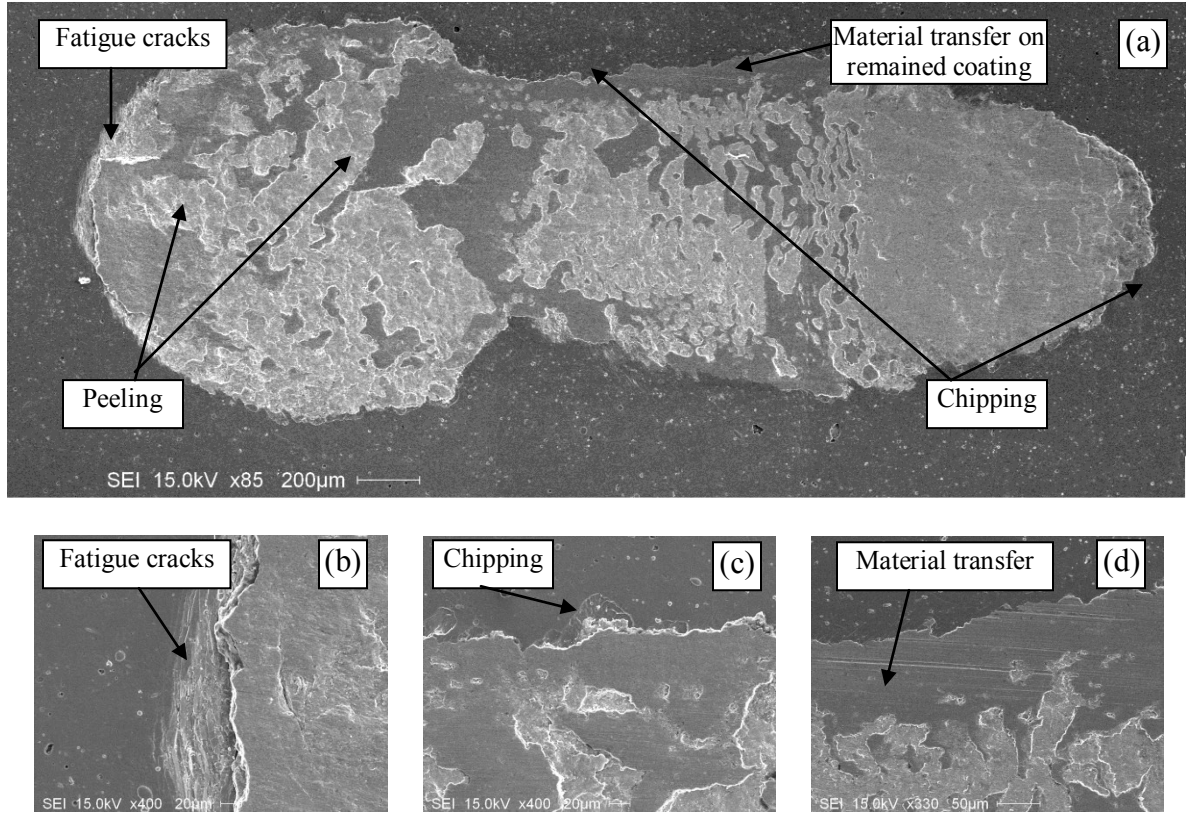


Figure 6.7 SEM images of the impact-sliding track of B-TiAlN after 1500 cycles. (a) Overview; (b) local view showing fatigue cracks; (c) chipping; (d) material transfer.

Two CrN samples tested after 1500 cycles are presented in Fig. 6.8 and Fig. 6.9. The coating in the crater of the A-CrN disappeared and the substrate was exposed (Fig. 6.8a). Fatigue cracks were found around the head of the crater. The A-CrN coating material still remained in the area between the crater and the tail of the track with some Fe transferred from the steel ball. Fig. 6.8b shows fatigue cracks around the failure area of the crater head, and Fig. 6.8c illustrates chipping and peeling failures at the tail area of the sliding track.

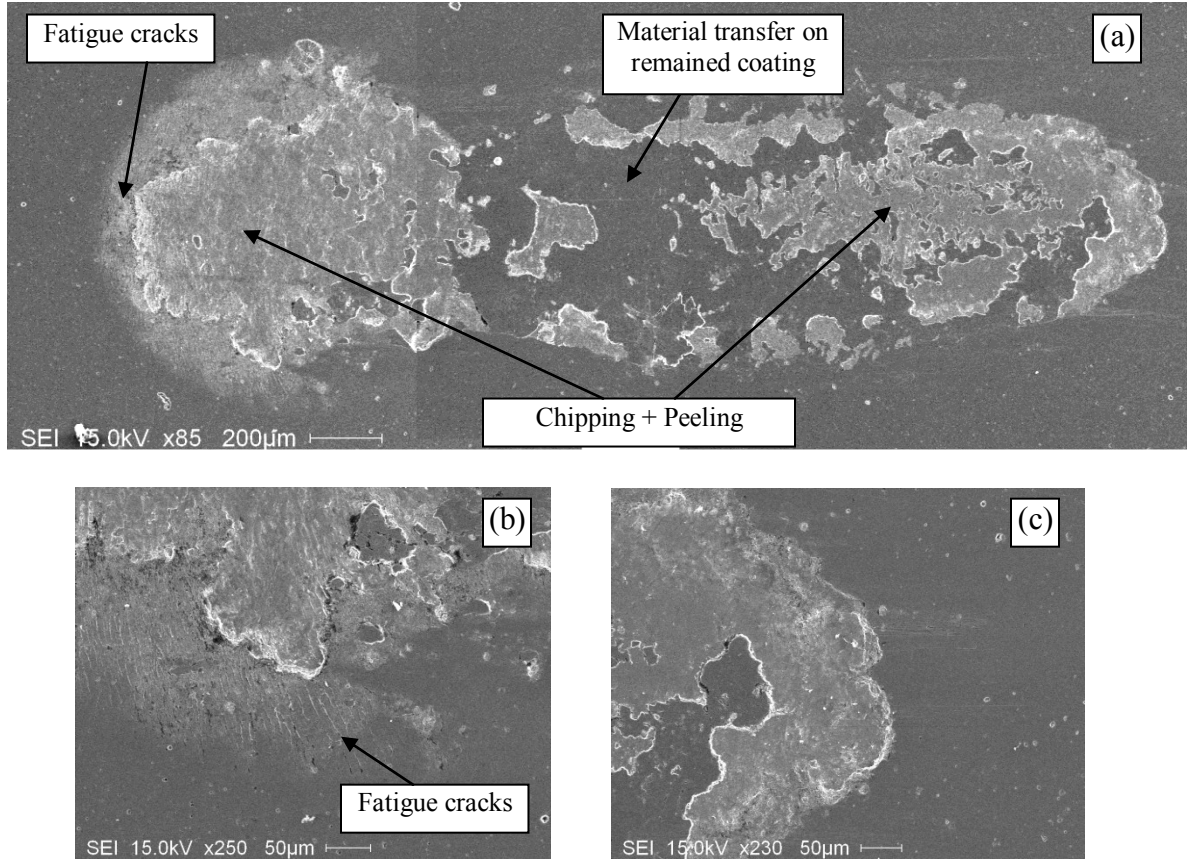


Figure 6.8 SEM images of the impact-sliding track of A_CrN after 1500 cycles. (a) Overview; (b) local view showing fatigue cracks; (c) tail of the track.

B_CrN performed better than A_CrN in the steel ball impact-sliding test. The dark areas in the crater shown in Fig. 6.9a contained Fe transferred from the steel ball during the impact. Fatigue cracks and chipping were found at the top head of the crater (Fig. 6.9b) and also at the middle head of the crater (Fig. 6.9c). Although most coating materials remained in a good shape on the sliding track, it was also found that chipping occurred at both the tail and the track (Fig. 6.9d). Material transfer from the steel ball also appeared on the surface of the remained coating in the wear track.

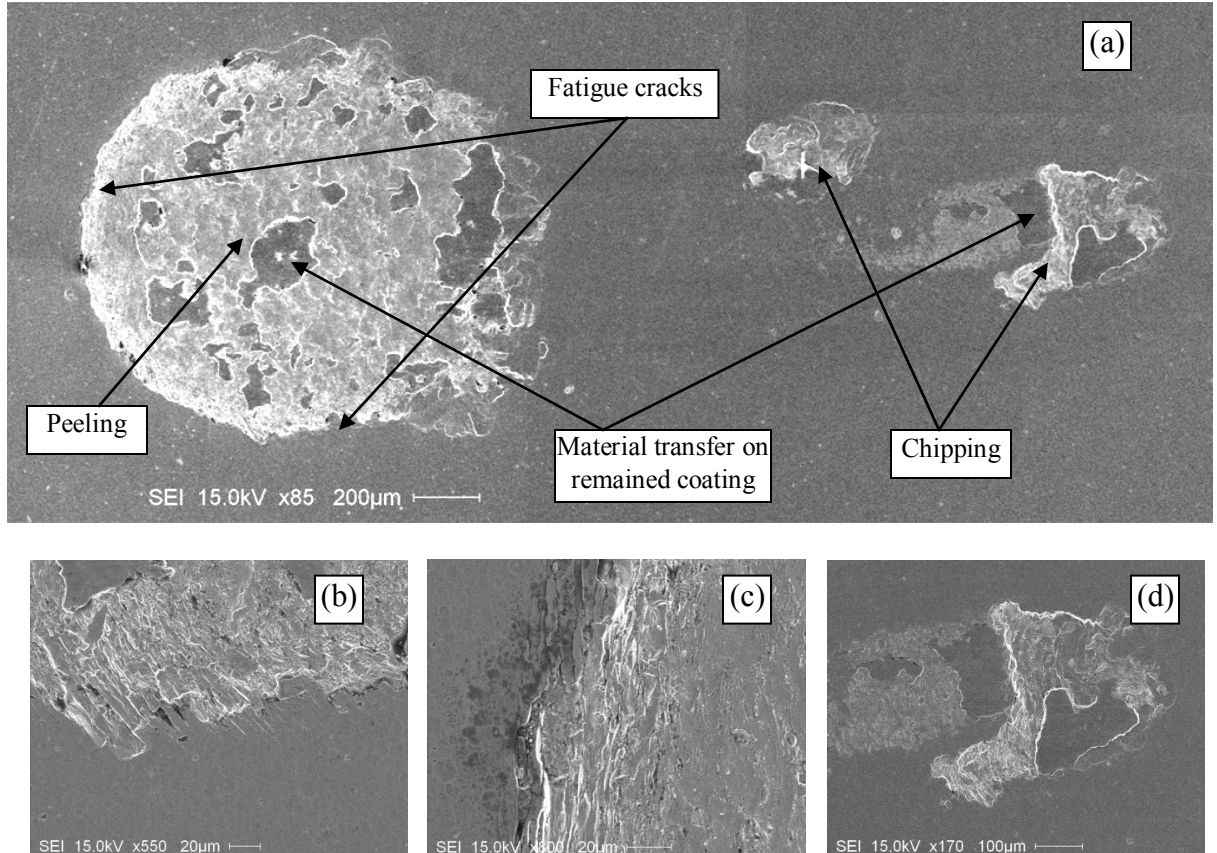


Figure 6.9 SEM images of the impact-sliding track of B_CrN after 1500 cycles. (a) Overview; (b) local view showing fatigue cracks and peeling; (c) fatigue cracks and chipping; (d) chipping.

SEM images of TiC samples tested after 1500 cycles are shown in Fig. 6.10 and Fig. 6.11. B_TiC performed well like its counterpart in Phase I. Only material transfer and small chippings were found after the test of 1500 cycles (Fig. 6.10). Fig. 6.11 shows the impact-sliding track of the C_TiC coating with occurrence of localized peeling, chipping, material transferring and fatigue cracking. Material transfer occurred on the remained TiC coating and along the track.

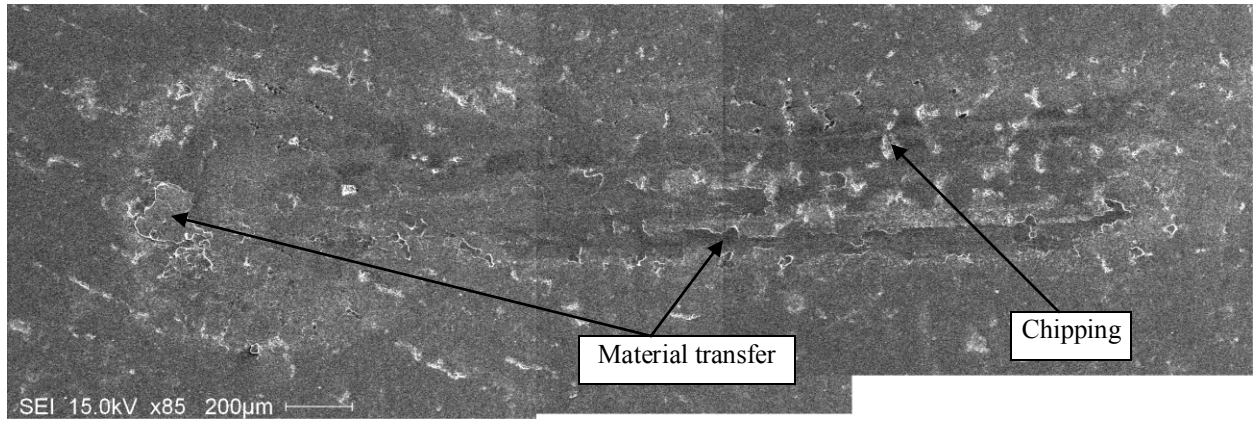


Figure 6.10 SEM image of the impact-sliding track of B-TiC after 1500 cycles

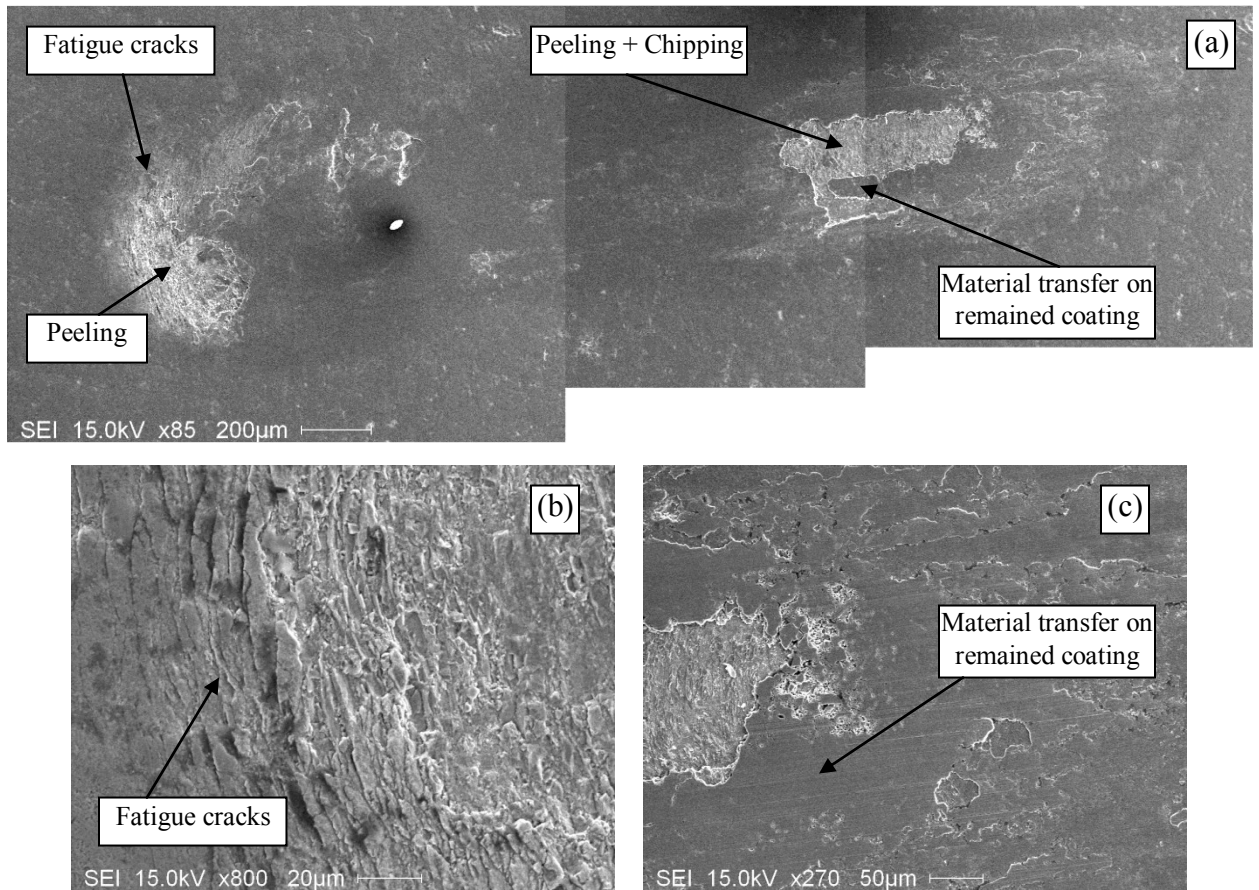


Figure 6.11 SEM images of the impact-sliding track of C-TiC after 1500 cycles. (a)

Overview; (b) local view showing fatigue cracks; (c) material transfer.

3.2.3.2 Hardened SAE 52100 steel ball, 10000 cycles

Since the B_TiC coated sample showed the least failures during the 1500 cycles' tests, an impact test up to 10000 cycles was also conducted on the sample to study the high cyclic test effect on impact fatigue of the B_TiC coating. After 10000 cycle impact test, most TiC coating materials in the crater disappeared, Fig. 6.12a. Peeling, material transfer and fatigue cracks exhibited on the impact crater area, Fig. 6.12b, while only chipping and material transfer were shown on the sliding track area, Fig. 6.12c.

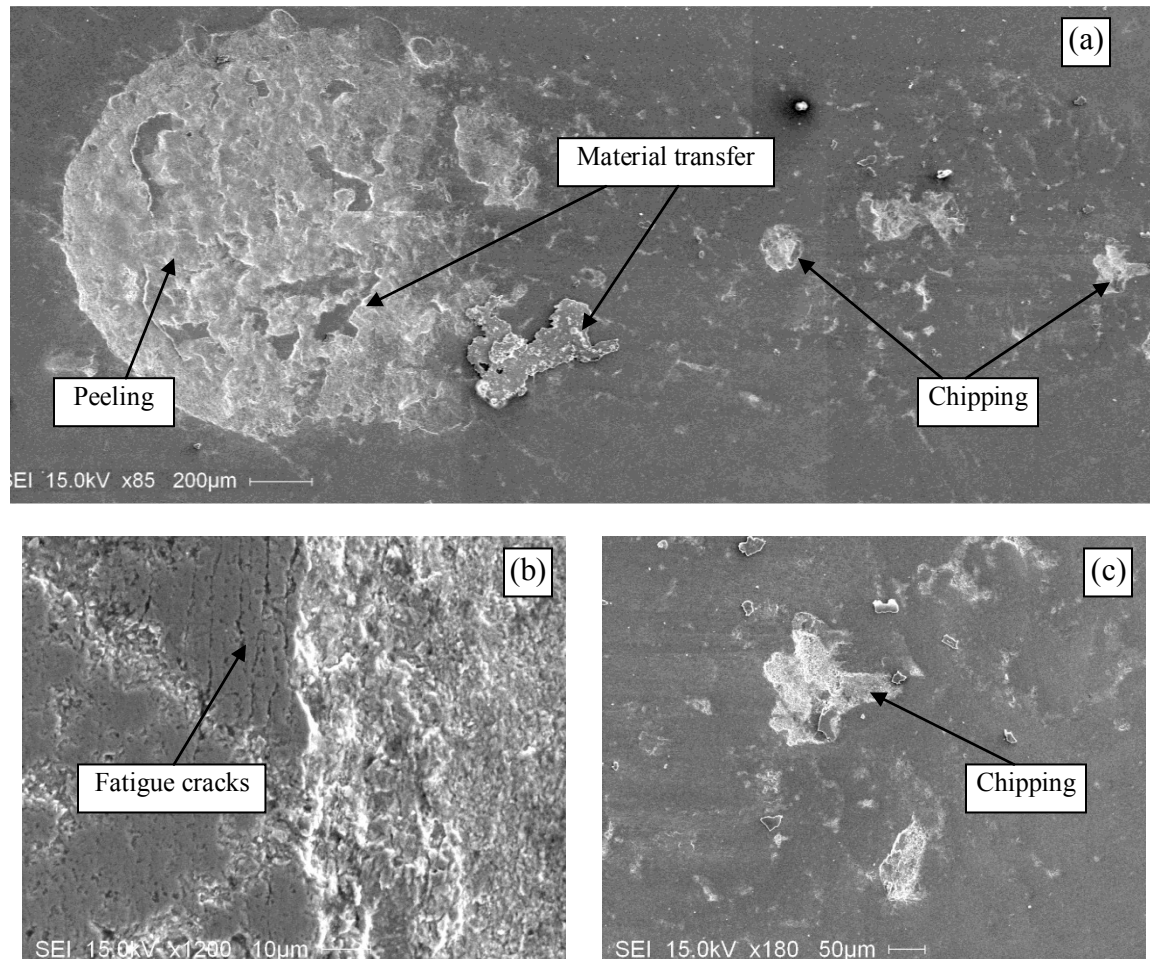


Figure 6.12 SEM images of the impact-sliding track of B_TiC after 10000 cycles. (a) Overview; (b) local view showing fatigue cracks; (c) chipping.

All impact-sliding tracks of six coatings are summarized in Fig. 6.13 which shows the failure severity of different coatings in comparison. From these images, ranking their performance in the test conditions becomes possible.

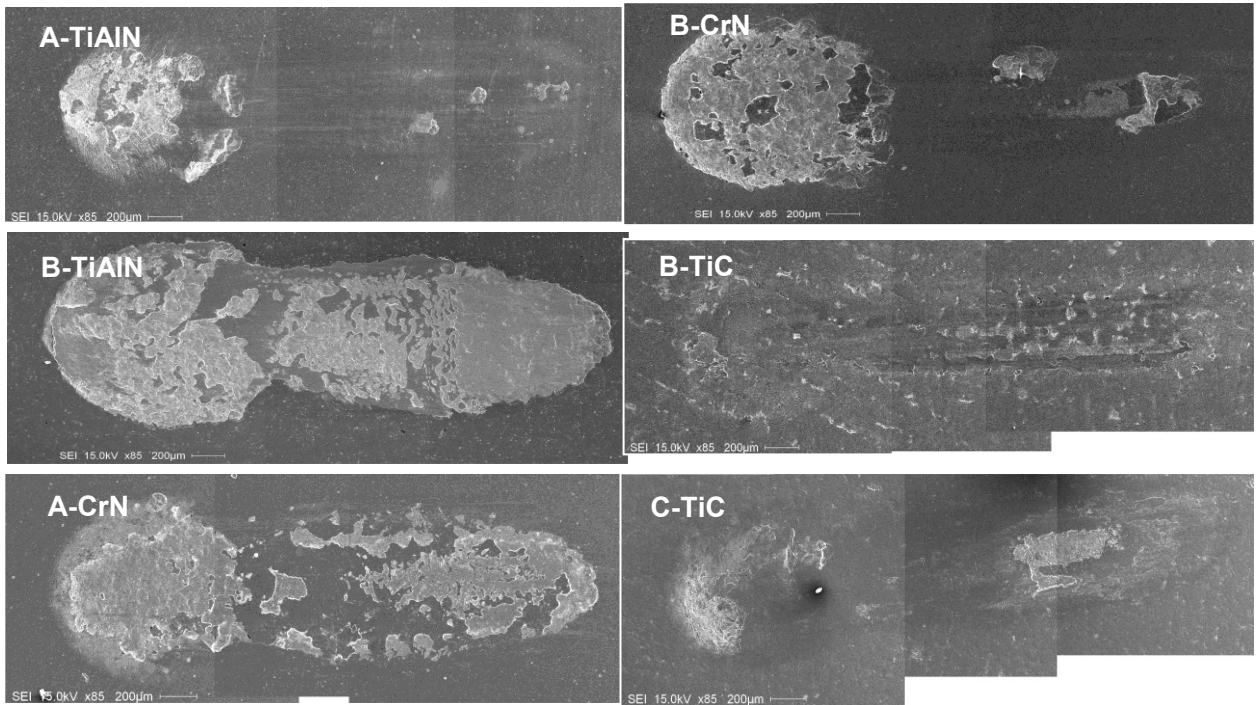


Figure 6.13 Summary of the impact-sliding tracks of six coatings after 1500 cycles. using steel balls (aspect ratio is not accurate).

3.2.3.3 Cross section of selected impact-sliding tracks

Cross sectioning was used to study the fatigue crack propagation and failure mechanisms of coatings. Although transmission electron microscopy (TEM) was originally proposed to be used in investigation of the coating failures in the thickness direction, preparations of TEM specimen from areas around the craters and along the long wear tracks of the coatings were found to be real time and money consuming. Every coating would need at least 10 TEM specimens. Each specimen can only be prepared using a Focus Ion Beam (FIB) instrument.

An alternative method was figured out at the late stage of Phase II. That is, Electrical Discharging Machining (EDM) wire cutting were used to dissect the coatings along impact-sliding wear tracks first, then SEM was used to observe the coating failure behavior along the cross sections and the top surfaces of the impact-sliding tracks. A number of SEM images were taken on the cross sections of coatings, which provided valuable information from micrometer scale up to millimetre scale, contrary to nano- and micro-scales of TEM. From the images, an overall view of impact-sliding wear track could be constructed and used to illustrate coating failures. There were three kinds of coating materials. TiAlN, CrN and TiC used in this project. For each kind of the coating materials, two coatings were deposited, from which the one with better performance was selected for dissection. Therefore, coatings of B_CrN 1500 cycles, A_TiAlN 1500 cycles and B_TiC 10000 cycles were chosen to be cut along the trail of the impact-sliding tracks using EDM wire cutting. The cross sections were then mechanical polished and observed using SEM. Cross sections of B_CrN impact-sliding track are presented and described in Fig. 6.14 and Fig. 6.15.

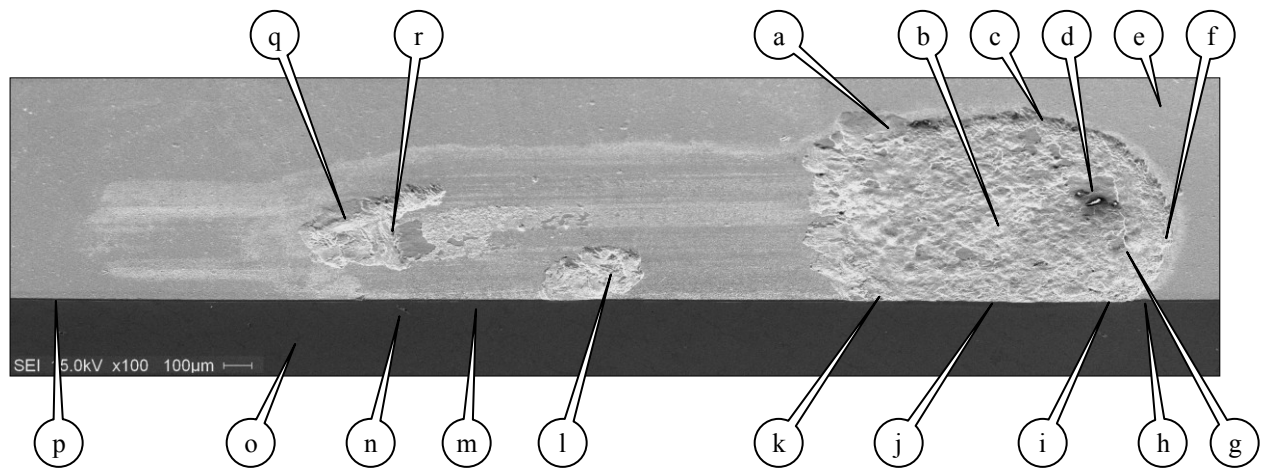
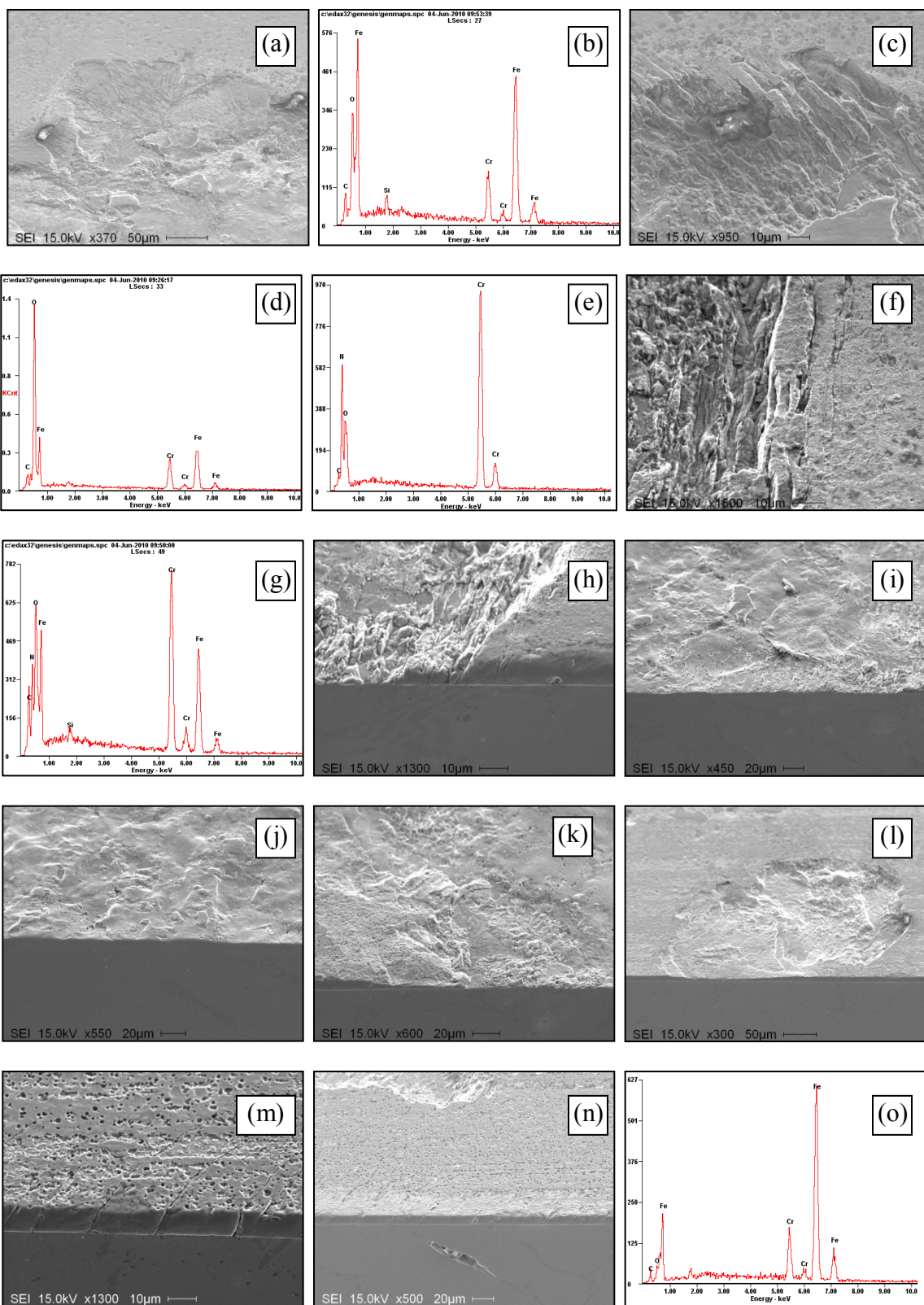


Figure 6.14 Overall SEM image of the cross section of the B_CrN impact-sliding track after 1500 cycles using a steel ball.



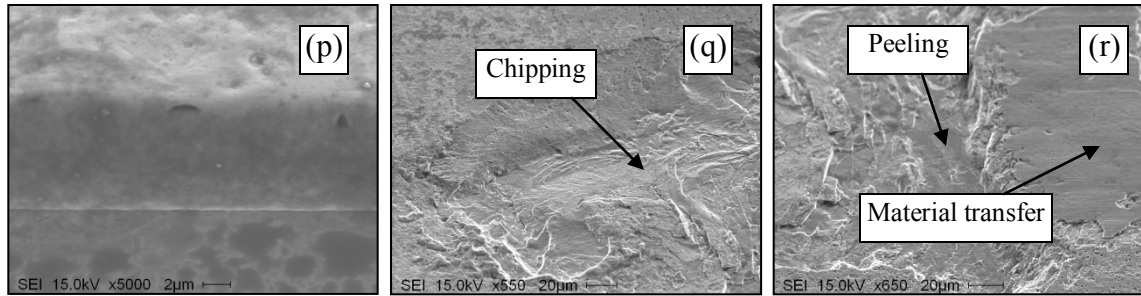


Figure 6.15 Local views of the cross section in Figure 6.14: (a) chipping at the edge of the crater; (b) EDX spectrum showing inexistence of CrN coating; (c) fatigue cracks around the crater; (d) EDX spectrum showing Fe transferred from the steel ball to the remained coating; (e) composition of the CrN coating; (f) fatigue cracks at the head of the crater; (g) EDX spectrum showing the existence of CrN coating; (h) fatigue cracks at the cross section; (i) coating remained near the head; (j) deformed substrate without coating; (k) the end of the crater; (l) chipping; (m) fatigue cracks along the impact-sliding track with a porous oxide layer which might be caused by EDM wire cutting; (n) a defect in substrate; (o) EDX spectrum showing composition of the substrate; (p) intact coating; (q) chipping at the track; (r) peeling and material transfer.

Based on the information in Fig. 6.14 and Fig. 6.15, the failure of the B₂CrN coating may follow the sequences as:

1. Fatigue cracks occurred at the center of the crater and reached the substrate during the initial stage of impact-sliding;
2. Cracked CrN coating separated from substrate piece by piece when the adjacent cracks are crossover in near horizontal directions and was brought away by abrasive wear from the center of the crater;

3. The separation of small pieces from the CrN coating propagated outward during the following cycles and formed the jagged steps around the crater except the end part of the crater;
4. At the end of the crater, shear stress began to dominate due to the sliding movement and led to both the fatigue cracks and chipping (the tail part of the crater in Fig. 6.14);
5. The shear stress continued to increase due to the increasing of the pressing load (up to 200 N) during the sliding procedure and produced more chippings along the track (Fig. 6.15l and 15q); with the increasing of the shear stress, peeling also happened (Fig. 6.15r).

However, chipping might initiate from coating defects and not always occur right at the tail of the track, where the pressing load was the maximum (200 N) but the shear stress was low due to no inclined sliding force involved in this position.

A cross section of A_TiAlN impact-sliding track was cut from the A_TiAlN coating. But this wear track was less damaged than the one shown in Fig. 6.6. This would allow us to clearly observe coating failure processes at the interface between the coating and substrate and fatigue cracks within the coating. The cross section is presented and described in Fig. 6.16 and Fig. 6.17.

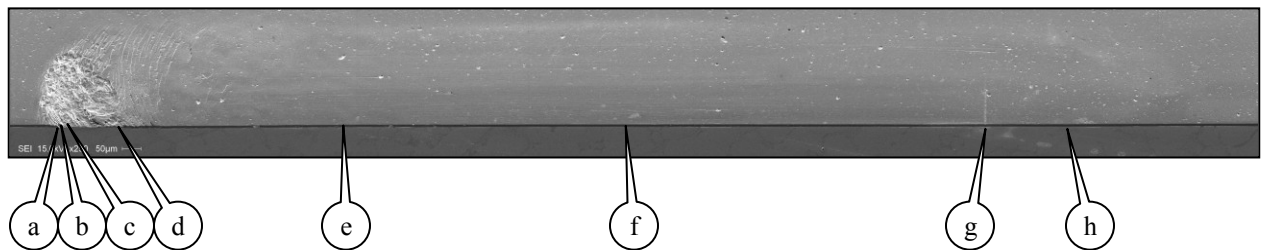


Figure 6.16 Overall SEM image of the cross section of the A_TiAlN impact-sliding track after 1500 cycles using a steel ball.

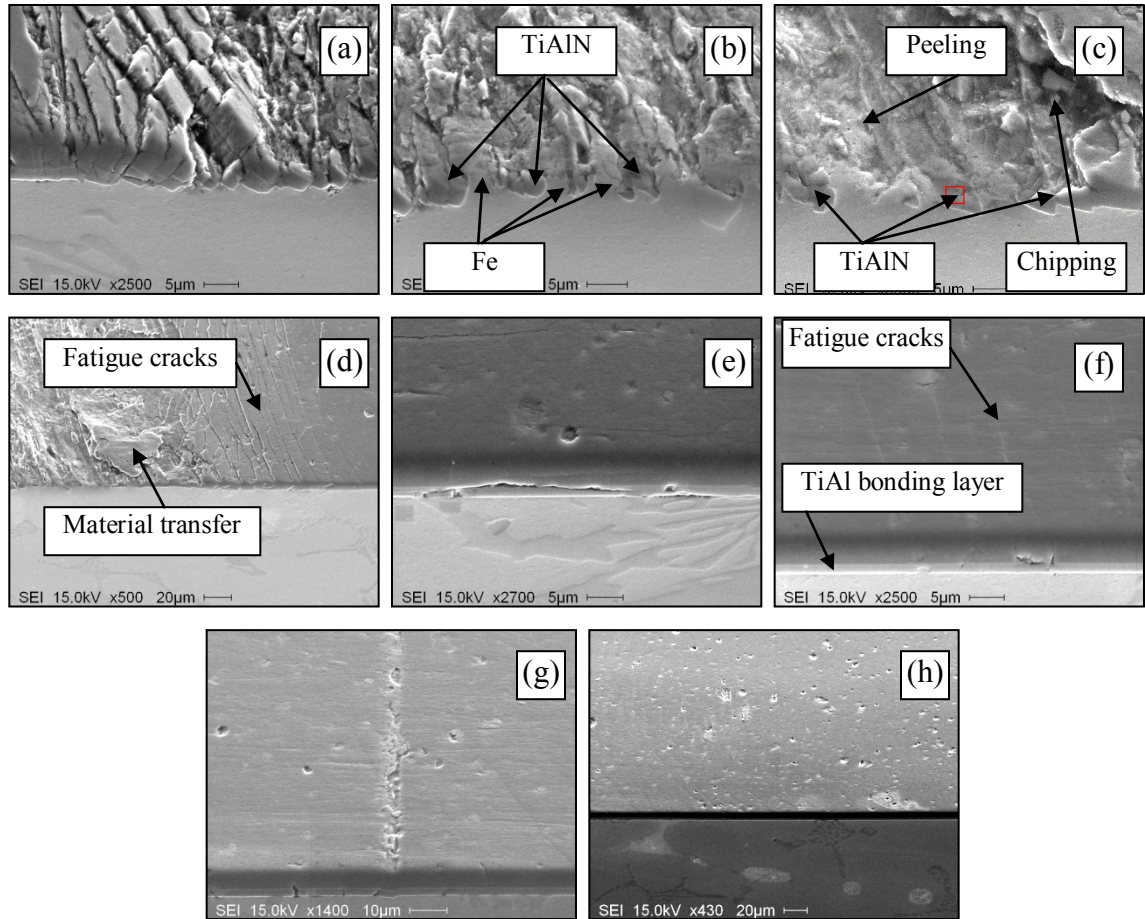


Figure 6.17 Local views of the cross section in Figure 6.16: (a) sinking of fatigue crack layers at the head of the crater; (b) interlaced TiAlN coating and Fe substrate; (c) peeling and chipping; (d) material transfer and fatigue cracks; (e) crack and debonding of TiAl interface/bonding layer, needlelike islands in substrate are Cr-rich intermetallic phase; (f) fatigue cracks at the center of the track and TiAl interface/bonding layer; (g) surface defects; (h) tail of the track showing fatigue cracks.

Like B_CrN, jagged steps were found around the crater on the A_TiAlN sample. Contrary to B_CrN, cracked A_TiAlN coating pieces sunk into the substrate segment by

segment (Fig. 6.17a) and formed interlaced mixture (Fig. 6.17b) during the impacts. Such a sinking phenomenon did not appear in B_CrN coating. Furthermore, the substrate was less exposed on A_TiAlN coating than on B_CrN coating after the tests (Fig. 6.6 vs. Fig. 6.9). These two different behaviors of the coatings may be explained by the fact that the A_TiAlN coating had high hardness and elastic modulus compared to B_CrN. For both of the coatings, fatigue cracks reached the substrate and spread along the entire sliding track. However, the fatigue cracking was more intense for A_TiAlN coating. Also, coating defects such as cracks in the coating bonding layer were usually related to the underlying Cr-rich intermetallic phase (Fig. 6.17e). This phenomenon was found in all the three coatings.

B_TiC under the 1500 cycles' impact-sliding showed no severe failures.

Therefore, the track of B_TiC tested with 10000 cycles was cut and presented and described in Fig. 6.18 and Fig. 6.19.

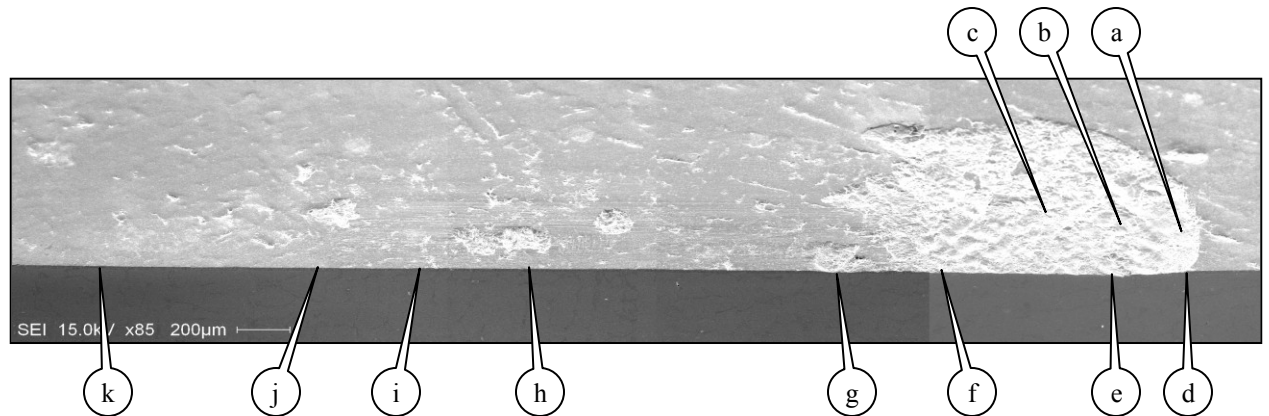


Figure 6.18 Overall SEM image of the cross section of the B_TiC impact-sliding track after 10000 cycles using a steel ball.

The porous structure of the CVD B₄TiC coating seemed to contribute to the best performance among the three coatings. Only small chippings and material transfer occurred after impacts of 1500 cycles. The cross section of the coating after 10000 cycles' test shows that the propagation of fatigue cracks might be stopped by small holes in the coating. With the increasing of impact cycles, abrasive wear occurred and the coating disappeared at the center of the crater. Similar to the other two coating samples, chipping appeared from the crater to the end of the track. Again, the defects shown in bright areas of Fig. 6.19i might be caused by the interaction of the Cr-rich intermetallic phases and coating materials during the coating fabrication process.

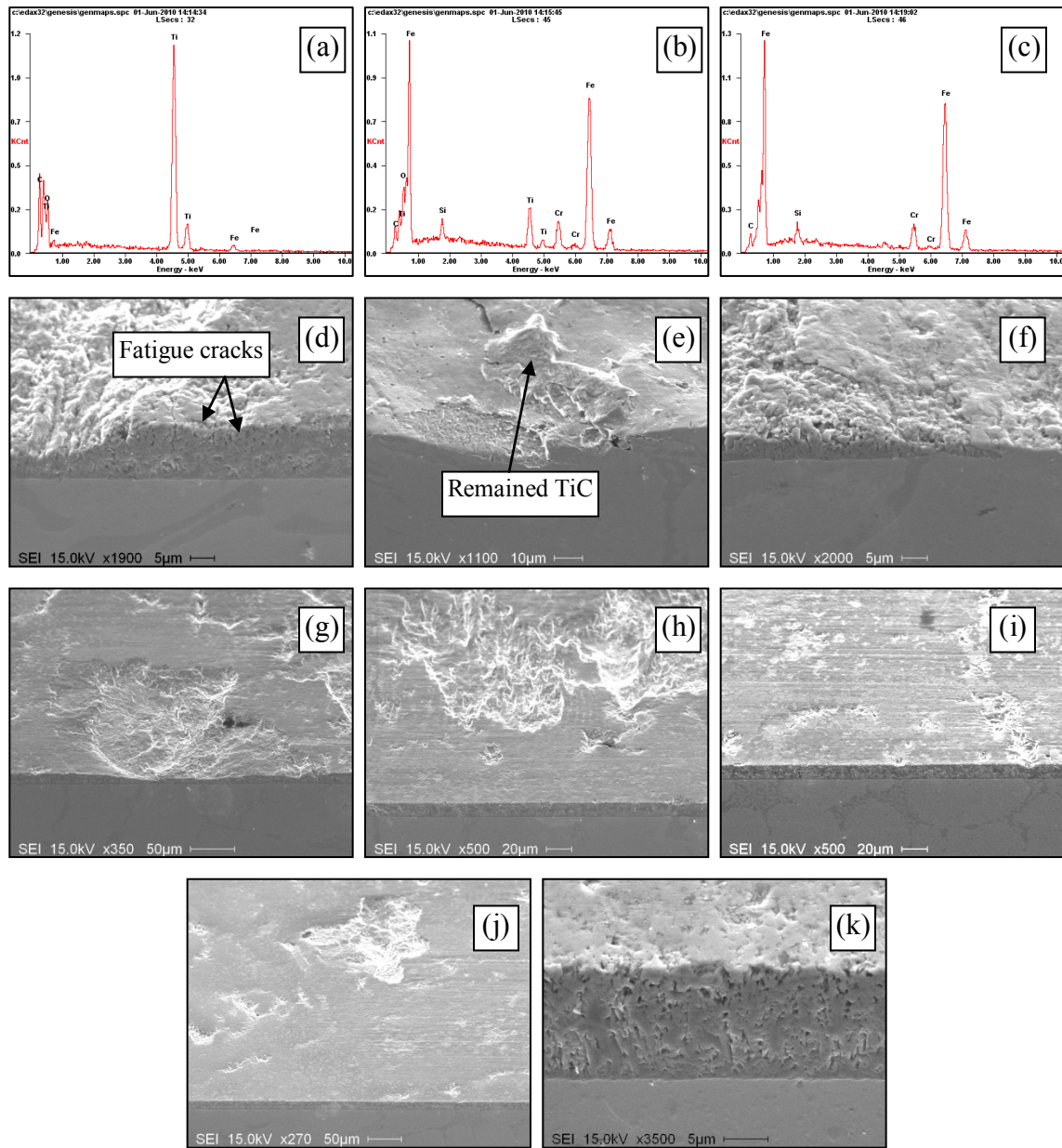


Figure 6.19 Local views of the cross section in Figure 6.18: (a) EDX spectrum showing the dominance of TiC with little amount of Fe transferred from the steel ball; (b) EDX spectrum showing that Fe from the substrate dominated and TiC still existed; (c) EDX spectrum showing nonexistence of TiC ; (d) SEM image showing fatigue cracks stopped in the middle of the coating; (e) remained TiC coating at the center of the crater; (f) end of the crater showing sinking of the coating; (g) chipping; (h) chipping; (i) surface defects and underlying Cr-rich intermetallic phase; (j) scratches and chipping at the tail

of the track; (k) cross section of intact coating showing the porous structure of the CVD B₄TiC coating.

3.3 Ranking of coatings

The coating failure behaviors were described using the possible failure sequences presented in the previous section. In general, all kinds of failures occur at the crater center; chipping/peeling occur near the end of the track. With the increasing of impact cycles, failure areas at the crater and along the sliding track become larger and connect to each other to form the final shape as illustrated in Fig. 6.1. Based on those observations, the performances of different coatings against steel balls are distinguished and evaluated as in Table 6.1. From Table 6.1, B₄TiC is the best coating under the condition of the inclined impact-sliding fatigue testing.

Table 6.1: Ranking of coating failures in inclined impact-sliding tests using steel balls

Coatings	Head (impact)	Middle (sliding)	Tail (sliding)	Subtotal♣ (impact)	Subtotal♦ (sliding)	Subtotal♠ (fatigue)	Total	Rank (impact)	Rank (sliding)	Rank (fatigue)	Rank (overall)
A_TiAlN	xx/xxx/x*	o/xx/o	x/x/x	2/3/1 (6)	1/3/1 (5)	6	11	3	2	6	3
B_AlTiN	xxxxx/xx/x	xxxxx/xx/xx	xxxxx/o/x	5/2/1 (8)	8/2/3 (13)	4	21	6	6	5	6
A_CrN	xxxx/xxx/o	xx/o/x	xxxx/o/o	4/3/0 (7)	6/0/1 (7)	3	14	5	5	3	5
B_CrN	xxx/xx/x	x/o/o	xx/x/x	3/2/1 (6)	3/1/1 (5)	3	11	3	2	3	3
B_TiC	x/x/x	x/o/x	x/o/x	1/1/1 (3)	2/0/2 (4)	1	7	1	1	1	1
C_TiC	xx/xx/o	x/o/o	xxx/o/xx	2/2/0 (4)	4/0/2 (6)	2	10	2	3	2	2

*Note: (peeling + chipping) / fatigue crack/ material transfer: (xxx)/(xxx)/(xxx)

Key: X: severity, O: N/A.

♣Note: impact-induced failures at the head of the impact-sliding wear track

♦Note: sliding-induced failures at the sliding (middle and tail) portion of the impact-sliding wear track

♠Note: fatigue failures occurred at the head, middle and tail portions of the wear track

4. CONCLUSIONS IN PHASE II

Inclined impact-sliding fatigue testing methodology and cross-sectioning technique using EDM cutting were used to study coating failure behavior under the test

conditions representative of stamping applications. Experiments of ball-on-plate inclined impact-sliding fatigue tests (i.e. EIFT) have been performed on six coating samples. After the tests, peeling, chipping, fatigue cracking, and ball material transfer appeared in the impact-sliding wear trails, which can be clearly observed from the sample surface and cross sections. The research results demonstrated that the testing methodology was effective and explicit in evaluation of PVD and CVD coating performance under impact and sliding load conditions.

The findings derived from the testing method for the six coatings were summarized as follows. After EIFT tests, a large number of fatigue cracks can be observed on A_TiAlN and B_CrN coating surfaces, most of which connected to the interface next to the D2 substrate. For A_TiAlN coating, fatigue cracking appeared along the entire impact-sliding trail, and local substrate deformations can be seen in the impact crater where the fatigue cracks occurred. For B_CrN coating, the enlarged crater size, compared to that of A_TiAlN coating, was likely due to the impact ball's flattened surface, caused by abrasive wear from debris of the peeled and chipped coating. Less fatigue cracking and peeling was found on B_TiC coating after 1,500 test cycles. At 10,000 cycles, there was more chipping and peeling. The CVD B_TiC coating was considered the best, and B_CrN performed similarly well to A_TiAlN coating. Although A_TiAlN seems slightly better than B_CrN at 1,500 cycles, it exhibited more fatigue cracking than B_CrN.

CHAPTER 7

INCLINED IMPACT-SLIDING WEAR TESTS OF TiN/Al₂O₃/TiCN COATINGS ON CEMENTED CARBIDE SUBSTRATES

1. INTRODUCTION

The good mechanical properties of titanium nitride (TiN) have made it a common single layer coating used for many applications. TiN improve the life span of tools working at high speeds by modifying surface properties such as decreasing the coefficient of friction, increase hardness and improving wear resistance [1-3]. Past works have also studied the coating structures as well as the effects of coating thickness on properties like hardness, residual stress and wear behaviors [4-6]. However, TiN coatings do not offer optimal performance. Past literatures have reported that coating failure occurs when TiN coated tools performed under low cutting speeds and at elevated temperatures [2, 7]. Thus several works are examining new developments in TiN coatings. Modifications in the composition by including Al, Si or C have shown significant improvement in cutting tool performance and tool life [7, 8]. Furthermore, studies have investigated multilayer coatings and observed better mechanical properties that can provide better wear and corrosion protection [9-12].

In manufacturing or biomedical implant applications, the coated components usually have to withstand repetitive movements of impact and sliding motions with high contact loads. For example, during milling, the interrupted cutting generates impact and sliding forces that can wear out the coating. A multilayer coating on cemented carbide tools has been commercially made for these procedures [13]. This multilayer coating

consists of TiCN, Al₂O₃, and TiN layers. Each layer provides an attractive feature that gives superior coating properties. TiN reduces friction from the contact forces; Al₂O₃ increases oxidation and wear resistance under elevated temperatures and TiCN increases coating hardness. The cemented carbide substrates provide a very strong loading supportive capability to the coating, compared to other substrates such as steel and titanium. However, the cobalt composition in the substrate can affect the substrate hardness and toughness. Usually a higher hardness would decrease the toughness of cemented carbide substrates.

Many well-established testing methods such as the pin-on-disk test, impact test and scratch test have been used to study the coating failures on various substrates [14-16]. However, no adequate testing method is available to test coating wear properties under a combination of impact and sliding motions at an extremely high contact stress condition. There is still a need for a testing method that can study wear caused by the repetitive impact-sliding motions. Thus a new inclined impact-sliding wear testing method was introduced in this paper to simulate those loading conditions. The testing machine applies a normal load to a hard ball which impacts and slides on the coating surface. The impact and sliding motions are controlled by a double-air cylinder driven by compressing air. The pressure of the air cylinder, impact frequency and ball and coating distance can also be adjusted.

The objective of the present work is to use the inclined impact-sliding wear testing instrument to study the failure behavior of a coating on strong substrates (i.e., carbides instead of steels) at ambient temperature. Cemented carbide substrates with the same multilayer coating but with different cobalt contents have been prepared for this

investigation. The coating failures and any correlation with the substrate hardness and toughness are also discussed.

2. EXPERIMENTAL DETAILS

Three different cemented carbide (WC-TiC-Co) substrates were obtained for this investigation. The commercial names of the samples are PM10C, PM25C and PM30C (Sowa Tool & Machine Co. Ltd). A TiN/Al₂O₃/TiCN multilayer has been deposited on the substrates beforehand by using chemical vapor deposition (CVD) method. The thicknesses of TiN/Al₂O₃/TiCN layers in the coatings were obtained by cross sectional observations as 1 µm, 2 µm and 7 µm, respectively. Vickers hardness tests were also performed on the coatings and the substrates. A light load of 25g was used for the coatings while a heavier load of 500g was used for the substrates. Each hardness test was conducted with a loading time 15 seconds. The average hardness of the multilayer coating was 2050HV. The substrate hardness of PM10C, PM25C and PM30C measured were 1720HV, 1440HV and 1610HV, respectively.

A schematic drawing of the inclined impact-sliding wear tester is provided in Refs [17,18]. In this newly developed testing method, the specimen is positioned on an inclined sample holder which is under a hard ball. Similarly to the impact testers used in past works [19], the hard ball oscillates vertically to impact the specimen. Since the specimen is fixed on an inclined sample holder which can rock and swing around an axis, the ball not only presses but also slides on the specimen. A spring allows the sample holder to move back to the original position after each impact. The impacting and sliding motions are controlled by a double-air cylinder driven by compressing air. The pressure

of the air cylinder, the strain of the spring and the ball and specimen distance can be adjusted to calibrate for the required impact and pressing loads. Usually, the pressing force is pre-set by changing air pressure in the cylinder. The impact force requested is then obtained by varying the gap distance between the pact ball and the sample surface to be tested. Prior to the tests, an OMEGA LCKD-500 load cell was placed on the sample holder to record the impact and pressing forces, also shown in Ref [17]. This load cell was used to measure the forces so the test instrument produced the desired impact and pressing forces.

This inclined impact-sliding wear tester was used to carry out the wear tests on the coated cemented carbide samples. The normal impact and pressing forces set were 400N and 200N, respectively. Each sample was impacted by a SAE 51000 steel ball (10mm in diameter) for 1500 cycles. The hard ball was replaced after each test. The testing frequency was 5 Hz, and the ball and sample gap distance before impact was 1.5 mm. The tests were carried out in dry conditions and at room temperature.

After the impact-sliding tests, the coatings were then analyzed by optical microscope and Scanning Electron Microscopy (SEM) to study the coating failure mechanisms. Energy-dispersive X-ray spectroscopy (EDX) was also used to examine the elemental compositions for the different coating failure behaviors. These analytic methods assisted to find any correlation between the wear behaviors of the coatings and the properties of strong substrates.

3. RESULTS

The inclined impact-sliding wear tester had created wear scars on all three coating surfaces. Fig. 7.1 shows the optical images of the wear scars produced on both coatings and counterpart balls. An impact head and a sliding tail are evident in the case of PM10C (Fig. 7.1a). The color of the wear scar is not completely gold; indicating that material from the steel ball may have been transferred or parts of the protective TiN layer may have been removed. Similar results are shown in the case of PM30C (Fig. 7.1c); however, the head and tail components are not as explicit as the ones produced in PM10C. In the case of PM25C (Fig. 7.1b), the wear scar appears to be different than the other samples. Although the head and tail components are present in PM25C, the wear track bulges out more than the other two wear tracks. As well, at least three distinct colors are observed in PM25C. Wear scars on balls are presented in Fig. 7.1d, 1e and 1f. All the wear scars are alike in that they are elliptical with narrow impact heads and sliding tails. The wear scar of PM25C is more severe than of PM10C and PM30C. The sliding distance was around 26 mm in this project which depended on the preloaded spring and pre-set final air pressure for the air cylinder.

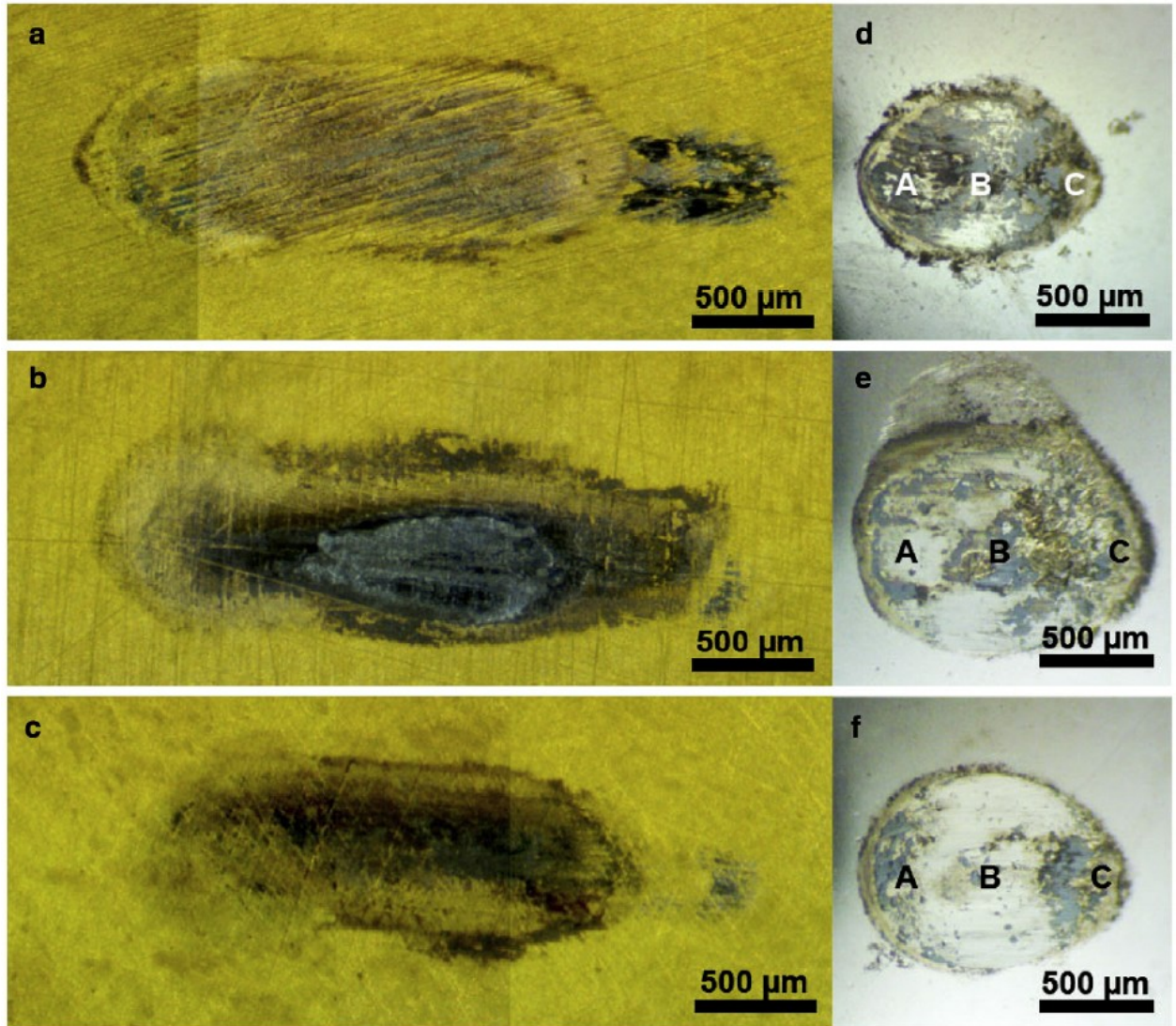


Figure 7.1 Optical images of the wear tracks (craters at left and tails at right) on (a) PM10C, (b) PM25C, (c) PM30C and wear scars on counterpart balls corresponding to (d) PM10C, (e) PM25C and (f) PM30C.

After observing with optical microscope analysis, the coating failures were further analyzed using SEM and EDX analytic techniques. The SEM images of the wear scars are provided in Fig. 7.2. In most cases, SEM and EDX have confirmed at least three primary types of coating failure mechanisms: cohesive failures (or chipping), material

transfer from the steel ball and fatigue cracking. EDX analysis did not detect any tungsten on the damaged coating surfaces.

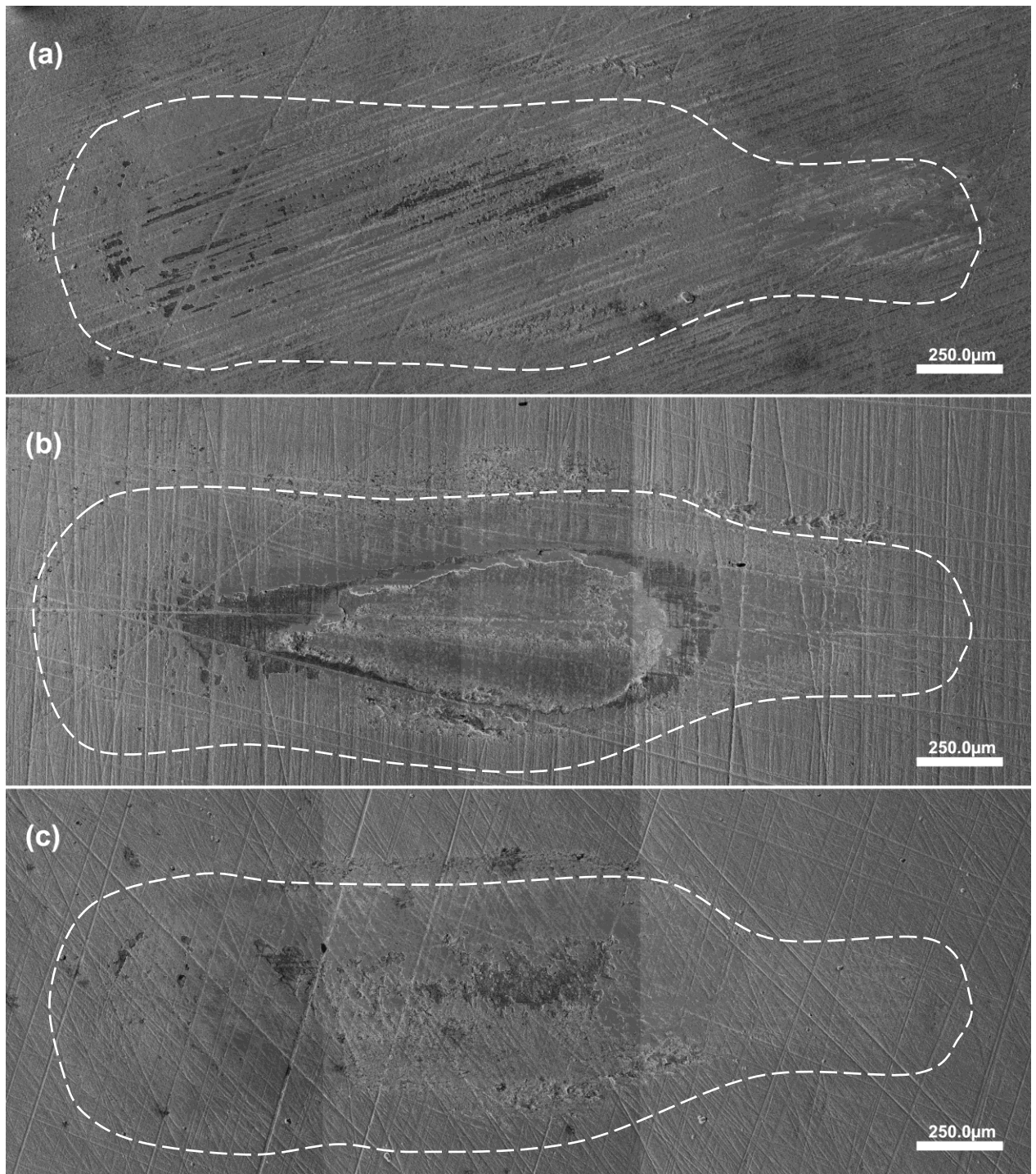


Figure 7.2 SEM (SE) images of the wear scars on (a) PM10C, (b) PM25C and (c) PM30C.

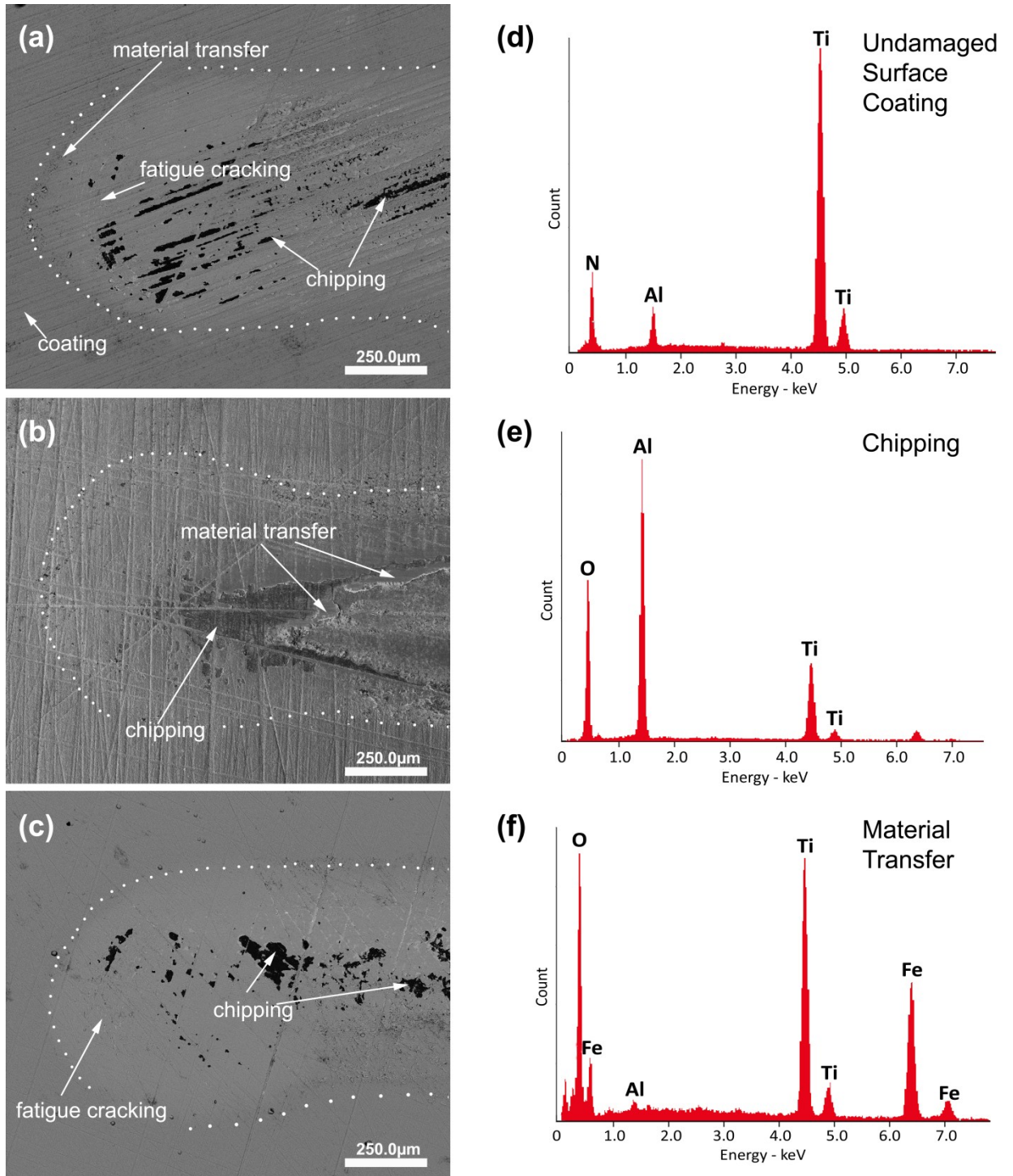


Figure 7.3 The coating failure mechanisms of the impact heads; SEM images of (a) PM10C, (b) PM25C and (c) PM30C; EDX analysis of (d) the undamaged coating surface, (e) chipping and (f) material transfer.

The results from the impact component after 1500 cycles are given in Fig. 7.3. In the case of PM10C (Fig. 7.3a), the thin area surrounding the crater head contained Fe. High intensities of Al and O were found in the dark regions from chipping. Fatigue cracks were also seen around the impact head. Likewise, the impact head of PM30C coating surface (Fig. 7.3c) also contained chipping and fatigue cracks and material transfer. Fig. 7.4 shows the fatigue cracking on PM10C and PM30C at 400X magnification. However, less fatigue cracks and material transfer were observed in this case. In the case of PM25C (Fig. 7.3b), material transfer of Fe and chipping of TiN were observed, but fatigue cracking was not found.

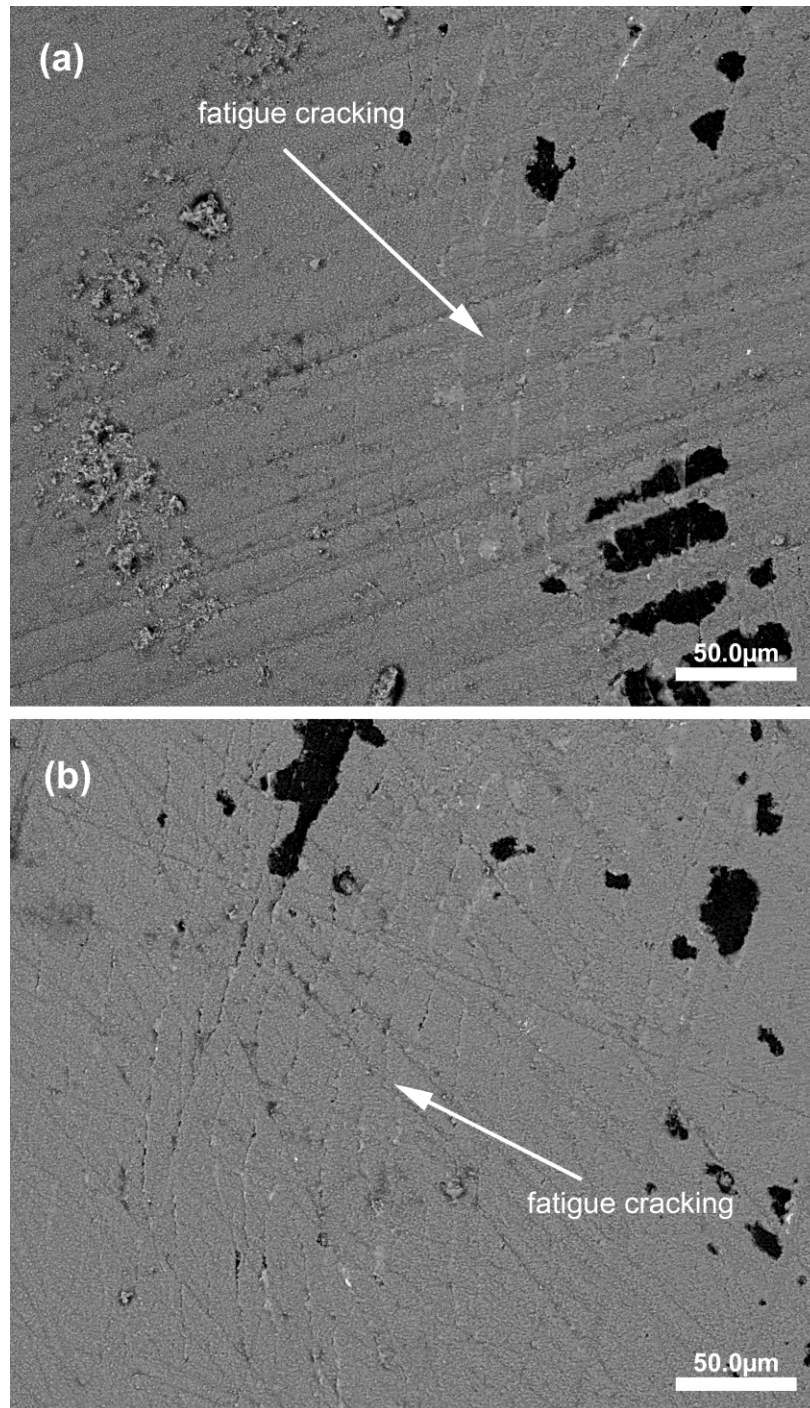


Figure 7.4 Backscattering secondary electron SEM images of impact heads on (a) PM10C and (b) PM30C at 400 \times magnification.

EDX spectra were also obtained for the undamaged coating surface and for the areas with different coating failures behaviors. On the undamaged coating surface (Fig. 7.3d), EDX revealed a high intensity for Ti as well as the presence of Al and N. The low Al peak can be explained by the penetration of X-rays through the thin TiN layer. In the cases of chipping (Fig. 7.3e), EDX detected high intensities for Al and oxygen from the Al_2O_3 beneath the protective layer. Low Ti peaks were also present in the chipping cases. In the case of material transfer (Fig. 7.3f), Fe peaks and high amounts of oxygen were detected. Fe was from the steel ball and oxygen was present due to oxidation after material transfer when high temperatures were locally generated during the ball/coating contact. Carbon was not found in any of the three impact head which means the third TiCN layer was not exposed.

Fig. 7.5 shows the results of the sliding component of the impact-sliding wear testing method. In the case of PM10C (Fig. 7.5a), high intensities of Al and O were found in the dark regions. High amounts of Fe were also found in the end of the tail. In the case of PM25C (Fig. 7.5b); however, the Al_2O_3 and TiCN layers were observed. The dark regions showed high Al and O peaks, while the lighter inner area of the tail contained only Ti, C and N peaks. In addition, material transfer of Fe occurred more at the darker regions than the lighter regions. Fe was also found at the end of the tails. The results of the sliding tail created on the PM30C coating (Fig. 7.5c) were similar to the PM10C case. The TiCN layer was not found and material transfer of Fe was also present in the end of the tail.

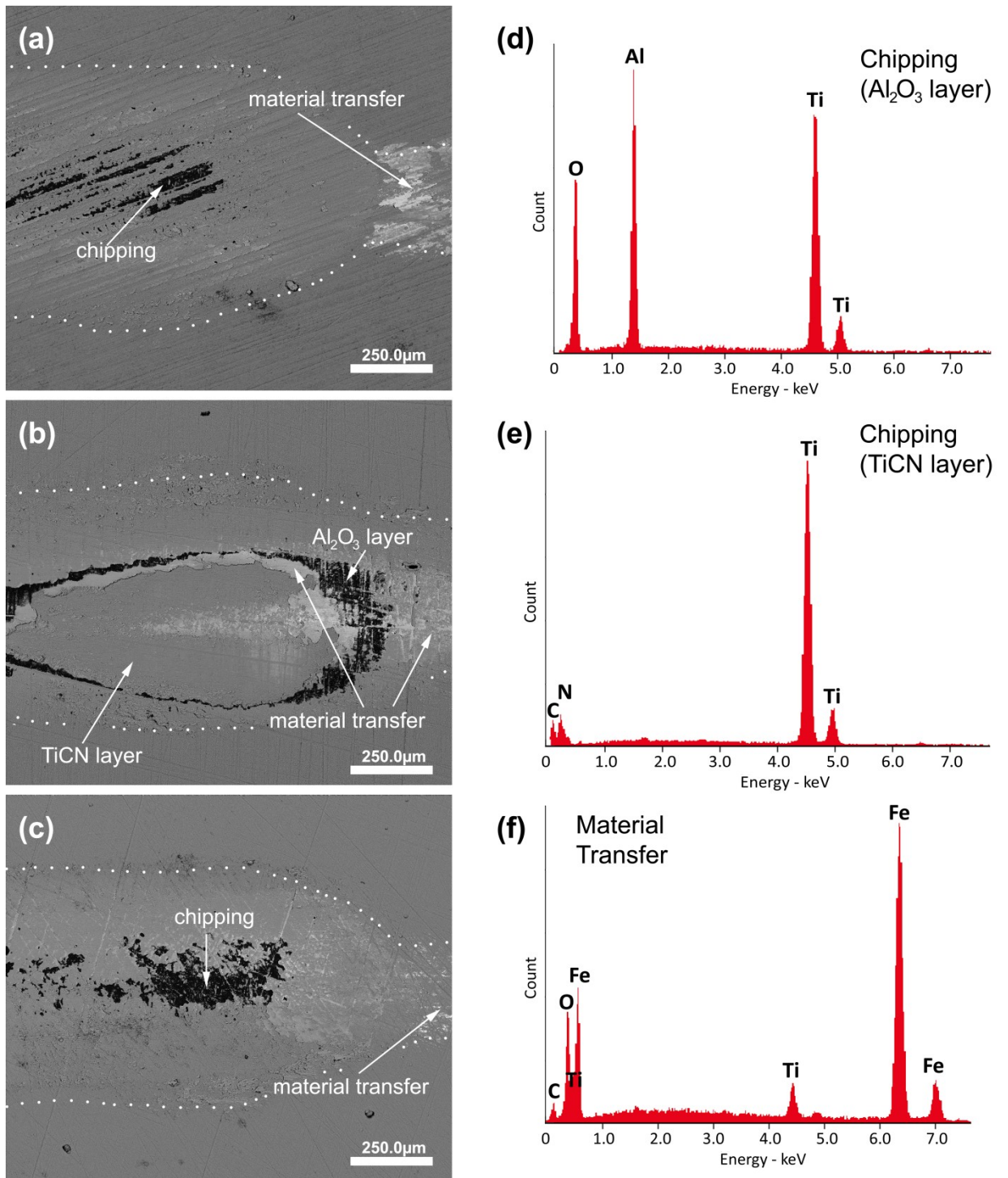


Figure 7.5 Coating failure mechanisms of the sliding tails; SEM images of (a) PM10C, (b) PM25C and (c) PM30C; EDX Analysis of (d) the Al₂O₃ layer, (e) TiCN layer and (f) material transfer.

EDX analysis of the coating failure mechanisms at the sliding tails were also compared with the results from the impact head. Similarly, the spectra did not reveal any tungsten peaks, indicating the coating was not entirely gone. High Al and oxygen peaks were shown in the case of chipping of TiN layer (Fig. 7.5d). In the case of PM25C only; however, one small carbon peak was revealed from the EDX spectra (Fig. 7.5e) indicating the removal of the Al_2O_3 second layer. Unlike the material transfer results in Fig. 7.3f, Fe had higher intensities than Ti at the end of the tails (Fig. 7.5f). This can be explained by the process of the impact-sliding testing method. When the steel ball slides on the coating surface, the ball also pushes the transferred Fe and piles it at the end of the tail.

4. DISCUSSION

This impact-sliding tester was originally designed for simulated tests of coatings in applications of stamping of advanced high-strength steel (AHSS) [13]. Using this method, coatings behaved well in lab also acted well in factories. The sliding behavior of the test during loading (pressing force from 0 N to 200 N) is similar to that of a reciprocal ball-on-plate tribometer, but the sample is held on a tilted plate that changes its inclined angles during the test. At both ends of the sliding wear track, the sliding speed is zero while the speed reaches maximum in the middle area. On the other hand, during the unloading part of each cycle (pressing force quickly dropped from 200 N to 0 N), the sliding speed increases from zero to the maximal till ball/sample contact ends. It is difficult to determine the instant speeds, but the average sliding speed was 0.26 m/s in this case.

The wear scars on coating surfaces were mainly influenced by applied loads and sliding speed. After the impact peak, the force from air cylinder must increase to overcome the spring preload to push down the sample. Before the balance moment is reached, the sliding will not start. Due to the complexity in determination of air pressure increasing behavior in air cylinder, it is hard to tell exactly when the sliding begins. The best approach to study the sliding speed may be to use a slow motion analysis using high speed video camera.

During the loading (pressing force from 0 N to 200 N), the sliding speed was higher in the middle area than at the impact head and sliding tail, as explained above. The higher sliding speed in the middle area resulted in a wider worn area on the sliding ball as shown by Area B (Figures. 1d, 1e and 1f). Area B was a widened worn area in the middle of wear scars on the counterpart balls. In fact, the contact areas on the balls were changed from A to B then to C during the loading period and back to B and A during the unloading period of each cycle. Area A was corresponding to the area of impact crater on the coating, Area B the middle area of the sliding track, and Area C the tail of the track. The crater size of impacted area mainly depended on the impact load used; the end (tail) of wear track was more like a pointed contact due to less sliding wear of the counterpart ball (Area C). During the unloading (pressing force from 200 N to 0 N), the sliding speed increased from zero to the maximal due to the acceleration movement from both the retracting of air cylinder and the returning force of the spring. However, since the pressing force also quickly decreased from 200 N to zero, the unloading part may have a less effect on the wear behavior. If a consideration were needed for the unloading part,

the sliding wear may still be maximal in the middle area due to both the moderate sliding speed and pressing force.

The impact-sliding wear tests showed that the arrangement of the TiN/Al₂O₃/TiCN multilayer coating had superior wear resistance and mechanical properties for commercial uses that involve impact and sliding motions. The results from this laboratory impact-sliding wear tests show that more Fe from the steel ball was transferred on the Al₂O₃ layer than the TiN layer. This reveals that TiN is more appropriate for a protective layer than Al₂O₃ in terms of reducing the material transferring from steel. Fe may have a less chemical affinity to Al₂O₃ than TiN. In addition, the SEM and EDX analyses show that TiN wear in all three sample coating surfaces, but Al₂O₃ was only removed in the case of PM25C. Since Al₂O₃ has a higher oxidation resistance than TiN, Al₂O₃ is suitable for the middle layer for slowing down oxygen diffusion at high temperature during the machining. In the case of PM25C, EDX analysis did not detect any tungsten on the surface, which means that TiCN also has a good wear resistance. TiCN also has higher hardness [8] than TiN and can act as another protective layer.

The results of fatigue cracking at the impact heads can be explained by the substrate hardness and toughness. As the substrate hardness increases, the degree of fatigue cracking observed also increases. The PM10C substrate had the highest hardness value among the coatings and had more fatigue cracks than the other two samples. The high hardness has also decreased the substrate's toughness, which makes the sample the most brittle and the easiest to crack. In the case of PM30 substrate, fatigue cracking was present but not as severe as the PM10 case. Conversely, the PM25C substrate had the

lowest hardness value and also had no fractures at the impact head under the tested condition. Since the substrate was softer than the other two, the substrate may have a slightly plastic deformation instead of cracking. The increase in toughness substrate had made the sample more fatigue cracking resistant. Therefore, a less brittle substrate is more suitable for applications that have to withstand dynamic impact loads.

The presence of carbon at the sliding tail in the case of PM25C can be explained by the substrate hardness. The surface profile measurement on the head and tail of the impact-sliding scar indicated that a slight plastic deformation of the substrate had occurred from the stress caused by the steel ball. Substrate deformation will also cause the coating to deform. This will create more wear by chipping of the top TiN layer followed by adhesive wear between the steel ball and the Al_2O_3 layer. As a result, the TiCN bottom hard layer was exposed. On the other hand, the TiCN layer was not shown in the cases of PM10C and PM30C because the substrates were harder and less prone to the problem caused by even tiny plastic deformation of substrate. In fact, SEM analysis show that the wear scar produced on the PM10C sample had less dark regions (Al_2O_3 layer) than the wear scar produced on the PM30C coating surface. These observations show that the increase of substrate hardness also increases the wear resistance of the coatings. Therefore, the harder substrates are more suitable for applications that involve repetitive sliding.

5. CONCLUSION

The inclined impact-sliding wear tester has been used to study the coating failures mechanisms on strong cemented carbide substrates. The results show that:

1. The TiN/Al₂O₃/TiCN multilayer coating arrangement has shown excellent wear resistance. TiN reduces material transfer build-up from the steel ball, and TiCN has a good wear resistance.
2. The carbide substrate hardness does affect the degree of coating failures. The results from the impact component show that fatigue cracking increases when the substrate hardness increases. The results from the sliding component show that the wear resistance of the coating decreases as the substrate is softer.
3. The CVD TiN/Al₂O₃/TiCN-coated carbide PM10C offers good wear resistance; PM25C provides good fatigue cracking resistance and PM30C can withstand the impact and sliding. These results are useful for development and selection of coatings and substrates where impact and sliding motion forces are involved.

REFERENCE

1. P. Hedenqvist, M. Olsson, P. Wallen, A. Kassman, S. Hogmark, S. Jacobson, *How TiN coatings improve the performance of high speed steel cutting tools*. Surface and Coatings Technology, 1990. **41**(2): p. 243-256.
2. J. Ghani, I. Choudhury, H. Masjuki, *Wear mechanism of TiN coated carbide and uncoated cermets tools at high cutting speed applications*. Journal of Materials Processing Technology, 2004. **153**: p. 1067-1073.
3. J. Gu, G. Barber, S. Tung, R.J. Gu, *Tool life and wear mechanism of uncoated and coated milling inserts*. Wear, 1999. **225**: p. 273-284.
4. W.J. Chou, G.P. Yu, J.H. Huang, *Mechanical properties of TiN thin film coatings on 304 stainless steel substrates*. Surface and Coatings Technology, 2002. **149**(1): p. 7-13.
5. J. Takadoun, H.H. Bennani, *Influence of substrate roughness and coating thickness on adhesion, friction and wear of TiN films*. Surface and Coatings Technology, 1997. **96**(2-3): p. 272-282.
6. F. Lang, Z. Yu, *The corrosion resistance and wear resistance of thick TiN coatings deposited by arc ion plating*. Surface and Coatings Technology, 2001. **145**(1-3): p. 80-87.
7. K.D. Bouzakis, G. Skordaris, S. Gerardis, G. Katirtzoglou, S. Makrimalakis, M. Pappa, E. Lili, R. M'Saoubi, *Ambient and elevated temperature properties of TiN, TiAlN and TiSiN PVD films and their impact on the cutting performance of coated carbide tools*. Surface and Coatings Technology, 2009. **204**(6-7): p. 1061-1065.

8. P. Jindal, A.T. Santhanam, U. Schleinkofer, A.F. Shuster, *Performance of PVD TiN, TiCN, and TiAlN coated cemented carbide tools in turning*. International Journal of Refractory Metals and Hard Materials, 1999. **17**(1-3): p. 163-170.
9. M. Okumiya, M. Griepentrog, *Mechanical properties and tribological behavior of TiN-CrAlN and CrN-CrAlN multilayer coatings*. Surface and Coatings Technology, 1999. **112**(1-3): p. 123-128.
10. M. Bromark, M. Larsson, P. Hedenqvist, S. Hogmark, *Wear of PVD Ti/TiN multilayer coatings*. Surface and Coatings Technology, 1997. **90**(3): p. 217-223.
11. H.C. Barshilia, A. Jain, K. Rajam, *Structure, hardness and thermal stability of nanolayered TiN/CrN multilayer coatings*. Vacuum, 2003. **72**(3): p. 241-248.
12. S. Bull, A. Jones, *Multilayer coatings for improved performance*. Surface and Coatings Technology, 1996. **78**(1-3): p. 173-184.
13. <http://www.sowatool.com/catalogue/pdfs/IndexableCuttingTools/p526-527.pdf>
14. K.D. Bouzakis, A. Asimakopoulos, N. Michailidis, S. Kompogiannis, G. Maliaris, G. Giannopoulos, E. Pavlidou, G. Erkens, *The inclined impact test, an efficient method to characterize coatings' cohesion and adhesion properties*. Thin Solid Films, 2004. **469**: p. 254-262.
15. R. Bantle, A. Matthews, *Investigation into the impact wear behaviour of ceramic coatings*. Surface and Coatings Technology, 1995. **74**: p. 857-868.
16. G. Berg, C. Friedrich, E. Broszeit, C. Berger, *Scratch test measurement of tribological hard coatings in practice*. Fresenius' Journal of Analytical Chemistry, 1997. **358**(1): p. 281-285.

17. <http://www.a-sp.org/database/custom/Coating%20Impact%20Fatigue%20Test%20-%20Phase%20II.PDF>
18. Y. Chen, X. Nie, *Study on Fatigue and Wear Behaviors of a TiN Coating using an Inclined Impact-sliding Test*. Surface and Coatings Technology, 2011. **206**: p. 1977-1982
19. J.F. Su, X. Nie, T. Mulholland, *Combinative Influence of Impact and Pressing Forces on Coating Failure Behaviour*, Surface & Coatings Technology, 2010. **205**: p. 1520–1526

CHAPTER 8

SUBSTRATE EFFECTS ON FAILURE BEHAVIOR OF HARD COATINGS UNDER INCLINED CYCLICAL LOADING CONDITIONS

1. INTRODUCTION

To reduce fuel consumption and CO₂ emission, the advanced high strength steels (AHSS) have been increasingly used as body panels and structures in automotive industry due to their relatively low cost with superiority in the energy absorption during impact which ensures safety whilst reducing vehicle weight [1, 2]. However, due to the increased AHSS strength, forming load and springback also increase dramatically, which result in more frequent die fractures, increased galling and rapid die wear [3]. To extend die life and improve stamping performance, surface treatment or coatings technology are commonly used. Taking advantages of both technologies, a duplex treatment, consisting of plasma nitriding prior to the deposition of PVD coating, provides elastic modulus and hardness gradients in the substrate and improves the load bearing capacity of the substrate and therefore prevents the plastic deformation of the substrate and the delamination of coatings [4-7]. However, a thorough understanding of the substrate effects such as hardness and morphology is still demanded for applications with high and complex loads. For applications that dynamic repetitive loadings are applied, a ball-on-plate impact test has been first introduced by Knotek et al. [8] to evaluate the adhesive and cohesive failures of hard coatings. Bantle and Matthews [9] indicated that three failure zones are involved in the impact indent: a central zone with cohesive failure, an

intermediate zone with cohesive and adhesive failure, and a peripheral zone with circular cracks failure plus pilling up of the material. Knotek et al. [8] and Bouzakis et al. [10, 11] showed that the degradation of the coating induced by repetitive dynamic impact is a fatigue behavior. For coatings experiencing a combination of normal and tangential loadings such as gear coating and die coating, an inclined impact test has been used to examine cohesion and adhesion properties of coatings by applying simultaneously normal and tangential loads [12-19]. Among these testers, the inclined impact-sliding tester developed for Auto/Steel Partnership projects can simultaneously simulate the impact and sliding movements under continuously variable contact stresses and sliding velocities occurred during steel sheet forming and stamping, and has been used successfully to evaluate different hard coatings [15-19]. In this research, the inclined impact-sliding tester was used to study failure behavior of PVD CrN coatings on three plasma nitrided tool steel substrates, i.e., AISI D2, NAAMS S2333 and prehardened Toolox 44. The hardness of the coatings and nitrided substrates was measured. The coating wear tracks after the tests were observed using a scanning electron microscope (SEM) at both top view and cross-sectional view, and the substrate effects were discussed.

2. EXPERIMENTAL DETAILS

The compositions of three tool steel substrates AISI D2, NAAMS S2333 and Toolox[®] 44 are listed in Table 8.1. The first two substrates were treated to have a hardness of HRC 45, and the Toolox 44 was a prehardened steel with HRC 44. All the substrates having a similar initial hardness were then treated at the same time using a plasma nitriding. The nitrided samples were finally coated with a PVD CrN top layer by a

commercial coating supplier to fulfill the duplex treatment requirement for this study. The Vickers hardness of the treated substrates were obtained using Vickers hardness tester (300 gf) at polished cross sections underneath the coatings (Fig. 8.1).

Table 8.1 Chemical Composition of substrates

	C	Si	Mn	Cr	Mo	V
AISI D2	1.55	0.3	0.4	11.8	0.8	0.8
NAAMS S2333	0.56~0.64	0.2~0.5	0.7~0.9	4.3~4.7	0.4~0.6	0.2~0.3
Toolox 44	0.32	0.6~1.1	0.8	1.35	0.8	0.14

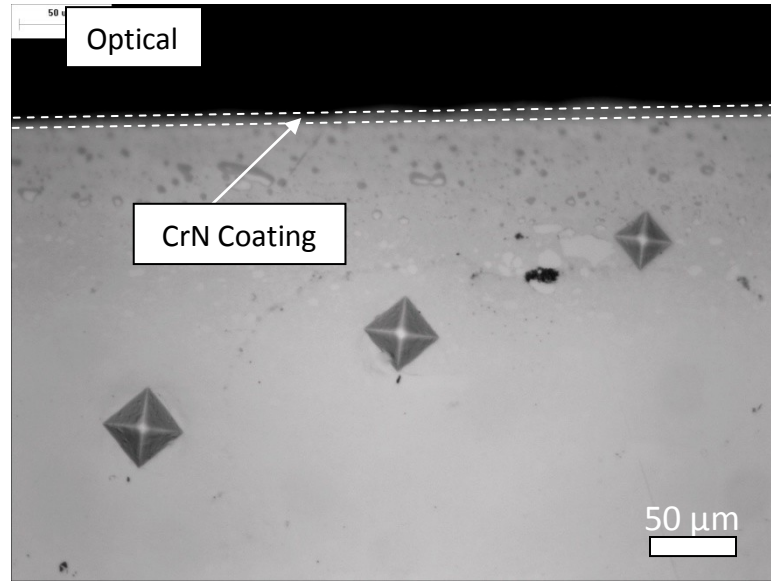


Figure 8.1 Vickers indents beneath the CrN coating

Berkovich hardness and elastic modulus of CrN coatings were obtained using Hysitron Ubi1 nano mechanical testing instrument, and the applied force was 1 mN. Vickers hardness of coatings were obtained using Vickers hardness tester with 300 gf force; the hardness of coatings was the average value of at least 5 indentations for each coating. Coating thicknesses were obtained through SEM observations on cross sections of the samples. To investigate the contact fatigue wear, the duplex treated samples were

tested using an inclined impact-sliding tester as shown in Fig. 8.2. AISI 52100 steel balls of 10 mm diameter were used as counterparts. During the inclined impact-sliding test, a counterpart ball was mounted on the shaft of a two-way air cylinder with the piston driven by compressed air producing vertical oscillatory motions. The sample was set on an inclined rotary sample holder which could return the sample to its original position by a spring. An OMEGA LCKD-500 load cell was placed on the sample holder to record the normal force during the impact-sliding movement. The desired normal impact and pressing forces were obtained by adjusting the pre-strain of the spring and the pressure in the air cylinder. After the impact and pressing forces were measured and recorded, the load cell was removed and the coated coupon was placed on the sample holder for the tests. The gap distance d between the ball and the sample kept the same as the distance between the load cell and the ball.

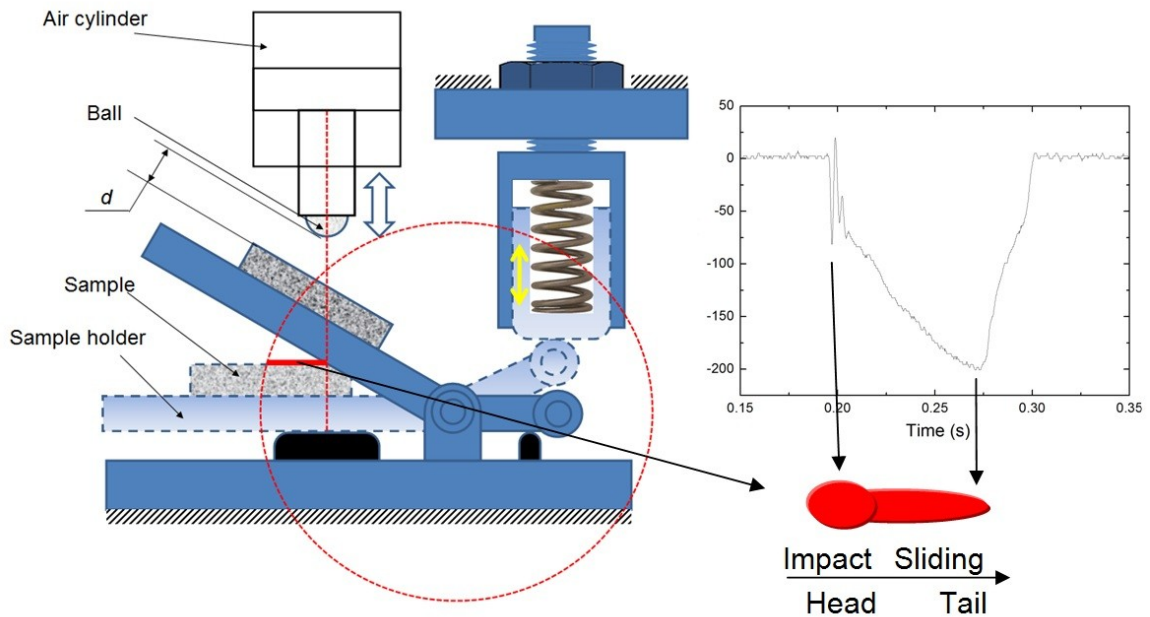


Figure 8.2 Schematic of an inclined impact-sliding tester. To the right, a typical normal force vs. time curve during an impact-sliding cycle [15].

The load condition of the inclined impact-sliding test was presented in Fig. 8.3. The impact frequency, f , was set at 2.5 Hz in all tests and the static air pressure, P , was set around 0.11 MPa. The samples were tested under dry conditions. The impact balls were replaced by a new one after each sample was tested. After the tests, coatings were cut along the center of the impact-sliding tracks using EDM wire cutting and then mechanical sanded and polished. Scanning electron microscopy (SEM) with EDX and an optical microscope were used to observe the morphology of the coating surface, the impact sliding wear tracks and cross-sectional microstructures.






Substrate	1000 cycles, 200/400 N	3000 cycles, 200/400 N	15000 cycles, 200/400 N	5000 cycles, 300/600 N
TOOLOX 44				
NAMMS S2333				
AISI D2				

Figure 8.3 Load conditions for inclined impact-sliding tests.

3. RESULTS AND DISCUSSIONS

3.1 Mechanical properties of CrN coating and steel substrates

Thickness, hardness and elastic modulus of coatings on different substrates are presented in Table 8.2. Fig. 8.4 shows the hardness gradient of three plasma nitrided substrates. For D2, the nitride case had the highest hardness value (17 GPa) but the value decreased rapidly, indicating the nitrided case is thinnest among three samples. For S2333 and Toolox samples, the highest hardness were 15 GPa and 12 GPa, respectively. The hardness of all three substrates at 300 μm away from the coating was almost the same around 700 HV_{0.3}.

Table 8.2 Thickness, hardness and elastic modulus of coatings on the tested substrates

CrN Coatings	Average Thickness (μm)	Berkovich/Vickers Hardness (GPa)	Elastic Modulus (GPa)
on D2 substrate	7.9	21.26 / 20	307.47
on S2333 substrate	7.9	24.84 / 23	328.72
on Toolox substrate	8.0	25.42 / 26	347.89

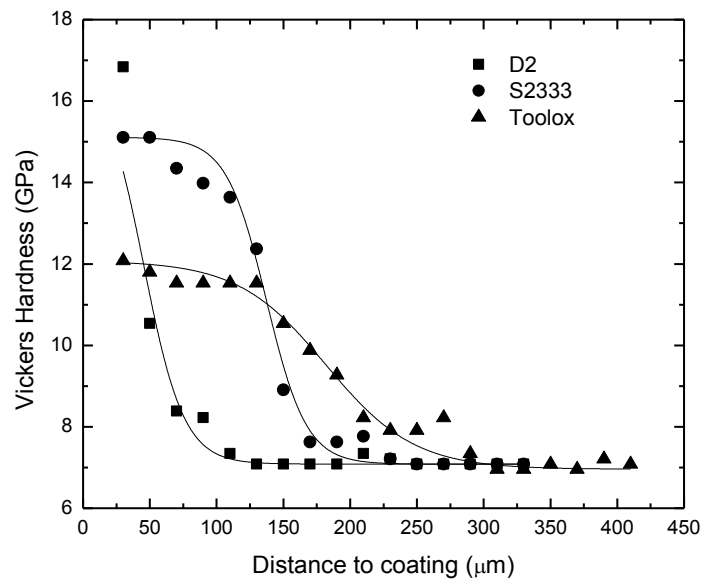


Figure 8.4 Hardness gradients beneath the CrN coating in three substrates.

3.2 Inclined impact-sliding wear tracks

3.2.1 AISI D2

The duplex treated D2 sample was least performed among three samples with the same treatment. After impacted 1000 cycles under 200 N impact and 400 N pressing forces, the coating displayed cohesive failure - chipping, adhesive failure - peeling, materials transfer and fatigue cracks (Fig. 8.5). Fig. 8.5a shows the overall optical image and Fig. 8.5b shows the 45° tilted SEM cross section of as-deposited coating of 8 μm thickness. The EDS spectrum of stable chromium vanadium rich carbides is given in Fig. 8.5c. In Fig. 8.5d, layered structures were found in the chipping area near the crater (the head of wear track) which demonstrated the gradual coating spalling of the coating. In the severely damaged middle part of the wear track (Fig. 8.5e), the coating was peeled off from the substrate and the substrate was uncovered. Fig. 8.5f shows the materials transfer phenomenon where the substrate was covered by iron transferred from the steel ball. Also fatigue cracks were found to prolong from the coating into the substrate. Fig. 8.5g presents the optical image of the tail part in cross section view, where the pressing force was the maximal 400 N. The substrate was plastically deformed and the work hardening likely occurred due to the maximal pressing force. As a result, the hardened substrate showed the hardness gradient, indicated by the winkle structure after polishing. Also, that coating defects such as cracks in the substrate seems to be related to the incoherent carbide particles.

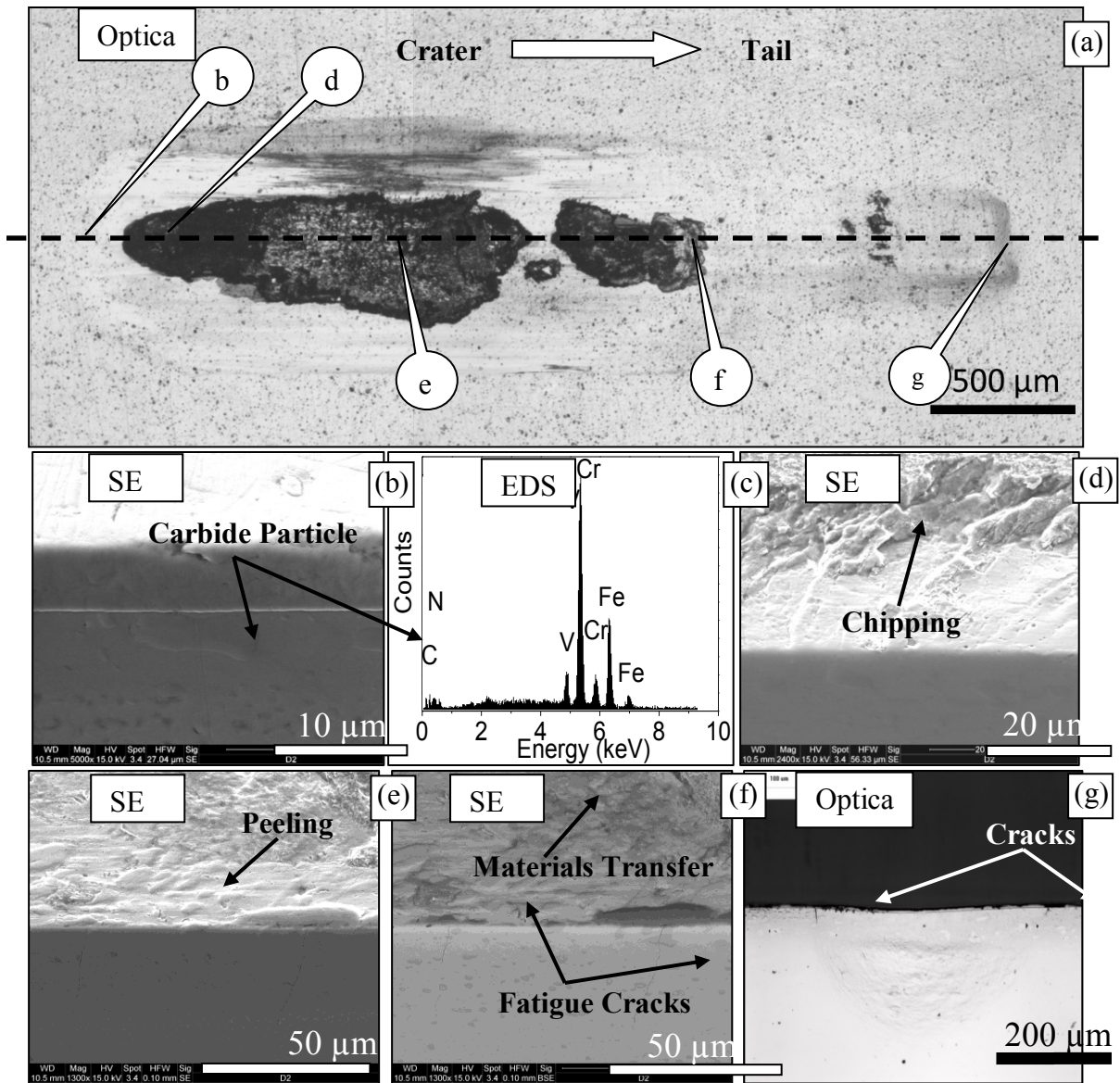


Figure 8.5 The wear track of CrN on D2 substrate after 1000 cycles, 200/400 N

impact/pressing forces. (a) Overall optical view; (b) 45° tilted SEM cross section image of as-deposited coating; (c) EDS spectrum of chromium vanadium rich carbides (darker particles); (d) wear track near the crater head; (d) middle part of wear track; (e) cracks in both the coating and substrate at the middle of the wear track; (f) the tail part of wear track showing plastically deformed wrinkle structure and substrate cracks.

3.2.2 NAAMS S2333

NAAMS S2333 is a medium carbon alloyed steel for die stamping. The CrN coating performed better on the S2333 substrate than on the D2 substrate. Fig. 8.6 shows the impact-sliding wear track of CrN on S2333 substrate after 3000 cycles, 200N impact and 400 N sliding load tests. Only slight scratches were observed along the track. A further test at 15000cycles was carried on at a new location on the same sample. Fig. 8.7 presents the cross section observations of the damaged coatings. Fig. 8.7a is the overall image of the wear track with noticeable fatigue cracks. Fig. 8.7b is the as-deposited coating in a 45° tilted SEM view. Peeling and chipping are shown at the sliding parts of wear track in Fig. 8.7c and Fig. 8.7d, respectively. On the top of the coating in both Fig. 8.7c and Fig. 8.7d, there was an iron layer transferred from the steel ball during the impact-sliding, which was locally eroded during the EDM (electrical discharge machining - wire cutting) processing for the cross sectional sample preparation and presented numerous micro-pores. Fig. 8.7d also demonstrates that the fatigue cracks stopped at the interface of the coating and the substrate. The segments of the cracked coating sunk into the substrate to some extent and formed slightly jagged steps. Obviously, a slower decrease in hardness and elastic modulus of the nitrided S2333 case layer offered better load bearing capacity and elastic bridging than that of D2 substrate.

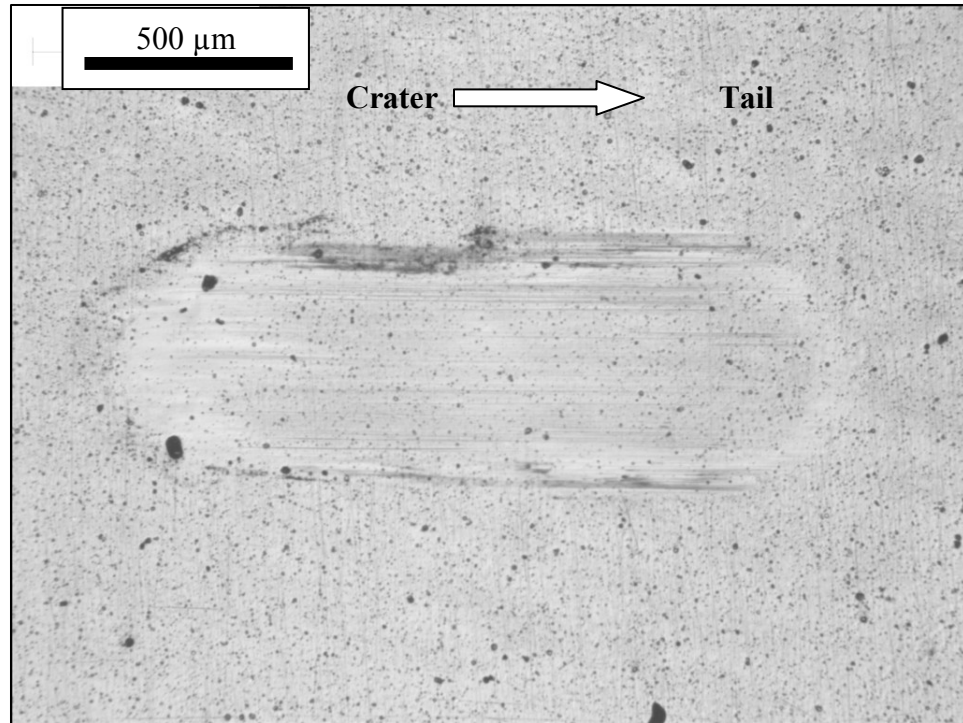


Figure 8.6 Impact-sliding wear track of CrN coating on NAAMS S2333 substrate (impact load 200 / 400 N, 3000 cycles).

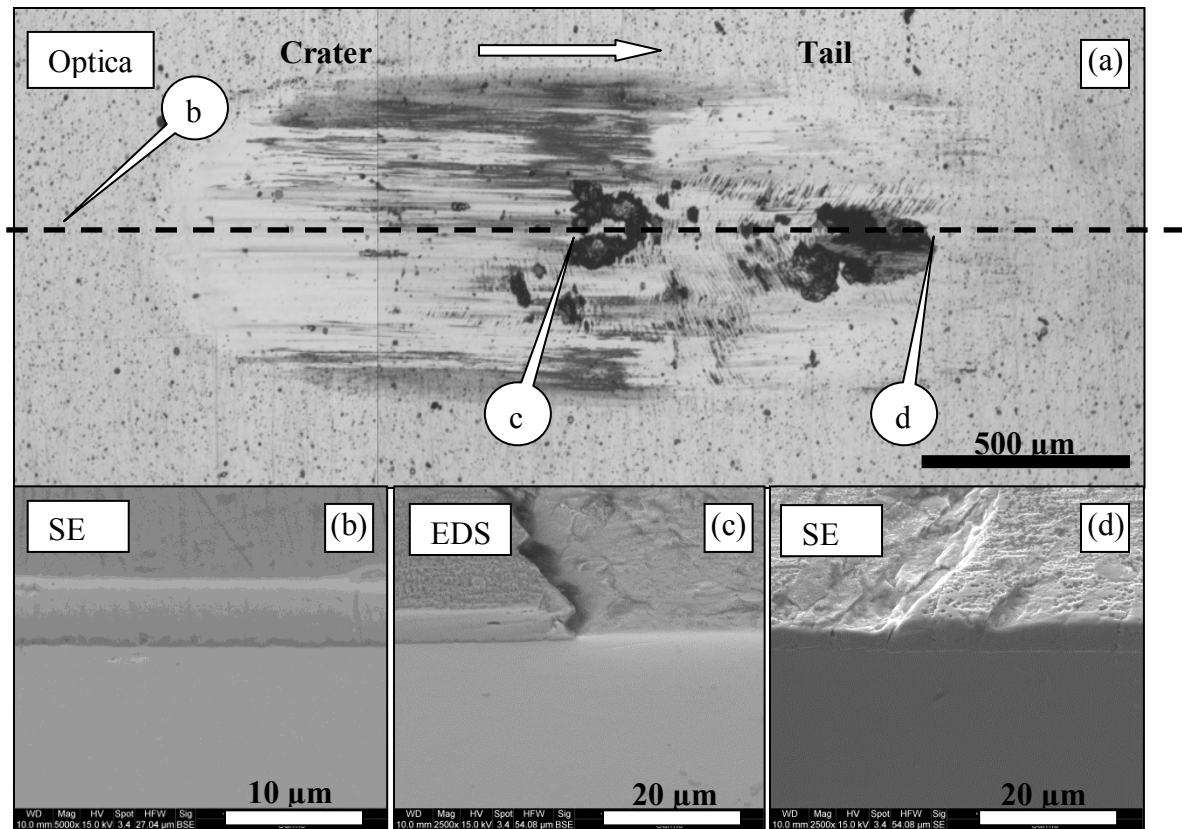


Figure 8.7 The wear track of CrN on S2333 substrate after 15000 cycles, 200/400 N impact/pressing forces. (a) Overall optical view; (b) 45° tilted SEM cross section image of as-deposited coating; (c) peeling of the coating at middle of the track; and (d) chipping of the coating near the tail with slightly jagged steps into the substrate.

3.2.3 Toolox 44

Toolox 44 which has the lowest carbon content among three substrates. Fig. 8.8 shows the wear track of 15000 cycles' impact test under 200 N impact and 400 N maximum pressing load. Scratches were observed along the wear track while the coating still survived after the test. A higher load of 300 N impact and 600 N pressing was applied to investigate the coating capability. After a test of 5000 cycles, coating failures

such as chipping and fatigue cracks appeared. Fig. 8.9a shows that fatigue cracks could be found from the crater to the tail. The as-deposited coating is presented in Fig. 8.9b. No intermetallic precipitates or carbide particle unlike the D2 substrate were observed in the substrate. Fatigue cracks are illustrated in Figs. 8.9c and 8.9d shows a chipping area. Overall, Toolox 44 substrate provided the best load bearing capacity and wear resistance among three substrates.

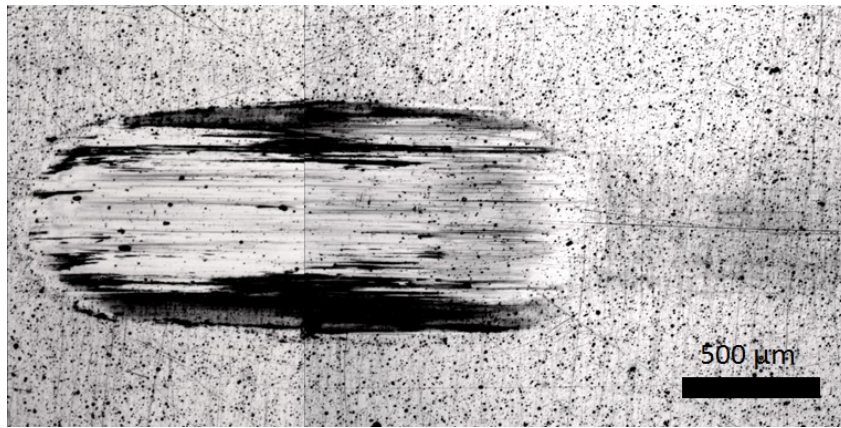


Figure 8.8 Optical image of the wear track of CrN/Toolox coating after 15000 cycles, 200/400 N impact test.

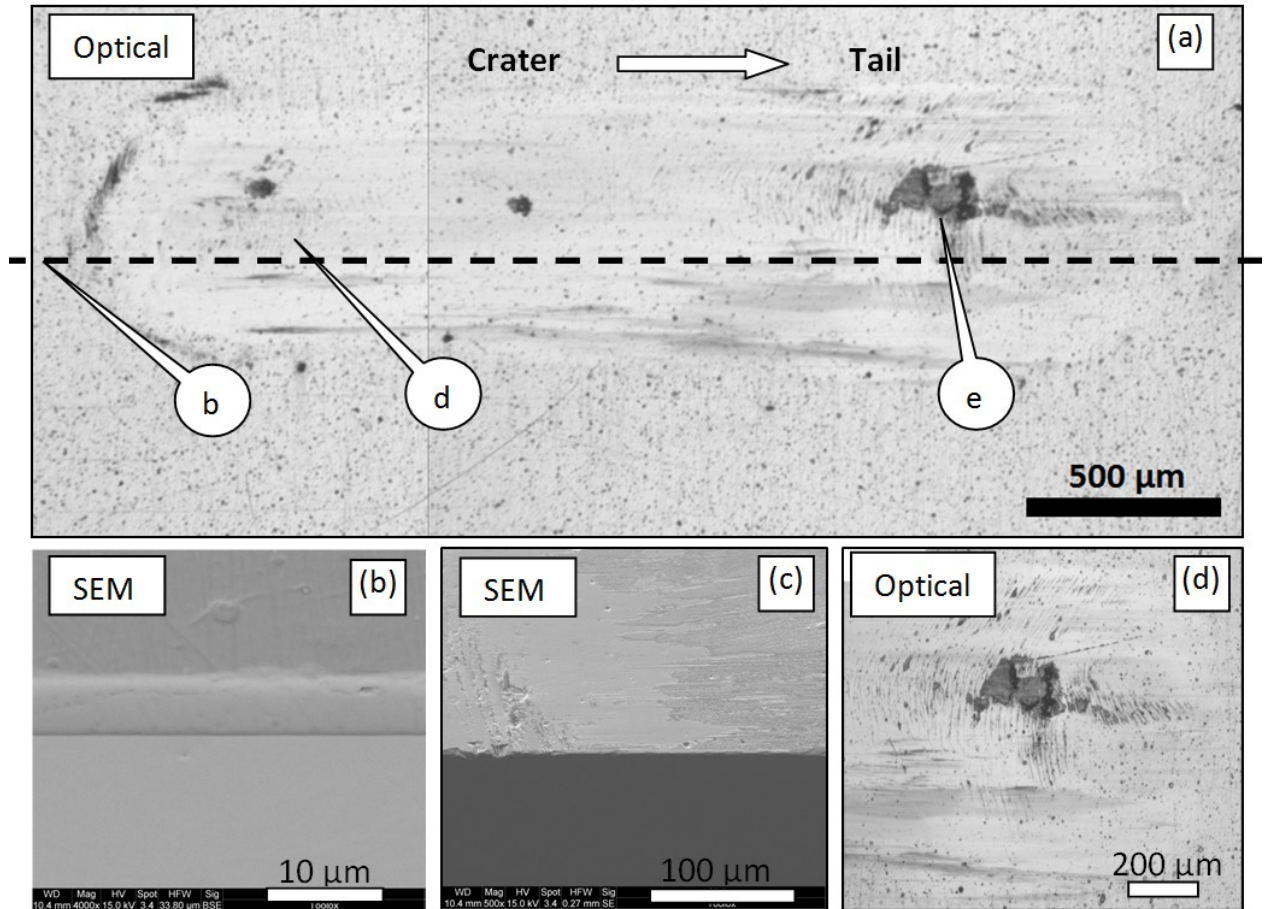


Figure 8.9 The wear track of CrN on Toolox substrate after 5000 cycles, 300/600 N impact/pressing forces. a) Overall optical view; (b) 45° tilted SEM cross section image of as-deposited coating; (c) fatigue cracks near the crater and materials transfer from the steel ball; (d) a chipping area surrounded by fatigue cracks.

3.3 Discussion

Nitrided steels are generally medium-carbon (quenched and tempered) steels that contain strong nitride-forming elements such as aluminum, chromium, vanadium, and molybdenum. Of the alloying elements commonly used in commercial steels, aluminum, chromium, vanadium, tungsten and molybdenum are beneficial in nitriding because they form nitrides that are stable at nitriding temperatures. Molybdenum in addition to its

contribution as a nitride former also reduces the risk of embrittlement at nitriding temperatures. Other alloying elements such as nickel, copper, silicon and manganese have little, if any, effect on nitriding characteristics. Nitralloy types of steels contain about 1% aluminum which forms AlN particles during the nitriding for material strengthening. For the steels studied in this work, chromium would be the main source to enhance case hardness. However, case depth decreased as alloy content increased.

During the plasma nitriding, all the three steels were capable of forming iron nitrides. The D2 steel had a much higher Cr content and thus higher case hardness than NAAMS S2333 and Toolox 44. The total alloy content in D2 was also the highest which would cause the case depth to be the smallest when they were treated at the same condition. The Toolox 44 had the least amount of alloying elements, and as a result, the averaged hardness of the case hardened layer was the lowest but the case depth was the largest among the nitrided steels (Fig. 8.4). The thick case layer would provide a strong load bearing capability. With the elastic modulus bridging effect plus the much increased hardness compared to an untreated steel substrate, the nitrided sample with a thicker case layer (as for Toolox 44) would be able to withstand a higher testing load and defer the initiation of fatigue cracking, as shown by the Toolox 44 case vs. the NAAMS S2333 case in Table 2. That was also true for the cases NAAMS S2333 vs. D2.

Unlike NAAMS S2333 and Toolox 44, the D2 contained a large number of carbide precipitates. The non-uniform microstructure of D2 might cause local strains different when the loading force was applied. The carbide precipitates in D2 steel would interrupt the continuity of the elastic modulus property, leading to a localized strain difference between the steel matrix and the intermetallic compounds (i.e., carbides). The

strain-induced stress might result in additional cracking initiation sites for the top coating and the reason of crack propagation into the substrate as observed in the duplex treated D2.

4. Conclusions:

Inclined impact-sliding contact fatigue wear testing method has been utilized to study substrate effects on failure behavior of duplex treated tool steels under inclined cyclical loading conditions. The following key points can be concluded:

- The substrates have influenced the plasma nitriding case depth (nitride layer thickness) and hardness due to their different amount of alloying elements.
- The thicker hardness case layer and smaller hardness gradient in samples NAAMS S2333 and Toolox 44 would provide a stronger loading support to the coatings, compared to the D2 case.
- The thickest case layer in the Toolox sample would provide the best bridging between the hard coating and substrate in mechanical properties of loading support and particularly elastic modulus.
- Besides the thin nitrided case layer of the D2 providing an insufficient loading bearing capability to the extremely high contact loads, the carbide precipitates in the steel maybe negatively affect the continuity of the elastic module property which would cause a localized strain difference between the steel matrix and the intermetallic compounds. The strain-induced stress may lead to additional cracking initiation sites as observed in the D2 substrate.

- The nitrided sample with a thicker case layer (NAAMS S2333 and Toolox 44) would be able to withstand a higher testing load and defer the initiation of fatigue cracking.
- The samples with more uniform and homogeneous steel substrates Toolox 44 and NAAMS S2333 performed better than the D2 of which the substrate had intermetallic carbide precipitates.
- In general, the steel substrates with different alloying elements could alter mechanical properties of the plasma nitriding case layers which as a result influenced the load support capability to the hard coatings and maybe more importantly, the bridging effect of elastic modules between the coatings and substrate. The substrate microstructural uniformity seems also to play a critical role in performance of the duplex treated samples under the extremely high cyclic contact stress conditions.

REFERENCE

1. T. Senuma, *Physical Metallurgy of Modern High Strength Steel Sheets*, ISIJ International, 2001. **4**: p. 520-532.
2. T. Heller, B. Engl, B. Ehrhardt and J. Esdohr. *New high-strength steels--production, properties and applications*, in Iron and Steel Society/AIME, 40 th Mechanical Working and Steel Processing Conference Proceedings, 1998.
3. J.R. Fekete, J.N. Hall, D.J. Meuleman, and M. Rupp, *Progress in implementation of advanced high-strength steels into vehicle structures*, Iron & steel technology, 2008. **5(10)**: p. 55-64.
4. B. Podgornik and J. Vizintin, *Tribology of thin films and their use in the field of machine elements*, Vacuum, 2002. **68**: p. 39-47.
5. J.C.A. Batista, C. Godoy, V.T.L. Buono and A. Matthews, *Characterisation of duplex and non-duplex (Ti, Al) N and Cr–N PVD coatings*, Materials Science and Engineering: A, 2002. **336**: p. 39-51.
6. P. Panjan, M. Čekada, R. Kirn and M. Soković, *Improvement of die-casting tools with duplex treatment*, Surface and Coatings Technology, 2004. **180**: p. 561-565.
7. M.U. Devi and O.N. Mohanty, *Plasma-nitriding of tool steels for combined percussive impact and rolling fatigue wear applications*, Surface and Coatings Technology, 1998. **107**: p. 55-64.
8. O. Knotek, B. Bosserhoff, A. Schrey, T. Leyendecker, O. Lemmer and S. Esser, *A new technique for testing the impact load of thin films: the coating impact test*, Surface and Coatings Technology, 1992. **54**: p. 102-107.

9. R. Bantle and A. Matthews, *Investigation into the impact wear behaviour of ceramic coatings*, Surface and Coatings Technology, 1995. **74-75**: p. 857-868.
10. K.D. Bouzakis, N. Vidakis, T. Leyendecker, O. Lemmer, H.G. Fuss and G. Erkens, *Determination of the fatigue behaviour of thin hard coatings using the impact test and a FEM simulation*, Surface and Coatings Technology, 1996. **86**: p. 549-556.
11. K.D. Bouzakis, N. Vidakis, T. Leyendecker, G. Erkens, and R. Wenke, *Determination of the fatigue properties of multilayer PVD coatings on various substrates, based on the impact test and its FEM simulation*, Thin Solid Films, 1997. **308**: p. 315-322.
12. K.D. Bouzakis, A. Asimakopoulos, N. Michailidis, S. Kompogiannis, G. Maliaris, G. Giannopoulos, E. Pavlidou and G. Erkens, *The inclined impact test, an efficient method to characterize coatings' cohesion and adhesion properties*, Thin Solid Films, 2004. **469**: p. 254-262.
13. K.D. Bouzakis, A. Asimakopoulos, G. Skordaris, E. Pavlidou and G. Erkens, *The inclined impact test: A novel method for the quantification of the adhesion properties of PVD films*, Wear, 2007. **262**: p. 1471-1478.
14. E.S. Zanoria and L.E. Seitzman, *Characterization of thin metallurgical coating systems by repetitive inclined impact test in dry condition*, Surface and Coatings Technology, 2004. **182**: p. 161-170.
15. J.F. Su and X. Nie, *Coating Impact Fatigue Test - Phase II Final Report*, A/SP Project: ASP230. Project No.: 10-2338. Auto/Steel Partnership, July 2010.

16. Tecnie Corporation, *Impact-Sliding Wear Tests on Duplex-Treated Die Materials - Final Report*, A/SP Project: ASP360. Project No.: 11-2538-AMP, August 2011.
17. J.F. Su, D. Yu, X. Nie and H. Hu, *Inclined impact-sliding wear tests of TiN/Al₂O₃/TiCN coatings on cemented carbide substrates*, Surface and Coatings Technology, 2011. **206**: p. 1998-2004.
18. Y. Chen and X. Nie, *Study on fatigue and wear behaviors of a TiN coating using an inclined impact-sliding test*, Surface and Coatings Technology, 2011. **206**: p. 1977-1982.
19. Y. Chen and X. Nie, *Study of the fatigue wear behaviors of a tungsten carbide diamond-like carbon coating on 316L stainless steel*, Journal of Vacuum Science & Technology A, 2012. **30**: p. 051506-10.

CHAPTER 9

CONCLUSIONS AND FUTURE WORK

1. GENERAL CONCLUSIONS

Applications of metallurgical coatings for automotive components and toolings, from fabrication to characterization, are reported. Traditional materials such as aluminum alloys are demanded due to their high strength weight ratio. However its relatively soft surface limits its application in applications such as engine cylinder. The economical, nontoxic PEO coating has been fabricated on an aluminum cylinder bore surface to resist wear and reduce friction in this project. Both experimental and numerical approaches were applied in this study to evaluate PEO coatings tribological performances under boundary/mixed lubrication conditions.

New materials also bring new opportunities for industry applications. AHSS brings weight loss and crash strength increase, and the tool wear and galling in the mean time. Without proper protection, tools and dies will be worn out soon. Some coatings such as CrN, TiN, TiAlN are all used widely to protect tools and dies. A convenient and effective inclined impact slider tester has been successfully developed to fulfill the task on characterize different hard coatings. With such a tester, the die life in the field testing extended largely. Then main conclusions of above studies can be summarized as following:

- PEO coatings have a low coefficient of friction and minimal wear, compared to the PTWA coating. The variation in tribological behavior and counterface

wear among the tested materials was likely due to different topographic features such as skewness and kurtosis caused by microbump distribution, porosity, and valleys on as-prepared, sanded, and polished coating surfaces. A surface with a lower R_{sk} and a higher R_{ku} can offer a large contact surface area, less sharp asperities—cutting/scratching, and consequently cause less wear of the counterpart surface. Therefore, wear losses of the counterface balls appeared to have an exponential relationship to the R_{sk} and R_{ku} values in the study;

- A numerical lubrication model based on EHL/asperity contacts was built for determination of friction and wear of coated surfaces. Simulations demonstrated that topographic features such as asperity radius of curvature, asperity density and elastic modulus of coated surfaces played key roles in the boundary/mixed lubrication regimes. The simulation predicted that PEO coated samples with lower asperity density and higher asperity radius of curvature (PEO S2) under boundary/mixed lubrication had the lowest friction;
- A novel inclined impact-sliding testing methodology has been developed based on traditional impact testers and the new impact-sliding mechanism successfully to investigate coating failures. Various PVD/CVD coatings were tested by using the inclined impact-sliding tester. Although all coatings showed good adhesion to substrates, they failed under either high impact loads or large number impact cycles. The coating failures were observed and analyzed mainly by using SEM/EDX. Main failure mechanisms of coatings under inclined impact-sliding conditions catalogued as were chipping, peeling,

materials transfer and fatigue cracks. FEM analysis were also carried on and revealed that a harder impact WC ball causes a wider area having a maximum stress in the coating/substrate system than that of a steel ball;

- Further experiments using steel balls were carried on to investigate the effects of impact forces and substrates. As expected, increased impact forces caused the increase in deformation sizes of the craters, severity of cohesive and adhesive failures as well as of fatigue cracks. For the coatings with a less degree of failure, the crater sizes were less dependent on the hardness and thickness of coatings but more dependent on the property of the substrate. The crater sizes almost linearly increased with the impact forces.
- EDM was utilized to cut the impact-sliding tracks to facilitate the observation at the cross-section of the tracks. By using the inclined impact-sliding tester/SEM/EDX/EDM combination, six PVD/CVD coatings were tested to fail and observed to show failure mechanisms. For instance, fatigue cracking appeared along the entire impact-sliding trail of A_TiAlN and B_CrN, and local substrate deformations can be seen in the impact crater where the fatigue cracks occurred. For B_CrN coating, the enlarged crater size, compared to that of A_TiAlN coating, was likely due to the impact ball's flattened surface, caused by abrasive wear from debris of the peeled and chipped coating. Less fatigue cracking and peeling was found on B_TiC coating after 1,500 test cycles. Again, under higher number impact cycles, all coatings failed and failures were observed via above method. Experimental results demonstrated

that the new testing methodology was effective and explicit in evaluation of CVD and PVD coating performance;

- Further study on multilayer coatings showed that multilayer coatings such as TiN/Al₂O₃/TiCN have excellent wear resistance for tooling applications. Fatigue cracking increased for the coating on a harder substrate likely due to the lower toughness of the substrate. The wear resistance of the coating decreased as the substrate was softer. The carbide substrate hardness does affect the degree of coating failures;
- Other than coatings themselves, substrate effects were also investigated. Duplex treated samples, Toolox 44 and NAAMS S2333 performed better than the treated D2 sample likely due to their thicker plasma nitriding cases and more uniform and homogeneous steel substrates, which provided a stronger loading support to the coatings, compared to the D2 case. The substrate microstructural uniformity also played a critical role in performance of the duplex treated samples under the extremely high cyclic contact stress conditions. The carbide precipitates in the steel affected negatively the continuity of the elastic module property which would cause a localized strain difference between the steel matrix and the intermetallic compounds. Therefore, the strain-induced stress may lead to additional cracking initiation sites as observed in the D2 substrate.

In conclusion, the state of art PEO process endows the coating with high hardness, strong adhesion to the substrate and neglectable wear, and comparable low friction like PTWA coating under boundary/starve lubrication conditions. This research with system

analysis proves that PEO is a promising candidate for bore surface treatment of aluminum engines. A numerical simulation of boundary/mixed lubrication of PEO coatings under point contacts was successfully fulfilled to analyze experimental results and predict the tribological performance dependence on surface topography.

A convenient and effective inclined impact slider tester has been successfully developed to fulfill the task on characterize different hard coatings. Such a tester enables the evaluation of the die life in the field testing. Also, examination of on coating failure mechanisms reveals the importance of fine microstructure of the substrate and pre-treatment of the substrate before coating. By utilizing the above novel experimental approaches and numerical simulation technique, a systematic methodology of coating applications for automotive applications can be draw successfully from demand analysis, method determination, and system development to the verification of experimental results and numerical prediction.

2. SUGGESTIONS FOR FUTURE WORK

The study carried out in this dissertation provides the groundwork of PEO coatings under boundary/mixed lubrication conditions and PVD/CVD hard coatings under impact-sliding loads. However, the bench tests had their limitations. For instance, cylinder bores work at high temperature and high load environments where lubricant viscosity changes accordingly. Also lubricants are usually applied to protect die molds, while lubricant was not applied in this study to simulate extreme starve condition and to accelerate the fatigue test. Therefore, suggested future work may include the following:

- Extending the lubrication study on PEO coatings with different surface topography, and investigating the oil retention capability of porous surface of PEO coatings under different temperature/load/speed combinations;
- Verifying numerical simulation with more experimental cases and exploring the possibility on designing PEO surface topography by varying processing parameters;
- Developing ring/bore test rig to construct conformal contact to simulate engine running environment;
- Constructing multiphysics model for inclined impact-sliding testing to simulate dynamic response of coating/substrate system under cyclic loading and lubrication conditions; and
- Performing FEM analysis on coating/substrate system to investigate coating failure mechanism.

CHAPTER 10

CLAIMS TO ORIGINALITY

The following aspects of this study, in terms of the author's opinion, are novel and distinct contributions to original knowledge:

- The performance of PEO coatings on an A356 aluminum alloy under boundary/mixed lubrication conditions was investigated by experimental ball-on-plate tests and hydrodynamic/asperity contacts simulation. The PEO coatings behaved well in experiments, showing high wear resistance and low friction for aluminum alloy engine cylinder bore protection. Surface morphology including skewness and kurtosis was found to affect the tribological behavior. The numerical simulation model based on hydrodynamic lubrication and asperity contact predicted the friction in boundary/mixed lubrication regimes with regards to different coating's elastic modulus, asperity density and asperity radius of curvature.
- The inclined impact-sliding tester was developed for evaluating PVD/CVD hard single/multilayer protective coatings for die mold of AHSS die stamping and tooling. Coating failure mechanisms under simulated impact-sliding motions were experimentally investigated by micro indentation, SEM/EDX and optical observation at both top and cross-section views. In addition, the coatings with more uniform and homogeneous steel substrates performed better than the one which had intermetallic carbide precipitates under the extremely high cyclic contact stress conditions.

APPENDIX A COPYRIGHT RELEASES FROM PUBLICATIONS

Chapter 2

from: **AlPRights**
Permissions Rights@aip.org

to: Jun Feng Su
<sus@uwindsor.ca>

date: Fri, Feb 22, 2013 at 2:46 PM

subject: RE: Request for permission
to include the paper in my
dissertation

Dear Dr. Su:

Thank you for requesting permission to reproduce material from American Vacuum Society publications.

Permission is granted – subject to the conditions outlined below – for the following:

Jun Feng Su, Xueyuan Nie, Henry Hu, and Jimi Tjong. "Friction and counterface wear influenced by surface profiles of plasma electrolytic oxidation coatings on an aluminum A356 alloy", J. Vac. Sci. Technol. A 30, 061402 (2012).

To be used in the following manner:

Reproduced in your doctoral dissertation at the University of Windsor entitled, "Investigation of Metallurgical Coatings for Tooling Applications".

1. The American Vacuum Society grants you non-exclusive world rights in all languages and media.
2. This permission extends to all subsequent and future editions of the new work.
3. The following copyright notice must appear with the material (please fill in the information indicated by capital letters): "Reprinted with permission from [FULL CITATION]. Copyright [PUBLICATION YEAR], American Vacuum Society."
Full citation format is as follows: Author names, journal title, Vol. #, Page #, (Year of publication).
For an article, the copyright notice must be printed on the first page of the article or book chapter. For figures, photographs, covers, or tables, the notice may appear with the material, in a footnote, or in the reference list.
4. This permission does not apply to any materials credited to sources other than the copyright holder.

Please let us know if you have any questions.

Sincerely,
Susann Brailey

Manager, Rights and Permissions
American Institute of Physics
Suite 1NO1
2 Huntington Quadrangle
Melville, NY 11747-4502

Chapter 4 & 6

from: Terry Cullum TCullum@steel.org
to: Jun Su <sus@uwindsor.ca>
cc: Carolyn Philpott <cphilpott@steel.org>
date: Mon, Apr 14, 2014 at 6:20 AM
subject: RE: FW: Request for permission to include the paper in my dissertation
: Important mainly because of the words in the message.

Jun,
Attached is the decision from the A/SP Stamping Tooling Optimization Team.

Terry,

The team approved Jun Feng Su's request to use A/SP STO data and information in his Ph.D. thesis.

We wish him success.

Regards,

Rich.

Good luck and best wishes to you Jun.

Terry

Terry Cullum
Director
Auto Steel Partnership
2000 Town Center Suite 320
Southfield, MI 48075
(248) 945-4770
www.a-sp.org

Auto Steel Partnership Member Companies:

AK Steel Corporation, ArcelorMittal LLC, Chrysler Group LLC, Ford Motor Company, General Motors Company, Nucor Corporation, Severstal North America, United States Steel Corporation

Chapter 5

ELSEVIER LICENSE TERMS AND CONDITIONS

Apr 05, 2014

This is a License Agreement between Jun F. Su ("You") and Elsevier ("Elsevier") provided by Copyright Clearance Center ("CCC"). The license consists of your order details, the terms and conditions provided by Elsevier, and the payment terms and conditions.

All payments must be made in full to CCC. For payment instructions, please see information listed at the bottom of this form.

Supplier	Elsevier Limited The Boulevard, Langford Lane Kidlington, Oxford, OX5 1GB, UK
Registered Company Number	1982084
Customer name	Jun F. Su
Customer address	2281 Bethlehem Ave Windsor, ON N9E4W9
License number	3079370203908
License date	Jan 31, 2013
Licensed content publisher	Elsevier
Licensed content publication	Surface and Coatings Technology
Licensed content title	Combinative influence of impact and pressing forces on coating failure behaviour
Licensed content author	J.F. Su, X. Nie, T. Mulholland
Licensed content date	25 November 2010
Licensed content volume number	205
Licensed content issue number	5
Number of pages	7
Start Page	1520
End Page	1526
Type of Use	reuse in a thesis/dissertation
Portion	full article
Format	both print and electronic
Are you the author of this Elsevier article?	Yes
Will you be translating?	No
Title of your thesis/dissertation	Investigation of Metallurgical Coatings for Tooling Applications
Expected completion date	May 2013

Estimated size (number of pages)	
Elsevier VAT number	GB 494 6272 12
Permissions price	0.00 USD
VAT/Local Sales Tax	0.00 USD / 0.00 GBP
Total	0.00 USD
Terms and Conditions	

INTRODUCTION

1. The publisher for this copyrighted material is Elsevier. By clicking "accept" in connection with completing this licensing transaction, you agree that the following terms and conditions apply to this transaction (along with the Billing and Payment terms and conditions established by Copyright Clearance Center, Inc. ("CCC"), at the time that you opened your Rightslink account and that are available at any time at <http://myaccount.copyright.com>).

GENERAL TERMS

2. Elsevier hereby grants you permission to reproduce the aforementioned material subject to the terms and conditions indicated.

3. Acknowledgement: If any part of the material to be used (for example, figures) has appeared in our publication with credit or acknowledgement to another source, permission must also be sought from that source. If such permission is not obtained then that material may not be included in your publication/copies. Suitable acknowledgement to the source must be made, either as a footnote or in a reference list at the end of your publication, as follows:

“Reprinted from Publication title, Vol /edition number, Author(s), Title of article / title of chapter, Pages No., Copyright (Year), with permission from Elsevier [OR APPLICABLE SOCIETY COPYRIGHT OWNER].” Also Lancet special credit - “Reprinted from The Lancet, Vol. number, Author(s), Title of article, Pages No., Copyright (Year), with permission from Elsevier.”

4. Reproduction of this material is confined to the purpose and/or media for which permission is hereby given.

5. Altering/Modifying Material: Not Permitted. However figures and illustrations may be altered/adapted minimally to serve your work. Any other abbreviations, additions, deletions and/or any other alterations shall be made only with prior written authorization of Elsevier Ltd. (Please contact Elsevier at permissions@elsevier.com)

6. If the permission fee for the requested use of our material is waived in this instance, please be advised that your future requests for Elsevier materials may attract a fee.

7. Reservation of Rights: Publisher reserves all rights not specifically granted in the

combination of (i) the license details provided by you and accepted in the course of this licensing transaction, (ii) these terms and conditions and (iii) CCC's Billing and Payment terms and conditions.

8. License Contingent Upon Payment: While you may exercise the rights licensed immediately upon issuance of the license at the end of the licensing process for the transaction, provided that you have disclosed complete and accurate details of your proposed use, no license is finally effective unless and until full payment is received from you (either by publisher or by CCC) as provided in CCC's Billing and Payment terms and conditions. If full payment is not received on a timely basis, then any license preliminarily granted shall be deemed automatically revoked and shall be void as if never granted. Further, in the event that you breach any of these terms and conditions or any of CCC's Billing and Payment terms and conditions, the license is automatically revoked and shall be void as if never granted. Use of materials as described in a revoked license, as well as any use of the materials beyond the scope of an unrevoked license, may constitute copyright infringement and publisher reserves the right to take any and all action to protect its copyright in the materials.

9. Warranties: Publisher makes no representations or warranties with respect to the licensed material.

10. Indemnity: You hereby indemnify and agree to hold harmless publisher and CCC, and their respective officers, directors, employees and agents, from and against any and all claims arising out of your use of the licensed material other than as specifically authorized pursuant to this license.

11. No Transfer of License: This license is personal to you and may not be sublicensed, assigned, or transferred by you to any other person without publisher's written permission.

12. No Amendment Except in Writing: This license may not be amended except in a writing signed by both parties (or, in the case of publisher, by CCC on publisher's behalf).

13. Objection to Contrary Terms: Publisher hereby objects to any terms contained in any purchase order, acknowledgment, check endorsement or other writing prepared by you, which terms are inconsistent with these terms and conditions or CCC's Billing and Payment terms and conditions. These terms and conditions, together with CCC's Billing and Payment terms and conditions (which are incorporated herein), comprise the entire agreement between you and publisher (and CCC) concerning this licensing transaction. In the event of any conflict between your obligations established by these terms and conditions and those established by CCC's Billing and Payment terms and conditions, these terms and conditions shall control.

14. Revocation: Elsevier or Copyright Clearance Center may deny the permissions described in this License at their sole discretion, for any reason or no reason, with a full refund payable to you. Notice of such denial will be made using the contact information provided by you. Failure to receive such notice will not alter or invalidate the denial. In

no event will Elsevier or Copyright Clearance Center be responsible or liable for any costs, expenses or damage incurred by you as a result of a denial of your permission request, other than a refund of the amount(s) paid by you to Elsevier and/or Copyright Clearance Center for denied permissions.

LIMITED LICENSE

The following terms and conditions apply only to specific license types:

15. Translation: This permission is granted for non-exclusive world **English** rights only unless your license was granted for translation rights. If you licensed translation rights you may only translate this content into the languages you requested. A professional translator must perform all translations and reproduce the content word for word preserving the integrity of the article. If this license is to re-use 1 or 2 figures then permission is granted for non-exclusive world rights in all languages.

16. Website: The following terms and conditions apply to electronic reserve and author websites:

Electronic reserve: If licensed material is to be posted to website, the web site is to be password-protected and made available only to bona fide students registered on a relevant course if:

This license was made in connection with a course,

This permission is granted for 1 year only. You may obtain a license for future website posting,

All content posted to the web site must maintain the copyright information line on the bottom of each image,

A hyper-text must be included to the Homepage of the journal from which you are licensing at <http://www.sciencedirect.com/science/journal/xxxxx> or the Elsevier homepage for books at <http://www.elsevier.com> , and

Central Storage: This license does not include permission for a scanned version of the material to be stored in a central repository such as that provided by Heron/XanEdu.

17. Author website for journals with the following additional clauses:

All content posted to the web site must maintain the copyright information line on the bottom of each image, and the permission granted is limited to the personal version of your paper. You are not allowed to download and post the published electronic version of your article (whether PDF or HTML, proof or final version), nor may you scan the printed edition to create an electronic version. A hyper-text must be included to the Homepage of the journal from which you are licensing at <http://www.sciencedirect.com/science/journal/xxxxx> . As part of our normal production process, you will receive an e-mail notice when your article appears on Elsevier's online service ScienceDirect (www.sciencedirect.com). That e-mail will include the article's Digital Object Identifier (DOI). This number provides the electronic link to the published article and should be included in the posting of your personal version. We ask that you wait

until you receive this e-mail and have the DOI to do any posting.

Central Storage: This license does not include permission for a scanned version of the material to be stored in a central repository such as that provided by Heron/XanEdu.

18. **Author website** for books with the following additional clauses:

Authors are permitted to place a brief summary of their work online only.

A hyper-text must be included to the Elsevier homepage at <http://www.elsevier.com>. All content posted to the web site must maintain the copyright information line on the bottom of each image. You are not allowed to download and post the published electronic version of your chapter, nor may you scan the printed edition to create an electronic version.

Central Storage: This license does not include permission for a scanned version of the material to be stored in a central repository such as that provided by Heron/XanEdu.

19. **Website** (regular and for author): A hyper-text must be included to the Homepage of the journal from which you are licensing at <http://www.sciencedirect.com/science/journal/xxxxx>. or for books to the Elsevier homepage at <http://www.elsevier.com>

20. **Thesis/Dissertation**: If your license is for use in a thesis/dissertation your thesis may be submitted to your institution in either print or electronic form. Should your thesis be published commercially, please reapply for permission. These requirements include permission for the Library and Archives of Canada to supply single copies, on demand, of the complete thesis and include permission for UMI to supply single copies, on demand, of the complete thesis. Should your thesis be published commercially, please reapply for permission.

21. **Other Conditions**:

v1.6

If you would like to pay for this license now, please remit this license along with your payment made payable to "COPYRIGHT CLEARANCE CENTER" otherwise you will be invoiced within 48 hours of the license date. Payment should be in the form of a check or money order referencing your account number and this invoice number 500947108. Once you receive your invoice for this order, you may pay your invoice by credit card. Please follow instructions provided at that time.

Make Payment To:
Copyright Clearance Center
Dept 001
P.O. Box 843006
Boston, MA 02284-3006

For suggestions or comments regarding this order, contact RightsLink Customer Support: customercare@copyright.com or +1-877-622-5543 (toll free in the US) or +1-978-646-2777.

Gratis licenses (referencing \$0 in the Total field) are free. Please retain this printable license for your reference. No payment is required.

Chapter 7

ELSEVIER LICENSE TERMS AND CONDITIONS

Apr 05, 2014

This is a License Agreement between Jun F. Su ("You") and Elsevier ("Elsevier") provided by Copyright Clearance Center ("CCC"). The license consists of your order details, the terms and conditions provided by Elsevier, and the payment terms and conditions.

All payments must be made in full to CCC. For payment instructions, please see information listed at the bottom of this form.

Supplier	Elsevier Limited The Boulevard, Langford Lane Kidlington, Oxford, OX5 1GB, UK
Registered Company Number	1982084
Customer name	Jun F. Su
Customer address	2281 Bethlehem Ave Windsor, ON N9E4W9
License number	3079370408753
License date	Jan 31, 2013
Licensed content publisher	Elsevier
Licensed content publication	Surface and Coatings Technology
Licensed content title	Inclined impact-sliding wear tests of TiN/Al ₂ O ₃ /TiCN coatings on cemented carbide substrates
Licensed content author	J.F. Su, D. Yu, X. Nie, H. Hu
Licensed content date	25 December 2011
Licensed content volume number	206
Licensed content issue number	7
Number of pages	7
Start Page	1998
End Page	2004
Type of Use	reuse in a thesis/dissertation
Intended publisher of new work	other
Portion	full article
Format	both print and electronic
Are you the author of this Elsevier article?	Yes
Will you be translating?	No

Title of your thesis/dissertation	Investigation of Metallurgical Coatings for Tooling Applications
Expected completion date	May 2013
Estimated size (number of pages)	
Elsevier VAT number	GB 494 6272 12
Permissions price	0.00 USD
VAT/Local Sales Tax	0.00 USD / 0.00 GBP
Total	0.00 USD
Terms and Conditions	

INTRODUCTION

1. The publisher for this copyrighted material is Elsevier. By clicking "accept" in connection with completing this licensing transaction, you agree that the following terms and conditions apply to this transaction (along with the Billing and Payment terms and conditions established by Copyright Clearance Center, Inc. ("CCC"), at the time that you opened your Rightslink account and that are available at any time at <http://myaccount.copyright.com>).

GENERAL TERMS

2. Elsevier hereby grants you permission to reproduce the aforementioned material subject to the terms and conditions indicated.

3. Acknowledgement: If any part of the material to be used (for example, figures) has appeared in our publication with credit or acknowledgement to another source, permission must also be sought from that source. If such permission is not obtained then that material may not be included in your publication/copies. Suitable acknowledgement to the source must be made, either as a footnote or in a reference list at the end of your publication, as follows:

“Reprinted from Publication title, Vol /edition number, Author(s), Title of article / title of chapter, Pages No., Copyright (Year), with permission from Elsevier [OR APPLICABLE SOCIETY COPYRIGHT OWNER].” Also Lancet special credit - “Reprinted from The Lancet, Vol. number, Author(s), Title of article, Pages No., Copyright (Year), with permission from Elsevier.”

4. Reproduction of this material is confined to the purpose and/or media for which permission is hereby given.

5. Altering/Modifying Material: Not Permitted. However figures and illustrations may be altered/adapted minimally to serve your work. Any other abbreviations, additions, deletions and/or any other alterations shall be made only with prior written authorization of Elsevier Ltd. (Please contact Elsevier at permissions@elsevier.com)

6. If the permission fee for the requested use of our material is waived in this instance,

please be advised that your future requests for Elsevier materials may attract a fee.

7. **Reservation of Rights:** Publisher reserves all rights not specifically granted in the combination of (i) the license details provided by you and accepted in the course of this licensing transaction, (ii) these terms and conditions and (iii) CCC's Billing and Payment terms and conditions.

8. **License Contingent Upon Payment:** While you may exercise the rights licensed immediately upon issuance of the license at the end of the licensing process for the transaction, provided that you have disclosed complete and accurate details of your proposed use, no license is finally effective unless and until full payment is received from you (either by publisher or by CCC) as provided in CCC's Billing and Payment terms and conditions. If full payment is not received on a timely basis, then any license preliminarily granted shall be deemed automatically revoked and shall be void as if never granted. Further, in the event that you breach any of these terms and conditions or any of CCC's Billing and Payment terms and conditions, the license is automatically revoked and shall be void as if never granted. Use of materials as described in a revoked license, as well as any use of the materials beyond the scope of an unrevoked license, may constitute copyright infringement and publisher reserves the right to take any and all action to protect its copyright in the materials.

9. **Warranties:** Publisher makes no representations or warranties with respect to the licensed material.

10. **Indemnity:** You hereby indemnify and agree to hold harmless publisher and CCC, and their respective officers, directors, employees and agents, from and against any and all claims arising out of your use of the licensed material other than as specifically authorized pursuant to this license.

11. **No Transfer of License:** This license is personal to you and may not be sublicensed, assigned, or transferred by you to any other person without publisher's written permission.

12. **No Amendment Except in Writing:** This license may not be amended except in a writing signed by both parties (or, in the case of publisher, by CCC on publisher's behalf).

13. **Objection to Contrary Terms:** Publisher hereby objects to any terms contained in any purchase order, acknowledgment, check endorsement or other writing prepared by you, which terms are inconsistent with these terms and conditions or CCC's Billing and Payment terms and conditions. These terms and conditions, together with CCC's Billing and Payment terms and conditions (which are incorporated herein), comprise the entire agreement between you and publisher (and CCC) concerning this licensing transaction. In the event of any conflict between your obligations established by these terms and conditions and those established by CCC's Billing and Payment terms and conditions, these terms and conditions shall control.

14. **Revocation:** Elsevier or Copyright Clearance Center may deny the permissions

described in this License at their sole discretion, for any reason or no reason, with a full refund payable to you. Notice of such denial will be made using the contact information provided by you. Failure to receive such notice will not alter or invalidate the denial. In no event will Elsevier or Copyright Clearance Center be responsible or liable for any costs, expenses or damage incurred by you as a result of a denial of your permission request, other than a refund of the amount(s) paid by you to Elsevier and/or Copyright Clearance Center for denied permissions.

LIMITED LICENSE

The following terms and conditions apply only to specific license types:

15. Translation: This permission is granted for non-exclusive world **English** rights only unless your license was granted for translation rights. If you licensed translation rights you may only translate this content into the languages you requested. A professional translator must perform all translations and reproduce the content word for word preserving the integrity of the article. If this license is to re-use 1 or 2 figures then permission is granted for non-exclusive world rights in all languages.

16. Website: The following terms and conditions apply to electronic reserve and author websites:

Electronic reserve: If licensed material is to be posted to website, the web site is to be password-protected and made available only to bona fide students registered on a relevant course if:

This license was made in connection with a course,

This permission is granted for 1 year only. You may obtain a license for future website posting,

All content posted to the web site must maintain the copyright information line on the bottom of each image,

A hyper-text must be included to the Homepage of the journal from which you are licensing at <http://www.sciencedirect.com/science/journal/xxxxx> or the Elsevier homepage for books at <http://www.elsevier.com> , and

Central Storage: This license does not include permission for a scanned version of the material to be stored in a central repository such as that provided by Heron/XanEdu.

17. Author website for journals with the following additional clauses:

All content posted to the web site must maintain the copyright information line on the bottom of each image, and the permission granted is limited to the personal version of your paper. You are not allowed to download and post the published electronic version of your article (whether PDF or HTML, proof or final version), nor may you scan the printed edition to create an electronic version. A hyper-text must be included to the Homepage of the journal from which you are licensing at <http://www.sciencedirect.com/science/journal/xxxxx> . As part of our normal production process, you will receive an e-mail notice when your article appears on Elsevier's online service ScienceDirect (www.sciencedirect.com). That e-mail will include the article's

Digital Object Identifier (DOI). This number provides the electronic link to the published article and should be included in the posting of your personal version. We ask that you wait until you receive this e-mail and have the DOI to do any posting.

Central Storage: This license does not include permission for a scanned version of the material to be stored in a central repository such as that provided by Heron/XanEdu.

18. **Author website** for books with the following additional clauses:

Authors are permitted to place a brief summary of their work online only.

A hyper-text must be included to the Elsevier homepage at <http://www.elsevier.com>. All content posted to the web site must maintain the copyright information line on the bottom of each image. You are not allowed to download and post the published electronic version of your chapter, nor may you scan the printed edition to create an electronic version.

Central Storage: This license does not include permission for a scanned version of the material to be stored in a central repository such as that provided by Heron/XanEdu.

19. **Website** (regular and for author): A hyper-text must be included to the Homepage of the journal from which you are licensing at <http://www.sciencedirect.com/science/journal/xxxxx>. or for books to the Elsevier homepage at <http://www.elsevier.com>

20. **Thesis/Dissertation**: If your license is for use in a thesis/dissertation your thesis may be submitted to your institution in either print or electronic form. Should your thesis be published commercially, please reapply for permission. These requirements include permission for the Library and Archives of Canada to supply single copies, on demand, of the complete thesis and include permission for UMI to supply single copies, on demand, of the complete thesis. Should your thesis be published commercially, please reapply for permission.

21. **Other Conditions**:

v1.6

If you would like to pay for this license now, please remit this license along with your payment made payable to "COPYRIGHT CLEARANCE CENTER" otherwise you will be invoiced within 48 hours of the license date. Payment should be in the form of a check or money order referencing your account number and this invoice number 500947114. Once you receive your invoice for this order, you may pay your invoice by credit card. Please follow instructions provided at that time.

**Make Payment To:
Copyright Clearance Center
Dept 001
P.O. Box 843006
Boston, MA 02284-3006**

For suggestions or comments regarding this order, contact RightsLink Customer

Support: customercare@copyright.com or +1-877-622-5543 (toll free in the US) or +1-978-646-2777.

Gratis licenses (referencing \$0 in the Total field) are free. Please retain this printable license for your reference. No payment is required.

PUBLICATION LIST

REFEREED JOURNAL PUBLICATIONS

1. **Jun Feng Su**, Xueyuan Nie, Henry Hu and Jimi Tjong, “Friction and counterface wear influenced by surface profiles of plasma electrolytic oxidation coatings on an aluminum A356 alloy”, *Journal of Vacuum Science & Technology A*, (2012) Vol. 30, 061402-1-11.
2. **Jun Feng Su**, Xueyuan Nie, Tareena Mulholland, “Combinative influence of impact and pressing forces on coating failure behaviour”, *Surface & Coatings Technology* (2010) Vol. 205, pp. 1520-1526.
3. **Jun Feng Su**, David Yu, Xueyuan Nie, Henry Hu, “Inclined impact–sliding wear tests of TiN/Al₂O₃/TiCN coatings on cemented carbide substrates”, *Surface & Coatings Technology* (2011) Vol. 206, pp. 1998-2004.
4. Linlin Wang, **Jun Feng Su** and Xueyuan Nie, “Corrosion and tribological properties and impact fatigue behaviors of TiN-and DLC-coated stainless steels in a simulated body fluid environment”, *Surface and Coatings Technology* (2010) Vol. 205(5), pp. 1599-1605.
5. Riyad Hussein, Derek Northwood, **Jun Feng Su** and Xueyuan Nie, “A study of the interactive effects of hybrid current modes on the tribological properties of a PEO (plasma electrolytic oxidation) coated AM60B Mg-alloy”, *Surface and Coatings Technology* (2013) Vol. 215, pp. 421-430.
6. Ding, Ting, **Jun Feng Su**, Henry Hu, Xueyuan Nie and Ronald Barron, "Mathematical Modeling of Heat Transfer and Thermal Behaviour of Tool Steel

H13 in Molten Aluminum Alloy A380." *Materials Processing Fundamentals* (2013) pp. 99-108.

OTHER REFEREED CONTRIBUTIONS

7. **Jun Feng Su**, Xueyuan Nie, “Coating Impact Fatigue Test: Phase I”, *Auto/Steel Partnership*, (2009) Project: ASP230, No.09-2330, <http://www.a-sp.org/en/Enabling%20Technologies.aspx>.
8. **Jun Feng Su**, Xueyuan Nie, “Coating Impact Fatigue Test: Phase II”, *Auto/Steel Partnership*, (2010) Project: ASP230, No. 10-2338, <http://www.a-sp.org/en/Enabling%20Technologies.aspx>

REFEREED CONFERENCE PRESENTATIONS

9. **Jun Feng Su**, Xueyuan Nie and Henry Hu, “Fatigue Behavior of TiN coating on WC-Co cemented carbides”, 38th ICMCTF, San Diego, California, USA (2010).
10. **Jun Feng Su**, Linlin Wang and Xueyuan Nie, “Effects of Impact and Sliding Forces on Failure Behavior of a DLC Coating”, AVS 57th International Symposium & Exhibition, Albuquerque, New Mexico, USA (2010).
11. **Jun Feng Su**, Ying Chen, Xueyuan Nie and Ronghua Wei, “Wear properties of thick TiSiCN coatings”, 38th ICMCTF, San Diego, California, USA (2010).
12. **Jun Feng Su**, Xueyuan Nie and Henry Hu, “Tribological Properties of Plasma Electrolytic Oxidation (PEO) Coatings on an Aluminum A356 alloy”, AVS 58th International Symposium & Exhibition, Nashville, Tennessee, USA (2011).

13. **Jun Feng Su**, Xueyuan Nie and Henry Hu, “Tribological contact analysis of a CrN coated surface under inclined impact-sliding wear tests against steel and WC balls”, 39th ICMCTF, San Diego, California, USA (2012).
14. **Jun Feng Su**, Xueyuan Nie and Henry Hu, “Substrate effects on failure behavior of hard coatings under inclined cyclical loading conditions”, 40th ICMCTF, San Diego, California, USA (2013).

VITA AUCTORIS

NAME: Jun Feng Su

PLACE OF BIRTH: Wuhan, China

DATE OF BIRTH: Jan 1971

EDUCATION: University of Windsor, Windsor, ON, Canada

2010-2014 Ph.D. in Engineering Materials

2007-2009 M.Sc. in Material Engineering

Nanyang Technological University, Singapore

2003-2005 M.Eng. in Mechanical Engineering

Nanjing University of Science & Technology, China

1988-1992 B.Sc. in Mechanical Engineering